AFRL-SN-WP-TR-2006-1004

FEATURE EXTRACTION USING ATTRIBUTED SCATTERING CENTER MODELS FOR MODEL-BASED AUTOMATIC TARGET RECOGNITION (ATR)

Randolph L. Moses, Lee C. Potter, and Inder J. Gupta

The Ohio State University
Department of Electrical and Computer Engineering
2015 Neil Avenue
Columbus, OH 43210

OCTOBER 2005

Final Report for 01 December 1996 – 30 October 2005

STINFO FINAL REPORT

SENSORS DIRECTORATE
AIR FORCE RESEARCH LABORATORY
AIR FORCE MATERIEL COMMAND
WRIGHT-PATTERSON AIR FORCE BASE, OH 45433-7320

NOTICE

Using Government drawings, specifications, or other data included in this document for any purpose other than Government procurement does not in any way obligate the U.S. Government. The fact that the Government formulated or supplied the drawings, specifications, or other data does not license the holder or any other person or corporation; or convey any rights or permission to manufacture, use, or sell any patented invention that may relate to them.

This report was cleared for public release by the Air Force Research Laboratory Wright Site (AFRL/WS) Public Affairs Office (PAO) and is releasable to the National Technical Information Service (NTIS). It will be available to the general public, including foreign nationals.

PAO Case Number: AFRL/WS-06-0079, 9 Jan 2006.

THIS TECHNICAL REPORT IS APPROVED FOR PUBLICATION.

_____   _____
Kevin Priddy, Ph.D.   Ricardo A. Diaz
Project Engineer   Acting Chief, ATR & Fusion Algorithms Branch
ATR & Fusion Algorithms Branch   Sensor ATR Technology Division
Sensor ATR Technology Division   Sensors Directorate

_____
Patrick D. Kee
Lt. Col., USAF
Deputy, Sensor ATR Technology Division
Sensors Directorate

This report is published in the interest of scientific and technical information exchange and its publication does not constitute the Government's approval or disapproval of its ideas or findings.

REPORT DOCUMENTATION PAGE

The public reporting burden for this collection of information is estimated to average 1 hour per response, including the time for reviewing instructions, searching existing data sources, gathering and maintaining the data needed, and completing and reviewing the collection of information. Send comments regarding this burden estimate or any other aspect of this collection of information, including suggestions for reducing this burden, to Department of Defense, Washington Headquarters Services, Directorate for Information Operations and Reports (0704-0188), 1215 Jefferson Davis Highway, Suite 1204, Arlington, VA 22202-4302. Respondents should be aware that notwithstanding any other provision of law, no person shall be subject to any penalty for failing to comply with a collection of information if it does not display a currently valid OMB control number. **PLEASE DO NOT RETURN YOUR FORM TO THE ABOVE ADDRESS**.

1. REPORT DATE *(DD-MM-YY)*	2. REPORT TYPE	3. DATES COVERED *(From - To)*
October 2005	Final	12/01/1996 – 10/30/2005

4. TITLE AND SUBTITLE
FEATURE EXTRACTION USING ATTRIBUTED SCATTERING CENTER MODELS FOR MODEL-BASED AUTOMATIC TARGET RECOGNITION (ATR)

5a. CONTRACT NUMBER
F33615-97-1-1020

5b. GRANT NUMBER

5c. PROGRAM ELEMENT NUMBER
62301E

6. AUTHOR(S)
Randolph L. Moses, Lee C. Potter, and Inder J. Gupta

5d. PROJECT NUMBER
ARPA

5e. TASK NUMBER
AA

5f. WORK UNIT NUMBER
1F

7. PERFORMING ORGANIZATION NAME(S) AND ADDRESS(ES)

The Ohio State University
Department of Electrical and Computer Engineering
2015 Neil Avenue
Columbus, OH 43210

8. PERFORMING ORGANIZATION REPORT NUMBER
1034-000-39

9. SPONSORING/MONITORING AGENCY NAME(S) AND ADDRESS(ES)

Sensors Directorate
Air Force Research Laboratory
Air Force Materiel Command
Wright-Patterson AFB, OH 45433-7320

Defense Advanced Research Projects
Agency (DARPA)
3701 N. Fairfax Drive
Arlington, VA 22203-1714

10. SPONSORING/MONITORING AGENCY ACRONYM(S)
AFRL/SNAT

11. SPONSORING/MONITORING AGENCY REPORT NUMBER(S)
AFRL-SN-WP-TR-2006-1004

12. DISTRIBUTION/AVAILABILITY STATEMENT
Approved for public release; distribution is unlimited.

13. SUPPLEMENTARY NOTES
Report contains color.

14. ABSTRACT
This report summarizes our research accomplishments for Contract F33615-97-1-1020, "Feature Extraction using Attributed Scattering Center Models for Model-Based Automatic Target Recognition." The primary research goal of the program was to develop fundamental understanding and advanced signal processing techniques for feature extraction to support feature-based automatic target recognition (ATR) systems employing synthetic aperture radar. This report summarizes the major technical accomplishments that were realized. We developed a set of attributed scattering center models for SAR ATR whose model primitives that balance between modeling fidelity and estimation accuracy. We developed computationally-efficient algorithms for automatic feature extraction of attributed scattering center features from complex SAR image-domain data. We analyzed feature uncertainty and derived analytical uncertainty bounds. We implemented stand-alone match scoring methods to evaluate target discriminability and feature estimation tradeoffs. We developed STAP/SFAP-Based Adaptive Antennas. We developed techniques for understanding rough surface scattering. We developed ultrawide bandwidth antennas, and slot array antennas with wide scan angles. Finally, we increased the U.S. technology base by training of graduate students and by disseminating research through technical publications and presentations.

15. SUBJECT TERMS
Feature extraction; automatic target recognition, ATR performance prediction, synthetic aperture radar

16. SECURITY CLASSIFICATION OF:			17. LIMITATION OF ABSTRACT:	18. NUMBER OF PAGES	19a. NAME OF RESPONSIBLE PERSON (Monitor)
a. REPORT Unclassified	**b. ABSTRACT** Unclassified	**c. THIS PAGE** Unclassified	SAR	180	Dr. Kevin Priddy

19b. TELEPHONE NUMBER *(Include Area Code)*
(937) 255-1115 x4029

Contents

List of Figures

ABSTRACT

This report summarizes our research accomplishments for Contract F33615-97-1-1020, "Feature Extraction using Attributed Scattering Center Models for Model-Based Automatic Target Recognition." The primary research goal of the program was to develop fundamental understanding and advanced signal processing techniques for feature extraction to support feature-based automatic target recognition (ATR) systems employing synthetic aperture radar. This report summarizes the major technical accomplishments that were realized. We developed a set of attributed scattering center models for SAR ATR whose model primitives that balance between modeling fidelity and estimation accuracy. We developed computationally-efficient algorithms for automatic feature extraction of attributed scattering center features from complex SAR image-domain data. We analyzed feature uncertainty and derived analytical uncertainty bounds. We implemented stand-alone match scoring methods to evaluate target discriminability and feature estimation tradeoffs. We developed STAP/SFAP-Based Adaptive Antennas. We developed techniques for understanding rough surface scattering. We developed ultrawide bandwidth antennas, and slot array antennas with wide scan angles. Finally, we increased the US technology base by training of graduate students and by disseminating research through technical publications and presentations.

1. INTRODUCTION

This report summarizes our research accomplishments for Contract F33615-97-1-1020, "Feature Extraction using Attributed Scattering Center Models for Model-Based Automatic Target Recognition." The contract was originally funded by the DARPA Image Understanding Program, and later by DARPA under the MSTAR Enhancements Program (MEP). From December 1996 through April 2002 the project was funded to carry out research on feature extraction using attributed scattering center models for model-based automatic target recognition (ATR). Since April 2002, the project has received funding from Air Force Research Laboratory (AFRL) with a primary focus on funding US graduate students to pursue graduate research on advanced topics related to automatic target recognition.

The primary research goal of the program was to develop fundamental understanding and advanced signal processing techniques for feature extraction to support feature-based automatic target recognition (ATR) systems. Our focus was on synthetic aperture radar (SAR) ATR, although our methods also apply to non-SAR radar ATR, such as high range resolution radar ATR. Our four primary research objectives have been:

1. Develop and validate physically-based models for scattering that can be used for model-based ATR.

2. Develop practical feature estimation algorithms.

3. Measure efficacy of these features for improvements to SAR ATR performance.

4. Enhance the US technology base by training US graduate students in topics related to sensor exploitation systems.

Significant accomplishments of this research program are summarized below:

Developed a set of attributed scattering center models for SAR ATR whose model primitives that balance between modeling fidelity and estimation accuracy. Our work has been aimed at developing attributed scattering center models for radar scattering. These models are founded on electromagnetic scattering theory (uniform theory of diffraction and physical optics). We based our models on scattering theory to ensure that the derived models are physically meaningful.

Electromagnetic scattering models, however, can be too detailed to be of practical use for ATR; we developed models that contain a small number of parameters which can be accurately estimated, and which at the same time describe scattering behavior in sufficient detail to effectively discriminate between targets. We developed physics-based scattering center feature models that characterize RF backscatter responses using multiple attributes for each scattering center; this gives an increased level of target discriminability, which improves ATR performance. Richer features are especially important in extended operating conditions, when fewer target scattering centers are observable.

Developed computationally-efficient algorithms automatic feature extraction of attributed scattering center features from complex SAR image-domain data. The aim has been to derive estimation algorithms that can be implemented in SAR ATR systems. Such algorithms should be computationally practical, should determine model order autonomously, and should be "hands off" algorithms, requiring little or no hand-tuning by the user.

Our effort has focused on developing algorithms that estimate model parameters from complex-valued SAR imagery in the image domain. This is in contrast to many existing parameter estimation methods that operate on SAR phase history data. Image domain processing is more practical, because existing ATR systems operate on SAR image "chips" that have been prescreened by front-end processing. In addition, we developed model order detection and image segmentation algorithms needed for feature extraction. Finally, computational speed of the algorithms is of importance; we have developed algorithms with good statistical properties while minimizing computation.

Analyzed feature uncertainty and derived analytical uncertainty bounds. The goal has been to quantify the ATR performance improvement afforded by our new models and estimation algorithms. We quantifed improvement first by determining the uncertainty of the estimated features. Feature uncertainty is needed in Bayesean evidence accrual used for scoring of candidate target hypotheses to the measured target data. We developed feature extraction algorithms based on maximum likelihood statistical estimation theory, and we derived corresponding Cramér-Rao lower bounds on feature uncertainty. The smaller the feature uncertainty, the more discriminable are targets, and ATR performance improves. Because our models are physically based, we were able to exploit prior information in the feature extraction stage to improve resolution. We achieve sub-pixel accuracy and superresolution of target scattering phenomena.

We characterized achievable estimation accuracy as a function of system parameters, such as bandwidth, center frequency, and signal-to-clutter ratio.

Implemented stand-alone match scoring to evaluate target discriminability and feature estimation tradeoffs. We developed a geometric hashing-based algorithm for match scoring. The purpose was twofold: (i) to consider feature extraction and feature match scoring in a tight loop to exploit synergy for improved ATR, and (ii) to quantitatively evaluate feature extraction performance at the system level as target detection probabilities. We developed match scoring rules that are tailored to the features and extraction algorithms we developed. By characterizing feature uncertainty and coding this uncertainty in a match score, we further increased target discriminability.

Increased the US technology base by training of graduate students and by disseminating research through technical publications and presentations. Thirteen graduate students, nine of which are US citizens, have been supported under this contract to pursue graduate research degrees. Five of these students have taken up jobs with US government or defense related industry after completing their Masters degree. Six of the

students have completed or are pursuing their Ph.D. degree (five at OSU); one is currently in the second year of the Masters degree program. Two former graduate students have taken faculty or postdoctoral research positions at universities, and continue to conduct research and publish on topics related to this program. Some of the research topics used to train these students are outlined below:

3-Dimensional Target Reconstruction: Three-dimensional reconstruction of targets from radar measurements provides for increased discriminability and improved ATR performance. We investigated the use of interferometric synthetic aperture radar (IFSAR) processing for the 3D reconstruction of radar targets. A major source of reconstruction error is induced by multiple scattering responses in a resolution cell, giving rise to height errors. We developed a model for multiple scattering centers within a resolution cell, and analyzed the errors that result using traditional IFSAR height estimation. We developed a simple geometric model that characterizes the height error and suggests tests for detecting or reducing this error. We investigated the use of image magnitude difference as a test statistic to detect multiple scattering responses in a resolution cell, and we analyzed the resulting height error reduction and hypothesis test performance using this statistic. Finally, we considered phase linearity test statistics when three or more IFSAR images are available. Examples using synthetic Xpatch backhoe imagery were generated.

STAP/SFAP-Based Adaptive Antennas: For airborne ATR systems, one needs to update the platform information continuously. Current and future airborne platforms are relying more and more on Global Positioning System (GPS) for navigation and geolocation. GPS, though very accurate and reliable, is vulnerable to radio frequency interference and jamming. The reason for vulnerability is that the GPS signals are very weak (approximately 30 dB below the receiver noise). Adaptive antenna arrays are being used with GPS receivers to suppress interfering signals. The current adaptive antenna based GPS AJ systems (GAS-1 AE) use space-only processing; whereas, the next generation AJ systems will use space-time adaptive processing (STAP) and/or space-frequency adaptive processing (SFAP). STAP/SFAP improves adaptive antenna performance for CW as well as wideband interfering signals and can better handle mismatches between various channels as well as platform generated multipaths. Under this research program, we developed analytical models to predict the performance of STAP/SFAP based antenna electronics [74],[75]. These models were used to study various implementations of STAP/SFAP. It was shown [76] that in the presence of strong wide band interfering signals, STAP, like space-only processing, has to use extra degrees of freedom to suppress interfering signals. Analytical models were also used to compare the performance of space-only, STAP and SFAP based AE under many interference scenarios. It was demonstrated that SFAP performs as well as STAP and for interference scenarios containing wideband as well as narrow band signals, SFAP performs

better than STAP [77]. The performance of space-only processing, STAP and SFAP in the presence of interference multipath was also studied [78]. Simulated as well as real world interference multipath (antenna near a structure and on a platform) were considered. It was shown interference multipath affect the performance of all three systems. As expected, space-only processing suffers the most degradation and in real world scenarios 128-bin SFAP outperforms 5-tap STAP.

Rough Surface Scattering: The performance of radar systems utilized for ATR is typically limited by the signal-to-clutter, rather than signal-to-noise ratio. Signal-to-clutter ratio problems can be improved only by developing effective means for removing clutter from the received signal. While large targets or targets moving at appreciable velocities can often be easily separated from clutter returns, slow moving targets of more moderate cross sections can be very difficult to detect in the presence of clutter. One source of clutter involves microwave backscattering from natural rough surfaces such as terrain or the sea. Understanding physical properties of this rough surface clutter is critical for designing sensors that can separate clutter and target scattering. Accordingly, a study of the properties of rough surface clutter was performed as part of the project. Results of the study show that surface clutter can vary strongly with the physical properties of the observed medium, and that it can be a significant source of errors for ATR systems. As part of the study, the performance of a recent model for computing scattering from rough surfaces (the "small slope approximation") was explored and quantified.

Ultrawide Bandwidth Antennas: Many target recognition applications require ultrawide bandwidth signals for extracting target signatures associated with different geometry and material features of the target. As a part of this effort, a small low profile and UWB antennas that operates from 50 MHz to 2000 MHz was investigated. Antenna miniaturization techniques such as dielectric or reactive loading are commonly used to increase the antenna's electrical size without increasing its physical size. However, each of these miniaturization techniques by itself faces important performance trade-offs for large miniaturization factors. A hybrid approach that involves both dielectric and reactive loading was used to maximize the miniaturization factor while minimizing any adverse effects. Our approach to miniaturizing an UWB antenna involved the use dielectric material on both sides of the antenna (substrate and superstrate) to maximize the miniaturization factor for a given dielectric. In addition, the thickness of the dielectric material was tapered to suppress dielectric resonance oscillation (DRO) modes and surface waves as well as to maintain high-frequency performance. To maximize the miniaturization factor while minimizing the negative effects of dielectric loading, reactive loading or the artificial transmission line was also used. This allowed us to minimize the dielectric constant which results in less impedance reduction, a minimal antenna weight and reduces possible surface wave effects.

Slot Array Antennas with Wide Scan Angle: The uses of Unmanned Air Vehicles (UAV) are likely to increase in the future. These vehicles will be used for reconnaissance, surveillance as well as for mapping small areas. Because the platform size is relatively small and useable space for large antennas is at a premium, it is important to understand the relationship between viable antenna performance and radar system requirements. For these applications, a broad band wide scan angle Synthetic Aperture Radar (SAR) antenna array is of interest. The challenge is to design the array so that it can be placed on a relatively flat surface underneath the belly of the vehicle. Because of the directions that the SAR needs to operate relative to the array surface, wide scan angle ability is desirable. In addition, since future SAR systems' would benefit from the highest resolution possible, as large a bandwidth as possible is desired. All of these requirements present a difficult challenge for present day antenna manufacturing. Under this research effort, an antenna array design was determined that can provide the needed requirements for the desired radar system performance on such a UAV location. It can provide a thin conformal shape for the antenna elements and feed structure. Based on possible "behind the ground plane" components available in the next few years a one band design is achievable. It also easily provides for extension into a two band design when small enough components can be manufactured in the future.

An outline of the report is as follows. Chapter 2 introduces attributed scattering models for SAR, and presents feature extraction algorithms, feature uncertainty, and results on synthetic and measured SAR data. Chapter 3 presents an algorithm for model-based classification of radar images, using the attributed scattering center features of Chapter 2. Chapters 4–8 present research results from several graduate students who were funded as AFRL fellowship students during the latter part of the program. Chapter 4 presents research on interferometric SAR for 3D target reconstruction; Christian Austin conducted this research and was advised by Prof. Randolph Moses. Mr. Austin will complete his M.S. degree in December 2005 and continue for a Ph.D. degree at Ohio State. Chapter 5 presents research on a large bandwidth slot array with wide scan angle; John McCann conducted research on, and was advised by Dr. Ronald J. Marhefka and Prof. Benedikt A. Munk. Chapter 6 presents research on rough surface clutter; Michael S. Gilbert conducted this research and was advised by Prof. Joel T. Johnson. Chapter 7 presents research conducted by Thomas D. Moore and Matthew L. Rankin on STAP/SFAP based adaptive antennas, advised by Dr. Inder J. Gupta. Dr. Moore received his Ph.D. from the Ohio State University in December 2002, and Mr. Rankin received his M.Sc. in Electrical and Computer Engineering from the Ohio State university in June 2004. Finally, Chapter 8 presents research conducted by Brad Kramer on miniature UWB antenna designs; he was advised by Dr. Chi-Chih Chen, and Prof. John L. Volakis.

2. ATTRIBUTED SCATTERING MODELS FOR SYNTHETIC APERTURE RADAR

2.1 Introduction

The electromagnetic reflectivity of an object is closely related to its geometry and orientation. Reflectivity data of an object can be obtained by a synthetic aperture radar (SAR) by illuminating a region with electromagnetic radiation and measuring the energy scattered back. The data obtained as a result of this process is a finite-extent, noisy set of information about the scattering structures of the object. We wish to process this data and extract information regarding the object's features, which may then be used to identify the object.

When SAR data is gathered at high frequencies, the geometric theory of diffraction [8] allows us to view a target as a collection of simple, isolated scattering structures referred to as scattering centers. Hence, the total response from the complex target can be approximated as the sum of responses of these individual scattering centers. We employ this assumption throughout our study and approach the feature extraction problem at a scattering center level.

We assume that the backscatter from a scattering structure complies with a parametric model. This model is developed by Gerry [6] and it contains parameters that are related to the location, orientation and geometry of the scatterer. Using this model, the noisy SAR measurements from a complex target are approximated as the sum of the models of the individual scattering centers and a Gaussian noise term. Feature vectors for the scattering geometries are then obtained by estimating the parameters in their corresponding model. Furthermore, these estimated features can be matched to the features of known targets for target recognition applications.

With the adoption of the parametric model, we have expressed the feature extraction problem as a parameter estimation problem. Given the SAR data of a target, we wish to obtain the estimates of the parameters of its scattering centers.

There are two possible domains in which we can perform the estimation process. The first is the frequency domain. The measurements made at various frequencies and aspect angles constitute the frequency domain data. In this domain, the response from a scattering center is observed throughout the entire frequency grid, and the total response is the sum of several of these individual scattering center responses. Determining the number of scatterers that form the total response is a difficult model order selection problem. In addition, all of the scatterers have to be processed simultaneously since their responses cannot be isolated from one another; this results in a high dimensional estimation problem with no practical solution.

The second possible domain is the image domain. The frequency domain measured data is

6

pre-processed and transformed to form the corresponding SAR image. In the image domain, most of the energy from scattering centers is isolated in small regions. This property allows sequential processing of scatterers, so that practical estimation algorithms can be developed.

In [6], Gerry describes some algorithms to obtain the parameter estimates. These algorithms require a lot of human interface at the stages of order selection, scattering center region extraction and parameter initialization, which is not desirable in automatic target recognition applications. Koets developed an estimation algorithm in [10] that eliminated the user interface. However, this automated algorithm is slow and has convergence problems in most cases. Also, some ad-hoc techniques have been implemented that have questionable applicability to general targets.

In this report, we have developed a fast algorithm that is shown to give very satisfactory results. As a first step, a user-friendly program asks the data collection and image formation parameters to be input. This is the only human interface required in the algorithm. Following this, a region is extracted that contains most of the energy from a single scattering center. The extracted scatterer is classified as a localized or a distributed scattering center. Since the parametric models for the two scattering structures differ, localized/distributed classification allows us to choose the appropriate model for the response of interest. We then assign initial values to the parameters in the corresponding model. Effective initialization is crucial for the algorithm to converge to the correct solution. A numerical optimization routine follows the initialization and obtains the final estimates by minimizing a cost function according to a maximum likelihood criterion. Several algorithm modifications have been developed to decrease the computational cost and improve the overall performance.

We have performed an extensive study on the problem of classifying scattering centers as localized or distributed structures. We propose a generalized likelihood ratio test (GLRT) and two computationally more efficient heuristic tests. We present performance evaluation of these proposed tests through simulations.

We have first applied our parameter estimation algorithm to noisy SAR images that we generate using the parametric model. By generating the data ourselves, we know the actual values of the parameters and can therefore derive theoretical bounds on the minimum achievable estimate variances. We compare the obtained parameter estimate variances to the theoretical bounds (Cramér-Rao Bound) in order to assess the statistical performance of the algorithm; we find the algorithm is performing successfully. We have also performed experiments on Xpatch simulated data and measured data of a test target (SLICY) [12]. We present the parameter estimates obtained and discussed the results.

Finally, we have performed a side study on establishing a correspondence between the physical scattering structures being imaged and the SNR value observed in their corresponding SAR image. We make use of a concept called the radar cross section (RCS), which is a measure of a target's reflectivity. Assuming a specific imaging scene, we predict the SNR through the RCS of the object and the background in the scene. We also obtain estimates of SNR from available measured data. We present the results of both the prediction and

7

the estimation approaches.

An outline of this chapter is as follows.

In Section 2.2 we provide a brief background on synthetic aperture radars. We explain the data collection and image formation scenarios. We then introduce the scattering center approach and present the assumed parametric model for radar backscatter. Section 2.3 discusses the parameter estimation approaches we have developed. We also provide a statistical performance evaluation. In Section 2.10 we discuss the structure selection problem. Section 2.11 demonstrates the algorithm's performance on synthetic and measured SAR data of the SLICY test target. Section 2.12 includes some concluding remarks.

2.2 Attributed Scattering Center Model

2.2.1 Introduction

In this section, we first provide a brief background on synthetic aperture radar (SAR), focusing on the spotlight mode of operation. We describe the data collection process for this specific operating mode. We then explain the image formation process that transforms the measured frequency domain data into a SAR image. Finally, we introduce an attributed scattering center model that represents the electromagnetic backscatter from an object.

2.2.2 Background on Synthetic Aperture Radar (SAR)

In synthetic aperture radar, a region in space is illuminated with electromagnetic radiation, and the backscatter from that region is measured. This illumination-measurement process is repeated at several locations, hence forming the aperture of the radar. There are three main modes of operation for SAR, corresponding to different ways in which the aperture is created [11]. In strip-mapping SAR mode, the aperture is formed by flying the radar in a straight trajectory along the scene. The radar always points to the side at a right angle to the flight path, so the imaging scene changes as the radar moves. As a result, the whole area that the radar beam sweeps is mapped with this mode of operation. In the inverse SAR (ISAR) mode, the radar is fixed while the target rotates, and measurements are taken at various angles of rotation. The ISAR mode is mathematically equivalent to the spotlight SAR mode, in which the object is fixed and the measurements are obtained along a path, as seen in Figure 2.1. We are primarily interested in the spotlight mode of operation.

2.2.3 Data Collection

In spotlight mode SAR, data are collected at several aperture points along the path. At each aperture point, the object of interest is illuminated with electromagnetic radiation, and the

8
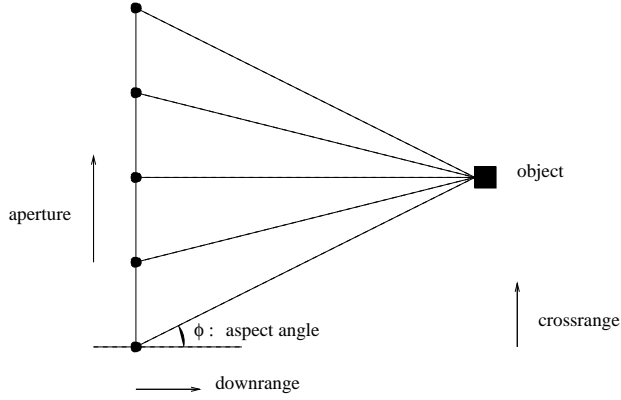
Figure 2.1: SAR Spotlight Mode of Operation

backscattered energy is measured as a complex-valued quantity. The radar is assumed to be fixed in its position from the time it sends the signal to the time it receives the backscatter. Then, the radar moves to the next aperture point to repeat the process.

The angle that the direction of radiation makes with the normal to the broadside of the object is called the aspect angle and is represented by ϕ. Each aperture point corresponds to a different aspect angle, and ϕ forms the first dimension of our measurements. The second dimension is the frequency, f. The electromagnetic signal that is sent has nonzero components in a band of frequencies. Therefore, the response obtained contains information at frequencies within the band. The larger the width of the band, the better the resolution will be in the downrange direction. The cross-range resolution improves as the angular data collection region becomes wider.

As a result of this process, complex-valued backscatter measurement data is collected over a range of aspect angles and frequencies. This data collection range corresponds to a segment of an annular region in the polar plane [11, 2], as seen in solid lines in Figure 2.2. The aspect angle ϕ takes values between $-\phi_m/2$ and $\phi_m/2$, and is expressed in units of degrees. The frequency f ranges from $\left(1 - \frac{\beta}{2}\right) \cdot f_c$ to $\left(1 + \frac{\beta}{2}\right) \cdot f_c$ and it is in units of GHz, where f_c correspond to the center frequency of the band. The relative bandwidth β is defined as the ratio of the total bandwidth to the center frequency.

2.2.4 Image Formation

At the end of the data collection process, we have the complex-valued measurements $\tilde{D}(f, \phi)$ in polar coordinates (f, ϕ). For imaging purposes, this polar domain data is first resampled to a uniform grid on Cartesian coordinates (f_x, f_y) where

$$f_x = f \cos(\phi) \qquad f_y = f \sin(\phi) \tag{2.1}$$

9
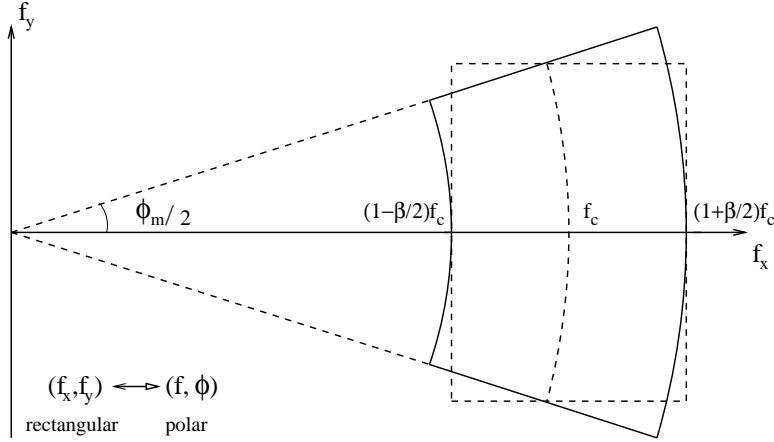
Figure 2.2: SAR Data Collection Range

The resampled data $\tilde{D}(f_x, f_y)$ consists of uniformly spaced data points within the region enclosed by the dotted rectangle in Figure 2.2 [11]. In this new Cartesian grid, f_x ranges from $f_c \cdot \left(1 - \frac{\beta}{2}\right)$ to $f_c \cdot \left(1 + \frac{\beta}{2}\right)$, whereas $f_y \in \left[-f_c \cdot \sin\left(\frac{\phi_m}{2}\right), f_c \cdot \sin\left(\frac{\phi_m}{2}\right)\right]$[1]. We assume M data points in the f_x range and N data points in the f_y range.

As a result of resampling, we have an $M \times N$ array of data $\tilde{D}(f_x, f_y)$ which is in the frequency domain. We need to transform this data into the image domain to obtain the SAR image. This task can be achieved by two-dimensional inverse Fourier transforming the frequency domain data. However, some pre-processing of the data is required before performing the 2D-IFFT in order to improve the quality of the resulting image.

The data collected has finite extent. This finite extent data can be thought of as having data over the entire (f_x, f_y) space and multiplying it with a rectangular window which leaves us with our current data set. If a 2D-IFFT is performed on this data, the image obtained would be the convolution of the actual image with the 2D-IFFT of the rectangular window. This would result in large sidelobes that degrade the image quality. In order to reduce the effects of large sidelobes, the data at hand is first multiplied by a window. This windowing process reduces the sidelobes by smoothing the transition from the no-data region to the rectangular data grid. One drawback of this windowing is a reduction in resolution due to the reduced effective width of the window [13]; however, this drawback is tolerable. A common window used for this purpose is the Taylor window. In our studies we have employed a Taylor window with a -35 dB sidelobe level.

Another pre-processing step is to zero-pad the windowed data before transforming it to the image domain. Although this process does not improve the resolution property of the image, it helps us obtain a smoother image by reducing the actual size of the image pixel.

---

[1]Sometimes the rectangular region is decreased so that it lies entirely within the annular region.
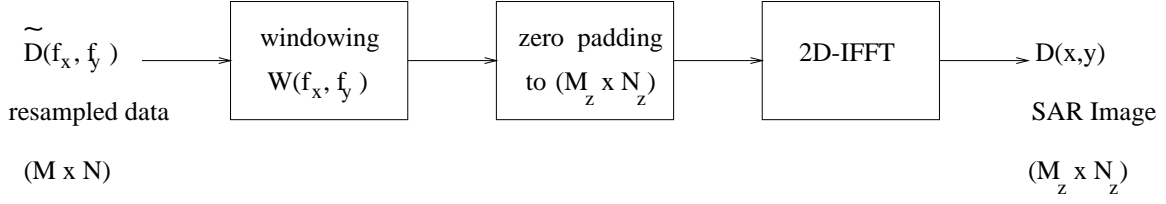
Figure 2.3: SAR Image Formation Block Diagram

Therefore we zero-pad the $M \times N$ sized windowed data to a new size of $M_z \times N_z$. We typically use 50% zero padding; that is $M_z = 1.5M$ and $N_z = 1.5N$.

The overall imaging process can be seen as a block diagram in Figure 2.3. At the end, the SAR image $D(x, y)$ is obtained.

2.2.5 Parametric Model

In this section, we present a parametric model for the backscattered field of an individual scattering mechanism. This model is developed by Gerry [6, 31] and is based on a high-frequency approximation of electromagnetic scattering. According to the geometric theory of diffraction, if the wavelength of the incident radiation is small compared to the size of an object, then the object is assumed to consist of electrically isolated scattering centers [8]. Therefore, the total response $\tilde{E}(f, \phi; \theta)$ of the object can be modeled as the sum of its individual scattering center models

$$\tilde{E}(f, \phi; \theta) = \sum_{i=1}^{n} \tilde{E}_i(f, \phi; \theta_i) \qquad (2.2)$$

where $\theta^T = [\theta_1^T, \ldots, \theta_n^T]$ and

$$\begin{aligned}
\tilde{E}_i(f, \phi; \theta_i) &= A_i \cdot \left(j \frac{f}{f_c} \right)^{\alpha_i} \cdot \exp\left(\frac{-j4\pi f}{c} (x_i \cos\phi + y_i \sin\phi) \right) \\
&\quad \cdot \operatorname{sinc}\left(\frac{2\pi f}{c} L_i \sin(\phi - \bar{\phi}_i) \right) \cdot \exp(-2\pi f \gamma_i \sin\phi) \qquad (2.3)
\end{aligned}$$

Each term $\tilde{E}_i(f, \phi; \theta_i)$ represents the backscatter from a single scattering mechanism as a function of frequency f, aspect angle ϕ and parameter set $\theta_i = [x_i, y_i, \alpha_i, \gamma_i, \bar{\phi}_i, L_i, A_i]$. The propagation velocity of the electromagnetic signal is denoted by c, where $c = 0.3 \times 10^9$ m/sec.

The set of parameters $\{x_i, y_i, \alpha_i, \gamma_i, \bar{\phi}_i, L_i, A_i\}$ used in the model have physical interpretations related to the location and the geometry of the scatterer. The parameters x_i and y_i

11
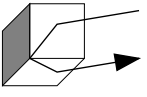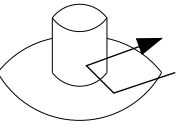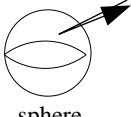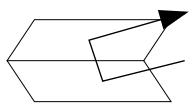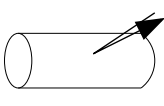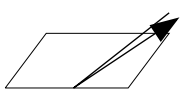
	α = 1	α = 1/2	α = 0
L = 0	corner	top hat	sphere
L > 0	dihedral	cylinder	edge

Figure 2.4: Scattering Primitives

correspond to the downrange and crossrange location of the scattering center, in meters. The relative amplitude of the measured field is represented by $A_i \in \mathbb{C}$ [2]. In the case of multiple polarization data, A_i is a vector. The parameter α_i characterizes the frequency dependence of the response and is discrete-valued taking half integer values less than or equal to one. Values of α_i less than zero correspond to diffractive scattering and such responses are very weak at high frequencies. The length of the scattering center is denoted by L_i, and $\bar{\phi}_i$ is its orientation angle with respect to the broadside. The parameter γ_i models the mild aspect dependence of localized scattering center cross section.

There are two types of scattering centers: localized and distributed. As the name suggests, localized scattering centers have responses that are localized in the image domain. For these scatterers, the length parameter L is equal to zero and the orientation angle $\bar{\phi}$ is undefined. Distributed scattering responses usually span several image pixels along the crossrange direction. The parameter γ equals zero for distributed scattering mechanisms.

The parameters α and L contain information about the geometry of the scatterers. A zero-valued length parameter corresponds to a localized scattering center whereas $L > 0$ means that the scatterer is distributed. The frequency dependence parameter α is related to the curvature information. It takes the value 1 for flat surfaces, 1/2 for singly-curved surfaces and 0 for doubly-curved surfaces. Negative values of α correspond to diffraction scattering terms; at high frequencies, these terms typically have very low amplitude. The two parameters (α, L) can be used to distinguish among several scattering primitives. In Figure 2.4, some examples of these scattering primitives are displayed along with their corresponding α and L values.

---

[2]For perfectly electric conductors measured in the far-zone, it has been hypothesized that $A_i \in \mathbb{R}$ [6]; however, we assume $A_i \in \mathbb{C}$ in this work.

2.2.6 Parameter Normalization

In order to provide a resolution-independent description of the model, we normalize the model parameters. The normalization process also provides a scaling among the parameters that results in improved numerical properties of parameter estimation algorithms.

The downrange and crossrange dimensions of an image pixel, in meters are given by

$$p_x = \frac{1}{f_c} \cdot \frac{c}{2\beta} \cdot \eta_x, \qquad p_y = \frac{1}{f_c} \cdot \frac{c}{4\sin(\phi_m/2)} \cdot \eta_y \tag{2.4}$$

The factors η_x and η_y correspond to the effect of zero-padding during image formation. They are given by:

$$\eta_x = \frac{M-1}{M_z - 1}, \qquad \eta_y = \frac{N-1}{N_z - 1} \tag{2.5}$$

We then define the normalized parameters as follows:

$$x_p = \frac{x}{p_x} \qquad y_p = \frac{y}{p_y} \qquad L_p = \frac{L}{p_y} \tag{2.6}$$

$$\gamma_p = \gamma \cdot 4\pi f_c \sin(\phi_m/2) \tag{2.7}$$

$$\bar{\phi}_p = \frac{\bar{\phi}}{\phi_m/2} \tag{2.8}$$

The parameters x, y and L are normalized by the downrange and crossrange pixel dimensions, so that the new parameters x_p, y_p and L_p are in units of pixels instead of units of meters. The normalized parameter $\bar{\phi}_p$ ranges from -1 to 1, representing the orientation angle as a percentage of the maximum aperture. The parameter γ_p corresponds to the dispersion as a function of aspect angle. For example, $\gamma_p = 1$ means that as we go from the left extreme of the aperture to the right extreme, the amplitude changes by a factor of e^1. We further define a new length parameter L_c which is normalized to the crossrange resolution of the system. It is independent of the amount of zero-padding used.

$$L_c = L \cdot \frac{4 f_c \sin(\phi_m/2)}{c} = L_p \cdot \eta_y \tag{2.9}$$

The Cartesian frequency coordinates are also scaled as

$$f_{xn} = \frac{f_x}{f_c} \qquad f_{yn} = \frac{f_y}{f_c} \qquad f_2 = \frac{f_{yn}}{2\sin(\phi_m/2)} \tag{2.10}$$

As a result of the scaling, $f_{xn} \in [1 - \beta/2, 1 + \beta/2]$, $f_{yn} \in [-\sin(\phi_m/2), \sin(\phi_m/2)]$, and $f_2 \in [-1/2, 1/2]$.

With the use of these normalized parameters, the scattering center model becomes

$$
\begin{aligned}
E(f_{xn}, f_{yn}) &= A \cdot \left(j\sqrt{\left(f_{xn}{}^2 + f_{yn}{}^2\right)} \right)^{\alpha} \cdot \exp\left(-j2\pi \left(\frac{f_{xn}}{\beta} x_p \eta_x + f_2 y_p \eta_y \right) \right) \\
&\quad \cdot \operatorname{sinc}\left(\frac{\pi \sqrt{\left(f_{xn}{}^2 + f_{yn}{}^2\right)} L_p \eta_y}{2\sin(\phi_m/2)} \sin\left(\tan^{-1}(f_{yn}/f_{xn}) - \bar{\phi}_p \phi_m/2 \right) \right) \\
&\quad \cdot \exp(-f_2 \gamma_p) \quad\quad\quad\quad\quad\quad\quad\quad\quad\quad\quad\quad\quad\quad (2.11)
\end{aligned}
$$

We assume that scattering responses comply with the model in Equation 2.11. Our main goal in this study is to obtain the estimates of the model parameters that best fit a given response. Parameter estimation is performed through the minimization of a cost function that represents the difference between the model and the actual response. By normalizing the model parameters, we scale their effect on the cost function, hence improve the numerical stability of the estimation problem.

2.3   Parameter Estimation

2.4   Introduction

In this section we explain the estimation of the parameters in the model introduced in Section 2.2.5. We first discuss several parameter estimation approaches implemented by Gerry [6] and Koets [10], and introduce our approach. Then, we explain each stage of this approximate maximum likelihood (AML) parameter estimation technique. We provide details of the image segmentation process where regions of interest are extracted from a given SAR image. It is followed by a structure selection stage where the scatterer of interest is classified as either a localized or a distributed scattering center. This procedure is discussed in more detail in Section 2.10. Then, we describe the steps of the numerical optimization process which are parameter initialization and nonlinear minimization. In order to evaluate the performance achieved, the Cramér-Rao Bound is derived for the parameters in the model. Some performance results are presented, comparing the estimated parameter variances with the calculated Cramér-Rao bounds. Finally, we discuss variations of this algorithm that compromise accuracy for increased computational speed.

2.5   Parameter Estimation Approaches

The parameter estimation problem can be stated as follows: Given a SAR image $D(x, y)$, find the set of parameters $\theta^T = [\theta_1^T, \ldots, \theta_n^T]$ that best fit the n scattering mechanisms present in the object that is imaged.

Let $\tilde{D}(f_x, f_y)$ be the resampled frequency domain measurements used to obtain the SAR image $D(x, y)$. (The tilde sign is used to refer to the frequency domain variables). It is assumed that these measurements consist of a model term $\tilde{E}(f_x, f_y; \theta)$ that exactly fits the parametric model and a noise term $\tilde{N}(f_x, f_y)$ that is complex white Gaussian.

$$\underbrace{\tilde{D}(f_x, f_y)}_{\text{measurements}} = \underbrace{\tilde{E}(f_x, f_y; \theta)}_{\text{model term}} + \underbrace{\tilde{N}(f_x, f_y)}_{\text{noise term}} \tag{2.12}$$

For the sake of simplicity, we will stack these two dimensional $(M \times N)$ terms into a vector of size $MN \times 1$ and refer them with lowercase letters.

$$\tilde{d}(f_x, f_y) = \tilde{e}(f_x, f_y; \theta) + \tilde{n}(f_x, f_y) \tag{2.13}$$

The noise $\tilde{n}$ is a normally distributed random vector, $\tilde{n} \sim \mathcal{N}(0, \tilde{\Sigma} = \sigma^2 I)$. Since $\tilde{e}$ is deterministic, we can conclude that the measurement vector $\tilde{d} \sim \mathcal{N}(\tilde{e}(\theta), \tilde{\Sigma} = \sigma^2 I)$ and has the following probability distribution function (pdf).

$$f(d) = \frac{1}{\pi^{MN} \cdot \sigma^2} \cdot \exp\left(-\frac{\|\tilde{d} - \tilde{e}(\theta)\|^2}{\sigma^2}\right) \tag{2.14}$$

The maximum likelihood parameter estimates are then given by:

$$\hat{\theta}_{ML} = \arg\min_{\theta} \|\tilde{d} - \tilde{e}(\theta)\|^2 \tag{2.15}$$

However, this parameter estimation problem is very difficult to solve as it is stated in Equation 2.15. Since the whole image is treated at the same time, the dimension of the problem is very high. For example, assume that there are 10 scattering centers in the image. Each scattering center has 7 parameters, $\theta_i = \{x_i, y_i, \alpha_i, \gamma_i, \bar{\phi}_i, L_i, A_i\}$, resulting in a total of 70 parameters to estimate. This is a very high-dimensional problem, with a highly nonlinear cost function. The minimization task is computationally very expensive to implement. Therefore we wish to simplify this problem by reducing its dimension.

Previous Work

Simplification can be achieved by exploiting the fact that scattering center responses are isolated in the image domain when data is gathered at high frequencies. Let us first introduce the image domain representation of the data. The image formation process described in Section 2.2.4 is a linear operator, denoted by B. The SAR image vector d is therefore given by

$$d = B \cdot \tilde{d} = B \cdot [\tilde{e}(\theta) + \tilde{n}] \tag{2.16}$$

The model term $\tilde{e}(\theta)$ can be written as the sum of individual scattering center models.

$$d = B \cdot \left[\sum_{i=1}^{n} \tilde{e}(\theta_i)\right] + n \tag{2.17}$$

where $n = B \cdot \tilde{n}$ and $n \sim \mathcal{N}(0, \Sigma = B\tilde{\Sigma}B^H)$. We further define the image formed from a single scattering center model $\tilde{e}(\theta_i)$ by $e(\theta_i) = B \cdot \tilde{e}(\theta_i)$, so

$$d = \sum_{i=1}^{n} e(\theta_i) + n = e(\theta) + n \tag{2.18}$$

The noise term n is a colored Gaussian noise vector and $e(\theta)$ is deterministic. Therefore the $M_z N_z \times 1$ image vector d has the following Gaussian pdf.

$$f(d) = \frac{1}{\pi^{M_z N_z} \cdot |\Sigma|} \cdot \exp\left[-(d - e(\theta))^H \Sigma^\dagger (d - e(\theta))\right] \tag{2.19}$$

where † denotes the Moore-Penrose pseudo-inverse. The parameter estimates that maximize the likelihood are given by:

$$\hat{\theta}_{ML} = \arg\min_{\theta} [d - e(\theta)]^H \Sigma^\dagger [d - e(\theta)] \tag{2.20}$$

At this point, we can make use of the fact that scattering center responses are isolated in the image domain. This way, we can decouple the minimization problem and treat each scattering center separately.

First step is to isolate a region of high energy R in the image which consists of the response from the kth scattering center. We denote the image pixels within that region by d_R, and θ_k corresponds to the parameters of that scattering center. We employ the ML criterion presented in Equation 2.20 for this region of interest, obtaining an approximate maximum likelihood (AML) estimation criterion.

$$\hat{\theta}_{k,AML} = \arg\min_{\theta_k} [d_R - e_R(\theta_k)]^H \Sigma_R^\dagger [d_R - e_R(\theta_k)] \tag{2.21}$$

This estimation method is implemented by Koets [10]. Although the complexity of the problem is significantly reduced compared to Equation 2.20, it is still computationally expensive. The cost function minimization is achieved by an iterative numerical optimization algorithm, starting at a set of initial parameter estimates $\hat{\theta}_k^0$. At each iteration t, the whole frequency domain model data $\tilde{e}_k(\hat{\theta}_k^t)$ has to be calculated and transformed into the image domain, $e(\hat{\theta}_k^t) = B \cdot \tilde{e}(\hat{\theta}_k^t)$. As the size of the data increases (as it does for the case of high resolution data), this process becomes more and more expensive.

In [6], Gerry developed an image domain model, so that given a set of parameters θ_k, the image data can be directly calculated (instead of calculating the frequency domain data and transforming it). However, this new image domain model has approximations that introduce inaccuracies. Also, the model includes terms that are difficult to compute, so direct image data calculation is not computationally favorable either.

Our Approach

For further simplification of the problem, we again exploit the fact that the response of a scattering center $e(\theta_k)$ is isolated in a region R and is very small outside that region. Therefore we can tolerate aliasing due to a possible decimation in the frequency domain. Let us denote the windowed and zero-padded $M_z \times N_z$ frequency domain data by $\tilde{S}(f_x, f_y)$. The corresponding image $E(x, y)$ is obtained by performing a 2D-IFFT on $\tilde{S}(f_x, f_y)$.

$$\tilde{S}(f_x, f_y) @ > 2D - IFFT >> E(x, y) \tag{2.22}$$

If we decimate $\tilde{S}(f_x, f_y)$ by a factor of m in the downrange direction and a factor of n in the crossrange direction, we obtain $\tilde{S}(m \cdot f_x, n \cdot f_y)$ of size $M_z/m \times N_z/n$. Performing the 2D-IFFT on this decimated data, we obtain an image $E'(x, y)$.

$$\tilde{S}(m \cdot f_x, n \cdot f_y) @ > 2D - IFFT >> E'(x, y) \tag{2.23}$$

Let us now derive the relationship between the actual image $E(x, y)$ and the aliased image $E'(x, y)$ for the case where the decimation factor is 2 for both directions. We assume that M_z and N_z are even integers.

$$\tilde{S}(f_x, f_y) = \sum_{x=0}^{M_z-1} \sum_{y=0}^{N_z-1} E(x, y) \cdot \exp\left(\frac{-j2\pi f_x x}{M_z}\right) \cdot \exp\left(\frac{-j2\pi f_y y}{N_z}\right) \tag{2.24}$$

$$\tilde{S}(2f_x, 2f_y) = \sum_{x=0}^{M_z-1} \sum_{y=0}^{N_z-1} E(x, y) \cdot \exp\left(\frac{-j2\pi 2f_x x}{M_z}\right) \cdot \exp\left(\frac{-j2\pi 2f_y y}{N_z}\right) \tag{2.25}$$

$$
\begin{aligned}
\tilde{S}(2f_x, 2f_y) = {}& \sum_{x=0}^{\frac{M_z}{2}-1} \sum_{y=0}^{\frac{N_z}{2}-1} E(x, y) \cdot \exp\left(\frac{-j2\pi f_x x}{M_z/2}\right) \cdot \exp\left(\frac{-j2\pi f_y y}{N_z/2}\right) \\
& + \sum_{x=0}^{\frac{M_z}{2}-1} \sum_{y=\frac{N_z}{2}}^{N_z-1} E(x, y) \cdot \exp\left(\frac{-j2\pi f_x x}{M_z/2}\right) \cdot \exp\left(\frac{-j2\pi f_y y}{N_z/2}\right) \\
& + \sum_{x=\frac{M_z}{2}}^{M_z-1} \sum_{y=0}^{\frac{N_z}{2}-1} E(x, y) \cdot \exp\left(\frac{-j2\pi f_x x}{M_z/2}\right) \cdot \exp\left(\frac{-j2\pi f_y y}{N_z/2}\right) \\
& + \sum_{x=\frac{M_z}{2}}^{M_z-1} \sum_{y=\frac{N_z}{2}}^{N_z-1} E(x, y) \cdot \exp\left(\frac{-j2\pi f_x x}{M_z/2}\right) \cdot \exp\left(\frac{-j2\pi f_y y}{N_z/2}\right)
\end{aligned} \tag{2.26}
$$
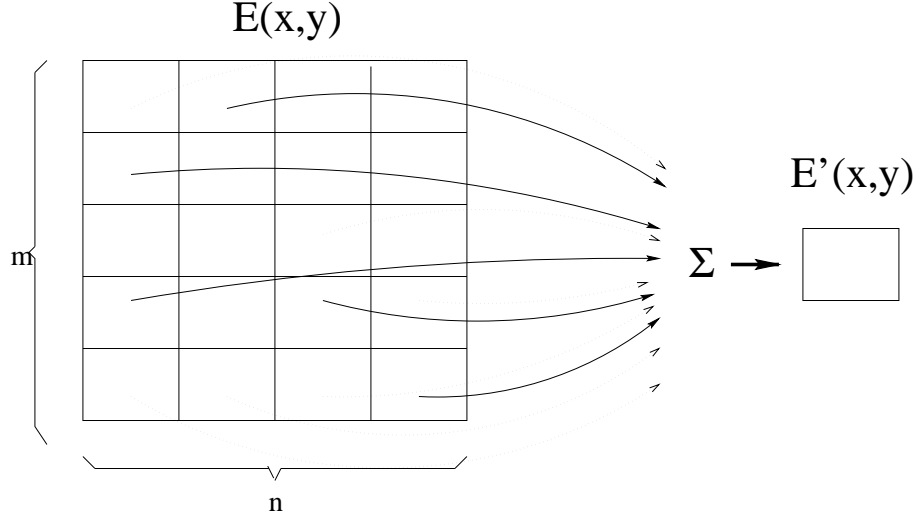
Figure 2.5: The relation between an original SAR image and the image formed by decimating the frequency domain data.

$$\tilde{S}(2f_x, 2f_y) = \sum_{x=0}^{\frac{M_z}{2}-1} \sum_{y=0}^{\frac{N_z}{2}-1} \left[E\left(x,y\right) + E\left(x + \frac{M_z}{2}, y\right) + E\left(x, y + \frac{N_z}{2}\right) \right.$$
$$\left. + E\left(x + \frac{M_z}{2}, y + \frac{N_z}{2}\right) \right] \cdot \exp\left(\frac{j2\pi f_x x}{M_z/2}\right) \cdot \exp\left(\frac{j2\pi f_y y}{N_z/2}\right) \qquad (2.27)$$

Thus,

$$E'(x,y) = E\left(x,y\right) + E\left(x + \frac{M_z}{2}, y\right) + E\left(x, y + \frac{N_z}{2}\right) + E\left(x + \frac{M_z}{2}, y + \frac{N_z}{2}\right) \qquad (2.28)$$

As seen in Equation 2.28, the aliased image $E'(x,y)$ is a sum of subimages of $E(x,y)$. For arbitrary m and n values, the aliased image would correspond to the summation of subimages formed by dividing $E(x,y)$ into m segments in the downrange direction and n segments in the crossrange direction. This relation is depicted in Figure 2.5.

If the isolated scattering response region R is concentrated in a subimage-sized area, the summation in Equation 2.28 has at most one summand that is not close to zero. Since sidelobe suppression is achieved by windowing prior to inverse Fourier transforming, the pixels outside R have small amplitudes. Therefore the effect of adding several sidelobe pixels to the response does not cause significant degradation.

We can determine the rules for choosing the decimation factors m and n. First, m and n should properly divide M_z and N_z respectively. We also should be able to enclose region R within at least an $\left(\frac{M_z}{m} \times \frac{N_z}{n}\right)$ rectangle. Finally, the summation of $m \times n$ sidelobes should

not exceed a certain amplitude. As an example, let us pick this amplitude threshold to be 10 dB below the peak. When we use a Taylor window with a -35 dB sidelobe level (s_ℓ) during the image formation, we guarantee that the resulting image will have sidelobes lower than 35 dB below the peak. Assuming the worst case scenario of all the sidelobes adding constructively, the summation will have an amplitude of $m \times n$ times a single sidelobe level. The requirement can then be expressed as

$$20 \log_{10}(m \cdot n \cdot s_\ell) < -10$$
$$\underbrace{20 \log_{10}(s_\ell)}_{-35} + 20 \log_{10}(m \cdot n) < -10$$
$$m \cdot n < 17.78 \tag{2.29}$$

Since the sidelobes are usually much lower than the -35 dB level and do not always add constructively, the choice of -10 dB as a threshold is capable of preventing significant degradation to the actual scattering response.

2.6   Estimation Algorithm Outline

In this section, we explain the steps of the parameter estimation algorithm in detail. The approximate maximum likelihood estimates of the parameters are obtained using the criterion given in Equation 2.21. This criterion requires sequential processing of the scattering centers. Furthermore, frequency domain decimation is performed for cost function evaluations during numerical minimization, as explained in Section 2.5.

Since we are implementing sequential processing, the first step is to extract a segment of high energy within the image that includes the response of a single scattering center. Then, we classify that scattering response as distributed or localized, so that we know which set of parameters to estimate. This is followed by numerically obtaining the set of parameter values that minimize the cost function. As with every numerical optimization process, an initial set of values is required to start the iterations. After the parameter estimates are obtained, the scattering response is simulated by evaluating the model with the estimated values. Then, this simulated response is subtracted from the original image. The whole process is repeated for the next scattering center[3].

2.6.1   Image Segmentation

In the image segmentation stage, the aim is to extract a region within a given SAR image that encloses most of the energy from a single scattering center. Once the pixel indices of

---

[3]Note that we could perform an iterative minimization not only on the parameters of the current scattering center, but on all previous scattering center parameters as well. Doing so would be the realization of the Expectation-Maximization (EM) algorithm.

a segment are determined, all the following processing of the scattering center is confined to those pixels.

We employ an algorithm known as the Watershed segmentation for this task [18]. The Watershed segmentation algorithm is best understood by the help of a landscape analogy. We can visualize the magnitude of the SAR image as a three-dimensional landscape where the magnitude values of the pixels correspond to their heights. This landscape is first submerged into water. Then, the water is slowly drained so that the landscape emerges at the surface, starting with the highest points. Every time a new peak appears, it is assigned a new segment number. These segments are grown as new pixels belonging to that peak surface. After all the water is drained, we have segmented the image into regions of peaks. The segment corresponding to the highest peak is the region we are interested in.

As a result of the Watershed segmentation, each peak is assigned to a new segment. There are two cases in which this property would cause problems. The first one is the presence of ripples due to noise in the scattering response and windowing in the image formation. In this case, each small peak within the ripple would be assigned to a different segment, preventing us from capturing the whole response in a single region. The second case is the responses of long distributed scatterers with significant tilt angles. These responses have a two-humped profile which would result in each bump to be assigned to a different segment. In order to overcome these problems, we have modified the Watershed segmentation algorithm.

In the modified algorithm, we assume that the peaks that unite within the 3 dB region below the largest peak are combined and treated as a single segment. This would prevent small noise ripples to be assigned to different segments. It would also allow us to extract tilted distributed responses as single segments, since the region between the two peaks of such a response does not go below the -3 dB level for most tilt angles ($|\bar{\phi}_p| \lesssim 0.8$) [10]. We also assume that the pixels below the -20 dB level (20 dB below the current peak) correspond to noise and clutter, and we disregard them. Nearly all energy of the scattering response is captured until the -20 dB level is reached, therefore this process does not cause elimination of a significant amount of information. By keeping the extracted region small, it also reduces the computational cost of the parameter optimization stage.

Let us now explain the steps of this segmentation algorithm. First, we compute the magnitude of the SAR image. We find the highest pixel value and determine the -3 dB and -20 dB levels below the peak. We process the pixels one at a time and in a descending magnitude order. Until we reach the -3 dB level, we process each pixel in the following way: We first search the segment assignments of its 8 neighboring pixels. There are three cases possible.

1. no neighbors are assigned to a segment

2. one or more neighbors are assigned to a single segment

3. one or more neighbors are assigned to multiple segments

The first case corresponds to a new peak, so the pixel of interest is assigned a new segment

20

number. In the second case, the pixel is assigned to the same segment as its neighbors. The third case is where multiple segments unite. In this situation, the pixel is assigned to the segment with the lowest index among the uniting segments. The segment assignments of all the pixels within the uniting peaks are also modified, so that they all have that same lowest index.

For the pixels between the -3 dB and -20 dB levels, a simpler processing scheme is used. We confine our interest to segment number 1, which is the one containing the largest peak. We similarly search the 8 neighbors of the processed pixel. This time, we distinguish among two possible cases.

1. no neighbors are assigned to segment 1

2. one or more neighbors are assigned to segment 1

In the first case, we discard the pixel of interest. This way we save ourselves from growing segments that we will not be needing. In the second case, we assign the pixel to segment 1. When we reach the -20 dB level, we have obtained our region that consists of pixels which were assigned to segment number 1.

In Figure 2.6, we can see a one-dimensional example. Since peaks 1 and 2 unite above the -3 dB threshold, they are combined as segment 1. Segment number 3 is discarded after the -3 dB level is passed.

2.6.2   Structure Selection

The parametric model we have introduced in Section 2.2.5 contains a total of seven parameters, $\{x, y, \alpha, \gamma, \bar{\phi}, L, A\}$. However, not all of them are defined and have non-zero values in all cases. Scattering centers can be classified as either localized or distributed. For localized scatterers, the parameter L equals zero and $\bar{\phi}$ is undefined. As a result, there are five remaining parameters to estimate, $\{x, y, \alpha, \gamma, A\}$. In the case of distributed scatterers, the parameter γ is zero, leaving us with six parameters to estimate, $\{x, y, \alpha, \bar{\phi}, L, A\}$.

Consequently, before we proceed with parameter estimation, we first have to decide which set of parameters we will estimate. In other words, we have to classify the scattering response of interest as localized or distributed. Following this classification, we may attempt to estimate the corresponding parameter set.

This structure selection problem is discussed in detail in Section 2.10. To summarize, we propose three different hypothesis testing algorithms in Section 2.10, and compare these algorithms in terms of performance and computational complexity. For the remainder of this section, we assume the structure is known or an estimate has been provided.
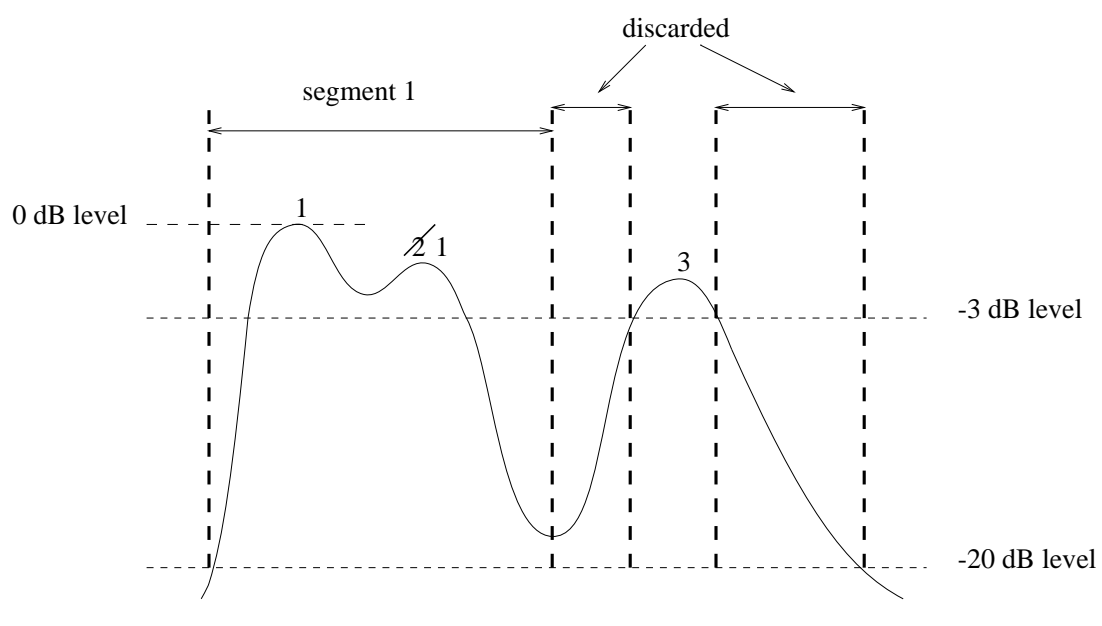
Figure 2.6: One-dimensional segmentation example

2.6.3 Parameter Initialization

Numerical optimization techniques converge to a solution iteratively, and iterative procedures require an initial point. Therefore, in order to obtain the parameter estimates by numerically minimizing the cost function, we need to initialize our parameters.

The cost function that we will be minimizing (Equation 2.21) is high-dimensional and non-convex. The cost surface contains several local minima along with the global minimum. Therefore, the starting point of the algorithm is very crucial. If the starting point is poorly chosen, the iterations might converge to a local minimum or not converge at all. In order to assure convergence to the global minimum and to achieve this quickly, we need to start as close to the actual solution as possible. In other words, our initial estimates of the parameters should be as close to their actual values as possible. Therefore, we exploit the parametric model and SAR image properties to obtain effective initialization.

For the sake of numerical stability of the optimization problem, we use the normalized parametric model introduced in Section 2.2.6 from this point on. The normalized set of parameters is $\{x_p, y_p, \alpha, \gamma_p, \bar{\phi}_p, L_p, A\}$.

We start the initialization process with the two location parameters x_p and y_p, which are in units of pixels. We use the method suggested and implemented by Koets in [10]: we compute the center of mass of the segmented region and assign them as our initial values x_p^{init} and y_p^{init}. The parameter γ_p that appears in the localized model is initialized to zero.

For distributed model parameters $\bar{\phi}_p$ and L_p, we exploit the parametric model to obtain good initial estimates. The normalized model for a distributed scatterer (with $\gamma_p = 0$) is as follows:

$$\tilde{E}(f_{xn}, f_{yn}) = A \cdot \left(j\sqrt{f_{xn}^2 + f_{yn}^2} \right)^{\alpha} \cdot \exp\left(-j2\pi \left(\frac{f_{xn}}{\beta} x_p \eta_x + f_2 y_p \eta_y \right) \right)$$
$$\cdot \mathrm{sinc}\left(\frac{\pi\sqrt{f_{xn}^2 + f_{yn}^2} L_p \eta_y}{2\sin(\phi_m/2)} \sin\left(\tan^{-1}(f_{yn}/f_{xn}) - \bar{\phi}_p \phi_m/2 \right) \right) \quad (2.30)$$

When we take the magnitude of the model, the complex exponential term disappears.

$$|\tilde{E}(f_{xn}, f_{yn})| = |A| \cdot \left| \sqrt{f_{xn}^2 + f_{yn}^2} \right|^{\alpha}$$
$$\cdot \left| \mathrm{sinc}\left(\frac{\pi\sqrt{f_{xn}^2 + f_{yn}^2} L_p \eta_y}{2\sin(\phi_m/2)} \sin\left(\tan^{-1}(f_{yn}/f_{xn}) - \bar{\phi}_p \phi_m/2 \right) \right) \right| \quad (2.31)$$

For fixed a frequency $f_n = \sqrt{f_{xn}^2 + f_{yn}^2}$, we can observe the $|\mathrm{sinc}(\cdot)|$ term by itself. A sinc term takes its maximum value when the argument is zero. In our case we have a $\sin(\cdot)$ term

in the argument, and it equals zero when

$$\underbrace{\tan^{-1}\left(\frac{f_{yn}}{f_{xn}}\right)}_{\phi} = \bar{\phi}_p \cdot \frac{\phi_m}{2} \tag{2.32}$$

$$\implies \frac{\phi}{\phi_m/2} = \bar{\phi}_p \tag{2.33}$$

This means that the magnitude of the frequency data has its peak when the normalized aspect angle $\left(\frac{\phi}{\phi_m/2}\right)$ is equal to the parameter $\bar{\phi}_p$.

The main lobe width of the sinc$(\cdot)$ term gives us information about the L_p parameter. If we move our aspect angle origin from 0 to $\bar{\phi}_p \frac{\phi_m}{2}$ by the transformation $\phi' = \phi - \bar{\phi}_p \frac{\phi_m}{2}$, the magnitude of the model becomes

$$|\tilde{E}(f_n)| = |A| \cdot |f_n|^\alpha \cdot \left| \operatorname{sinc}\left(\frac{\pi L_p \eta_y}{2\sin(\phi_m/2)} f_n \sin(\phi')\right) \right| \tag{2.34}$$

Let $f_n \sin(\phi') = f'_y = \Delta \cdot \nu$ where Δ is the interval between two consecutive points in the normalized f_{yn} grid and ν is an integer index that is zero at $\phi' = 0$. With the assumption $f_n \approx f_{xn}$, the frequency model magnitude along constant f_{xn} becomes

$$|\tilde{E}(\nu)| = K \cdot \left| \operatorname{sinc}\left(\frac{\pi L_p \eta_y}{2\sin(\phi_m/2)} \Delta \nu\right) \right| \tag{2.35}$$

where K is a constant. If we restrict ourselves to the main lobe of the sinc$(\cdot)$, we can eliminate the magnitude operation, so that

$$|\tilde{E}(\nu)| = K \cdot \operatorname{sinc}\left(\frac{\pi L_p \eta_y}{2\sin(\phi_m/2)} \Delta \nu\right), \quad \left| \frac{\pi L_p \eta_y}{2\sin(\phi_m/2)} \right| \leq \pi \tag{2.36}$$

We use a Taylor expansion around $\nu = 0$ and approximate the main lobe of the sinc with a quadratic function.

$$\operatorname{sinc}\left(\frac{\pi L_p \eta_y}{2\sin(\phi_m/2)}\right) \approx 1 - \frac{1}{6} \cdot \left(\frac{\pi L_p \eta_y}{2\sin(\phi_m/2)} \Delta\right)^2 \nu^2 \tag{2.37}$$

Therefore, if we fit a parabola of the form $f(\nu) = 1 + a\nu^2$ to the main lobe, we can solve for L from the parameter a.

We implement the above algorithm as follows. We first convert the image segment back to the frequency domain by performing a 2D-FFT, removing the zero padding and dividing by the imaging window. We remark that the result of this process is not the exact frequency domain data. In order to isolate a single scattering center, we have performed a windowing through the segmentation process. Therefore the resulting data we obtain is the actual frequency data convolved by a window. However, we ignore this convolution.

24
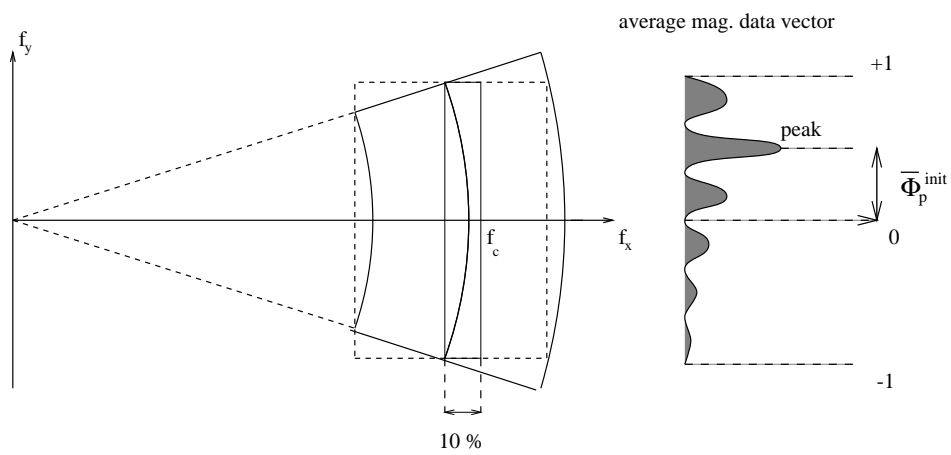
Figure 2.7: $\bar{\phi}_p$ and L_p initialization

The errors from interpolation from the polar coordinates to the Cartesian coordinates are lowest around the center frequency. For this reason we prefer to use the data around f_c. To achieve more stable results, we also perform averaging of constant f_x data vectors across a 10% bandwidth around f_c (see Figure 2.7). This magnitude data vector has a sinc-like characteristic. Assuming the vector lies between -1 and 1, the relative location of the peak gives us our $\bar{\phi}_p^{init}$. We then fit a parabola to the main lobe of this sinc and solve for L_p. The details of this parabola fitting procedure are discussed by Koets in [10].

The parameter α is discrete and can only take half integer values less than or equal to one. At high frequencies, scattering responses with $\alpha < 0$ are very weak and can be ignored in practice unless the noise level is very small. In this study, we assume that α takes values from the set $\{0, 1/2, 1\}$. Given the initial estimates of the other parameters, we calculate the cost function for all the three possible α values. The value that results in the minimum cost is chosen as α^{init}.

The amplitude parameter $A \in \mathbb{C}$ appears linearly in the model. Therefore, instead of implementing a numerical optimization, we can directly obtain a least squares fit estimate (Section 2.6.4). Hence, we do not require a parameter initialization for A. We will analytically solve for the A estimate at each iteration.

2.6.4 Parameter Optimization

We obtain approximate maximum likelihood estimates of the parameters by numerically minimizing the following cost function over the extracted region R (Section 2.5)

$$J(\theta_k) = [d_R - e_R(\theta_k)]^H \Sigma_R^\dagger [d_R - e_R(\theta_k)] \tag{2.38}$$

where θ_k is the set of parameter estimates for the scattering center isolated in region R. The image segment computed from the parametric model with parameters θ_k is denoted by $e_R(\theta_k)$. The SAR image data over the segment is represented by d_R, and Σ_R is the correlation matrix of the colored Gaussian noise pixels in R.

As discussed in Section 2.5, instead of computing the whole frequency domain model and forming the modeled image, we will be computing a decimated version of the frequency domain data. Therefore, we need to determine the decimation factors m and n in downrange and crossrange directions respectively. As previously discussed in Section 2.5, there are three rules for choosing these factors.

- m should divide M_z and n should divide N_z properly

- We should be able to enclose region R within at least an $\left(\frac{M_z}{m} \times \frac{N_z}{n}\right)$ rectangle: Letting s_x and s_y be the number of pixels the segmented region R spans in downrange and crossrange directions, we require

$$\frac{M_z}{m} \geq 2.5 \cdot s_x \quad \text{and} \quad \frac{N_z}{n} \geq 2.5 \cdot s_y \tag{2.39}$$

- The summation of mn sidelobes should not have an amplitude high enough to significantly degrade the actual scattering response: We restrict mn to be less than or equal to 16.

The next point to discuss is the estimation of the discrete-valued parameter α. Therefore, instead of estimating α via numerical optimization (where it will be treated as a real-valued parameter), we follow a different strategy. Once α is initialized, we keep its value fixed throughout the optimization process while we iterate on the other parameters. Even in the case where the initial estimate of α is wrong, it does not effect the solution of the optimization significantly. After the estimates of the other parameters are obtained, we calculate the cost function for all three possible values of α and pick the one with the lowest cost as the final estimate. This is a computationally efficient way of estimating α, since it results in a decrease in the dimension of the numerical minimization problem. The computation we save by the reduction in dimension is more than the computation required for the three cost function evaluations to estimate α at the end.

We achieve one more reduction in the dimension of our problem by excluding the complex-valued amplitude parameter A[4]. Since A appears in the model linearly, an analytical solution for its least squares estimate exists. Let us isolate the A factor from the model term $e_R(\theta_k)$ in Equation 2.38.

$$e_R(\theta_k) = A_k \cdot s_R(\theta_k) \tag{2.40}$$

Then,

$$A \cdot s_R(\theta_k) + n_R = d_R \tag{2.41}$$

and the least squares solution for A is given by [21]

$$\hat{A} = \frac{s_R(\theta_k)^H \cdot d_R}{s_R(\theta_k)^H \cdot s_R(\theta_k)} \tag{2.42}$$

We substitute this result into Equation 2.38 to obtain the modified cost function.

$$J(\theta_k) = [d_R - \hat{A} \cdot s_R(\theta_k)]^H \cdot \Sigma_R^\dagger \cdot [d_R - \hat{A} \cdot s_R(\theta_k)] \tag{2.43}$$

$$J(\theta_k) = \left[d_R - \frac{s_R(\theta_k)^H \cdot d_R}{s_R(\theta_k)^H \cdot s_R(\theta_k)} s_R(\theta_k) \right]^H \Sigma_R^\dagger \left[d_R - \frac{s_R(\theta_k)^H \cdot d_R}{s_R(\theta_k)^H \cdot s_R(\theta_k)} s_R(\theta_k) \right] \tag{2.44}$$

As a result of these exclusions, the parameters to be iterated on during numerical minimization are $\{x_p, y_p, \gamma_p\}$ for localized scatterers and $\{x_p, y_p, \bar{\phi}_p, L_p\}$ for distributed scatterers.

We perform the numerical optimization in two stages. In the first stage, we assume that the noise is white in the image domain. We take Σ in Equation 2.44 to be equal to $\sigma^2 I$. Following this, we perform the colored noise optimization where we use the correct value of

---

[4]We have assumed $A \in \mathbb{C}$ in this work; however, if we restrict $A \in \mathbb{R}$, a similar least squares solution for $\hat{A}$ can also be found.

$\Sigma = \sigma^2 BB^H$ (Section 2.5). The two-stage optimization is found to converge to the global minimum more often than a single colored noise optimization. We hypothesize the reason to be a longer region of attraction of the cost function about the global minimum when $\sigma^2 I$.

The numerical minimization is implemented by MATLAB. The `fminu.m` command within MATLAB's Optimization Toolbox is used, as Koets did in [10]. This is a command that finds the minimum of unconstrained multi-variable functions [7]. We do not provide an analytical expression for gradient vector calculation, so it is obtained through numerical differentiation. The `fminu` function implements the BFGS Quasi-Newton algorithm with a mixed quadratic and cubic line search procedure. Newton methods in general iterate by approximating the cost surface by a quadratic function around the iteration point and trying to find the minimum. In Quasi-Newton methods, the second derivative information (Hessian) used to obtain the quadratic approximation is not calculated directly. Instead, some iterative formulas are used. These update methods give the name of the specific Quasi-Newton method. BFGS corresponds to the formula developed by Broyden, Fletcher, Goldfarb and Shanno. More detailed information about these optimization techniques can be found in [1].

2.6.5 Summary

We have discussed the steps of the parameter estimation algorithm in detail. Let us summarize the complete procedure starting with the input SAR image, until the algorithm terminates.

The termination criteria are user specified. The user is asked for three stopping conditions:

1. The maximum number of scattering centers to be processed.

2. Maximum overall percentage fit: An error image is formed from the difference between the actual SAR image and the image that we simulate from the model by using estimated parameter values. The overall percentage fit is defined as one minus the ratio of the total energy in the error image to the total energy in the actual image.

3. Minimum peak level required to process a peak: The peak level of a scatterer is defined as the ratio of its peak amplitude to the amplitude of the highest peak in the image, in the dB scale.

The algorithm terminates when any one of the three conditions is satisfied.

As previously mentioned, the processed scattering centers are subtracted from the input image. This step may cause significant problems if the estimation process is not successful. Subtraction can introduce artificial peaks due to the mismatch between the actual image and the simulated image. Therefore, a quality control stage is inserted by Koets before subtraction [10]. We check whether the simulated image has an improved fit with the

28

```
while none of the stopping conditions are met
     extract scattering center by segmentation
     classify as localized or distributed
     if scattering response is localized
           initialize $x_p$, $y_p$ and $\gamma_p$
           initialize $\alpha$ to best fitting value
           determine decimation factors $m$ and $n$
           perform white noise minimization on $x_p$, $y_p$, $\gamma_p$
           perform colored noise minimization on $x_p$, $y_p$, $\gamma_p$
           estimate $\alpha$ as the best fitting value
     elseif scattering response is distributed
           initialize $x_p$, $y_p$, $\bar{\phi}_p$ and $L_p$
           initialize $\alpha$ to best fitting value
           determine decimation factors $m$ and $n$
           perform white noise minimization on $x_p$, $y_p$, $\bar{\phi}_p$, $L_p$
           perform colored noise minimization on $x_p$, $y_p$, $\bar{\phi}_p$, $L_p$
           estimate $\alpha$ as the best fitting value
     end if
     simulate scatterer with estimated parameters
     add this to previously simulated scatters
     if error energy decreases with the new scatterer estimate
           store estimated parameters
           subtract simulated scatterer from original image
     else
           reject the scatterer
           set image pixels within the segment to zero
     end if
end while
```

Table 2.1: Parameter Estimation Algorithm

addition of the newly processed scatterer. If the answer is yes, then there is no problem. If not, we conclude that the estimation failed, and we set the corresponding image pixels to zero and continue with the next scattering response. Setting the pixels to zero has the effect that subsequent modeling does not use pixels in this region.

The overall parameter estimation algorithm outline is given in Table 2.1.

2.7 Cramér-Rao Bound Derivation

In this section we evaluate the performance of our estimator. A very important statistical tool is the Cramér-Rao Bound. This bound reflects the limitations on performance imposed

29

by the assumed model [14]. For unbiased estimators, the CRB provides us with limits on minimum achievable parameter variances.

Let $p(y, \theta)$ be the likelihood function of the observed data y, where θ is the set of unknown parameters. The Fisher Information Matrix J is defined as:

$$J = E\left\{ \left[\frac{\partial \ln p(y, \theta)}{\partial \theta}\right] \cdot \left[\frac{\partial \ln p(y, \theta)}{\partial \theta}\right]^T \right\} \qquad (2.45)$$

Cramér-Rao bound matrix is found by inverting the Fisher information matrix J. The diagonal entries of this matrix correspond to the Cramér-Rao variance bounds of the unknown parameters. The derivation of this result can be found in [14] and [20].

The CRB for the parametric model we use have been previously derived by Gerry [6] and Koets [10]. In [6, 10], the authors treat the observation vector y as complex-valued. This approach complicates the derivation process. We provide another CRB derivation in terms of real-valued vectors where we treat the real and imaginary parts of the complex vectors separately.

The parametric model for a single scattering center is given by

$$\begin{aligned}
\tilde{E}_i(f, \phi; \theta_i) &= A_i \cdot \left(j\frac{f}{f_c}\right)^{\alpha_i} \cdot \exp\left(\frac{-j4\pi f}{c}(x_i \cos\phi + y_i \sin\phi)\right) \\
&\quad \cdot \text{sinc}\left(\frac{2\pi f}{c}L_i \sin(\phi - \bar{\phi}_i)\right) \cdot \exp(-2\pi f \gamma_i \sin\phi) \qquad (2.46)
\end{aligned}$$

The total response of an object can be approximated as the sum of responses of its electrically isolated scattering centers (Section 2.2.5).

$$\tilde{E}(f, \phi; \theta) = \sum_{i=1}^{p} \tilde{E}_i(f, \phi; \theta_i) \qquad (2.47)$$

The measured frequency domain data $D(f, \phi)$ is assumed to consist of a term that exactly fits the model and a zero-mean complex white Gaussian noise term.

$$\tilde{D}(f, \phi) = \tilde{E}(f, \phi; \theta) + \tilde{N}(f, \phi) \qquad (2.48)$$

Stacking these $M \times N$ dimensional matrices into vectors of size $MN \times 1$, we obtain

$$\tilde{d}(f, \phi) = \tilde{e}(f, \phi; \theta) + \tilde{n}(f, \phi) \qquad (2.49)$$

where $\tilde{n} \sim \mathcal{N}(0, \sigma^2 I)$. We further stack the real and imaginary parts of these complex vectors.

$$S = \begin{bmatrix} Re\{\tilde{e}\} \\ Im\{\tilde{e}\} \end{bmatrix} = \begin{bmatrix} Re\{\tilde{e}_1 + \tilde{e}_2 + \cdots + \tilde{e}_p\} \\ Im\{\tilde{e}_1 + \tilde{e}_2 + \cdots + \tilde{e}_p\} \end{bmatrix}_{2MN \times 1} \qquad (2.50)$$

$$X = \begin{bmatrix} Re\{\tilde{n}\} \\ Im\{\tilde{n}\} \end{bmatrix}_{2MN \times 1}, \qquad Y = S + X = \begin{bmatrix} Re\{\tilde{d}\} \\ Im\{\tilde{d}\} \end{bmatrix}_{2MN \times 1} \qquad (2.51)$$

30

where S and X are $2MN \times 1$ real vectors with $X \sim \mathcal{N}(0, \frac{\sigma^2}{2}I)$.

The likelihood function of the data vector Y is then a vector Gaussian distribution with mean S and covariance matrix $\frac{\sigma^2}{2}I$.

$$P(Y) = \frac{1}{\left(2\pi\sigma^2/2\right)^{2MN/2}} \cdot \exp\left\{\frac{-1}{2\sigma^2/2} \cdot (Y-S)^T(Y-S)\right\} \tag{2.52}$$

$$\log P(Y) = -MN\ln(\pi) - MN\ln(\sigma^2) - \frac{1}{\sigma^2} \cdot (Y-S)^T(Y-S) \tag{2.53}$$

The partial derivative of the log-likelihood function in Equation 2.53 with respect to a single parameter θ^k is given by

$$\frac{\partial \log P(Y)}{\partial \theta^k} = \frac{2}{\sigma^2} \cdot \left(\frac{\partial S}{\partial \theta^k}\right)^T \cdot (Y-S) \tag{2.54}$$

The $(k,q)^{th}$ entry of the Fisher Information matrix J is given by

$$J_{kq} = E\left[\frac{\partial \log P(Y)}{\partial \theta^k} \cdot \left(\frac{\partial \log P(Y)}{\partial \theta^q}\right)^T\right] \tag{2.55}$$

$$J_{kq} = \frac{4}{\sigma^4} \cdot \left(\frac{\partial S}{\partial \theta^k}\right)^T \cdot E\left[(Y-S)(Y-S)^T\right] \cdot \left(\frac{\partial S}{\partial \theta^q}\right) \tag{2.56}$$

$$J_{kq} = \frac{4}{\sigma^4} \cdot \left(\frac{\partial S}{\partial \theta^k}\right)^T \cdot E\left[XX^T\right] \cdot \left(\frac{\partial S}{\partial \theta^q}\right) \tag{2.57}$$

$$J_{kq} = \frac{4}{\sigma^4} \cdot \left(\frac{\partial S}{\partial \theta^k}\right)^T \cdot \frac{\sigma^2}{2}I \cdot \left(\frac{\partial S}{\partial \theta^q}\right) \tag{2.58}$$

$$J_{kq} = \frac{2}{\sigma^2} \cdot \left(\frac{\partial S}{\partial \theta^k}\right)^T \cdot \left(\frac{\partial S}{\partial \theta^q}\right) \tag{2.59}$$

We now need to find the partial derivative of the model term with respect to the unknown parameters. Assume that θ^k is a parameter of the ith scattering center. Consequently, among the p scattering centers that form the total response, only the ith scattering center model will be a function of θ^k. We have

$$\frac{\partial S}{\partial \theta^k} = \begin{bmatrix} Re\left\{\frac{\partial \tilde{e}_i}{\partial \theta^k}\right\} \\ Im\left\{\frac{\partial \tilde{e}_i}{\partial \theta^k}\right\} \end{bmatrix} \tag{2.60}$$

where $\frac{\partial \tilde{e}_i}{\partial \theta^k}$ is equal to the stacked version of the matrix $\frac{\partial \tilde{E}_i}{\partial \theta^k}$. Once we find the partial derivative of the model $\tilde{E}_i(f, \phi; \theta_i)$ with respect to each parameter, the derivation will be complete. These partial derivatives are found below:

$$\frac{\partial \tilde{E}_i(f, \phi; \theta_i)}{\partial x_i} = \tilde{E}_i(f, \phi; \theta_i) \cdot \left(-j\frac{4\pi f}{c}\cos\phi\right) \tag{2.61}$$

31

$$\frac{\partial \tilde{E}_i(f, \phi; \theta_i)}{\partial y_i} = \tilde{E}_i(f, \phi; \theta_i) \cdot \left(-j\frac{4\pi f}{c} \sin \phi \right) \tag{2.62}$$

$$\frac{\partial \tilde{E}_i(f, \phi; \theta_i)}{\partial \alpha_i} = \tilde{E}_i(f, \phi; \theta_i) \cdot \left[j\frac{\pi}{2} + \ln \left(\frac{f}{f_c} \right) \right] \tag{2.63}$$

$$\frac{\partial \tilde{E}_i(f, \phi; \theta_i)}{\partial \gamma_i} = \tilde{E}_i(f, \phi; \theta_i) \cdot (-2\pi f \sin \phi) \tag{2.64}$$

We define the argument of the sinc term as u in units of radians.

$$u = \frac{2f}{c} L \sin \left(\frac{\pi}{180} \cdot (\phi - \bar{\phi}_i) \right) \tag{2.65}$$

Then,

$$\frac{\partial \tilde{E}_i(f, \phi; \theta_i)}{\partial \bar{\phi}_i} = A_i \cdot \left(j\frac{f}{f_c} \right)^{\alpha_i} \cdot \exp \left(\frac{-j4\pi f}{c} (x_i \cos \phi + y_i \sin \phi) \right)$$
$$\cdot \frac{\partial \mathrm{sinc}(u)}{\partial u} \cdot \frac{\partial u}{\partial \bar{\phi}_i} \cdot \exp(-2\pi f \gamma_i \sin \phi) \tag{2.66}$$

$$\frac{\partial \tilde{E}_i(f, \phi; \theta_i)}{\partial L_i} = A_i \cdot \left(j\frac{f}{f_c} \right)^{\alpha_i} \cdot \exp \left(\frac{-j4\pi f}{c} (x_i \cos \phi + y_i \sin \phi) \right)$$
$$\cdot \frac{\partial \mathrm{sinc}(u)}{\partial u} \cdot \frac{\partial u}{\partial L_i} \cdot \exp(-2\pi f \gamma_i \sin \phi) \tag{2.67}$$

where

$$\frac{\partial \mathrm{sinc}(u)}{\partial u} = \frac{\partial}{\partial u} \cdot \frac{\sin(\pi u)}{\pi u} = \frac{\pi^2 u \cos(\pi u) - \pi \sin(\pi u)}{(\pi u)^2} \tag{2.68}$$

$$\frac{\partial u}{\partial \bar{\phi}_i} = -\frac{\pi}{180} \cdot \frac{2f}{c} L \cos \left(\frac{\pi}{180} (\phi - \bar{\phi}_i) \right) \tag{2.69}$$

$$\frac{\partial u}{\partial L_i} = \frac{2f}{c} \sin \left(\frac{\pi}{180} (\phi - \bar{\phi}_i) \right) \tag{2.70}$$

Since the amplitude parameter A is complex-valued, we separate it into its real and imagi-

32

nary parts and treat it as two parameters $(A = A_R + jA_I)$[5]. Then,

$$\frac{\partial \tilde{E}_i(f, \phi; \theta_i)}{\partial A_{R,i}} = \left(j\frac{f}{f_c}\right)^{\alpha_i} \cdot \exp\left(\frac{-j4\pi f}{c}(x_i \cos\phi + y_i \sin\phi)\right)$$
$$\cdot \operatorname{sinc}\left(\frac{2\pi f}{c}L_i \sin(\phi - \bar{\phi}_i)\right) \cdot \exp(-2\pi f \gamma_i \sin\phi) \qquad (2.71)$$

$$\frac{\partial \tilde{E}_i(f, \phi; \theta_i)}{\partial A_{I,i}} = j \cdot \left(j\frac{f}{f_c}\right)^{\alpha_i} \cdot \exp\left(\frac{-j4\pi f}{c}(x_i \cos\phi + y_i \sin\phi)\right)$$
$$\cdot \operatorname{sinc}\left(\frac{2\pi f}{c}L_i \sin(\phi - \bar{\phi}_i)\right) \cdot \exp(-2\pi f \gamma_i \sin\phi) \qquad (2.72)$$

For a given set of values θ and noise variance σ^2, the CRB computation starts with finding the partial derivative vectors $\left(\frac{\partial S}{\partial \theta^k}\right)$ for the non-zero parameters of either the localized or the distributed model. Then, the Fisher information matrix is formed according to Equation 2.59. The diagonal entries of the inverse of this matrix gives us the CRB for the parameters.

2.8   Performance Results versus CRB

In this section, we evaluate the performance of our parameter estimation algorithm on simulated data. We use the parametric model in Equation 2.2.5 to simulate a single scattering center response in the frequency domain. We add zero-mean complex white Gaussian noise with known variance to this model data. Passing this sum through the image formation process, we obtain a noisy SAR image. We input the simulated image to the parameter estimation algorithm. This process is repeated for numerous noise realizations. The variance of the parameter estimates within these simulations are calculated and compared to the Cramér-Rao Bound. The closer the observed variance is to the bound, the better the performance.

The performance results are presented versus two important image properties: resolution and signal-to-noise ratio (SNR). Let us now look at each case separately.

2.8.1   Performance versus Resolution

Resolution in simple terms is the required distance between two scattering centers to be distinguished as separate responses. It is related to the data collection frequency range.

---

[5]If we restrict $A \in \mathbb{R}$, then the partial derivative of the model with respect to the real amplitude A would be equal to the expression in Equation 2.71
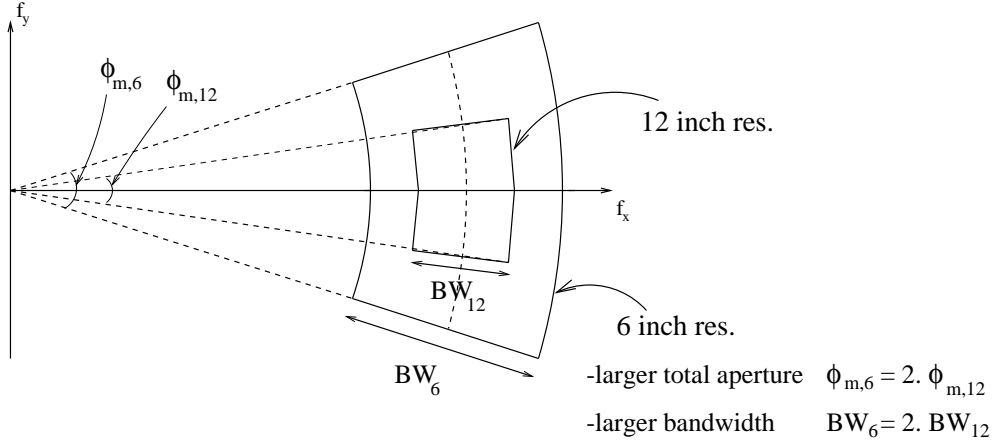
Figure 2.8: Resolution versus Data Collection Range

Wider total apertures and bandwidths result in improved resolution. In Figure 2.8, we can see that the data collection range of a 6 inch resolution SAR image has twice the total aperture and bandwidth compared to the 12 inch resolution image. Hence, it can resolve scatterers twice as close. Since more data is involved in the forming of the image, it is reasonable to expect better estimation capability with improved resolution.

To avoid confusion, let us clarify that higher or improved resolution means a lower resolution value, $i.e.$ 6 inch resolution is higher than 12 inch resolution.

A reasonable performance versus resolution study can be done by assuming that scattering data from an object is collected over a large range. Then, various sized segments of that data are used to generate the different resolution images. In this study, the parameters $x, y, \alpha, \gamma, \bar{\phi}, L$ and A are constant along with the frequency domain noise variance σ^2.

The experimental procedure is as follows: For a fixed resolution, we first simulate a distributed scattering response with parameters $x = 3.2$ m, $y = 5.7$ m, $\alpha = 1$, $\gamma = 0$, $\bar{\phi} = 1.15$ rad, $L = 0.5$ m and $A = 1$. We add zero-mean white Gaussian complex noise with variance $\sigma^2 = 0.6$ to this simulated response. We form the SAR image from the noisy frequency domain data. We then obtain the parameter estimates using the developed parameter estimation algorithm. We repeat this process for 100 different images corresponding to 100 different random noise realizations. We compute the sample variances of the parameter estimates. The variance data is obtained separately for 1.5, 3, 6 and 12 inch resolution scenarios. The corresponding Cramér-Rao bounds are also calculated with the designated parameter values and noise.

In Figure 2.9, we present the obtained estimate variances of the parameters x, y and L in units of m^2 and $\bar{\phi}$ in units of radians^2. The CRBs are also shown in the same plot. We can see that the estimate variances are either equal to the CRBs or very close to them.

34

Figure 2.9: Parameter estimate variances and CRB versus resolution for distributed scattering response with parameters $\{3.2, 5.7, 1, 0, 1.15, 0.5, 1\}$ and $\sigma^2_{freq} = 0.6$
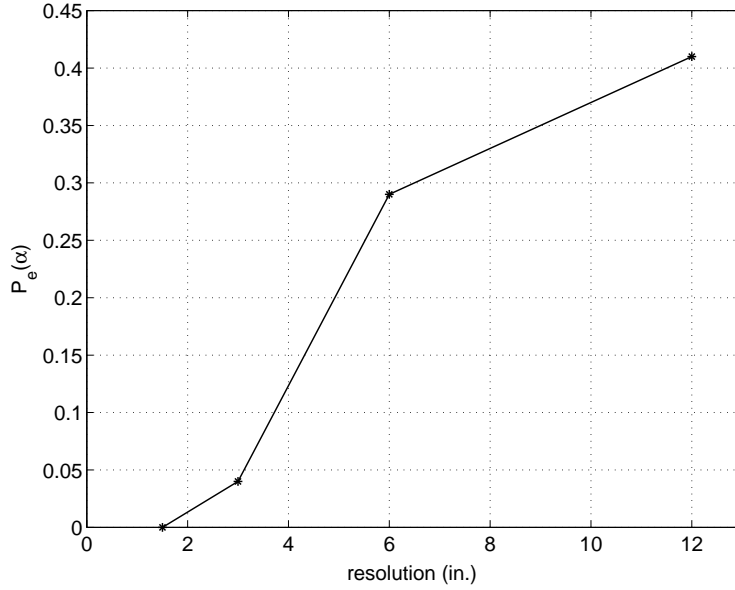
Figure 2.10: Observed error rate for α estimates versus resolution in 100 trials for distributed scattering response with parameters $\{3.2, 5.7, 1, 0, 1.15, 0.5, 1\}$ and $\sigma^2_{freq} = 0.6$

This means that the algorithm is performing as good as possible with the available amount of information. As expected, higher resolution results in lower parameter variances. The variances for the 1.5" resolution case are approximately two orders of magnitude lower than the 12" resolution variances. Even at the lowest resolution, the location parameters have standard deviations less than 1 cm.

Since the parameter α is discrete-valued, we choose not to plot its variance. Instead, we plot the probability of incorrect α estimation as a function of resolution in Figure 2.10. At 12 inch resolution, we see that the error probability is 0.4 and we cannot make a reliable estimate. However, this is an expected result due to the narrow bandwidth and is not an algorithm incapability. As we know, the α parameter enters the parametric model through the term $\left(j\frac{f}{f_c}\right)^\alpha$. In Figure 2.11, we plot $\left(\frac{f}{f_c}\right)^\alpha$ versus $\left(\frac{f}{f_c}\right)$ for $\alpha = 1$ and $\alpha = 1/2$. This demonstrates the amplitude factor induced by α versus normalized frequency. For 12 inch resolution, we have data from a narrower bandwidth which corresponds to the inner rectangular region in the figure. Over the narrow bandwidth, the difference between the amplitude factors for the two α values is very small. Hence, it is very difficult to make an accurate estimation. However, in the case of higher resolution more data is available (outer rectangular region in Figure 2.11). The effect of different α values are distinguishable, leading to very accurate α estimates. A more detailed study of α estimates can be found in [16].

Similar results are presented for a localized scatterer with parameters $x = 4.5$ m, $y = 2.9$

36
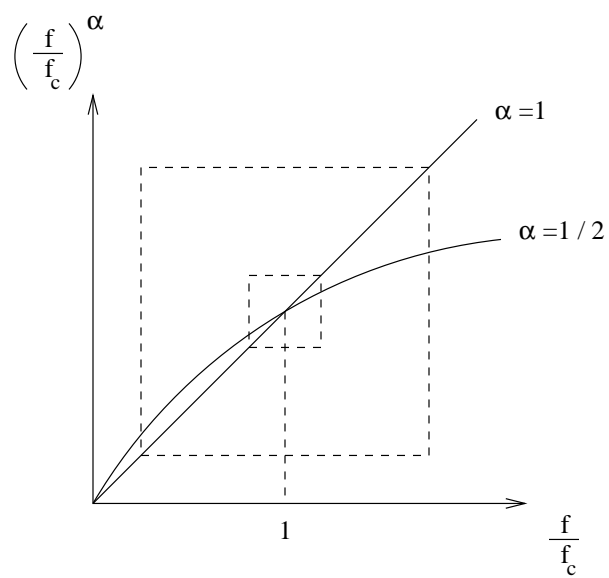
Figure 2.11: Effect of α on the backscatter response versus normalized frequency
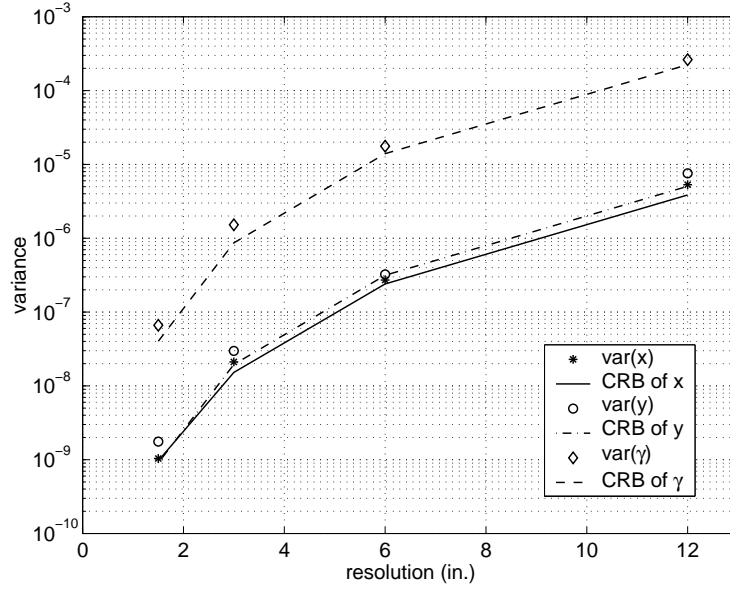
Figure 2.12: Parameter estimate variances and CRB versus resolution for localized scattering response with parameters $\{4.5, 2.9, 1, 0, 0, 0, 1\}$ and $\sigma^2_{freq} = 0.6$

m, $\alpha = 1$, $\gamma = 0$, $\bar{\phi} = 0$, $L = 0$ and $A = 1$ (Figures 2.12 and 2.13). The frequency domain noise variance is 0.6. The parameter variances obtained are very close to the CRB for the localized scatterer case as well.

2.8.2 Performance versus SNR

Signal-to-noise ratio (SNR) is a measure of the amount of noise present in the data. In our case, it is defined as the ratio of the peak image amplitude to noise standard deviation in image domain. SNR is expressed in the dB scale as follows:

$$\text{SNR} = 10 \log_{10} \left(\frac{|pk_{image}|^2}{\sigma^2_{image}} \right) \tag{2.73}$$

Similar to the performance versus resolution study, we simulate a single scattering center response, add noise to it and form its SAR image. The difference arises in the variance of the noise added. We first form the image without any noise and determine the peak image amplitude value. Then, we calculate σ_{image} corresponding to that peak value and the desired SNR from Equation 2.73.

The relation between the frequency domain and image domain noise variances is a simple scaling that depends on the imaging process used. Let $\tilde{N} \sim \mathcal{N}(0, \sigma^2_{freq}I)$ be the frequency
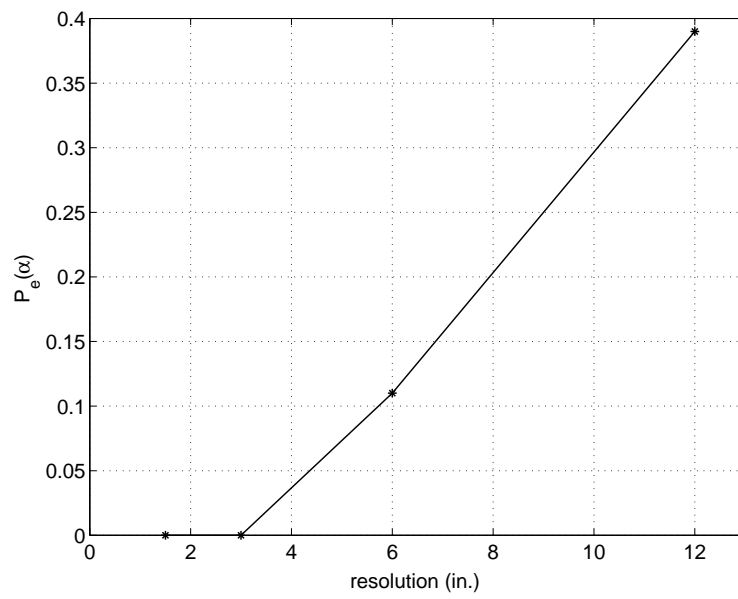
Figure 2.13: Observed error rate for α estimates versus resolution in 100 trials for localized scattering response with parameters $\{4.5, 2.9, 1, 0, 0, 0, 1\}$ and $\sigma^2_{freq} = 0.6$

domain noise and N be the image domain noise. They are related as follows:

$$N(x,y) = \frac{1}{M_z N_z} \cdot \sum_{k=1}^{M_z} \sum_{k=1}^{M_z} \tilde{N}(k,l) \cdot W(k,l) \cdot e^{j2\pi(k-1)(x-1)/M_z} \cdot e^{j2\pi(l-1)(y-1)/N_z} \quad (2.74)$$

It follows that

$$\sigma_{image}^2 = E[N^*(x,y) \cdot N(x,y)]$$

$$= \frac{1}{(M_z N_z)^2} \cdot \sum_k \sum_l \sum_p \sum_r E[\tilde{N}^*(x,y) \cdot \tilde{N}(p,r)] \cdot W(k,l) \cdot W(p,r)$$
$$\cdot e^{-j2\pi(k-1)(x-1)/M_z} \cdot e^{-j2\pi(l-1)(y-1)/N_z} \cdot e^{j2\pi(p-1)(x-1)/M_z} \cdot e^{j2\pi(r-1)(y-1)/N_z}$$

$$= \frac{1}{(M_z N_z)^2} \cdot \sum_k \sum_l \sigma_{freq}^2 \cdot |W(k,l)|^2$$

$$= \sigma_{freq}^2 \cdot \frac{1}{(M_z N_z)^2} \cdot \sum_k \sum_l |W(k,l)|^2 \quad (2.75)$$

where $W(k,l)$ is the window used during image formation. We thus can determine the frequency domain noise variance through Equation 2.75 for the desired SNR value.

In Figures 2.14 and 2.15, we present the observed parameter variances from 100 simulations for distributed and localized scattering responses. The calculated Cramér-Rao Bounds are also plotted. We see that the CRBs decrease linearly with increasing signal-to-noise ratio. This is an expected result, since less noise means less degradation, which naturally leads to better estimation capability. For both distributed and localized scatterer cases, the obtained parameter estimate variances are very close to the CRB. These results are displayed for the 3 inch resolution case; however, other resolution values have similar plots.

2.9   Fast Algorithm

At this point, we have a parameter estimation algorithm that employs an approximate maximum likelihood (AML) estimation criterion. The algorithm gives accurate results as displayed in Section 2.8. However, in some situations we may be willing to compromise accuracy for faster implementation. Therefore, we develop a modified version of the AML algorithm.

The most time-consuming stage of the algorithm is the nonlinear minimization. To reduce computation time, we may stop the minimization in a fewer number of steps. This can be achieved through an optimization parameter within MATLAB that specifies the maximum
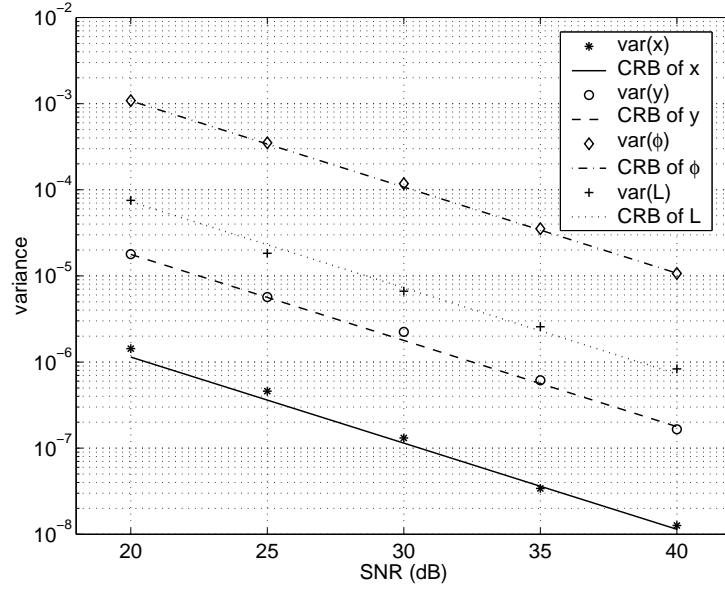
Figure 2.14: Parameter estimate variances and CRB for distributed scattering response with parameters $\{3.2, 5.7, 1, 0, 1.15, 0.5, 1\}$ versus SNR at 3 inch resolution
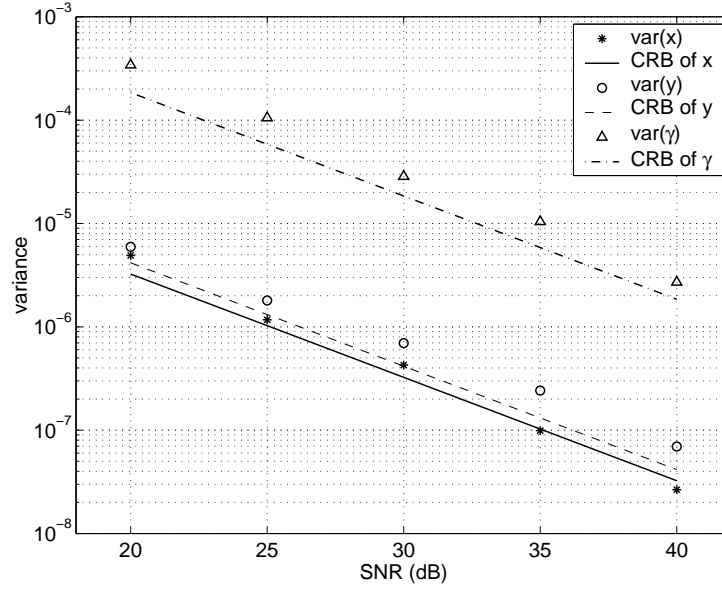
Figure 2.15: Parameter estimate variances and CRB for localized scattering response with parameters $\{4.5, 2.9, 1, 0, 0, 0, 1\}$ versus SNR at 3 inch resolution

number of iterations per variable. In the AML algorithm, this parameter is set to 100. By decreasing it, we can terminate the minimization earlier.

We performed a study to understand the relationship between computation and accuracy as we vary the maximum number of iterations parameter. We simulated data at 25 dB SNR level and applied the algorithm for different values of this parameter, {0, 10 ,20, 30, 40, 50}. We estimated the mean-squared error in the parameter estimates by averaging over 200 realizations. In Figure 2.16, we display these results for a distributed scatterer at 3 inch resolution. The six data points in the plots are the MSE of the parameter of interest versus the average computation time, for the six corresponding values of the maximum number of iterations parameter. The CRBs are also plotted as the horizontal lines. Similar results are presented for localized scattering centers in Figure 2.17.

We observe that the MSE decreases very slowly at the beginning of the minimization process. Then, it displays a steep decay over a small number of iterations. No significant decrease in MSE is observed after this stage. In order to save on computation time, we can stop the process immediately after the steep decay takes place. Since most of the error minimization has already been completed, the earlier termination is at the expense of only a small performance decay. We see from Figures 2.16 and 2.17 that at the end of 30 iterations, the MSE values have decreased to a level very close the CRB. Therefore, we choose the maximum iterations parameter to be 30. However, this choice is subject to change depending on the application and the desired accuracy. For example, if the accuracy needed on the location estimates is within 1 cm, then no iterations are needed. In Figure 2.16, we see that even the initial estimate MSEs are below 10^{-4} m^2, which correspond to a less than 1 cm deviation from the actual location.

In the AML algorithm, after obtaining the parameter estimates, we used to simulate the response with those estimated values and subtract this from the actual image. Since the parameter estimates obtained by the fast algorithm are not very accurate, the simulated response is more likely to differ from the response present in the starting SAR image. Subtraction of the simulated response may not totally eliminate the processed peak. Therefore, after obtaining the parameter estimates, we set the image pixels within the processed region to zero as described in [10]. We then continue with the next scattering center.

2.10   Structure Selection

2.10.1   Introduction

In Section 2.3 we developed estimation algorithms for both distributed and localized scattering centers. In doing so, we assumed prior knowledge of whether the scatterer was distributed or localized. In this section we address this structure selection problem in detail. We first present the problem statement. This is followed by a study that demonstrates the problem's limits; we try to establish qualitative rules on the distinguishability
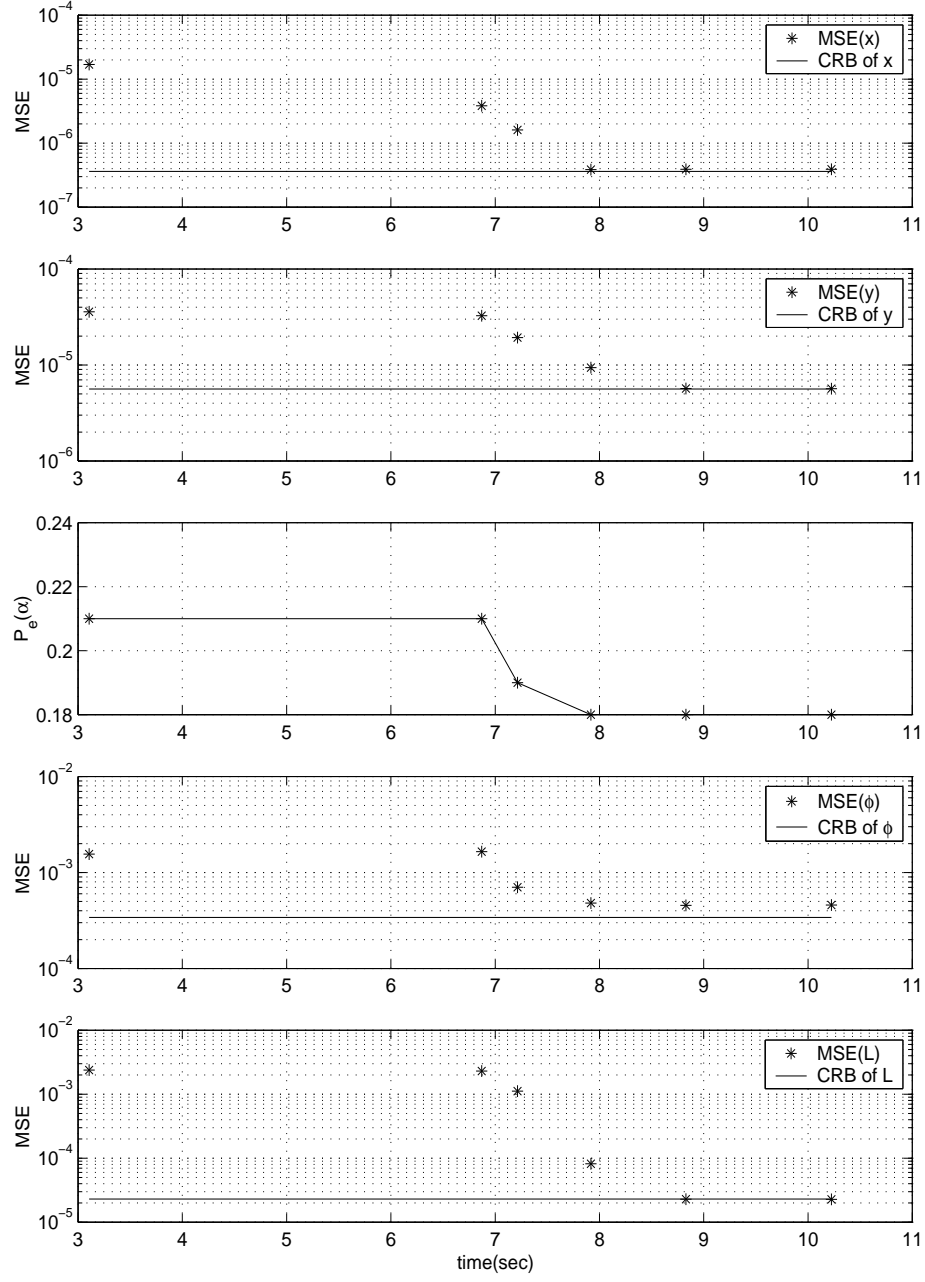
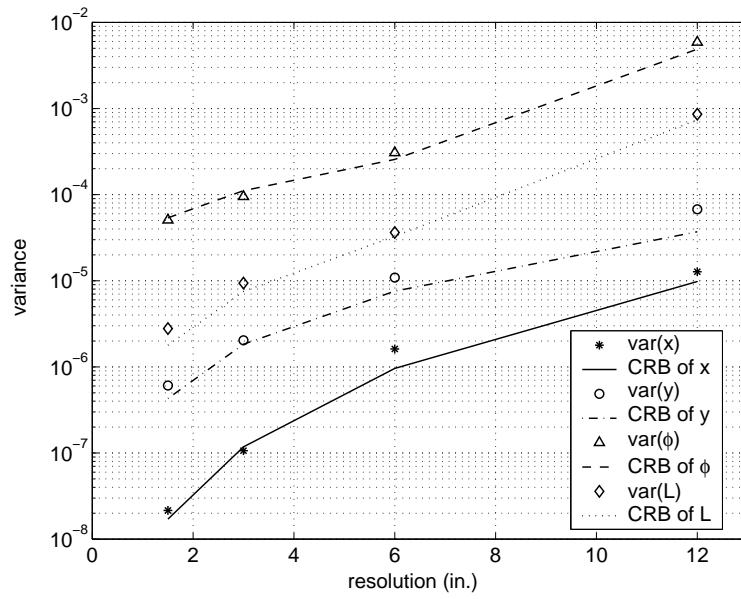Figure 2.16: Parameter estimate variances and CRB for distributed scattering response with parameters $\{3.2, 5.7, 1, 0, 1.15, 0.5, 1\}$ versus average computation time at 3 inch resolution

43
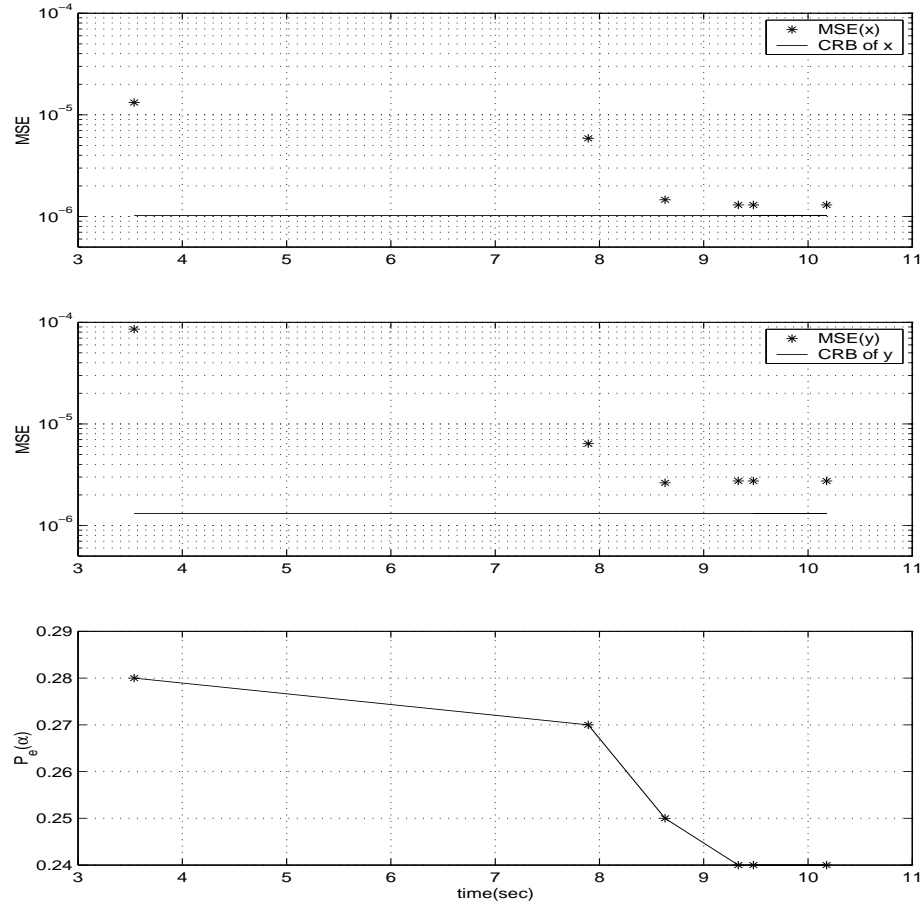
Figure 2.17: Parameter estimate variances and CRB for localized scattering response with parameters $\{4.5, 2.9, 1, 0, 0, 0, 1\}$ versus average computation time at 3 inch resolution

44

of the two structures, so that we can have an understanding of what to expect as detection performance. We then propose three different structure selection tests: a GLRT-based (generalized likelihood ratio test), an $\hat{L}$-based (estimated length test) and an image-based test. We finally present numerical results and compare the three tests in terms of performance and computational complexity.

Problem Statement

The parametric model for a single scattering mechanism is given as follows (Section 2.2.6).

$$
\begin{aligned}
\tilde{E}(f_{xn}, f_{yn}) &= A \cdot \left(j\sqrt{f_{xn}{}^2 + f_{yn}{}^2} \right)^\alpha \cdot \exp\left(-j2\pi \left(\frac{f_{xn}}{\beta} x_p \eta_x + f_2 y_p \eta_y \right) \right) \\
&\quad \cdot \mathrm{sinc}\left(\frac{\pi\sqrt{f_{xn}{}^2 + f_{yn}{}^2} L_p \eta_y}{2\sin(\phi_m/2)} \sin\left(\tan^{-1}(f_{yn}/f_{xn}) - \bar{\phi}_p \phi_m/2 \right) \right) \\
&\quad \cdot \exp(-f_2 \gamma_p)
\end{aligned}
\tag{2.76}
$$

The last two terms in the model, which are the $\exp(\cdot)$ and the $\mathrm{sinc}(\cdot)$ terms, are related to the aspect dependence of the response. However, these two terms do not appear in the model at the same time. For localized scatterers, the parameters L_p and $\bar{\phi}_p$ are zero, so the $\mathrm{sinc}(\cdot)$ term equals one. The remaining set of parameters is $\theta_\ell = \{x_p, y_p, \alpha, \gamma_p, A\}$. In the case of distributed scatterers, the parameter γ_p is zero, so the $\exp(\cdot)$ term equals one. The set of parameters for a distributed scattering center is $\theta_d = \{x_p, y_p, \alpha, \bar{\phi}_p, L_p, A\}$.

We can see the structure difference clearly in the following demonstration. In Figure 2.18, the magnitude frequency domain responses of two scattering centers are displayed: a localized scatterer ($L_p=0$, $\gamma_p=0.3$) and a distributed scatterer ($L_p=8$). When we look at these magnitude responses, we observe a very small exponential decay along the f_y direction for the localized case and a |sinc| profile along the same direction for the distributed case, corresponding to the different aspect dependences.

Our main goal is to estimate the parameters of the scattering mechanisms present in a given SAR image. In order to estimate the parameters, we need to know which one of the two structures is present. By detecting the structure, we identify the corresponding parametric model and the set of parameters to estimate. After this, we can proceed with the actual parameter estimation stage described in Section 2.3. In some cases the detection and parameter estimation steps are combined, as we will see below.

The difficulty of the structure selection problem is that localized scattering centers are well modeled as distributed responses with $L \approx 0$. The models do not exactly coincide except for the special case of a localized model with $\gamma_p = 0$ and a distributed model with $L_p = 0$. However, for small L_p values, the difference between them is very small, so that noisy data can be well-modeled by either choice. In Figure 2.19(a), distributed responses with various L_c values are shown (L_c: length in crossrange resolution units). The $L_c = 0$
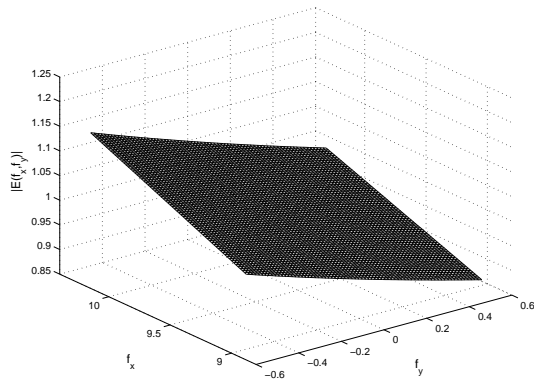
(a) localized response - $L_p = 0$, $\gamma_p = 0.3$
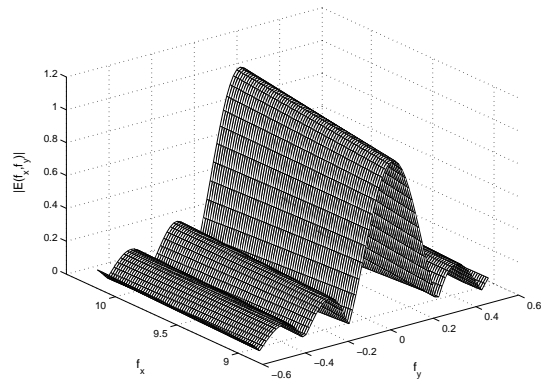
(b) distributed response - $L_p = 8$

Figure 2.18: Magnitude frequency domain responses of localized and distributed scatterers
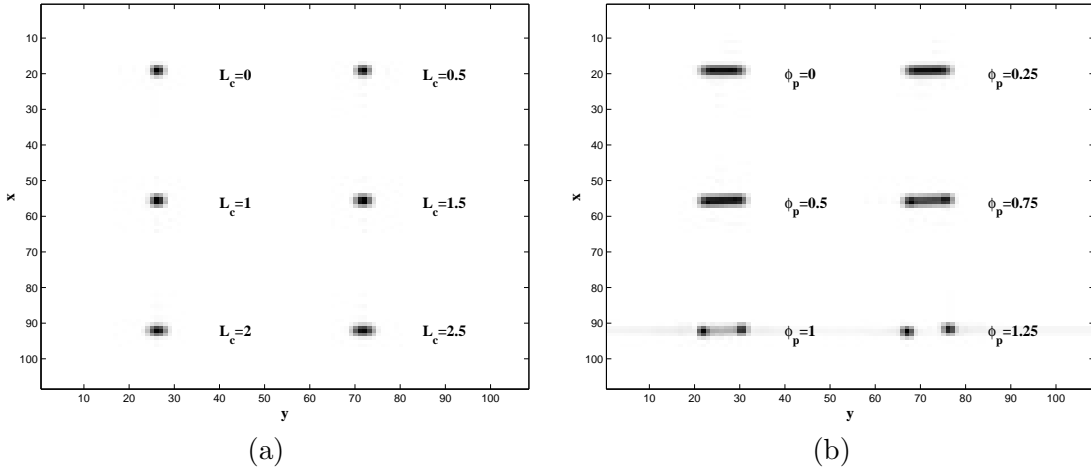
Figure 2.19: Distributed scattering center responses for various L_c and $\bar{\phi}_p$ values

response is identical to a localized scattering response with $\gamma = 0$. We see that for small L_c, the localized and distributed responses are indistinguishable. Figure 2.19(b) displays distributed scatterers with $L_c = 6$ and various $\bar{\phi}_p$ values. We observe that as the tilt angle increases, the response starts to look like two localized scattering responses.

We want to get an idea on the distinguishability of the two structures in an algorithm-independent way, so we perform the following study. We look at the fit error when a distributed and a localized model are used to model a distributed scattering center with length L_c. For each value of L_c, we generate 20 realizations of the scattering response with different center locations (x_p and y_p) to account for estimation differences as a function of location. For each realization, we obtain approximate maximum likelihood estimates of the parameters $\hat{\theta}_{AML,\ell}$ under the localized response assumption. We construct the image $s(\theta_\ell)$ with the estimated parameters. We compute the normalized difference $|||s(\theta_\ell)| - |d|||/||d||$ where d is the simulated distributed response. We also compute $||n||/||d||$ where n is the noise corresponding to the specified SNR value. In Figure 2.20, we plot the minimum, mean and maximum of these norm ratios versus L_c for 30 dB and 20 dB SNR. In qualitative terms, we expect to be able to reliably discriminate between localized and distributed scattering centers only when the differences in the model norms exceed noise. As seen in Figure 2.20, for a signal-to-noise ratio of 20 dB, an L_c value greater than about 1.6 is required to reliably detect a distributed scatterer. This value decreases to $L_c \approx 1$ for the 30 dB SNR case.

Structure Selection Tests

In previous parameter estimation algorithms [10, 6], either the structure is assumed to be known or it is estimated from the image segmentation. We propose three different approaches for structure selection: a GLRT approach, a test based on the estimated length,
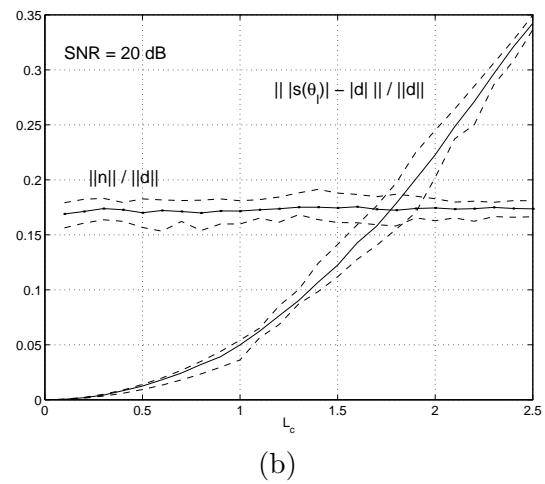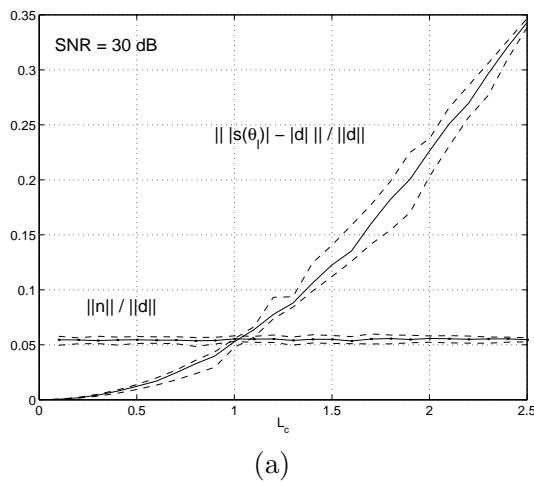
Figure 2.20: Normalized model differences at 20 dB and 30 dB SNR

$\hat{L}$ in the distributed model, and a computationally fast image based approach.

The structure selection problem is a hypothesis testing problem. We need to decide between the following two hypothesis:

H_ℓ : scattering center is localized.

H_d : scattering center is distributed.

We define the probability of false alarm P_{FA} as the probability of deciding that the scatterer is distributed when in fact it is localized. The P_D (probability of detection) is defined as the probability of correctly classifying distributed scattering centers. Let us now look at the proposed structure selection tests.

paragraphGLRT-Based Structure Selection

The generalized likelihood ratio test (GLRT) based structure selection involves comparing the ratio of the likelihood functions under the two hypothesis to a threshold.

$$\frac{f(d|H_d, \hat{\theta}_d)}{f(d|H_\ell, \hat{\theta}_\ell)} \underset{H_\ell}{\overset{H_d}{\underset{<}{>}}} \eta_{GLRT} \qquad (2.77)$$

With the Gaussian noise assumptions, the likelihood functions are given as follows:

$$f(d|H_d, \hat{\theta}_d) = \frac{1}{\pi^{M_z N_z} \cdot |\Sigma|} \cdot \exp\left[-(d - s(\hat{\theta}_d))^H \Sigma^\dagger (d - s(\hat{\theta}_d))\right] \qquad (2.78)$$

$$f(d|H_\ell, \hat{\theta}_\ell) = \frac{1}{\pi^{M_z N_z} \cdot |\Sigma|} \cdot \exp\left[-(d - s(\hat{\theta}_\ell))^H \Sigma^\dagger (d - s(\hat{\theta}_\ell))\right] \qquad (2.79)$$

where $\hat{\theta}_d$ and $\hat{\theta}_\ell$ are the set of parameter estimates obtained by the approximate maximum likelihood parameter estimation algorithm, assuming that the structure is distributed and localized respectively. When we take the logarithm of the ratio and cancel common terms, the test given by Equation 2.77 reduces to

$$||d - s(\hat{\theta}_\ell|H_\ell)||^2_{\Sigma^\dagger} - ||d - s(\hat{\theta}_d|H_d)||^2_{\Sigma^\dagger} \underset{H_\ell}{\overset{H_d}{\underset{<}{>}}} \eta'_{GLRT} \qquad (2.80)$$

If the difference between the weighted error norms of the localized model fit and the distributed model fit is greater than a threshold, we decide in favor of H_d; if it is less than the threshold η'_{GLRT}, we decide on H_ℓ. The threshold η'_{GLRT} is user selected.

For a specific choice of the threshold η'_{GLRT}, the GLRT test is in fact equivalent to the minimum description length (MDL) test [15]. The MDL test is a very common way of treating model selection problems. In this test, the minimum description length of the model under each hypothesis is calculated as follows:

$$MDL(H) = -2 \log f_{\hat{\theta}}(Y|H) + m \log n \qquad (2.81)$$

49

where m is the number of parameters in the model and n is the number of data points. Then, a decision is made in favor of the model with the smallest length. In our case, the MDL test can be stated as

$$MDL(H_\ell) \underset{H_\ell}{\overset{H_d}{\gtrless}} MDL(H_d) \tag{2.82}$$

$$-2\log f_{\hat{\theta}_\ell}(d) + m_\ell \log n \underset{H_\ell}{\overset{H_d}{\gtrless}} -2\log f_{\hat{\theta}_d}(d) + m_d \log n \tag{2.83}$$

Substituting the expressions for the log-likelihood functions and canceling common terms, we obtain

$$2||d - s(\hat{\theta}_\ell|H_\ell)||^2_{\Sigma^\dagger} + m_\ell \log n \underset{H_\ell}{\overset{H_d}{\gtrless}} 2||d - s(\hat{\theta}_d|H_d)||^2_{\Sigma^\dagger} + m_d \log n \tag{2.84}$$

$$||d - s(\hat{\theta}_\ell|H_\ell)||^2_{\Sigma^\dagger} - ||d - s(\hat{\theta}_d|H_d)||^2_{\Sigma^\dagger} \underset{H_\ell}{\overset{H_d}{\gtrless}} (m_d - m_\ell) \cdot \frac{\log n}{2} \tag{2.85}$$

The difference between the parameter vectors θ_d and θ_ℓ is that θ_d contains the two real-valued parameters $\{\bar{\phi}_p, L_p\}$ whereas θ_ℓ contains the single real-valued parameter γ_p. Thus, $m_d - m_\ell = 6 - 5 = 1$, and for $\eta'_{GLRT} = 1 \cdot \frac{\log n}{2}$, the GLRT test is the same as the MDL test.

As seen in Equation 2.80, in order to perform the GLRT test, we need to obtain both $\hat{\theta}_d$ and $\hat{\theta}_\ell$. This means that we need to fit both the distributed and the localized model to the data. This is a costly procedure. Also after the decision, the estimates corresponding to the rejected structure assumption are discarded and the computation performed to obtain those estimates is wasted. The computational cost of the GLRT test motivates us to develop some heuristic tests with possibly inferior performance but lower computational cost.

paragraph$\hat{L}$-Based Structure Selection

In the $\hat{L}$-test, we assume that the response of interest is distributed. Under this H_d assumption, we obtain the AML estimates of the corresponding parameters, $\hat{\theta}_d = [\hat{x}_p, \hat{y}_p, \hat{\alpha}, \bar{\hat{\phi}}_p, \hat{L}_p, \hat{A}]$. We then perform a threshold test on the estimated length $\hat{L}_p$.

$$\hat{L}_p \underset{H_\ell}{\overset{H_d}{\gtrless}} \eta_L \tag{2.86}$$

If $\hat{L}_p$ is greater than the user-selected threshold η_L, we decide that the scattering center is distributed. Since we already have the corresponding parameters estimates $\hat{\theta}_d$, the processing of the peak is completed. If $\hat{L}_p < \eta_L$, we choose H_ℓ. In this case, we have to fit the localized model to the data and obtain $\hat{\theta}_\ell$.
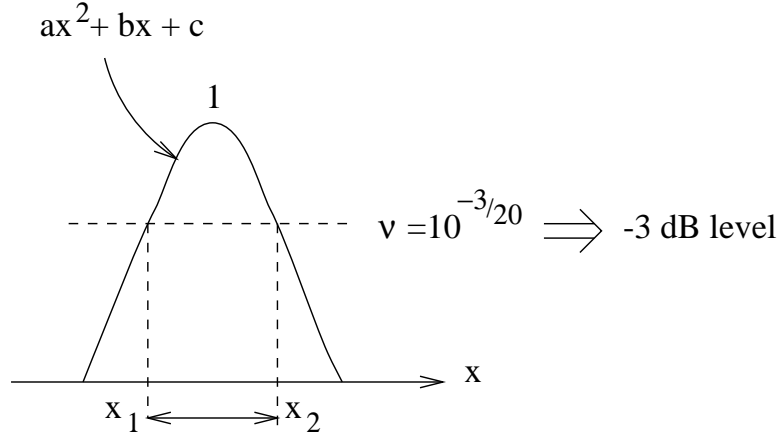
Figure 2.21: Estimation of -3 dB width of a scattering response by parabola fitting

The $\hat{L}$-test requires less computation than the GLRT test in the case of distributed scatterers by eliminating the localized model fitting stage. However for localized scatterers, the $\hat{L}$ and the GLRT tests are equally costly in terms of computation.

paragraphImage-Based Structure Selection

A computationally fast structure selection test can be derived by exploiting the shape of the scattering center response in the SAR image. We know that the crossrange extents of extracted distributed scattering center responses are larger than that of localized scattering centers.

The algorithm we propose is as follows: As a result of image segmentation, we have a region of high energy extracted. We further extract a strip of crossrange pixel samples from that region, passing through the peak pixel. This results in a vector of a small number of samples (usually between 3-20). We normalize these samples to have a peak value of one. We then fit a parabola, $ax^2 + bx + c$ to the samples using a least-squares fit for the parameters (a, b, c). Next, we select a threshold ν at which to estimate the width of the scatterer's crossrange response. We choose the -3 dB level, which corresponds to a value of $\nu = 10^{-3/20}$. When we equate $ax^2 + bx + c$ to $\nu = 10^{-3/20}$ and solve for the roots, we obtain x_1 and x_2 (Figure 2.21). The distance between these two roots correspond to the -3 dB width, $\hat{W} = |x_1 - x_2|$. The image-based hypothesis test for a localized or distributed scattering center is given by

$$\hat{W} \underset{H_\ell}{\overset{H_d}{\underset{<}{\gtrless}}} \eta_W \qquad (2.87)$$

where η_W is a user-selected threshold.

A parabola is chosen because for localized scatterers, the crossrange response is essentially the point spread function of the radar imaging process in the crossrange direction, and for

51

most windows used in image formation, this response is well-modeled by a parabola. For a distributed scattering center, the parabola is not a good fit, but still gives an estimate $\hat{W}$ which is above any threshold η_W chosen for practical false alarm probabilities. In addition, the parabola gives a real valued estimate of the width (not quantized by pixel samples), which provides robustness to the center location of the scattering center.

The image-based test is computationally much simpler than either the GLRT or the $\hat{L}$ test. By using this test, we make a decision on the structure of the scatterer prior to any model fitting. After the structure is selected, we only estimate the parameters of the corresponding selected model structure. This way, no computational power is wasted by fitting a rejected structure model. On the other hand, this algorithm is expected to have inferior performance because it only uses a subset of the available data and prior information about the scattering center responses.

Numerical Results

In this section we evaluate the performance of the proposed structure selection tests presented in the previous section. This evaluation is based on the probability of detection versus probability of false alarm plots (ROC curves) of the tests, obtained through Monte Carlo simulations.

We generate 200 localized scattering center responses in 20 dB SNR. We apply the proposed tests to these scattering centers for various choices of test thresholds. We calculate the probability of false alarm (the probability of classifying localized scatterers as distributed responses) for each of the threshold values. Following this, we simulate 200 distributed scatterers with fixed length in 20 dB SNR. We again apply the tests with the same threshold values and obtain the corresponding probabilities of detection (the probability of correctly classifying distributed scatterers). Finally, for each threshold value, we plot the detection probability versus the false alarm probability, which gives us the ROC curve. Several curves are obtained by varying the length of the distributed scattering centers.

In Figure 2.22 and Figure 2.23, the ROC curves for the GLRT test and the $\hat{L}$ test are presented respectively. We observe that for distributed scatterers with length less than or equal to 0.5 crossrange resolutions, the tests cannot perform better than chance. As the length of the scatterer increases, the performances improve. For distributed scatterers with $L_c \geq 1.5$, both tests give nearly perfect results. Given their similar overall performance, the $\hat{L}$ test is preferred over the GLRT test due to its lower computational cost.

The ROC curves for the image-based test are seen in Figure 2.24. Unlike the GLRT and the $\hat{L}$ tests, we do not observe nearly perfect results for an L_c value of 1.5. However, the performance is still very good. When $L_c \geq 2$, the image-based test also provides almost perfect detection capability. As we mentioned before, this test has much lower computational cost than the other two tests. Therefore, despite the slightly inferior performance, we choose the image-based test as the structure selection test to be implemented in our main
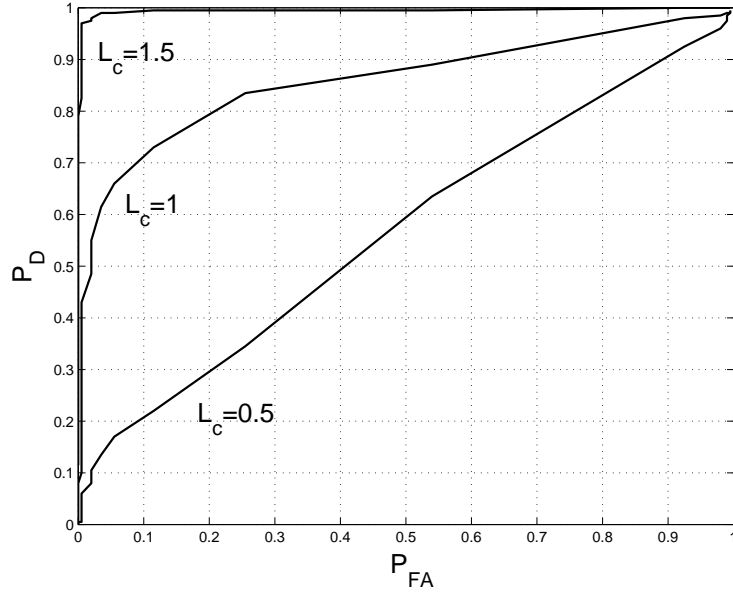
Figure 2.22: Detection probability ($P_D = P(H_d|H_d)$ versus false alarm probability ($P_{FA} = P(H_d|H_\ell)$) of the GLRT Test in 20 dB SNR

L_c	P_D
0.5	0.055
1.0	0.235
1.5	0.765
2.0	0.995

Table 2.2: Detection probabilities versus distributed scattering center length for the image-based test with $\eta_W = 1.5$

parameter estimation algorithm. The threshold we choose is $\eta_W = 1.5$ which corresponds to a false alarm probability of 0.01. The detection probabilities for various L_c values are presented in Table 2.2. If better performance is desired, the GLRT or the $\hat{L}$ test can be implemented.

2.11 Measured Data Results

2.11.1 Introduction

In this section we evaluate the performance of the parameter estimation algorithm we have developed using measured data. The measured data we use are SAR images of the
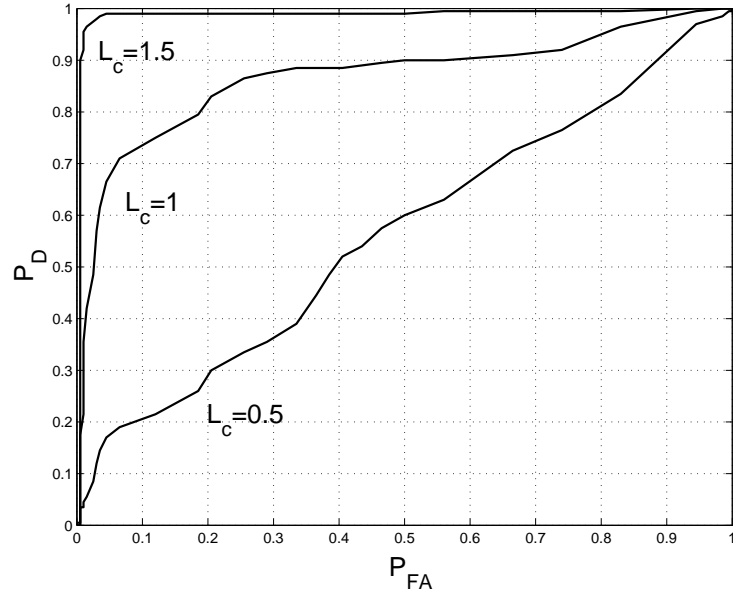
Figure 2.23: Detection versus false alarm probability of the $\hat{L}$ Test in 20 dB SNR
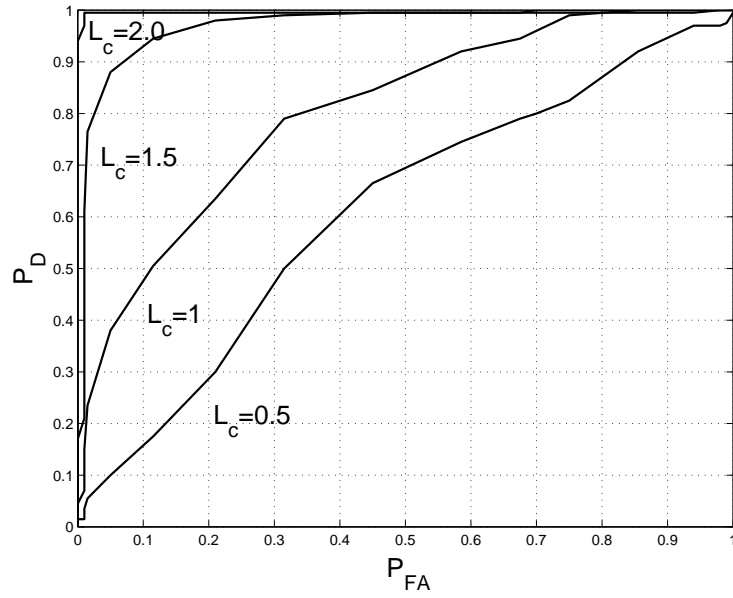
Figure 2.24: Detection versus false alarm probability of the Image-based Test in 20 dB SNR
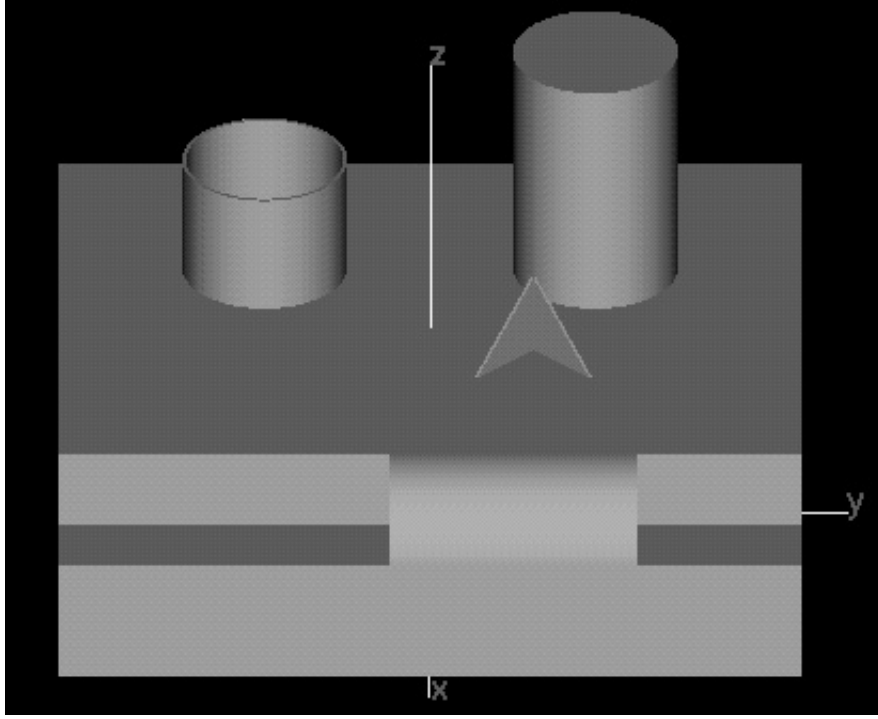
Figure 2.25: SLICY Test Target

test target SLICY (Sandia Laboratories Implementation of Cylinders II) [10]. We first introduce this target and present the data collection and image formation scenarios used to obtain the SAR images. We then discuss some difficulties encountered due to the low resolution (12" resolution) of these images. We propose some algorithm modifications to overcome these difficulties. Following this, the results of the modified parameter estimation algorithm are presented. We also generate synthetic SLICY images using the same scenario as the measured data. The synthetic images provide us with a better understanding of the scattering characteristics of the target and allow us to make comparison and calibration.

2.11.2 SLICY Test Target

The SLICY target is a metal object that consists of several simple scattering structures (Figure 2.25). Its base is roughly 2.75 m $\times$ 2.45 m, with a height of 0.75 m. There are two dihedrals and a horizontal quarter cylinder in front of the base which are all distributed scattering geometries. On top of the base, two upright cylinders of heights 0.9 m and 0.45 m are placed. There is also a trihedral formed by two right triangular plates with a common side length of 0.3 m. The cylinders and the trihedral are localized scatterers.

There are two image data sets of SLICY for 15° and 17° azimuth angles. At each data set,

(a) 3" Resolution   (b) 12" Resolution
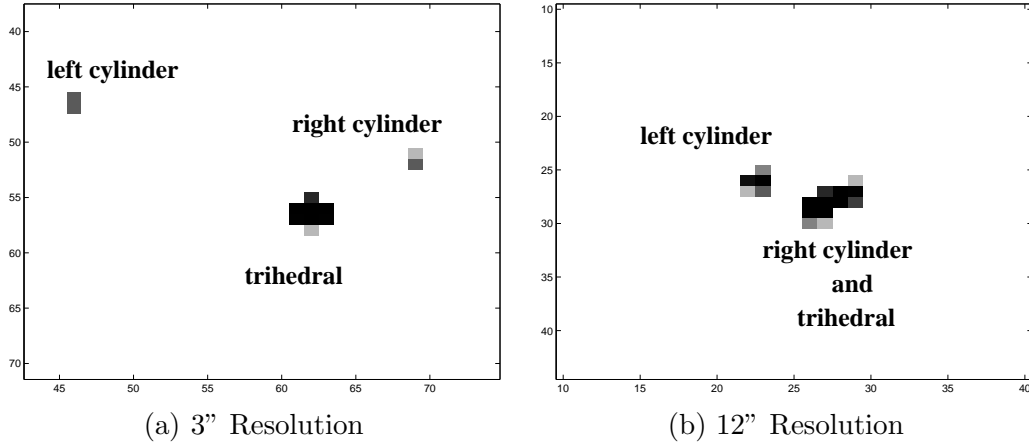
Figure 2.26: Synthetic SLICY images at 3" and 12" resolutions at a 13° aspect angle

SAR images are provided at 274 aspect angles rotating around the target. To form a single image, frequency domain data at a 42×42 uniform grid of spatial frequencies are used. The center frequency is 9.599 GHz. The bandwidth is 0.591 GHz in the downrange direction and 0.4923 GHz in the crossrange direction. This data is multiplied by a Taylor window with a sidelobe level of -35 dB and $\overline{n} = 4$, and then zero-padded to a 54×54 matrix. The SAR image is obtained by performing a 2D-IFFT on this matrix.

2.11.3   Algorithm Modifications

The SLICY data sets contain images at 12" resolution. The low resolution of the images effects the validity of the isolated scattering center assumption that allowed us to decouple the parameter estimation problem and perform sequential processing. This argument is more clearly understood with the following demonstration of two synthetically generated SLICY images with the same aspect angle at 3" and 12" resolution. In Figure 2.26(a) we see the 3" resolution image at a 13° aspect angle. Three strong isolated responses are observed: the two cylinders and the trihedral. When we aspect at the 12" resolution image, we see that the responses from the right cylinder and the trihedral cannot be distinguished. It is not possible to extract regions that contain the response from only one of these scatterers; therefore, processing them sequentially is not a good strategy. At the expense of increasing computational complexity, these two responses must be processed simultaneously. This requires us to modify the image segmentation algorithm described in Section 2.6.1, so that such cases will be detected and processed accordingly.

The modified image segmentation is the same as the original segmentation algorithm until the -3 dB level below the peak is reached while processing the pixels. At this point, the decision about the number of scatterers present in the region is made. The MSTAR Peak

56

Extractor program [4] is used for this purpose. This program first detects the local maxima in a SAR image. Then, it fits parabolas to the extracted local maxima to obtain location and amplitude estimates. The peaks which are no less than a user-specified amount (0.5 pixels in our case) apart are output by the program, along with their corresponding estimated locations and amplitudes. After we run the MSTAR peak extractor, we need to determine how many of the extracted peaks lie in the processed image region (above the -3 dB level). We propose an ad-hoc solution to this model selection problem; however, more sophisticated model selection methods could have been used, *e.g.* MDL as discussed in Section 2.10.1.

If there is only one peak in the region, then we conclude that there is a single scattering center. If the number of peaks is more than one, we look at the peaks' relative downrange locations. We know that in the case of a distributed scattering center with a high tilt angle, we may observe a two-humped profile in the response. However, the downrange location between the two humps (peaks) is very small for a 12" resolution scenario. Therefore, we pick a threshold of 0.25 pixels and assume that if the downrange locations of the two peaks differ less than 0.25 pixels, then they belong to a single distributed scattering response. Otherwise, we assume that they are different localized responses.

For the case where more than one peak is observed, the structure decision is also made within the image segmentation as described above. We know that the current decision strategy is ad-hoc; however since we cannot separate the responses from the different scatterers, we cannot apply the more sophisticated structure selection tests described in Section 2.10. If more reliable results are desired, new methods have to be developed.

Following the order selection stage, we continue with processing the pixels between the -3 dB and -20 dB levels. At this stage in the original algorithm, we confine our interest to segment number 1 and do not grow any of the other segments. However, for the 12" resolution case, the scatters are located closer to each other and it is important to keep track of each segment in order to extract their borders accurately. For this reason, we modify the algorithm and process a pixel as follows: We search the eight neighbors of the pixel of interest and distinguish among three possible cases.

1. no neighbors are assigned to a segment

2. one or more neighbors are assigned to a single segment

3. one or more neighbors are assigned to multiple segments

The first case corresponds to a new peak, so the pixel is assigned to a new segment. In the second case the pixel is assigned to the neighboring segment. The third case corresponds to a bordering pixel. We give priority to vertical and horizontal neighbors above the diagonal neighbors and we assign the pixel to the lowest indexed vertical or horizontal neighboring segment. If all the assigned neighbors are diagonal, then we choose the lowest indexed segment among them.

Keeping track of all the segments throughout the algorithm is very costly, especially for large-sized images. We know that an extracted scattering center segment is usually confined in a small area. Therefore, given the peak location of a response, we form a sub-image that takes the peak location as center and extends 5 pixels in all four directions (11×11 sub-image). We perform the described modified segmentation algorithm on this sub-image. At the end, we check whether the extracted segment contains any of the border pixels of the sub-image. If so, this means that the size of the sub-image was not large enough. We increase the size and repeat the segmentation process. Otherwise the algorithm terminates.

Besides the modifications on the image segmentation algorithm, we also make a few changes in the parameter initialization stage. The location parameters x_p and y_p are initialized as described in Section 2.6.3 when there is a single peak above the -3 dB level. If there are multiple peaks, the location initialization is performed using the MSTAR peak extractor's location estimates. For multiple localized scatterers the exact MSTAR estimates are used. For the case of distributed scatterers, the midpoint of the two peaks' locations is used as an initial estimate for the parameter estimation algorithm.

The only other initialization difference is on the parameter $\bar{\phi}_p$. The algorithm described in Section 2.6.3 for $\bar{\phi}_p$ initialization does not give satisfactory results for the 12" resolution case. At this resolution the total angular aperture is only about $3°$. The narrow total aperture does not allow us to observe the sinc profile wide enough to make a reliable estimation, based on the relative location of the sinc's peak. Inaccurate initial values that are much larger than the actual value are observed to cause the numerical minimization algorithm to converge to a wrong local minima. Therefore, we choose to initialize this variable to zero.

2.11.4   Numerical Results

The modified parameter estimation algorithm is applied to the SLICY data sets consisting of 274 images for both $15°$ and $17°$ angles of incidence. We also generate a set of images from Xpatch simulation data at a $15°$ azimuth. The synthetically generated images provide us with a better understanding of the scattering structures of the target, since they are free of measurement errors.

We focus our interest to the two upright cylinders and the trihedral on SLICY which are all localized scattering centers. The distributed responses of the two dihedrals and the quarter cylinder in front of the target are not clearly observed in the measured data set. These responses would be best seen at a $0°$ aspect angle. However, the data set we have starts from a $2°$ aspect angle and ends with $358°$.

For localized scatterers, the set of parameters is $\{x_p, y_p, \alpha, \gamma_p, A\}$. As discussed in Section 2.8.1, we are not capable of reliably estimating the α parameter from 12" resolution images. Therefore, we will limit our interest to the downrange and crossrange location parameters x_p and y_p, the angle response parameter γ_p and the magnitude of the complex amplitude $|A|$.
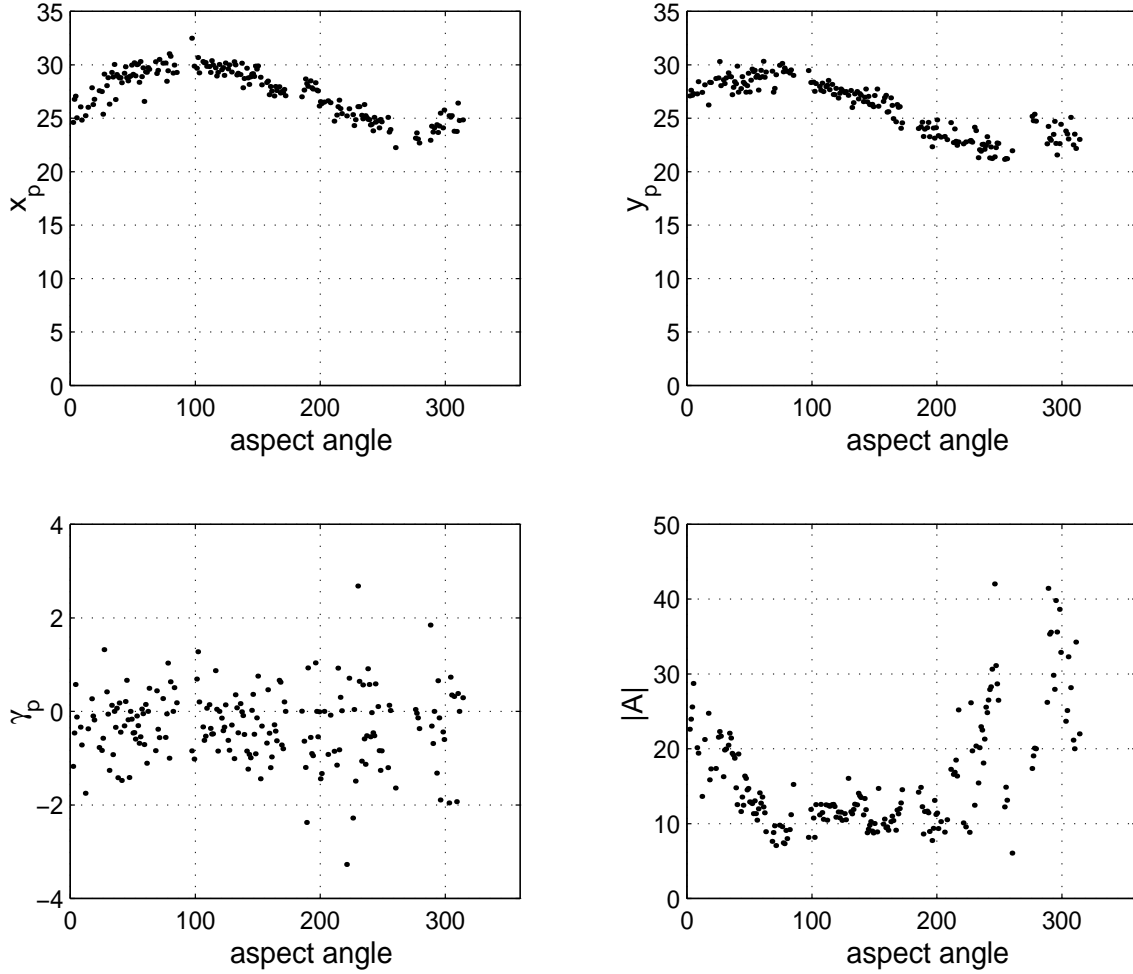
Figure 2.27: Parameter estimates of the right cylinder versus aspect angle from measured SLICY data set at 15° azimuth

We will present the estimation results of the 15° azimuth SLICY data set since we also have the synthetically generated images at that azimuth. The results for the 17° are similar. In Figure 2.27 we see the parameter estimates of the right cylinder versus aspect angle. The results are presented for the aspect angles where the response was observed clearly. About 90° and 180° aspect angles, the dihedral flashes from the side of the target prevent us from observing an isolated response from the right cylinder. We also cannot see a clear response about 270° due to the left cylinder's blocking and between 315° and 360° due to the trihedral's blocking.

In Figure 2.28 we present similar results for the left cylinder. For both cylinders, the amplitude of the response increases as the flat area in front of the cylinder gets wider and
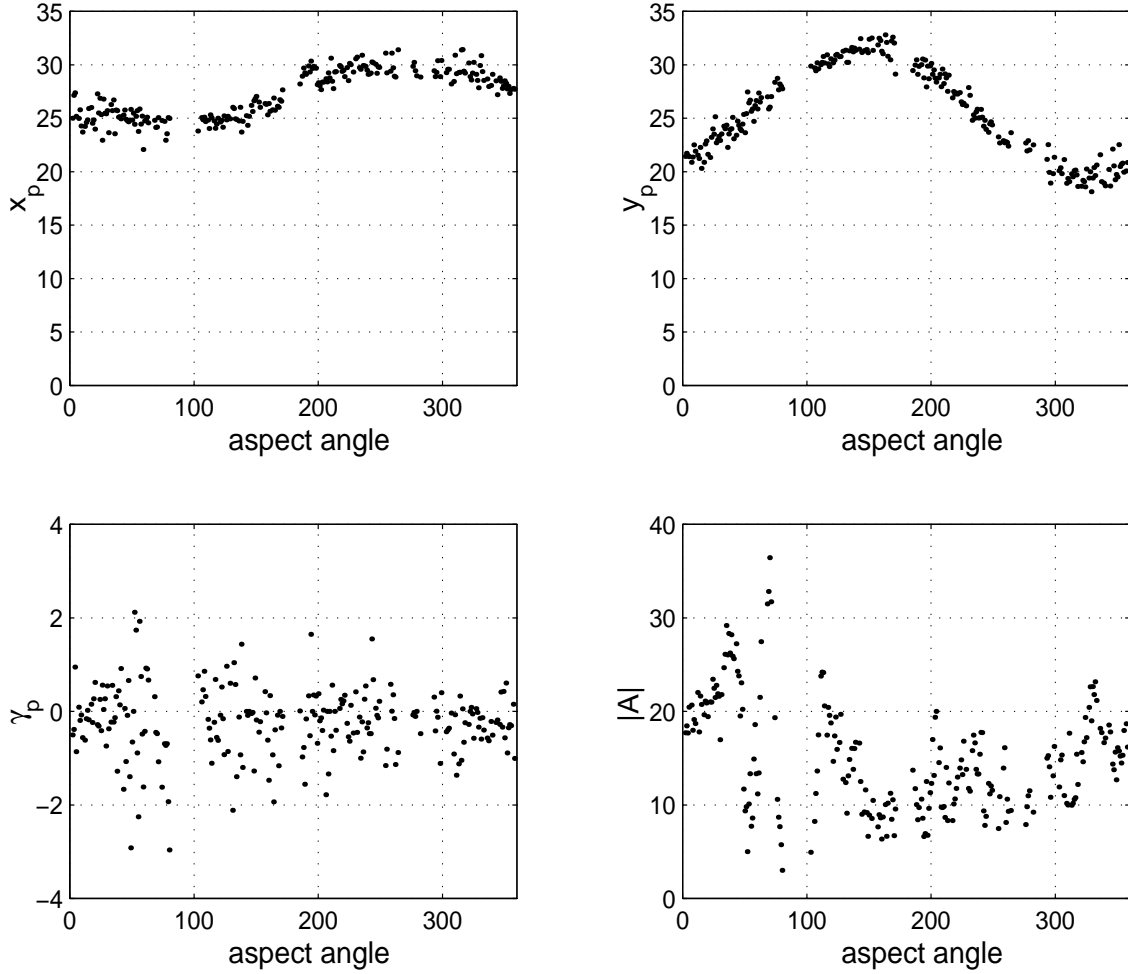
Figure 2.28: Parameter estimates of the left cylinder versus aspect angle from measured SLICY data set at 15° azimuth

so more energy is reflected back to the radar. We observe large variations in the location estimates. We believe that most of this variation is caused by inaccurate target centering in the scene for reasons we discuss later in this section. There is also a slow fluctuation observed in the location parameters. This is due to the change in the relative location of the cylinder reflection with respect to the scene's reference point as the aspect angle changes (as we rotate around the target about a rotation axis). The γ_p estimates also display variations; however, in most cases the value is between -2 and 2. We do not have a clear understanding of the source of the high variations in γ_p and $|A|$ parameter estimates.

The estimation results for the trihedral are presented in Figure 2.29. The trihedral's response can be observed from aspect angles between -50° (310°) and 50°. At -45° and 45°
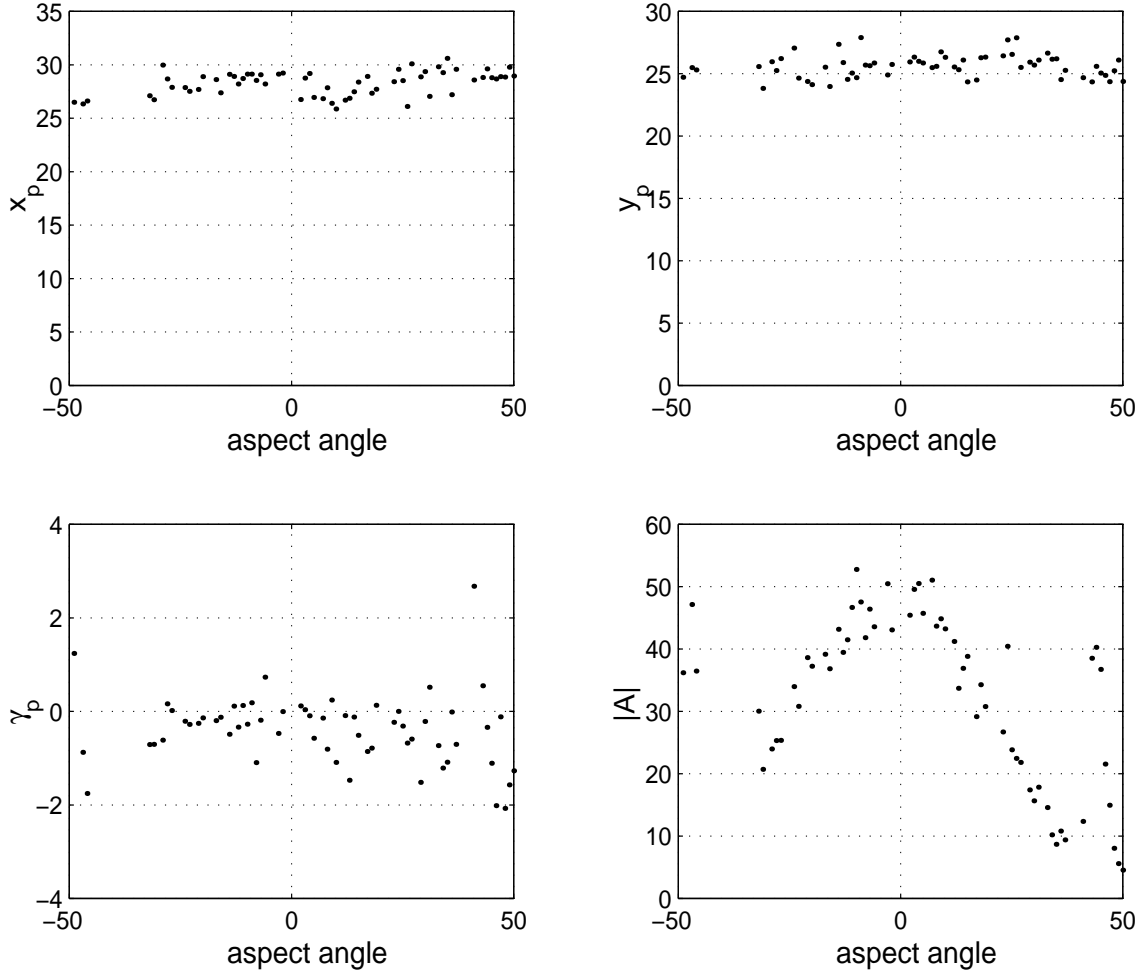
Figure 2.29: Parameter estimates of the trihedral versus aspect angle from measured SLICY data set at 15° azimuth

aspect angles, we see one of the triangular plates from its broadside. This structure is like a dihedral and it has a distributed response. However, the structure selection algorithm fails to detect these distributed responses. This is not surprising, since the length of the dihedrals is 12", which is definitely less than 1.5 crossrange resolutions. For this length, the structure selection algorithm is not expected to give correct results. The same situation is encountered at 90° and 270° aspect angles as well, where the dihedral base and the side of the quarter cylinder form distributed scatterers with length 12". These responses are not classified as distributed either.

The parameter estimation results for the right cylinder and the left cylinder from the synthetic data set are provided in Figures 2.30 and 2.31. The variations in the location estimates
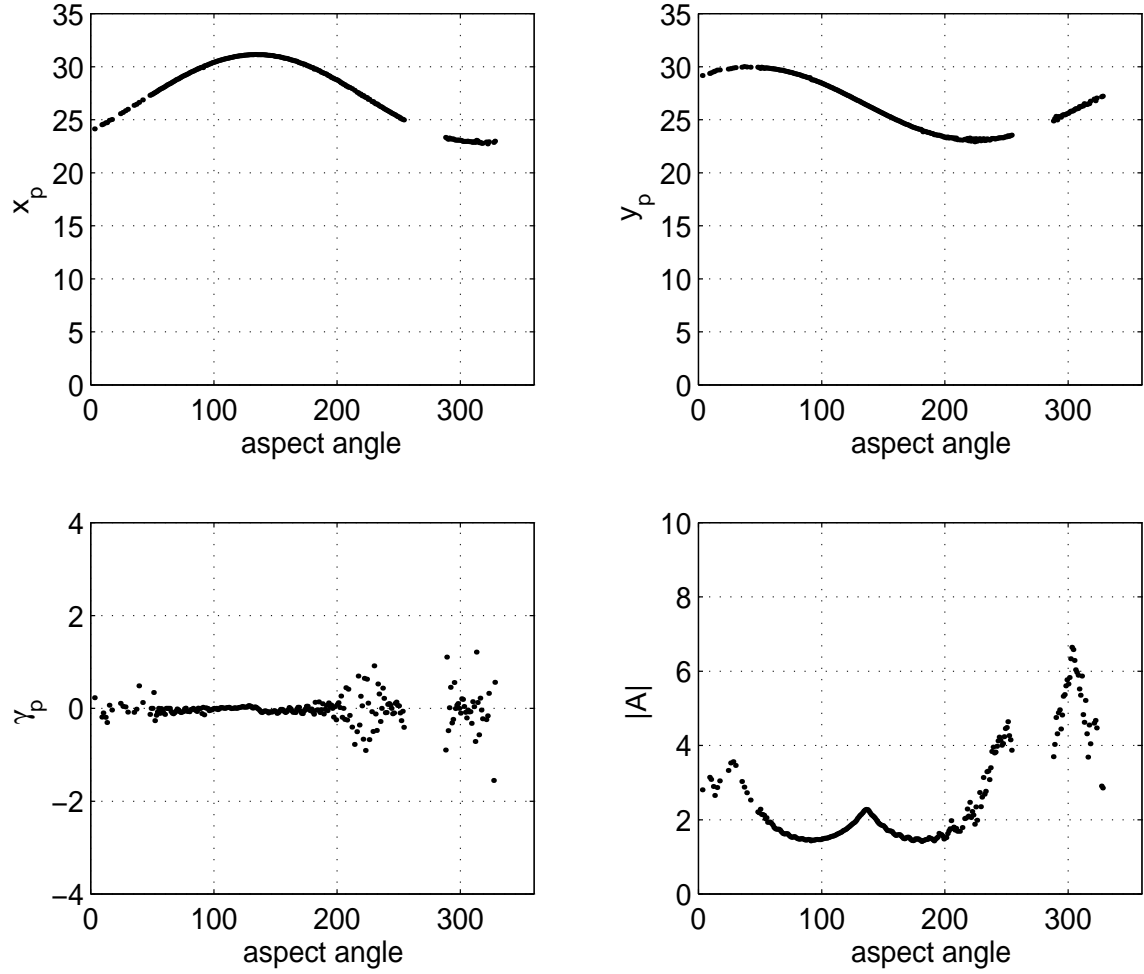
Figure 2.30: Parameter estimates of the right cylinder versus aspect angle from synthetic SLICY data set at 15° azimuth

are much smaller for the synthetic data compared to the measured data. The fluctuation of the estimates due to the change in the relative location of the scatterers versus aspect angle is clearly observed. The small variations in the magnitude of the amplitude parameter $|A|$ across some aspect angle intervals are a result of the interference from other scattering structures which prevents us from observing isolated responses.

The parameter estimates of the trihedral from the synthetic data are presented in Figure 2.32. As in the case of the two cylinders, the estimate variances are smaller for the synthetic data compared to the measured data results. The slope observed in the location estimates are due to the fact that as the aspect angle changes (as we rotate around the target about a rotation axis), the relative location of the trihedral with respect to the scene's
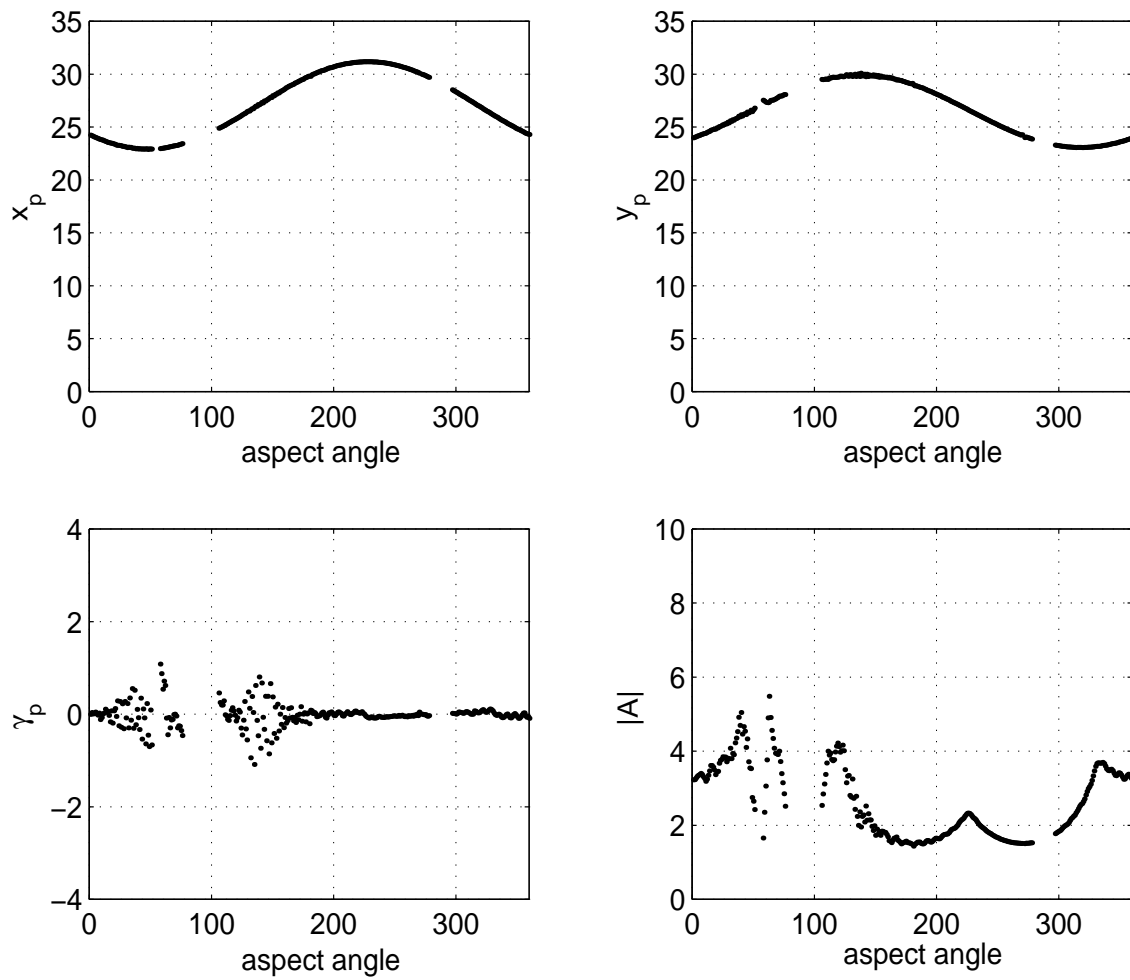
Figure 2.31: Parameter estimates of the left cylinder versus aspect angle from synthetic SLICY data set at 15° azimuth

reference point also changes. In the -50° to 50° interval which we observe the trihedral response, we see a portion of the sinusoidal location variance around the target. We claim that the amplitude of the sinusoid is small because the trihedral is close to the rotation axis, so the relative location change is not large. The variations observed in the γ_p and $|A|$ parameter estimates are due to the fact that the responses from the trihedral are not clearly isolated from the responses of the two cylinders for most aspect angles. For example, for aspect angles between -5° and 20°, the scattering response from the right cylinder interferes with the trihedral response (see Figure 2.26b). The exceptions occur at aspect angles approximately between -25° and -8°, where the left cylinder is well separated and the right cylinder is blocked (by the trihedral), so that clear isolated trihedral responses are observed. Between those aspect angles, the estimation results obtained are much better; the γ_p estimates are very close to zero and the $|A|$ estimates increase almost linearly.

For all three scatterers, we have observed that the location estimates display much smaller variation for the synthetic data when compared to the measured data. This observation suggests us that the variations in the measured data results are due to target centering inaccuracies. The argument about target centering inaccuracies is supported by the fact that when we aspect at the images one after the other, we see the same scatterer's response moving within the image in the range of 1 to 2 pixels. We want to calibrate these results using the synthetic data location estimates.

The calibration is performed by shifting the measured data locations, so that the left cylinder response is aligned in measured and synthetic data. The location parameters of the right cylinder as a result of this process are displayed in Figure 2.33. When we compare the original estimates in Figure 2.27 with the calibrated estimates, we observe a significant reduction in variation. This observation strengthens the claim that the measured data result variations are mostly due to target centering inaccuracies.

We also perform an alignment with respect to the right cylinder. The left cylinder's calibrated location estimates as a result of this process are presented in Figure 2.34. Similarly, the estimate variances are reduced with calibration. The calibrated location estimates of the trihedral are also presented in Figure 2.35.

We want to compare the parameter estimate variances obtained from the measured data to the Cramér-Rao Bounds. We choose the trihedral response between -25° and -8° aspect angles to make this comparison because we are able to observe a relatively isolated response within this interval.

In order to estimate the variance in the parameter estimates, we need to know the correct values of the parameters. However, we do not have exact information about the scene's reference point and the rotation axis; therefore, we cannot compute the parameter values. Instead, we assume that the estimated values from the synthetic data are correct.

We focus our interest to aspect angles between -25° and -8°. There is an average of 0.1937 pixel difference in the downrange location estimates and an average of 0.7414 pixel difference
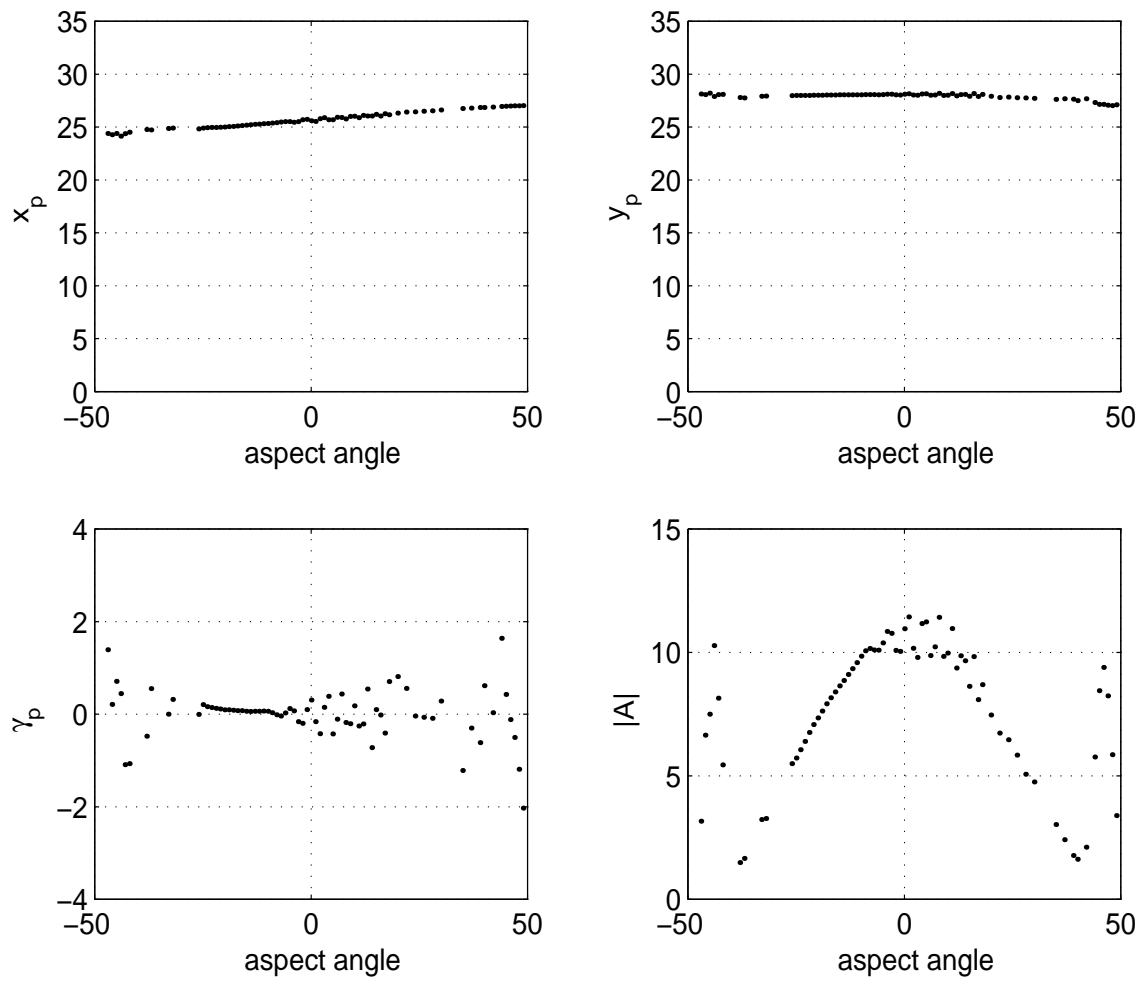
Figure 2.32: Parameter estimates of the trihedral versus aspect angle from synthetic SLICY data set at 15° azimuth
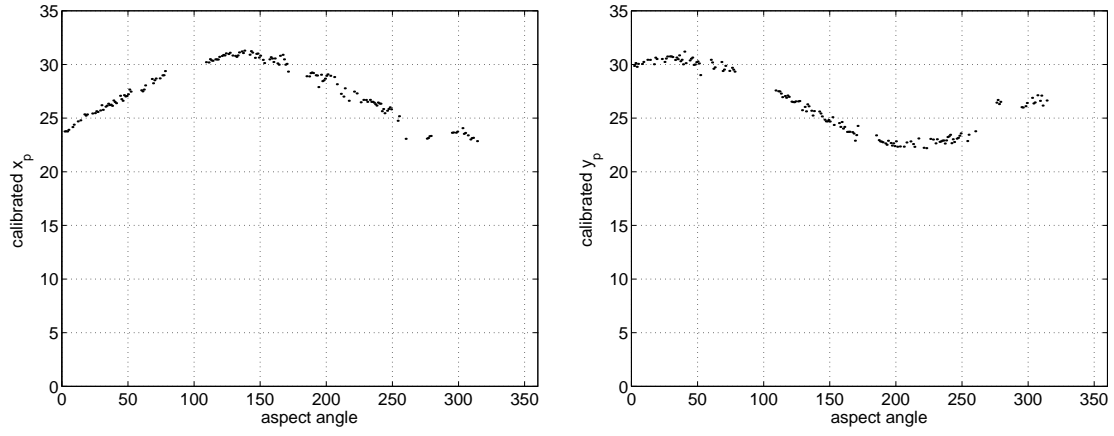
Figure 2.33: Calibrated location estimates of the right cylinder versus aspect angle from measured SLICY data set at 15° azimuth
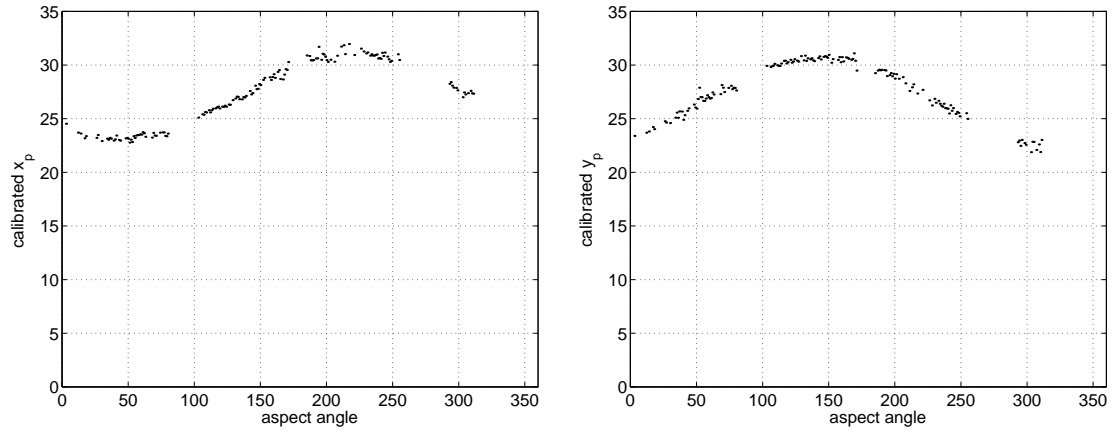
Figure 2.34: Calibrated location estimates of the left cylinder versus aspect angle from measured SLICY data set at 15° azimuth
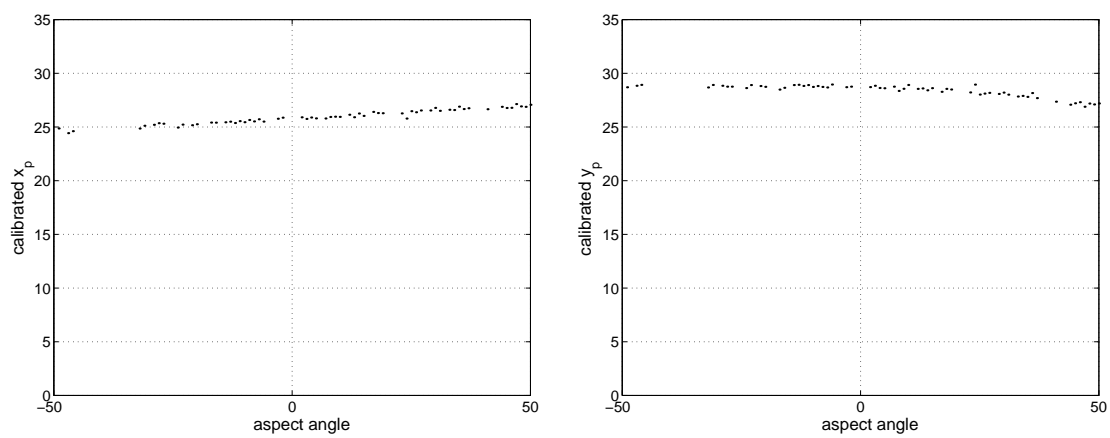
Figure 2.35: Calibrated location estimates of the trihedral versus aspect angle from measured SLICY data set at 15° azimuth

in the crossrange location estimates between the calibrated measured data results and the synthetic data results. We believe that this difference is due to the data collection and image formation procedure mismatch between the measured and the synthetic data sets. We compensate for this mismatch by shifting the synthetic data estimates by the average differences in both directions. We assume that these shifted synthetic data results are the true values of the parameters. We then estimate the standard deviation in the calibrated measured data results.

$$\text{stdev}(\hat{x}_p) = 0.0877 \text{ pixels}$$
$$\text{stdev}(\hat{y}_p) = 0.1285 \text{ pixels}$$
$$\text{stdev}(\hat{\gamma}_p) = 0.3194$$

To calculate the CRBs of the parameters, we first estimate the noise variance in the measured SLICY images: $\hat{\sigma}^2_{\text{image}} = 0.002$. We again assume that the synthetic data estimates are the true values of the parameters. By using these parameter values and the estimated noise variance, we calculate the CRBs as explained in Section 2.7. As an example, let us choose the -17° aspect angle. The square root of the CRBs are approximately 1×10^{-2} pixels for x_p and y_p and 0.0480 for γ_p.

When we compare the estimate standard deviations with the calculated CRB square roots, we observe about one order of magnitude difference. One reason for this difference is the interference form other scatterers. Also, the calibration procedure above effectively results in the trihedral location error variances to be the sum of the error variances for the trihedral and the left cylinder. Another possible reason is the mismatch between the parametric model and the actual response. For the -17° aspect angle, we calculate the average fit error power between the measured trihedral response and the localized model fitted to the response to be 0.3195. This value is much greater than 0.002 which is the estimated noise variance; suggesting the presence of interfering responses and a possible model mismatch.

The synthetic SLICY data we have used is generated using a solid model. We have also applied the estimation algorithm to another synthetic SLICY data set that is generated using a faceted model. The parameter estimates of the two cylinders obtained from this data set are presented in Figures 2.36 and Figure 2.37. We observe that the γ_p and amplitude estimate variances are unexpectedly high. However, these estimates seem to be fluctuating within a band of values according to a pattern. In order to detect a possible pattern, we estimate the power spectral densities of these parameter estimates using a periodogram spectral estimator [20]. We use the γ_p and A estimates of the right cylinder between 50° and 220° aspect angles. We remove the DC component by subtracting the mean from these estimates. The resulting periodogram spectral estimates $\hat{\phi}_A(f)$ and $\hat{\phi}_{\gamma_p}(f)$ are displayed in Figure 2.38.

In both parameters we observe frequency components at 0.12 deg^{-1}, which corresponds to a fluctuation with a period of approximately 8.3 deg. This value corresponds to a total number of about 43.2 periods around the cylinder. We believe that this effect is caused
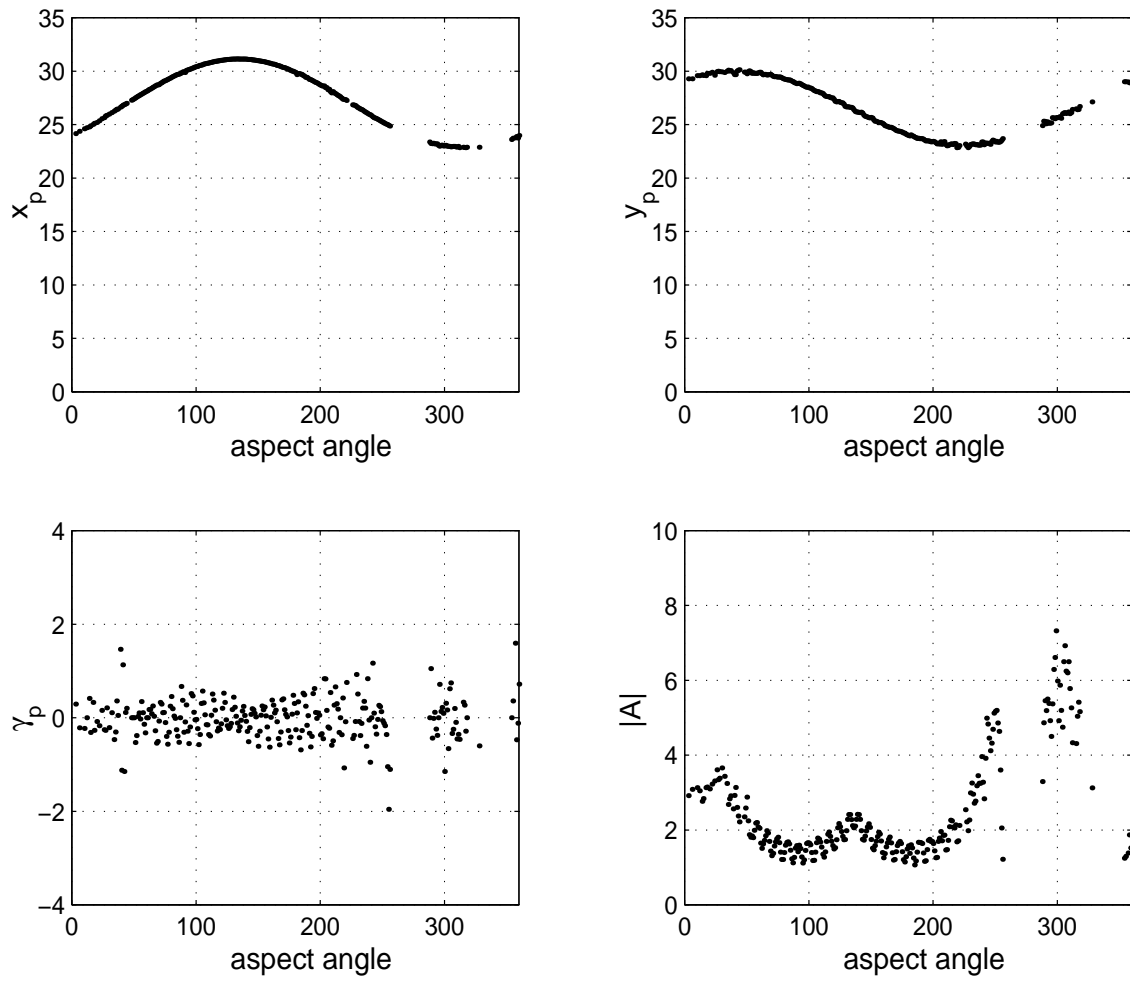
Figure 2.36: Parameter estimates of the right cylinder versus aspect angle from synthetic SLICY data set generated from faceted model at 15° azimuth

69
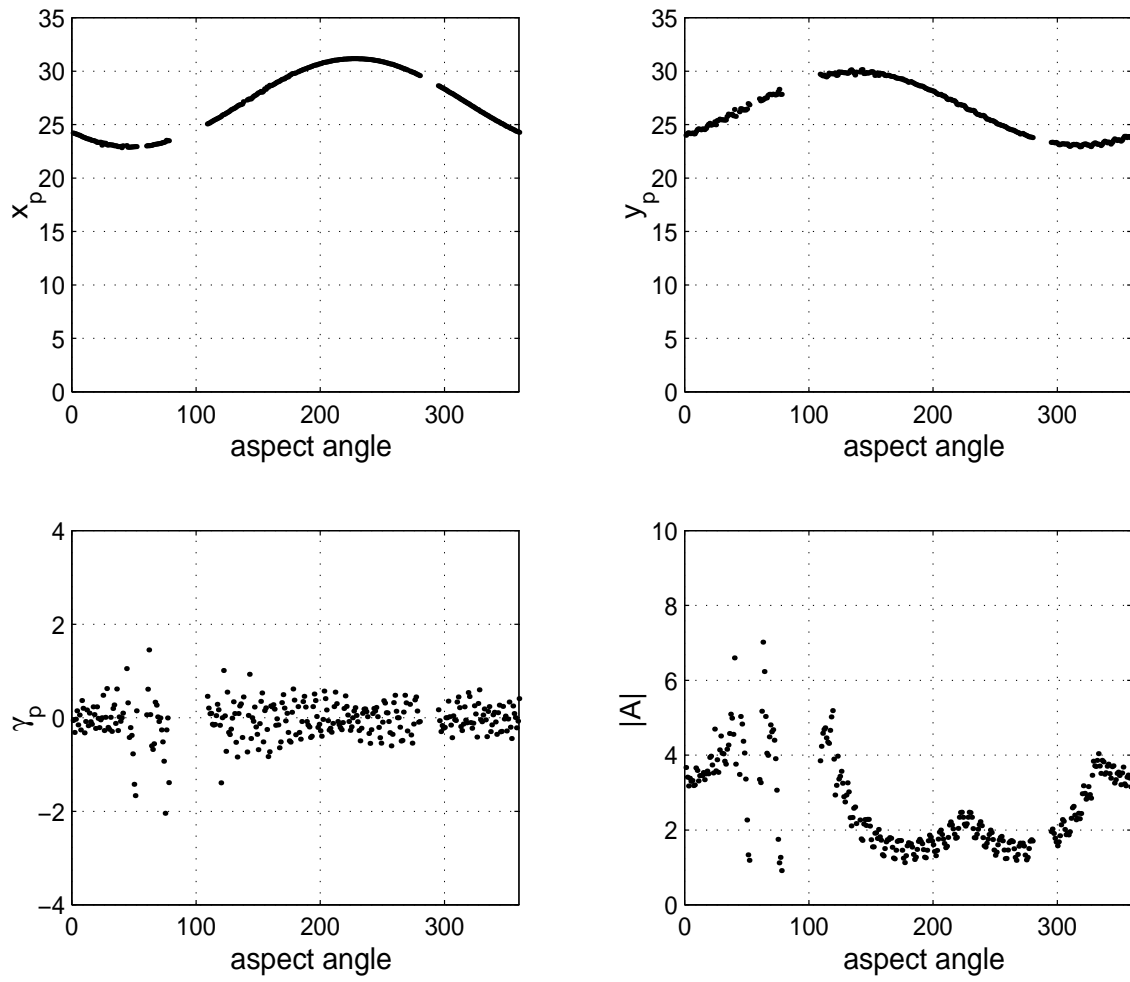
Figure 2.37: Parameter estimates of the left cylinder versus aspect angle from synthetic SLICY data set generated from faceted model at 15° azimuth

70

(a) $\hat{\phi}_A(f)$ (b) $\hat{\phi}_{\gamma_p}(f)$
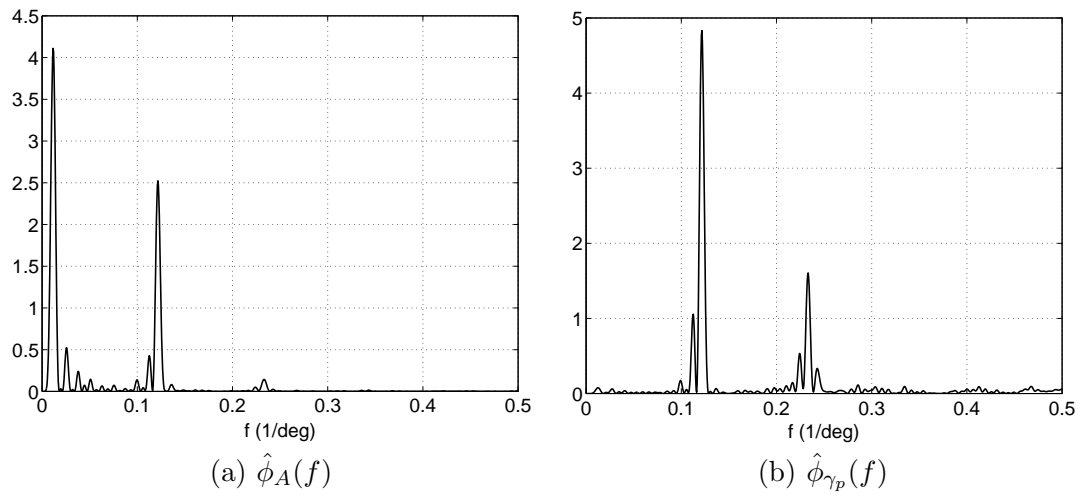
Figure 2.38: Estimated power spectral densities of the right cylinder's γ_p and A parameters obtained from synthetic data

71

by the faceted model, where the cylinder surfaces are approximated as regular polygons with 44 faces when synthetic data is generated. The amplitude of the response changes as the angle between the direction of illumination and the normal to the flat strip changes. Consequently, the γ_p parameter varies to capture the changes in the amplitude versus the aspect angle.

2.12   Summary

We have developed an automated algorithm that extracts features of scattering mechanisms present in a SAR image. The scattering responses are assumed to fit a parametric model. The algorithm obtains estimates of the model parameters that best represent the given data, according to an approximate maximum likelihood criterion. The parameters are describe the location, orientation and geometry of the scatterers and their estimates constitute the extracted feature vectors.

A statistical evaluation of the algorithm's performance can be made by using the Cramér-Rao Bound. We have derived the CRB of the parameters in the model that correspond to the minimum achievable estimate variances by unbiased estimators. Simulations on noisy scattering responses demonstrate that our algorithm achieves variances that are very close to the CRBs.

We have also presented an extensive study on the classification of scattering centers as localized or distributed structures. We have proposed three different structure selection tests and displayed performance results through simulations. We have shown that by using these tests, we are capable of distinguishing localized scatterers from distributed scatterers with lengths longer than approximately 1.5 crossrange resolutions. A possible future study would be to increase the robustness of the structure selection tests to closely spaced scattering responses.

We have then modified our algorithm to be applied to low resolution measured data and obtained parameter estimates for large sets of image data of the test target SLICY. However, these modifications were based on insight. A more detailed study is suggested for processing low resolution images. We have also applied the algorithm to Xpatch simulated data sets. We have used these results to interpret and calibrate the measured data results.

3. MODEL-BASED CLASSIFICATION OF RADAR IMAGES

3.1 Introduction

In this chapter, a Bayesian model-based imaging and decision approach is presented for classification of radar images. The approach provides a structured, implementable, scalable means for managing complexity of the hypothesis set and bypassing the complexity of joint distributions on image pixels. Model-based classification, or pattern matching, combines uncertainty in both the object class models and the sensor data to compute posterior probabilities of hypotheses. The Bayesian formalism allows clear and explicit disclosure of all assumptions. The pattern matching permits tractable performance estimation and provides robustness against environments previously not measured, and hence not available for construction of image templates.

3.1.1 Problem Complexity

Classification of radar images, like many image inference tasks, is characterized by a complex hypothesis space. The hypothesis set consists of M classes, or objects; typical cases are $8 \leq M \leq 32$. The complexity arises in that each object may be observed in a variety of poses, configurations, articulations, and environments, thereby resulting in an intractable density function for the radar image conditioned solely on the object class. To manage the complexity, object classes are each expressed as a mixture density of subclasses. Each subclass is defined by a deterministic description of object pose, configuration, articulation, occlusion, sensor orientation, etc. Additional variability within subclasses is modeled stochastically to account for object differences due, for example, to manufacturing variations or wear. The number of enumerated subclasses explodes exponentially; a typical application might dictate 10^{12} states for each hypothesis class [24]. Moreover, an application may dictate that many more than M decision classes be formed by defining sets of individual subclasses, H_{ij}; *e.g.*, the configuration of an object may be an important distinguishing characteristic.

Likewise, the classification of radar images is characterized by a high-dimensional observation space defying a direct random model. The observation, a collection of pixels, is a vector in R^N. A typical case is a 128-by-128 array of complex-valued pixels, yielding $N = 2^{15}$. A joint density on the N pixel values, when conditioned on a hypothesis H_{ij}, is non-Gaussian and may be multimodal [29]. For example, a simple Gaussian uncertainty on the location of a scattering mechanism leads to non-Gaussian image pixel uncertainties. Further, pixel values exhibit strong correlation due to the coherent combination of scattered energy from an object's constituent parts. Multiple reflections or large conducting surfaces can result in large distances between correlated pixels, and hence seemingly arbitrary correlation

matrices.

3.1.2 Model-based Classification

To proceed when confronting a large hypothesis space and complex image density functions, we adopt a model-based classification approach. First, a physically based feature set provides a simple, constructive alternative to joint densities on pixels for expressing uncertainty in the target and the sensor. The extraction of features is performed by statistical estimation using the physics-based parametric model of sensor data and specification of the image formation procedure. Second, a coarse-to-fine staged classification strategy is used to efficiently search the hypothesis space. Third, the sensor data model is combined with object models to predict features conditioned on a hypothesis. The on-line prediction of features eliminates the need for a prohibitively large catalog of image templates.

The model-based approach is depicted in Figure 3.1. A state of nature is characterized by the hypothesis of an object class, H_i, which is further specified by one of finitely many subclasses, H_{ij}. The SAR measurement resulting from a sensor and an image formation algorithm provides an image, U. Along the left branch in the figure, a Feature Extraction stage serves to compress the image and assign uncertainties to features. For SAR imaging, a sensor data model derived from high-frequency approximation to scattering physics provides a parametric family of densities for estimating features. Parameters are estimated from imagery and used as low-dimensional surrogates for sufficient statistics; each feature is a location together with a vector of attributes. The feature uncertainty is given as a density function, $f(Y|U)$, and acknowledges the sensitivity of parameter estimates, Y, to noisy sensor data given the image data, U.

Along the right branch in the figure, complexity of the hypothesis space is addressed in a coarse-to-fine approach. An Index stage provides a list of candidate subclass hypotheses, H_{ij}, $ij \in L$, based on a coarse partitioning of the hypothesis space. Evaluation of the candidate hypotheses then proceeds using a model for the observations. A Feature Prediction stage computes a predicted feature set by combining the sensor data model from the Feature Extraction stage and a computer-aided design (CAD) representation of a hypothesis H_{ij}. The feature set, X, has an associated uncertainty, acknowledging error in the modeling and variation among objects in the subclass. The uncertainty is expressed as a density $f(X|H_{ij})$. Importantly, the use of physically motivated features facilitates compatibility of extracted and predicted feature sets.

Finally, the predicted and extracted feature sets are combined in a Match stage to compute a posterior probability of a candidate hypothesis, $\Lambda(H_{ij})$. The top hypotheses, and their likelihoods, are reported as the output of the classification system. Computation of the likelihood scores requires a correspondence between the unordered lists of extracted and predicted features and an integration over feature uncertainty. Further, the likelihood must incorporate the possibilities of missing or spurious features in the predicted or extracted

State of
Nature, H_{ij}

SAR sensor and
image formation

Image, U

Index

H_{ij}, ij in L

Feature
Extraction

Feature
Prediction

f(Y | U)

Match

f(X | H_{ij})

$\Lambda(H_{ij})$
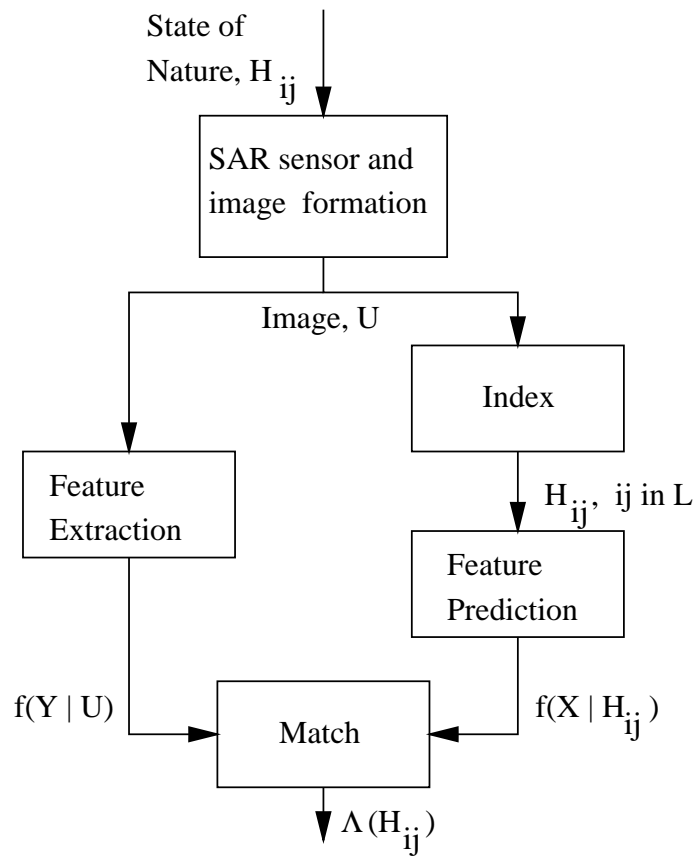
Figure 3.1: A model-based approach to classification

feature lists. The matching task can be viewed as a probablistic graph match of fully connected, attributed graphs with deletions and insertions of nodes.

3.1.3 Contributions and Organization

This chapter presents a Bayesian formalism for model-based classification. We demonstrate that the resulting hypothesis testing algorithm, including the feature correspondence, is tractable, even for problem sizes encountered in SAR target recognition. In addition, the chapter adopts a physics-based model for extracting features from SAR images; the features use the phase in complex-valued SAR images to infer the frequency and aspect dependent scattering behavior of objects. Recent advances in technology yield sensor bandwidths exceeding 20% of the center frequency; for such systems, the proposed feature sets provide much greater information than does processing motivated by a narrow-band point scattering model.

Detailed construction of the Index and Feature Prediction stages is not considered here; these stages are discussed in [25, 29]. An adaptive refinement of the candidate hypothesis list from the Index stage is considered in [28]. Moreover, a Feature Prediction stage that faithfully simulates frequency and aspect dependent scattering behavior is currently under development [29].

The chapter is organized as follows. In Section 2 we present a parametric model for radar sensor data, as required in the Feature Extraction and Feature Prediction stages. Maximum likelihood estimation of parameters from images computed using sensor data is discussed; also, parameter uncertainty, the definition of image resolution, and the Fisher information in image phase are addressed. Section 3 presents a Bayesian computation of a hypothesis likelihood given sets of extracted and predicted features. In particular, the problem of determining a feature correspondence is addressed.

In Section 4, synthetic classification results are computed using class means estimated from a measured set of X-band radar images for 10 objects. The simulation results illustrate four points: (i) the Bayes approach to model-based classification, including feature correspondence, is tractable; (ii) classification using the Bayes classifier permits estimation of the optimal error rate, given the assumed priors and feature uncertainties; (iii) classification using the Bayes classifier allows designers to explore the performance effects of sensor parameters, such as bandwidth; and (iv) classification using the Bayes classifier provides a simulation tool to investigate sensitivity of the estimated error rate to the assumed priors and feature uncertainties.

3.2 A Physical Model for Sensor Data and Feature Extraction

In this section we address the problem of feature extraction. We adopt a parametric model describing the sensor data, develop a feature estimation algorithm, and discuss feature uncertainty both for extraction and feature prediction. The model we employ is based on high-frequency approximation of electromagnetic scattering [6, 33] and represents the object of interest as a set of scattering centers. The scattering centers are described by attributes that characterize the scattering center geometry and orientation. The attributed scattering centers are used as features for both the prediction and extraction stages in Figure 3.1. The scattering model provides a method of constructing and succinctly representing hypotheses from CAD representations of class objects. Additionally, the model allows feature extraction to be cast as a parameter estimation problem.

For a Bayesian classifier uncertainty must be characterized for both predicted and extracted feature sets. Because the proposed features relate directly to physical components in a CAD representation, uncertainty in predicted features can be estimated from uncertainty in the CAD model. This is an important advantage of using a physics-based model; other parametric models could be used to represent the measured data, but unless the model parameters relate to scattering physics, it is very difficult to model the prediction uncertainty $f(X|H_{ij})$ in Figure 3.1. In addition, a parameter estimation formulation of feature extraction provides means for describing feature uncertainty $f(Y|U)$ and for bounding it with the Cramér-Rao bound.

The model-based interpretation of images permits an information-theoretic view of SAR imaging. We consider two implications of this viewpoint. First, we define SAR image resolution in terms of uncertainty in estimated parameters. Second, we consider performance degradation when incomplete data are available. Incomplete data results in higher feature uncertainty as measured by relative information; as an example, we consider the increase in uncertainty that results from the common practice of discarding the phase of the SAR image.

3.2.1 A Parametric Model for Object Scattering

Most feature extraction models used with SAR rely on processing of the magnitude image. For example, features used in the MSTAR program are peaks (local maxima of the SAR magnitude image) and ridges obtained from directional derivatives of the SAR magnitude image [25]. When the complex-valued SAR image is used, the point scattering model is most commonly employed; in this model the back-scattered amplitude is assumed to be independent of frequency and aspect. The point scattering assumption leads to a two-dimensional harmonic scattering model, and parameter estimation becomes a two-dimensional harmonic retrieval problem [26, 27]. One drawback of peak and point scattering models is that a single scattering object, such as a dihedral, is modeled as several peaks or point scatterers; in this case, the correlated uncertainty in the estimated parameters is difficult to model.

77

Similarly, the relationship of ridge features to scattering geometry is not well understood, and feature uncertainty is hard to predict.

In this chapter we adopt the physical radar scattering model from Gerry *et al.* [6], which assumes a data collection scenario consistent with SAR imaging. A reference point is defined, and the radar trajectory is required to be co-planar with the reference point. This plane, the imaging plane, is labeled using an $x - y$ Cartesian coordinate system with origin at the reference point. The radar position is then described by an angle ϕ defined counterclockwise from the x direction. Far zone backscatter is assumed, and therefore plane-wave incidence is obtained on illuminated objects.

From the geometric theory of diffraction (GTD) [34, 35], if the wavelength of the incident excitation is small relative to the object extent, then the backscattered field from an object consists of contributions from electrically isolated scattering centers. The backscattered field of an individual scattering center is described as a function of frequency ω and aspect angle ϕ, and the total scattered field from a target is then modeled as the sum of these individual scatterers [6].

$$s(\omega, \phi; \theta) = \sum_{k=1}^{N} A_k \left(j \frac{\omega}{\omega_c} \right)^{\alpha_k} \operatorname{sinc}\left(\frac{\omega}{c} L_k \sin(\phi - \bar{\phi}_k) \right)$$

$$\cdot \exp(-\omega \gamma_k \sin \phi) \exp\left(j \frac{\omega}{c/2}(x_k \cos \phi + y_k \sin \phi) \right) \qquad (3.1)$$

In (3.1), ω_c is the center frequency of the radar bandwidth, and c is the speed of propagation. Each of N scattering centers is characterized by seven attributes: (x_k, y_k) denotes the scattering center location projected to the (x, y)-plane, A_k is a relative amplitude, L_k is the scattering center length, $\bar{\phi}_k$ its orientation angle, α_k characterizes frequency dependence of the scattering center, and γ_k models the mild aspect dependence of scattering center cross-section (for example, the projected cross-sectional area of a trihedral changes slightly with aspect angle). The scattering model is described by the parameter set $\theta = [\theta_1, \ldots, \theta_N]$, where each vector $\theta_k = [x_k, y_k, A_k, \alpha_k, L_k, \phi_k, \gamma_k]$ is the collection of the seven parameters, or attributes, defining each scattering center.

The frequency and aspect dependence of the scattering centers is an important distinction of this model and permits description of a rich variety of scattering primitives. The frequency dependence relates directly to the curvature of the scattering object and is parameterized by α_k, which takes on integer or half-integer values. For example, $\alpha_k = 1$ describes flat surface scattering, $\alpha_k = 1/2$ describes scattering from singly-curved surfaces, and $\alpha_k = 0$ indicates scattering from doubly-curved surfaces or edges. Values of α less than zero describe diffraction mechanisms, such as edges and tips. In addition, the sinc aspect dependence in (3.1) reveals the effective length L_k of the scattering primitive. Many scattering geometries, such as dihedrals, corner reflectors, and cylinders, are distinguishable by their (α, L) parameters [6], as shown in Figure 3.2. Point scattering is a special case of the model in (3.1) for $\alpha_k = L_k = \gamma_k = 0$.
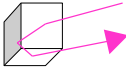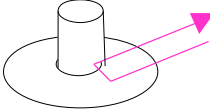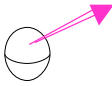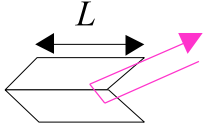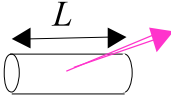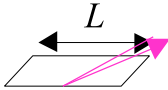
	α=1	α=1/2	α=0
L=0	Trihedral	Top Hat	Sphere
L>0	Dihedral	Cylinder	Edge

Figure 3.2: Canonical scattering geometries that are distinguishable from (α, L) pairs in the scattering model.

The model in (3.1) is based on GTD and physical optics approximations for scattering behavior and, while parsimonious, is able to describe a large class of scatterers. Scattering objects separated by approximately two or more wavelengths are distinguishable [32]. Physical behaviors not well modeled by (3.1) for small N include creeping waves and cavity scattering [6].

3.2.2 Parameter Estimation

Next, we describe an approximate maximum likelihood technique for extracting the model parameters in (3.1) from measured sensor data. The measured data is modeled as

$$r(\omega, \phi) = s(\omega, \phi; \theta) + n(\omega, \phi) \tag{3.2}$$

where $n(\omega, \phi)$ is a noise term that represents the modeling error (background clutter, sensor noise, model mismatch, incomplete motion compensation, antenna calibration errors, etc.) and can be modeled as a zero-mean, Gaussian noise process with known covariance.

The measured data is often transformed into the image-domain as an array of complex-valued pixels. The transformation comprises equalization (to compensate for non-ideal sensor characteristics), windowing, zero padding, and discrete Fourier transformation. The transformation can be represented by the linear operator $\mathcal{L}$; thus,

$$\tilde{r}(x, y) = \mathcal{L}\left[s(\omega, \phi; \theta) + n(\omega, \phi)\right] = \tilde{s}(x, y; \theta) + \tilde{n}(x, y) \tag{3.3}$$

for a finite array of sample points (x, y). We see that $\tilde{n}(x, y)$ is a zero-mean Gaussian noise process with known covariance. The feature extraction problem is thus one of estimating the parameter vector θ from the measurement $\tilde{r}(x, y)$.

R. A. Fisher's pioneering work laid a foundation for parametric modeling as a method of data compression, and established maximum likelihood procedures for estimation of the unknown parameters [30]. Since $\tilde{r}(x, y)$ are Gaussian measurements, the parameter vector θ which maximizes the likelihood function is found as:

$$\hat{\theta}_{ML} = \underset{\theta}{\operatorname{argmin}} \, J(\theta) \tag{3.4}$$

$$J(\theta) = [\tilde{r} - \tilde{s}(\theta)]^H \tilde{\Sigma}^\dagger [\tilde{r} - \tilde{s}(\theta)] \tag{3.5}$$

where $\tilde{r}$, $\tilde{n}$ and $\tilde{s}(\theta)$ are vectors obtained by stacking the columns of $\tilde{r}(x, y)$, $\tilde{s}(x, y; \theta)$, and $\tilde{n}(x, y)$, respectively, $\tilde{\Sigma} = \operatorname{cov}(\tilde{n})$, and $(\cdot)^\dagger$ denotes Moore-Penrose pseudoinverse. Furthermore, this estimator is robust to model mismatch [37]. Equation (3.4) is a nonlinear least squares minimization problem.

We make use of the fact that scattering center responses are localized in the image domain to develop a computationally simpler approximate maximum likelihood estimator for θ [36]. The minimization in (3.4) is decomposed into smaller estimation problems. We partition

the image into M disjoint regions R_i of high energy and a remainder region R_0. Defining Π_i as the projection onto region R_i, we have

$$J(\theta) \approx \sum_{i=0}^{M} [\tilde{r} - \tilde{s}(\theta^i)]^H \Pi_i \Sigma^\dagger \Pi_i [\tilde{r} - \tilde{s}(\theta^i)] + C \tag{3.6}$$

where θ^i is a vector containing the parameters for scattering centers in region R_i and C is a constant independent of θ. Since the number of pixels in R_i is much less than the total number of image pixels in $\tilde{r}$ and the θ^i form a partition of θ, the individual minimization problems in (3.6) are decoupled and have many fewer unknowns than the minimization problem in (3.5). The weighted least-squares estimator is tractable and provides nearly efficient parameter estimates for data satisfying the scattering model in (3.1) with colored Gaussian noise on image pixels [36].

An additional advantage of the approximate ML algorithm is its robustness to the assumed noise model. The assumption of correlated Gaussian noise across the entire image is not very accurate for scenes where clutter is present in the form of trees, power lines, etc. However, this assumption is much better over small image regions that primarily contain target scattering centers. Image segmentation also facilitates model order selection, which is implemented using the minimum description length principle.

As an illustration of the approximate ML estimation, Figure 3.3 shows the results of feature extraction on a measured SAR image from the MSTAR Public Targets dataset [48]. For $N = 30$, the algorithm models 96.5% of the energy in the image chip shown. In addition, the T-72 tank barrel segment is modeled as a single scattering center whose length is modeled within $10\,\mathrm{cm}$ of the actual $1.37\,\mathrm{m}$ length. In comparison, peak-based scattering center extraction methods model this segment as three peaks spaced along the barrel. Execution time for extraction of 30 scattering features using unoptimized Matlab code on a 450 MHz Pentium processor is approximately $140\,\mathrm{sec}$ using (3.5) and approximately $50\,\mathrm{sec}$ if a suboptimal but computationally efficient estimator is employed.

3.2.3   Parameter Uncertainty

Use of estimated model parameters for Bayesian hypothesis testing requires that an uncertainty be associated with each estimate. The inverse of Fisher information is used to predict the error covariance of the approximate maximum likelihood estimation algorithm in (3.6).

The Cramér-Rao lower bound is derived in [6] and provides an algorithm-independent lower bound on the error variance for unbiased estimates of the model parameters. The derivation assumes the data model in (3.3). For any choice of model parameters, the covariance bound is computed by inversion of the Fisher information matrix [38]

$$I(\theta) = -E\left\{ \frac{\partial^2 \ln f(s|\theta)}{\partial \theta^2} \right\} \tag{3.7}$$

where $f(s|\theta)$ is density on the sensor data s conditioned on the parameter θ.
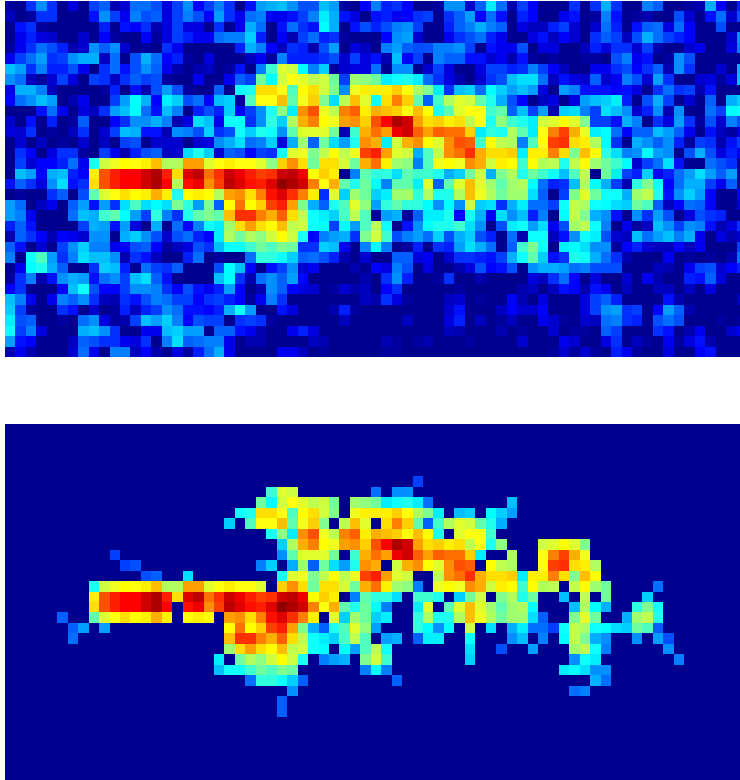
Figure 3.3: Measured SAR Image of T-72 Tank (top) and reconstruction from estimated parameters (bottom). Images are in dB magnitude with a total range of 40 dB.

3.2.4   Image Resolution

As noted in [39], "a universally acceptable definition of resolution as a performance measure is elusive." In synthetic aperture radar, image resolution is typically reported as the width of a point spread function. This definition is a Rayleigh resolution and is determined by sensor bandwidth, range of viewing angles and degree of side lobe suppression in image formation. In contrast, for model-based interpretation of SAR imagery we define resolution in terms of a bound on the uncertainty in estimated parameters. Prior knowledge of the scattering behavior, as encoded in (1), results in an uncertainty-based resolution that is often much finer than the Rayleigh resolution. For example, consider application of feature uncertainty to the classical notion of separating closely spaced point sources, $i.e.$, $\alpha = L = \gamma = 0$ in (3.1). For a given signal-to-noise ratio (SNR) of a single point scatterer (SNR per mode), let the resolution be defined as the minimum distance between two equal amplitude scattering centers resulting in nonoverlapping 95% confidence regions for the estimated locations [6, 40].

Adopting this definition, resolution versus SNR per mode is shown in Figure 3.4 for a SAR with Rayleigh resolution of 30 cm. The resolution depends on the orientation of the two point scatterers. The dashed line shows resolution for point scatterers separated an equal distance in both down range and cross range ($i.e.$, aligned 45° to the aperture). The solid line and the dash–dot line show resolution for two point scatterers aligned parallel and orthogonal to the aperture, respectively. For an SNR per mode of -5 dB and 500 MHz bandwidth, the limit of resolution achievable by model-based scattering analysis is approximately one-half the Rayleigh resolution; model-based resolution is limited by sensor bandwidth and SNR, which includes mismatch from the model in (3.3).

In the figure, we report signal-to-noise (SNR) values using the ratio of signal energy to noise energy computed for the frequency-aspect domain samples. Alternatively, SNR may be interpreted in the image space as a difference between peak signal level and clutter floor. However, this image space definition of SNR varies depending on the specific values of the parameter vector, θ, describing the scattering center.

3.2.5   Magnitude-only Fourier Data

The parameter uncertainty definition of resolution can be directly applied to image reconstruction from incomplete data; for example, in SAR image formation a common practice is to discard image phase. In this case, the estimation of $s(\omega, \phi)$ becomes reconstruction from magnitude-only Fourier data. The Fisher information, $I_{mag}(\theta)$, can be computed for the sampled magnitude of the image data, using (3.1) and knowledge of both the sensor transfer function and the image formation operator. The relative information [41] is the ratio of Fisher matrices, $I_{mag}(\theta)/I(\theta)$, and quantifies the loss of information incurred by discarding the image phase. Likewise, the increase in variance in any parameter estimate can be predicted, for efficient estimators, using the Cramér-Rao bounds.
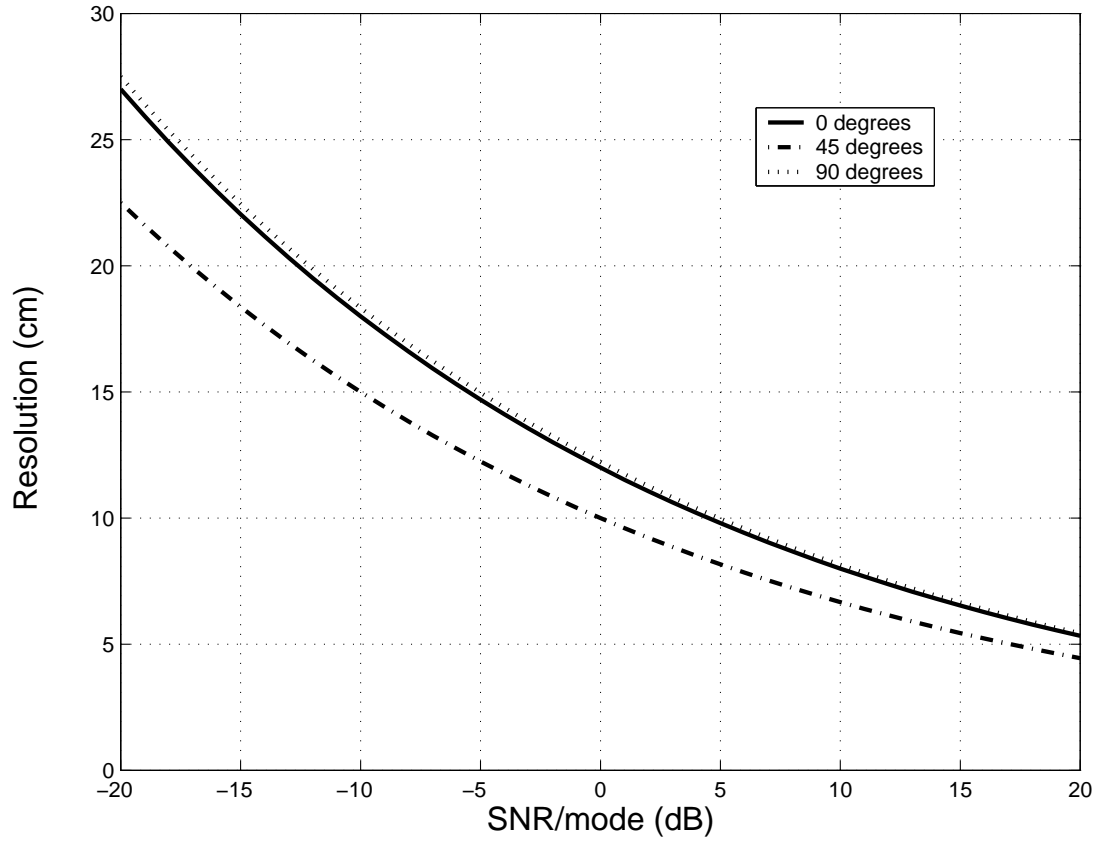
Figure 3.4: Resolution versus SNR for three different orientations of two point scatterers; $\omega_c/(2\pi) = 10\,\text{GHz}$, and bandwidth is $500\,\text{MHz}$.

For example, for $\omega_c/(2\pi) = 10\,\mathrm{GHz}$, $3\,\mathrm{GHz}$ bandwidth and $10\,\mathrm{dB}$ SNR, the Cramér-Rao bound on standard deviation in estimation error for α is $\sigma = 1.0$ using a magnitude image. In contrast, estimation of α from the complex-valued image results in $\sigma = 0.02$. Thus, use of complex-valued imagery allows inference of the frequency dependent scattering behavior, whereas use of magnitude-only imagery does not.

3.3   Hypothesis Testing

3.3.1   Problem Statement

In this section we derive the Bayes match function used for classification from feature vectors. At the input to the classifier stage, we have a given region of interest (a SAR image chip), along with a set $\mathcal{H} = \{H_{ij}, \ ij \in L\}$ of K candidate target hypotheses and their prior probabilities $P(H_{ij})$. Each hypothesis contains both target class and subclass information; the set $\mathcal{H}$ may contain all possible hypotheses but typically contains a reduced set as generated from an earlier Index stage as depicted in Figure 3.1. From the image chip we extract a feature vector Y, and from each candidate hypothesis $H \in \mathcal{H}$ we generate a predicted feature vector X, where

$$X = [X_1, X_2, \ldots, X_m]^T, \quad Y = [Y_1, Y_2, \ldots, Y_n]^T \tag{3.8}$$

and where m and n are the number of predicted and extracted features, respectively. Each feature X_i and Y_j is an ordered vector of feature attributes; for example, these attributes can be $(x, \ y, \ A, \ \alpha, \ L, \ \overline{\phi}, \ \gamma)$ parameters from the model in (3.1). However, the features themselves are unordered. In addition, there is uncertainty in both the predicted and extracted features.

There are two hypothesis testing goals that may be of interest. First, we may wish to classify the extracted feature vector Y as a measurement of one of the M class hypotheses. Second, we may wish to classify Y as one of the K class-subclass hypotheses in the set $\mathcal{H}$. For both cases we adopt a maximum *a posteriori* probability (MAP) rule; thus, we must find the posterior likelihoods

$$\Lambda_{ij} = P(H_{ij}|Y), \quad H_{ij} \in \mathcal{H}. \tag{3.9}$$

If our goal is to classify Y as one of the K Index hypotheses (which include both class and subclass information), we choose the hypothesis that corresponds to the maximum Λ_{ij}. If our goal is to classify Y as one of the M class hypotheses, we form

$$\tilde{\Lambda}_i = \sum_j \Lambda_{ij}, \quad 1 \le i \le M \tag{3.10}$$

and choose the class i corresponding to the maximum $\tilde{\Lambda}_i$.

The above formulation gives an interpretation of the Index block in Figure 3.1 as modifying the prior probabilities on the class and subclass hypotheses. The optimal MAP classifier maximizes or sums over all possible H_{ij} classes, and not just those provided by the Index stage. The Index stage computes a statistic $Z = g(U)$ from the image U, and essentially updates probabilities of hypotheses H_{ij} by finding posterior probabilities $P(H_{ij}|Z)$. A subset of hypotheses with sufficiently high posterior probabilities are retained for further processing. The final hypothesis test involves computing $P(H_{ij}|U)$; thus, the feature-based match processing seeks to extract information in U not contained in $Z = g(U)$ to obtain a final classification decision. We see that the Index stage does not impact optimality in (3.9) provided the correct hypothesis is one of the K hypotheses passed. On the other hand, from (3.10) we see that the optimal MAP rule involves summation over all subclasses in class i, not just those passed by the Index stage. Thus, (3.10) is optimal only under the stronger condition that the likelihoods $P(H_{ij}|Z)$ of all subclasses not passed by the Index stage are equal to zero. In either case, the computational reduction of maximizing or summing on a reduced set of subclasses often justifies the deviation from optimality of the resulting classifier.

To compute the posterior likelihood in (3.9), we apply Bayes rule for any $H \in \mathcal{H}^1$ to obtain

$$
\begin{aligned}
P(H|Y) &= P(H|Y,n) = \frac{f(Y|H,n)P(H|n)}{f(Y|n)} \\
&= \frac{f(Y|H,n)P(n|H)P(H)}{f(Y|n)P(n)}
\end{aligned} \tag{3.11}
$$

The conditioning on n is used because the number of features in Y is itself a random variable, but it suffices to consider only vectors Y of length n in the right-hand side of (3.11). Since the denominator of (3.11) does not depend on hypothesis H, the MAP decision is found by maximizing $f(Y|H,n)P(H)P(n|H)$ over $H \in \mathcal{H}$. The priors $P(H)$ and $P(n|H)$ are assumed to be known, or are provided by the Index stage.

The determination of $f(Y|H,n)$ includes both prediction and extraction uncertainties, which are related in the following way. Assume we have an object in the field with feature vector $\hat{X}$. We measure that object with a sensor, and obtain a feature vector Y. The measured feature vector differs from $\hat{X}$ due to noise, sensor limitations, etc. We write this difference notionally as $Y = \hat{X} + N_e$ where N_e is some extracton error described by an uncertainty pdf $f(Y|\hat{X})$. In addition, if we suppose a hypothesis H, we can predict a feature vector X that differs from $\hat{X}$ because of electromagnetic modeling errors, quantization errors of the assumed object subclass states (*e.g.*, pose angle quantization errors), and differences between the actual object in the field and the nominal object that is modeled. We express this difference as $\hat{X} = X + N_p$ where N_p is a prediction error which we describe with an uncertainty $f(\hat{X}|H)$. Note that X is completely determined from H. To find the conditional

---

[1]For notational simplicity, we drop the subscripts on the hypotheses in the sequel, and consider a general $H \in \mathcal{H}$.
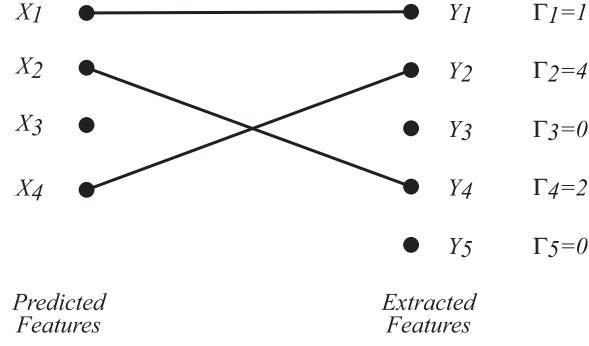
Figure 3.5: An example one-to-one correspondence mapping for $m = 4$ and $n = 5$. Extracted features Y_3 and Y_5 are false alarms, and predicted feature X_3 is missed.

uncertainty of Y given hypothesis H, we have

$$f(Y|H,n) = \int f(Y|\hat{X}, H, n) f(\hat{X}|H, n) \, d\hat{X} \tag{3.12}$$

where $f(\hat{X}|H,n)$ models the predict uncertainty, and $f(Y|\hat{X}, H, n)$ models extract uncertainty. The computation of $f(Y|\hat{X}, H, n)$ is complicated by the fact that the features in the Y and $\hat{X}$ vectors are unordered, so a correspondence between the elements of Y and $\hat{X}$, or equivalently between Y and X, is needed.

3.3.2 Feature Correspondence

Computing the likelihood $f(Y|\hat{X}, H, n)$ requires that we form a correspondence map Γ between extracted and predicted features. The correspondence map is a nuisance parameter that arises because an extracted feature vector is not ordered with respect to the predicted feature vector. The correspondence also accounts for extracted features that are not in the predicted vector (false alarms) as well as predicted features that are not extracted (missed features).

For general pattern matching applications, a predicted feature X_i may correspond to none, one, or several extracted features Y_j. Further, an extracted feature may correspond to one or more predicted features, or be a false alarm. We denote by $\mathcal{G}$ the set of all such correspondence maps. For specific applications a smaller set $\mathcal{G}_A \subset \mathcal{G}$ of admissible correspondence maps need only be considered. For example, in the SAR classification application presented in this chapter, $\mathcal{G}_A$ is the set of all one-to-one maps, where a one-to-one map corresponds at most one predicted feature with each extracted feature and conversely. An example one-to-one correspondence map is shown in Figure 3.5. Following [42], we let $\Gamma_j = i$ denote a correspondence between the X_i and Y_j. For notational conciseness, we write $\Gamma_j = 0$ to denote that Y_j does not correspond to any X_i, and therefore is a false alarm feature.

We consider two correspondence mappings, random and deterministic. These two correspondence mappings lead to two different expressions of the posterior likelihoods Λ_{ij}.

Probabilistic Correspondence
If we assume a probabilistic correspondence model, then we have the Bayes likelihood

$$f(Y|H,n) = \sum_{\Gamma \in \mathcal{G}_A} f(Y|\Gamma,H,n)P(\Gamma|H,n) \qquad (3.13)$$

where, similarly to (3.12),

$$f(Y|\Gamma,H,n) = \int f(Y|\hat{X},\Gamma,H,n)f(\hat{X}|\Gamma,H,n)\,d\hat{X} \qquad (3.14)$$

The conditioning on n, the number of extracted features, is needed above because Γ is a correspondence between m predicted features and n extracted features; without the conditioning on n, $P(\Gamma|H,n)$ cannot be computed independently of Y.

The main difficulties in implementing (3.13) are: i) knowledge of the priors $P(\Gamma|H,n)$ and ii) the high computational cost of summing over all possible correspondences. The correspondence prior probabilities can in principle be determined from knowledge of the predict and extract uncertainties for each hypothesis, but the derivation is quite difficult for many applications. More importantly, the summation contains a (very) large number of components; for example, there are more than $\min(m!,n!)$ possible one-to-one maps from a set of m predicted to n extracted features.

One can simplify computation of the large sum in (3.13) with assumptions of equal priors on Γ and independence of features [42, 43]. If the priors are not equal or the features are not independent, then the resulting classifier will be suboptimal. It is difficult to predict the performance loss due to mismatch between the assumed and actual priors.

Deterministic Unknown Correspondence
If we assume the correspondence is deterministic but unknown, then it becomes a nuisance parameter in the classification. In this case no uniformly most powerful test exists. We thus resort to the Generalized Likelihood Ratio Test (GLRT) classifier, in which we estimate Γ, then use the estimated Γ to estimate the likelihoods $f(Y|\hat{X},H,n)$:

$$f(Y|H,n) \approx \max_{\Gamma \in \mathcal{G}_A} f(Y|\Gamma,H,n) \qquad (3.15)$$

where $f(Y|\Gamma,H,n)$ is computed using (3.14). The GLRT approach in (3.15) avoids the summation in (3.13), but requires a search for the best correspondence. Graph matching algorithms [44] can be used to simplify this search.

Discussion
The GLRT estimate of the conditional likelihood is a good estimate of the Bayes likelihood if the "best" correspondence term (3.15) dominates the sum in (3.13). This happens in the SAR classification problem, for example, when the feature uncertainties are small compared to their feature distances; for example, the match likelihood when corresponding two

features with widely differing (x, y) locations is negligibly small compared to the likelihood found from associating all pairs of features with similar (x, y) locations. The presence of additional scattering attributes helps increase the feature distances even for scattering features that have similar locations; for example, two physically close scattering centers with different α and L parameters have lower likelihood of an incorrect match pairing than they would if match scores are based only on scatterer location and amplitude.

For the SAR classification application, we adopt both a one-to-one map and a GLRT classifier. The one-to-one map makes physical sense: an extracted scattering center corresponds to at most one predicted scattering center, and conversely. The GLRT classifier assumes a deterministic but unknown correspondence map, and avoids summation over a large set of possible correspondence maps. The probabilistic map assumption for this model is considered in [43]. In addition, [42] considers other classifiers derived for SAR features using only location attributes.

3.3.3 Conditional Feature Likelihood

To implement either equation (3.13) or (3.15), one must have available a model for $f(Y|\hat{X}, \Gamma, H, n)$. In this section we develop a model based on [42] that applies to SAR scattering center features.

We assume the X_i are conditionally independent given H, and that Y_j are conditionally independent given H, X, and n. The independence of the X_i is reasonable because the prediction errors of separate scattering centers are due to variations in components on the target that make up that scattering center, and these variations can be assumed to be unconnected. The independence of the Y_i is supported by the near block diagonality of the CRB matrix for well-separated scattering centers [6]. In addition, the independence assumptions simplify the Bayes matcher significantly. Thus, we have

$$f(Y|\Gamma, H, n) = \prod_{j=1}^{n} f(Y_j|\Gamma, H, n) \tag{3.16}$$

For a one-to-one correspondence, the jth extracted feature corresponds either to a particular predicted feature (say the ith one), or to a false alarm. We denote these two cases as $\Gamma_j = i$ or $\Gamma_j = 0$, respectively. Thus, for a given correspondence, there may be some predict-extract feature correspondences, some missed predicted features (which correspond to no extracted feature), and some false alarm extracted features which have no corresponding predict feature; see Figure 3.5. For a given correspondence, let n_F denote the number of false alarm features.

We model the conditional feature likelihood as:

$$
\begin{aligned}
f(Y|\Gamma, H, n) \;=\; & P(n_F \text{ false alarms}) \prod_{\{j:\Gamma_j=0\}} f_{FA}(Y_j) \\
& \cdot \prod_{\{j:\Gamma_j=i>0\}} P_i(H) f(Y_j|\Gamma_j=i, H, n) \\
& \cdot \prod_{\{i:\Gamma_j\neq i,\forall j\}} (1-P_i(H)) \quad\quad (3.17)
\end{aligned}
$$

where $P_i(H)$ is the detection probability of the ith predicted feature under hypothesis H. The first term on the right hand side models the likelihood of false alarm features, and $f_{FA}(Y_j)$ is the pdf of feature Y_j if it corresponds to a false alarm. The second line is the likelihood of extracted features that correspond to predicted features, and the third line represents the miss probabilities for predicted features that have no corresponding extract feature.

3.3.4   Implementation of the Correspondence Search

The GLRT hypothesis selection rule in equation (3.15) involves finding the correspondence Γ that maximizes $f(Y|\Gamma, H, n)$ in (3.17) for each candidate hypothesis $H \in \mathcal{H}$. In general, the search is computationally intensive, but for some cases can be implemented efficiently. Specifically, in the case that

$$
P(n_F \text{ false alarms}) = c\beta^{n_F} \quad\quad (3.18)
$$

for some constants c and β, the search can be efficiently implemented in $O((m+n)^3)$ operations using the Hungarian algorithm [44].

We briefly summarize the implementation of the Hungarian algorithm for this problem[2]. From equations (3.17) and (3.18) we have

$$
\begin{aligned}
-\log f(Y|X,\Gamma, H, n) \;=\; & -\log c - \sum_{\{j:\Gamma_j=0\}} \log[\beta f_{FA}(Y_j)] \\
& - \sum_{\{j:\Gamma_j=i>0\}} \log[P_i(H) f(Y_j|\Gamma_j=i, H, n)] \\
& - \sum_{\{i:\Gamma_j\neq i,\forall j\}} \log[1-P_i(H)] \quad\quad (3.19)
\end{aligned}
$$

We insert the elements of the above equation for all possible i and j into an $(m+n)\times(m+n)$ array, as shown in Figure 3.6. Then the minimum of equation (3.19) over all one-to-one maps reduces to the problem of selecting exactly one element from each row and column

---

[2]We thank William Irving for noting the application of the Hungarian algorithm to this search problem.

of the array such that the sum of the selected entries is minimized. The resulting solution also gives the optimal correspondence. Specifically, if c_{ij} is selected, then predicted feature X_i corresponds to extracted feature Y_j; if F_j is selected, then Y_j is a false alarm feature; if M_i is selected, then X_i is not present (missed) in the extracted features Y.

		Y_1	$\cdots$	Y_n	misses		
X_1		c_{11}	$\cdots$	c_{1n}	M_1		∞
$\vdots$		$\vdots$	$\ddots$	$\vdots$		$\ddots$	
X_m		c_{m1}	$\cdots$	c_{mn}	∞		M_m
false		F_1		∞	0	$\cdots$	0
alarms			$\ddots$		$\vdots$	$\ddots$	$\vdots$
		∞		F_n	0	$\cdots$	0

Figure 3.6: The cost matrix for the one-to-one matcher in equation (3.17). Here, $c_{ij} = -\log[P_i(H)f(Y_j|\Gamma_j = i, H)]$, $F_j = -\log[\beta f_{FA}(Y_j)]$, and $M_k = -\log[1 - P_k(H)]$.

The search is equivalent to finding a permutation of the cost matrix that minimizes its trace. Such a permutation is found efficiently using the Hungarian algorithm [44]. A related algorithm [45] can also find the k permutations that give the k smallest trace values, which is useful if the "best" k correspondences are of interest.

As an alternative, geometric hashing [46, 47] can be used to efficiently search a set of candidate hypotheses for the highest likelihood match. Hashing methods precompute information about patterns of features in a hash table that later can be efficiently searched to vote for hypotheses that are close matches. On the other hand, hashing requires the formation of a large table, containing entries for every hypothesis H_{ij}; this table can be prohibitively large for high-dimensional classification applications.

3.4   Bayes Classification Example

In this section we present an example of feature-based classification using SAR scattering center attributes. We use synthetic feature vector means based on measured SAR imagery and an assumed feature perturbation model. We select target classes, feature sets, feature attribute uncertainties, and priors to be representative of a realistic X-band SAR target recognition problem. The synthetic data results serve to emphasize, by example, that the Bayes classifier is tractable for problem sizes encountered in SAR target recognition given the assumption of conditionally independent features in Section III.C. The proposed technique permits estimation of the optimal error rate given a set of assumed priors and feature uncertainties. In addition, we demonstrate by example that the Bayes classifier can be used to explore the performance effects of sensor parameters. Finally, the Bayes classifier can be used as a simulation tool to investigate sensitivity of the estimated error

rate to errors in assumed priors and feature attribute uncertainty. Accurate prediction of absolute classification performance would require an electromagnetic prediction module as in Figure 3.1 and extraction uncertainties empirically verified from ground truth; neither is presently available.

We generate class means using a combination of synthetic generation and feature extraction from SAR imagery. We synthesize 2747 class mean features for 10 composite target classes in the MSTAR Public Targets dataset [48]. The data set contains X-band image chips with 128x128 pixels and 1ft×1ft resolution SAR data chips of 10 targets at 17 degree depression angle. For each target, approximately 270 images are available covering the full 360 degree aspect angles, for a total of 2747 images. Downrange and crossrange locations and amplitudes of scattering centers are synthesized from local maxima on the image chips. The targets are the 2S1, BMP-2, BRDM-2, BTR-70, BTR-60, D-7, T-62, T-72, ZIL-131, and ZSU-23-4. Examples of the SAR image chips are shown in Figure 3.7. From each image we extract locations and amplitudes of scattering centers from local maxima in the SAR image. The α and L parameters are not provided by current prediction modules, so are generated synthetically. The α attribute for each feature is generated as $\alpha \sim \mathcal{N}(0.5, 0.25)$. The Gaussian approximation to a discrete variable is used to avoid the combinatorial number of likelihood evaluations for all possible α choices from prediction and extraction; experiments verify that the Gaussian approximation gives very similar results at lower computational cost [43]. The length parameter is quantized to one bit ($L = 0$ or $L > 0$), and the nominal values of the length attribute are generated using a Bernoulli random variable with $P(L > 0) = 0.3$. We quantize L because existing electromagnetic prediction codes do not provide L; further, prediction uncertainty is unknown, so we choose to adopt only coarse uncertainty assumptions in the simulation. The γ and ϕ parameters in (3.1) are not used in the experiments because no strong evidence exists that these parameters can be predicted and extracted at 1 ft SAR resolution with sufficiently low uncertainty to substantially improve classification performance; nonetheless, these two parameters are retained in (3.1) both for reduced bias and for application to higher resolution SAR imagery. For example, using 2 in resolution SAR imagery at X-band, pose angle can be estimated to an accuracy that is a small fraction of the 20° phase history angle used in the image formation.

Prediction and extraction feature uncertainties are needed in the Bayes classifier. We evaluate $f(Y_j|\Gamma_j = i, H, n)$ in (3.17) as follows. Recall each Y_j is a feature vector $[Y_{j1}, \ldots, Y_{jS}]$, where the Y_{jk} are the individual feature attributes x_j, y_j, A_j, α_j, L_j, ϕ_j, and γ_j from the model in (3.1) (or a subset of these). For simplicity we assume the uncertainties of the feature attributes are independent; experiments using dependent attribute uncertainties are presented in [43]. For independent attributes,

$$f(Y_j|\Gamma_j = i, H, n) = \prod_k f(Y_{jk}|\Gamma_j = i, H, n) \tag{3.20}$$

where k denotes an index on the feature attributes. We further model each attribute k in an extracted feature Y_j that corresponds to predicted feature X_i with a conditional likelihood $f(Y_{jk}|\hat{X}_{ik}, H, n)$ as follows. If k corresponds to x, y, $\log|A|$, or α, the conditional likelihood
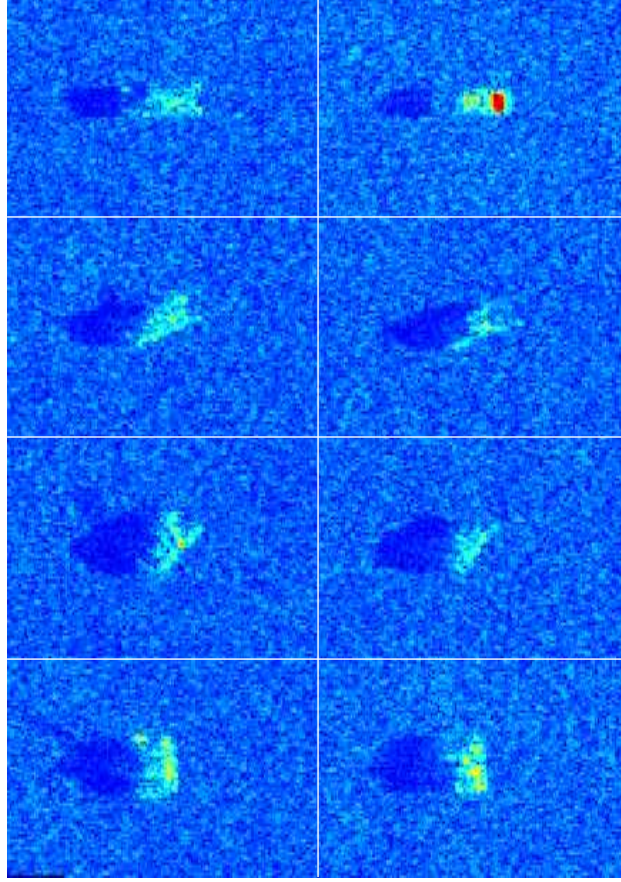
Figure 3.7: Examples of the MSTAR SAR image chips used in the Bayes classificaion example. Four T-72 (left) and BMP-2 (right) images are shown.

is assumed to be Gaussian

$$f(Y_{jk}|\hat{X}_{ik}, H, n) \sim \mathcal{N}(\hat{X}_{ik}, \sigma_{e,k}^2) \tag{3.21}$$

We assume a similar predict uncertainty for each attribute:

$$f(\hat{X}_{ik}|X_{ik}, H, n) \sim \mathcal{N}(X_{ik}, \sigma_{p,k}^2) \tag{3.22}$$

Thus, from (3.14), (3.21), and (3.22) we have

$$f(Y_{jk}|X_{ik}, H, n) \sim \mathcal{N}(X_{ik}, \sigma_{p,k}^2 + \sigma_{e,k}^2) \tag{3.23}$$

which gives the needed terms in (3.20). Similarly, for a discrete attribute (the quantized length L) the likelihood is a weighted sum

$$P(Y_{jk}|X_{ik}, H, n) = \sum_{\hat{X}_{ik}} P(Y_{jk}|\hat{X}_{ik}, H, n)P(\hat{X}_{ik}|X_{ik}, H, n) \tag{3.24}$$

Table 3.1: Sum of prediction and extraction feature attribute uncertainties used in the Bayes classifier example.

Feature Attribute	SAR Rayleigh Resolution			
	2 ft	1 ft	1/2 ft	1/4 ft
locations x, y $\mathcal{N}(0, \sigma^2)$	$\sigma = 2\,\text{ft}$	$\sigma = 1\,\text{ft}$	$\sigma^2 = 1/2\,\text{ft}$	$\sigma = 1/4\,\text{ft}$
amplitude $\log_{10}(|A|) \sim \mathcal{N}(0, \sigma^2)$	$\sigma^2 = 0.5$	$\sigma^2 = 0.5$	$\sigma^2 = 0.5$	$\sigma^2 = 0.5$
frequency dependence $\alpha \sim \mathcal{N}(0, \sigma_\alpha^2)$	$\sigma_\alpha = 1$	$\sigma_\alpha = 1/2$	$\sigma_\alpha = 1/4$	$\sigma_\alpha = 1/8$
length $\begin{bmatrix} P(L=0\|L=0) & P(L=0\|L>0) \\ P(L>0\|L=0) & P(L>0\|L>0) \end{bmatrix}$	$\begin{bmatrix} 0.7 & 0.3 \\ 0.3 & 0.7 \end{bmatrix}$	$\begin{bmatrix} 0.8 & 0.2 \\ 0.2 & 0.8 \end{bmatrix}$	$\begin{bmatrix} 0.9 & 0.1 \\ 0.1 & 0.9 \end{bmatrix}$	$\begin{bmatrix} 0.95 & 0.05 \\ 0.05 & 0.95 \end{bmatrix}$

Table 3.2: False alarm pdf $f_{FA}(Y_j)$ used in the Bayes classifier example.

Feature Attribute	Feature pdf used
number	Poisson with rate $\lambda = 3$ per image chip $P(n_F \text{ false alarms }) = e^{-\lambda} \lambda^{n_F} / (n_F!)$
locations x, y	uniformly distributed over the image
amplitude	$\log_{10}(|A|) \sim \mathcal{N}(\mu, 0.25)$ $\mu = \log_{10}(\text{median amplitude of predicted scattering centers})$
curvature	$\alpha \sim \mathcal{N}(0.5, 1)$
length	L is Bernoulli with $P(L > 0) = 0.3$

and is thus described by probability mass functions on the predicted features along with predict and extract confusion matrices.

From equations (3.23) and (3.24) we see that only the sum of prediction and extraction uncertainties is needed. Table 3.1 lists the uncertainty values used in the simulations. We assume no prediction uncertainty in α or L, and log normal uncertainty in $|A|$. The total location uncertainty is assumed to have a standard deviation of one Rayleigh resolution for both x and y. In addition, Table 3.2 specifies the false alarm pdf $f_{FA}(Y_j)$.

We emulate the Index stage as follows. For each of the 2747 target image chips, we find the 5 image chips in each of the 10 target classes that have the highest correlation. The target classes and poses (pose is in this case azimuth angle) corresponding to these 50 image chips form the initial hypothesis list generated by the Index stage. For each class mean vector, we generate a predict feature vector for each of the 50 hypotheses from the

Index stage by randomly perturbing the mean vector using the predict uncertainty model above. We similarly generate an extracted feature vector from the mean vector. The extracted feature vector assumes each scattering center has a probability of detection of $P_d = 0.5$, so not all scattering centers are present in the extracted feature vector. We also add clutter scattering centers to the extract feature vector. We then compute the GLRT hypothesis test using equations (3.11), (3.15), and (3.17), assuming equally likely priors $(P(H)P(H|n) = \text{constant})$ on the 50 Index hypotheses. We use the Hungarian algorithm to search for the best correspondence map, using $\beta = \lambda$ in (3.18). We record the target class corresponding to the one of the 50 hypotheses with the highest likelihood score. We repeat this experiment 10 times for each class mean vector; this gives a total of 27,470 classifications from 27,470×50 matches. For each candidate hypothesis, computation of the correspondence is $O(m^3)$, where m is the number of predicted features. Execution times for the 50 likelihood computations average 4.6 sec using unoptimized Matlab code on a 333 MHz Pentium processor.

Table 3.3 presents the results of the above experiment for a SAR Rayleigh resolution of 1 ft, using the uncertainty values in Table 3.1. We summarize the overall performance as an average probability of correct classification P_c, which is 86.8% for this case.

Table 3.3: One-to-one classification results using five feature attributes. The ijth entry gives the number of times the object was classified as object j given that object i is the true object. Overall $P_c = 86.8\%$.

Optimal One-to-One Map, five feature attributes, $P_d = 0.5$

	2S1	BMP 2	BRDM 2	BTR 70	BTR 60	D-7	T-62	T-72	ZIL 131	ZSU 23-4	Total
2S1	2574	42	33	48	43	38	72	52	56	32	2990
BMP-2	42	2023	55	37	29	29	30	31	29	25	2330
BRDM-2	60	41	2554	71	39	39	50	40	29	57	2980
BTR-70	29	32	46	2046	33	20	34	34	37	19	2330
BTR-60	45	28	38	36	2280	23	26	27	32	25	2560
D-7	49	35	39	13	25	2639	68	37	36	49	2990
T-62	51	44	58	31	36	37	2584	53	46	50	2990
T-72	36	43	38	36	32	20	44	1981	47	43	2320
ZIL-131	55	53	34	45	44	30	44	38	2614	33	2990
ZSU-23-4	37	61	52	39	33	63	60	57	45	2543	2990

Figure 3.8 presents probability of correct classification results as a function of both the number of feature attributes and the system bandwidth. First we compare the use of location features with location features coupled with other attributes. The amplitude attribute provides only modest improvement (1-2 dB) in the probability of error, due to its relatively high uncertainty. The addition of the frequency dependence and length attributes provides more significant improvement in classification performance, especially for the higher resolutions considered. The amount of improvement depends critically on the assumed attribute

uncertainty and its correlation with other attributes.

Figure 3.8 also presents results of an experiment in which we predict classification performance as a radar system parameter, namely Rayleigh resolution, changes. The bandwidths and integration angles correspond approximately to SAR image Rayleigh resolutions of 2, 1, $\frac{1}{2}$, and $\frac{1}{4}$ ft. We assume decreasing uncertainty in the location, frequency dependence, and length attributes as Rayleigh resolution becomes finer, as shown in Table 3.1. From Figure 3.8 we see that classification performance improves significantly as radar bandwidth and integration angle increase. Specifically, the error probability $1 - P_c$ decreases by about 15 dB as the SAR Rayleigh resolution improves from 2 ft to $\frac{1}{4}$ ft. Here we see a clear benefit of increased bandwidth because it results in decreased feature uncertainty.

Figure 3.9 shows the effect on classification performance when the assumed uncertainty model in the Bayes classifier is in error. In this experiment we set the location uncertainty standard deviation to 0.5, 1, and 2 times the correct location uncertainty; the other attributes use the correct uncertainty models. Here, $P_i(H) = 0.9$. We see the correct classification rate drops by 10%-20% as a result of the mismatch, and that a greater performance loss occurs when the model-based classifier assumes too low an uncertatinty.
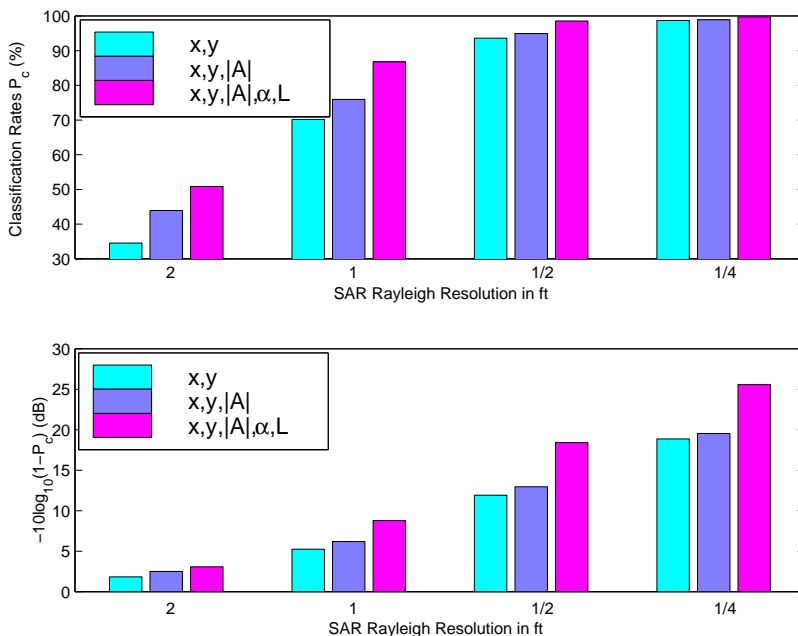
Figure 3.8: Classification performance as a function of number of feature attributes and radar bandwidth. The top figure shows average probability of correct classification (P_c); the bottom figure shows the same data plotted as average probability of error ($1 - P_c$) in dB.
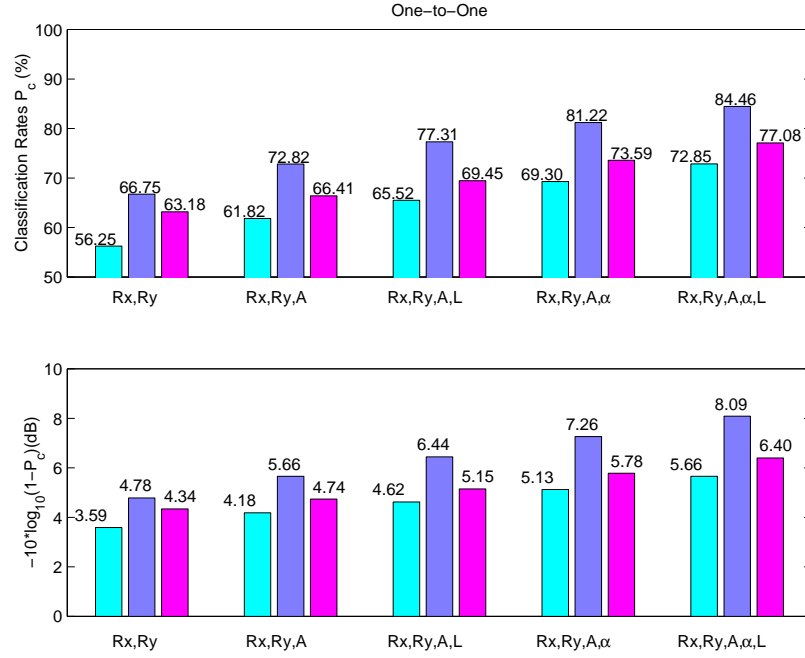
Figure 3.9: Classification performance using correct (center) and erroneous location uncertainties in the Bayes classifier. The left(right) bars assume 0.5(2) times the true location uncertainty. The top figure shows average probability of correct classification (P_c); the bottom figure shows the same data plotted as average probability of error ($1 - P_c$) in dB.

3.5 Conclusions

We have presented a model-based framework for image processing when the processing goal is object classification. The Bayesian formalism allows clear and explicit disclosure of all assumptions, in contrast to *ad hoc* classification procedures. Moreover, we demonstrated that the Bayes approach, including the associated correspondence problem, is tractable and leads to implementable algorithms.

We have presented the Bayes approach to model-based classification in the application context of synthetic aperture radar imagery. By modeling electromagnetic scattering behavior and estimating physically meaningful parameters from complex-valued imagery, we computed features as statistics for use in hypothesis testing. For radar systems with a significant fractional bandwidth, the features provide richer information than local peaks in magnitude imagery.

A complete empirical evaluation the proposed classifier requires an electromagnetic scattering code to provide predicted features conditioned on a target hypothesis; at the time of this publication, such a code is being developed by Veridian-ERIM International, Inc., as a hybrid combination of the ray tracing and scattering primitive codes. Further, the efficacy of the proposed likelihood estimation technique requires additional empirical verification of the feature uncertainties adopted in Section 4; to do so requires ground truth that is not currently available, but would be provided by the scattering prediction code under development.

The implementable Bayes classifier allows estimation of optimal error rates, given assumed priors and feature uncertainties, and the simulation of performance sensitivity to assumed priors, to assumed feature uncertainties, and to sensor characteristics.

4. IFSAR PROCESSING FOR 3D TARGET RECONSTRUCTION

4.1 Introduction

In this chapter we investigate the use of interferometric synthetic aperture radar (IFSAR) processing for the 3D reconstruction of radar targets. In particular, we are interested in using two or more phase-coherent, high resolution SAR images taken at slightly offset elevation angles. The idea is to use phase difference from corresponding pixels in the image to estimate the height of scattering responses, where height is measured in the direction normal to the slant plane on which the images are formed.

Traditional IFSAR processing assumes that a given image pixel is dominated by scattering from a single height.[49] This height is then estimated from the phase difference between corresponding pixels in two images. In practice, the height estimate is corrupted by noise or clutter in the image; in some applications, height estimates can be locally averaged to reduce effects of the noise.[49]

The IFSAR application we consider is reconstruction of targets. For this application, it is expected that a major source of error may arise from scattering at more than one height in a given image resolution cell. This scattering can arise from layover (e.g. from tree canopies or other parts of the target) and also from multiple-bounce scattering mechanisms or sidelobes from strong scattering components in other resolution cells that leak into the image pixels under study. In this chapter we analyze the effects of the presence of more than one scattering response on the resulting height estimate.

The approach we take is summarized as follows. We assume a model in which the IFSAR image pixels under study are the result of two scattering responses. Without loss of generality, we assume that there is a dominant scattering term at one height and a second, weaker term at a different height. We analyze the effect of this second term on IFSAR height estimates, as a function of scattering magnitude, its phase difference from the dominant scatterer, and its height difference from the dominant scatterer.

Second, we consider ways of detecting IFSAR pixels that are the result of more than one scattering center. We specifically consider the magnitude difference between IFSAR image pixels. We develop a statistical model for the joint probability of height errors and pixel magnitude errors, and develop a hypothesis test for detecting cells with more than one scattering center. We derive the RMS height error and the detection/false alarm probabilities for this hypothesis test. The analysis is aided by a geometric model that describes the tests, from which a qualitative detection and false alarm understanding can be derived. The test is applied to 3D object reconstruction from Xpatch SAR imagery of a backhoe ground target.

The notion of multiple scattering centers in a resolution cell fits into the framework of the general radar concept of unresolved targets, where each scattering center is a point-target. The problem is to estimate the location of the unresolved targets or to eliminate them from a radar image, if they detract from the image quality. This problem has been investigated in monopulse radar literature; a deterministic[50] solution and probabilistic[51, 52] estimates of the location of two unresolved targets using monopulse radar system measurements have been developed. Here we model the problem of multiple unresolved scatterers from a SAR standpoint and investigate ways of improving 3D IFSAR images based on analysis of the model.

We also use the scattering model and geometric interpretation to predict performance when three or more coherent IFSAR images are available. We consider hypothesis tests for detecting multiple scattering centers, which are based on phase linearity of pixels under consideration. The analysis suggests that rejection of multiple-scattering cells is not significantly better using three or more IFSAR images than using only two images.

4.2 Multiple Scatterer Model

In this section we develop a model for two or more IFSAR images. We consider the case in which an image pixel is the result of a single dominant scattering center in a corresponding resolution cell. We also consider a model for the case when multiple scattering terms are present. The two-scattering model will be developed, although an extension to three or more scattering terms follows similarly.

4.2.1 Coherent IFSAR Images

We assume that a set of F complex images of a scene is available. Each image is formed from a SAR aperture at center elevation Ψ_i ($i = 1, \ldots, F$), and the images are formed on a common slant plane whose elevation is Ψ_s. We denote these images as $s_i(x, y)$ for $i = 1, \ldots, F$, where the x-axis and y-axis are oriented in the crossrange and downrange directions on the slant plane, respectively. For simplicity of exposition, we further assume that the data collection apertures are equally-spaced in elevation,

$$\Psi_i = \Psi_1 + (i-1)\Delta\Psi, \quad i = 1, \ldots, F \qquad \text{and } \Delta\Psi \ll 1 \tag{4.1}$$

where $\Delta\Psi$ is a constant such that $|\Psi_F - \Psi_1| \ll 1$, and also that $|\Psi_i - \Psi_s| \ll 1$, so that $\sin(\Psi_i - \Psi_s) \approx \Psi_i - \Psi_s$ and $\cos(\Psi_i - \Psi_s) \approx 1$.

In traditional IFSAR processing it is assumed that at each (x, y) location in the slant plane, backscatter occurs at a (single) height $h(x, y)$ normal to the slant plane. In this case, for

Ψ_i satisfying (4.1), the image pixel response $s_i(x,y)$ at image location (x,y) is given by[49]

$$s_i(x,y) \approx \text{sinc}_{\Delta X,\Delta Y}(x,y) \otimes \left[r(x,y)e^{-j4\pi \sin(\Psi_i-\Psi_s)h(x,y)/\lambda}e^{-j4\pi \cos(\Psi_i-\Psi_s)y/\lambda} \right] \qquad (4.2)$$

$$\text{sinc}_{\Delta X,\Delta Y}(x,y) = \Delta X \Delta Y \text{sinc}\left(\tfrac{x\Delta X}{2\pi}\right) \text{sinc}\left(\tfrac{y\Delta Y}{2\pi}\right)$$

where λ is the (center frequency) wavelength of the radar and ΔX and ΔY are the width of the support of the data collection in the crossrange and downrange Fourier dimensions X and Y. Here, $r(x,y)$ is the reflectivity function of the scene, and $h(x,y)$ is the height of the image above the slant plane. In a SAR system, the image in (4.2) is sampled, and the sample $s_i(x_k,y_l)$ is denoted as the image pixel at (x_k,y_l).

Traditional IFSAR processing forms an estimate of the height $h(x,y)$ under the assumption that there is one scattering point per resolution cell. The z-coordinate of the image pixel can be calculated using the phase difference between two images at closely spaced elevation angles. The relation between image height and phase, for Ψ_i satisfying (4.1), is given by[49]

$$\gamma_i = \arg(s_{i+1}s_i^*) \approx k_I h(x,y). \qquad (4.3)$$

where

$$k_I = \frac{4\pi\Delta\Psi}{\lambda} \qquad (4.4)$$

is a proportionality constant that scales height to phase shift, and s_i is used to denote the image pixel value under consideration, $s_i(x_k,y_l)$, for simplicity of notation. From equation (4.3), the scattering height is estimated by

$$\hat{z}_i = \frac{1}{k_I}\arg(s_{i+1}s_i^*). \qquad (4.5)$$

From equation (4.5) we see that IFSAR mapping from phase difference to height is ambiguous if the true phase difference exceeds 2π. Hence, we define the unambiguous IFSAR height interval width as $2\pi/k_I$.

The resolution cell corresponding to an image pixel centered at some point (x_k,y_l) is given by

$$\mathbf{C_{k,l}} = \{(x,y,z): x_k - \frac{x_{res}}{2} \le x \le x_k + \frac{x_{res}}{2}, y_l - \frac{y_{res}}{2} \le y \le y_l + \frac{y_{res}}{2}, \frac{-z_{\max}}{2} \le z \le \frac{z_{\max}}{2}\},$$
$$(4.6)$$

where x_{res} and y_{res} are the resolutions in the x and y coordinates, respectively, and $z_{\max}$ is the maximum height range of the scene, which is often defined from the beamwidth of the radar. If more than one scatter lies within cell $C_{k,l}$, equation (4.3) no longer applies. The image pixel corresponding to (x_k,y_l) is the combined response of the scatterers within that cell, and application of equation (4.3) may result in height estimation errors. We quantify these height errors in Section 4.3.

If the height of scattering varies slowly with respect to the SAR image resolution (such as in terrain-mapping applications), the single-pixel height estimate (4.5) can be modified to

provide some averaging over multiple pixels [49]. However, in applications such as 3D target reconstruction, the scattering height varies rapidly with respect to image resolution, and height estimates are formed from single pixels to avoid bias due to smoothing. While much of the analysis that we present applies to the multiple-pixel case, we assume independent processing of individual pixels in the following.

In the ideal case of no noise and a single scattering response per pixel, $\hat{z}_i = z_i$. In practice, this height estimate will be corrupted by additional scattering terms and by noise. The effect of noise has been well-studied in the literature.[49] If each s_i measurement is corrupted by additive (complex) Gaussian noise with zero mean and variance σ_n^2, then for moderate to high SNR the height error is approximately Gaussian with zero mean and standard deviation given by

$$\text{stdev}(\hat{z}_i) = \frac{1}{k_I} \frac{\sigma_n}{|s_i|}. \tag{4.7}$$

The value of σ_n can be computed from knowledge of the SAR measurement system.[49] Another source of height error results when an image pixel is the superposition of more than one scattering response. These additional scattering responses could be effects of layover or multiple-bounce scattering whose responses project to the same image pixel. In the following sections, we will analyze the estimation error in the height estimate $\hat{z}_i$ of the "desired" scattering center, that results from a nonzero extraneous scattering term. This error can be compared with the noise-induced error in equation (4.7) to determine when errors due to extraneous scattering are significant compared to errors due to noise.

4.2.2 Model Description

In the discussion that follows, a two-scatterer model is established. This model can be generalized to more than two scatterers, but the generalization is not needed here.

We assume that a set of F complex images of a scene are available. Consider an arbitrary image resolution cell, or pixel, centered at coordinates (x_k, y_l) in the image plane and let $s_i, \ i = 1, \ldots, F$ denote the complex-valued pixel from the ith image. We assume that the scattering response that produces these values is comprised of two point scattering centers. The complex responses from the two scattering centers at elevation Ψ_1 are given by $A_1 e^{j\alpha_1}$ and $A_2 e^{j\alpha_2}$, respectively. Without loss of generality the first scattering center will be considered the dominant one, $A_1 \geq A_2$. We assume that the amplitude responses of the scattering centers are constant with respect to small elevation changes; however, the phase response is a function of elevation. These assumptions follow from the arguments presented during the the development of equation (4.3) for one scatterer[49]. The two scatterer model is the superposition of each scatterer in the resolution cell. Thus, we have

$$s_i = A_1 e^{j\alpha_1} e^{j(i-1)k_I z_1} + A_2 e^{j\alpha_2} e^{j(i-1)k_I z_2}, \qquad i = 1, \ldots, F \tag{4.8}$$

$$\stackrel{\triangle}{=} s_{i,1} + s_{i,2}$$

102

where z_1, z_2 are the heights of the scattering centers (in meters) from the slant plane, and k_I is given by (4.4); $s_{i,n}$ denotes the image pixel formed by the nth scatter at elevation Ψ_i. A diagram of this model is shown in Figure 4.1(a).

4.2.3 Error Model

The height estimation due to multiple scattering terms is a function of six parameters, namely the scatterer amplitudes A_1 and A_2, their response phases α_1 and α_2, and their heights z_1 and z_2. In this section, we develop an error model that reduces these six parameters to three parameters of interest, and we develop an intuitive geometric model that captures the essential characteristics of extraneous scattering on height estimation.

A vector diagram for s_i and s_{i+1} is shown in Figure 4.1(a). Using equation (4.5), the height estimate is given by the angle from s_i to s_{i+1}, ϕ_i, divided by a constant k_I.

To analyze the error resulting from two (or more) measurements containing two scattering terms, we consider the following error vector model. We define

$$\tilde{s}_i = \frac{s_i}{s_{i,1}} = 1 + \frac{A_2}{A_1}e^{j(\alpha_2 - \alpha_1)}e^{j(i-1)k_I(z_2 - z_1)} \qquad i = 1, \ldots, F \tag{4.9}$$

$$\triangleq 1 + fe^{j\alpha}e^{j\beta(i-1)} \tag{4.10}$$

The error model reduces the original six-parameter problem to one of three parameters. These three parameters of the error model have intuitive meanings. The parameter $f = A_2/A_1$ $(0 \leq f \leq 1)$, represents the fractional magnitude of the second scatterer with respect to the first. The parameter α is the difference in scattering response phases. The parameter β is an angle such that β/k_I is the height difference between the two scatterers. A vector diagram depicting these error terms is shown in Figure 4.1(b).
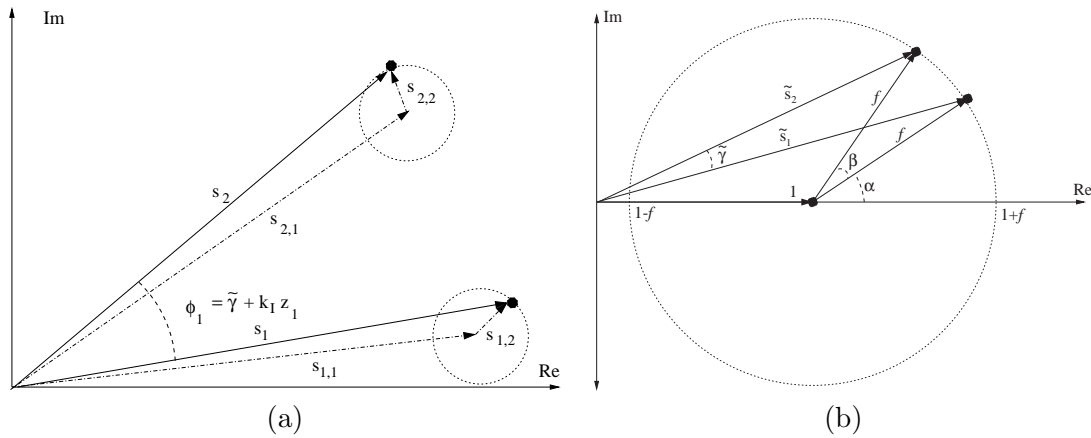
Figure 4.1: Vector diagrams for two point scattering model: (a) Unnormalized model (b) Normalized error model.

103

The angles between the s_i vectors encode a height estimate through the scaling factor k_I ; similarly, we define error angles as

$$\tilde{\gamma}_i = \arg(\tilde{s}_{i+1}\tilde{s}_i^*) \tag{4.11}$$

These angles encode the height errors given by

$$\tilde{z}_i = \hat{z}_i - z_{i,1} = \frac{1}{k_I}\left[\arg(s_{i+1}s_i^*) - \arg(s_{i+1,1}s_{i,1}^*)\right] = \frac{1}{k_I}\left[\arg(\tilde{s}_{i+1}\tilde{s}_i^*)\right] = \frac{1}{k_I}\tilde{\gamma}_i \tag{4.12}$$

derived from (4.5) and (4.9), using pixels in images at elevations Ψ_i and Ψ_{i+1}. $\hat{z}_i$ is the estimated height of the image resulting from two scattering centers, and $z_{i,1}$ is the height of the dominant scattering center; so, height error is the height that the estimate differs from the height of the dominant scatterer.

The error vector model in equation (4.10), and the corresponding angle errors in (4.11), provide a compact and geometric representation of the sources of height errors caused by a second scattering center. The parameters of $\tilde{s}_i$ determine the height error, as we discuss in Section 4.3 for IFSAR height estimation when $F = 2$ images are available. In Section 4.4 we address height estimation methods when $F \geq 3$ coherent images are available, and discuss error mechanisms there.

4.3   IFSAR Height Analysis Using Two SAR Images

Multiple scatterers in a resolution cell introduce height error into standard IFSAR processing. In this section we analyze errors obtained from height estimates found from two coherent SAR images (i.e. $F = 2$ in (4.8)). We consider height estimation error resulting from the estimator in equation (4.5), and the utility of using scattering magnitudes to detect height errors; we hypothesis a detection statistic and analyze its performance. Our analysis assumes noiseless measurements of one or two scattering centers.

Standard IFSAR processing estimates the height from the angle difference between the two complex pixel values from two SAR images that are closely-spaced in elevation. The height error due to the presence of a second scattering term in the measurements is given by (4.12). Thus, $\tilde{\gamma}$ characterizes height estimation error to within a constant k_I. We will analyze $\tilde{\gamma}$ in the following discussion. We note a related application in which a similar scattering model arises is that of monopulse radar[50]. However, the statistical performance analysis and the generalization to three or more measurements presented in this chapter appear to be novel, and in fact apply to the monopulse radar application as well.

Note that when $A_2 = 0$, $|s_1| = |s_2|$, but when $A_2 > 0$, $|s_1|$ and $|s_2|$ are in general not equal. This suggests a means of detecting the presence of a second scattering term. To this end, consider the normalized magnitude error

$$\tilde{m} = \frac{|s_1| - |s_2|}{|s_1| + |s_2|} = \frac{|\tilde{s}_1| - |\tilde{s}_2|}{|\tilde{s}_1| + |\tilde{s}_2|}. \tag{4.13}$$
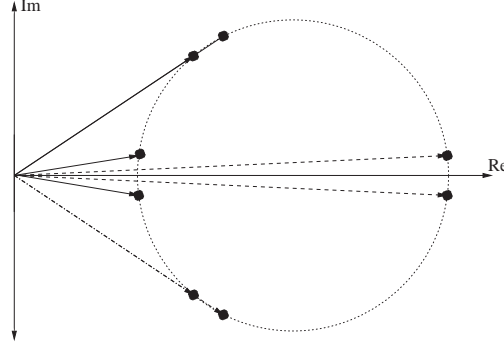
Figure 4.2: Vector diagram of four pairs of scattering vectors, corresponding to four values of α, and illustrating how error magnitude difference $\tilde{m}$ and error angle $\tilde{\gamma}$ are complementary. Extremal values of $\tilde{\gamma}$ are attained when $\tilde{m} = 0$ (left and right pairs), and when $\tilde{\gamma} = 0$ (top and bottom pairs) the normalized magnitude error is near its extremal values.

The geometry in Figure 4.1(b) provides an intuitive understanding of both the angle and magnitude error. The error depends on f, α, and β. When either $f = 0$ (i.e. $A_2 = 0$) or $\beta = 0$ (i.e. $z_1 = z_2$), there is no angle or magnitude error, regardless of α. Otherwise, both the error angle and magnitude depend on α. Figure 4.2 shows four pairs of $(\tilde{s}_1, \tilde{s}_2)$ that result in zero height or zero magnitude error, for fixed f, and β; note that they are complimentary in the sense that $\tilde{\gamma}$ achieves a local extremum when $\tilde{m} = 0$; similarly, when $\tilde{\gamma} = 0$, $\tilde{m}$ is close to its maximum or minimum value.

Figure 4.3 shows the relationship between error angle, $\tilde{\gamma}$, and normalized magnitude error, $\tilde{m}$, for selected values of f and β, over all values of $\alpha \in [0, 2\pi]$. The minima and maxima relationship between $\tilde{m}$ and $\tilde{\gamma}$ discussed above can be seen in this figure. In addition, for fixed f (β), smaller values of $|\beta|$ (f) result in smaller values for $|\tilde{\gamma}|$ and $|\tilde{m}|$; this can be seen from Figure 4.1(b). The complimentary nature of the extrema and zeros of $\tilde{\gamma}$ and $\tilde{m}$ are also evident.

4.3.1 Probabilistic Model for IFSAR Height Error

The previous subsections characterize IFSAR height error for particular parameters f, α, and β. In order to better characterize overall height error performance, we propose a probabilistic model, in which we assume prior probabilities on these parameters and characterize the resulting probability density function (pdf) of the height error.

Prior probabilities of the error parameters will depend on the application of interest, and
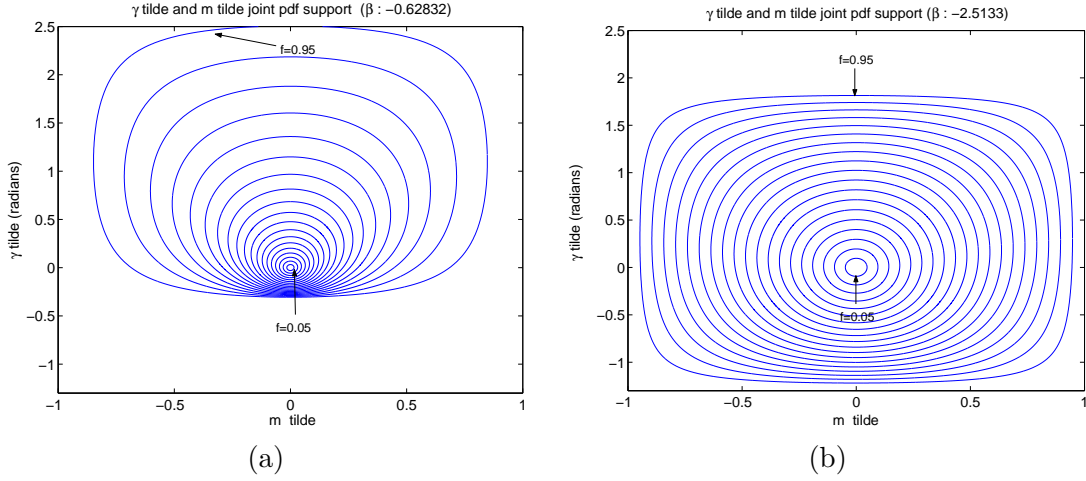
Figure 4.3: Plots of error angle $\tilde{\gamma}$ and normalized magnitude error $\tilde{m}$ for (a) $\beta = -0.2\pi$ and (b) $\beta = -0.8\pi$. Each figure shows results for values of $f \in [0, 0.95]$ at 0.05 increments and for all $\alpha \in [0, 2\pi]$.

in particular on the probabilistic characteristics of the physical parameters in the scene. We propose an example probabilistic model that applies to high-frequency (e.g. X-band) imaging of ground targets; other applications may dictate different priors.

Since knowledge of scattering response angle is often unknown or is highly sensitive to small changes in radar operating parameters, we assume that the relative phase α of the backscattered response between the two scattering centers is uniformly distributed between $-\pi$ and π (denoted $\mathcal{U}(-\pi, \pi)$) throughout our analysis.

The conditional pdf of $\tilde{\gamma}$ conditioned on β and f, $\mathrm{f}_{\tilde{\gamma}|\beta,f}$, can be derived analytically using the model in (4.10), but is omitted for brevity. Figure 4.4 shows two examples of $\mathrm{f}_{\tilde{\gamma}|\beta,f}$ for two sets of β and f. The pdfs have significant peaks at around the minimum and maximum values of $\tilde{\gamma}$, and most of the probability is concentrated around these values. The general shape of the conditional pdf can also be predicted from the vector diagram in Figure 4.1(b); varying α corresponds to traversing around the circle, and for most values of α, γ will be non-zero; this implies that most of the density will be located away form zero. Further analysis will show that most error angles are in fact close to the minimum and maximum error angles.

The conditional pdf, $\mathrm{f}_{\tilde{\gamma}|\beta,f}$, can be used to find the unconditional pdf of gamma, $\mathrm{f}_{\tilde{\gamma}}$, by integrating out the priors. $\mathrm{f}_{\tilde{\gamma}}$ summarizes the error introduced by an additional scattering center in a resolution cell. Thus, to find the unconditional density, we need to define a prior pdf for β and for f. Recalling that β relates to the physical height difference of interfering scattering terms, its distribution describes the difference between the height of a desired scattering center and that of an interfering one. We will assume a uniform pdf $\beta \sim \mathcal{U}[-\pi, \pi]$, to model cases in which layover (say, from trees) may occur at any height. A truncated
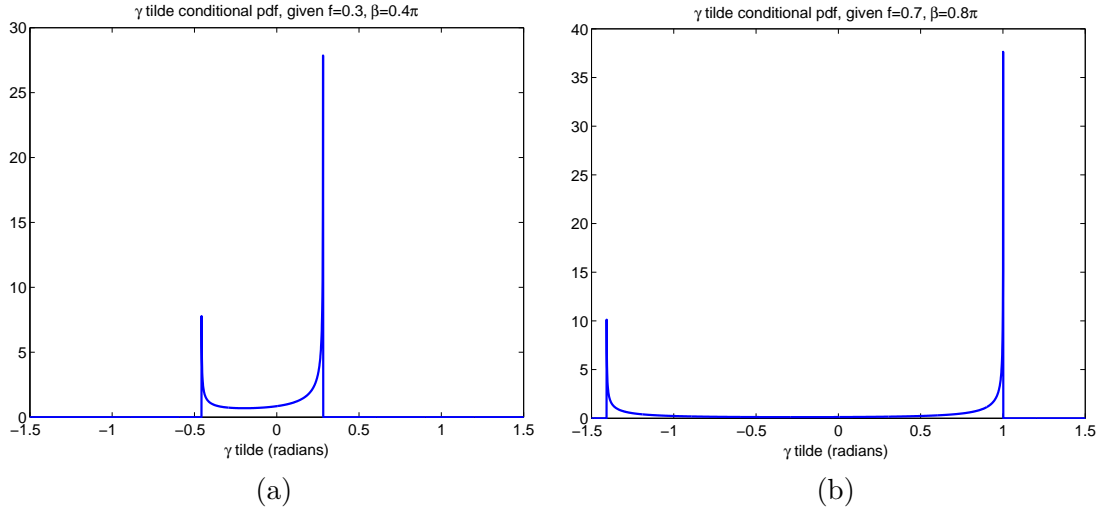
Figure 4.4: Conditional pdf of $\tilde{\gamma}$ given f and β, for (a) $f = 0.3$ and $\beta = 0.4\pi$; (b) $f = 0.7$ and $\beta = 0.8\pi$.

Gaussian pdf $\beta \sim \mathcal{TN}_{[-\pi,\pi]}(0, \sigma_\beta^2)$, where $\mathcal{TN}_{\text{support}}(\mu, \sigma)$ is a normal distribution with mean μ and standard deviation σ truncated to finite support and renormalized, will also be considered. This latter model might describe interfering scattering from other points on the target of interest, in which case the height of the interfering scatterer is likely to be limited by the height of the target (measured from the SAR slant plane). We assume no knowledge of f, except its maximum value. This parameter will be modeled as a uniform prior, $f \sim \mathcal{U}[0, f_{max}]$. Using these prior pdfs, we present results that predict height estimation error performance for cases of interest.

Figure 4.5 shows examples of the conditional pdf of $\tilde{\gamma}$ given a fixed value of f, $f_{\tilde{\gamma}|f}$, for the two choices for the prior on β discussed above. These pdfs are found from the conditional pdfs, $f_{\tilde{\gamma}|\beta,f}$ by integrating out β. The truncated normal pdf in Figure 4.5(b) is chosen such that the standard deviation of the height difference between the desired and interfering scattering center is 1 meter for a typical X-band radar scenario ($\lambda = 0.029$ m, $\Delta\Psi = 0.05°$), where the elevation angles satisfy (4.1); for this parameter selection $k_I = 0.373$ rad/m; so, 1 radian in Figure 4.5 corresponds to a height error of 2.68m.

We see that error angle probability in Figure 4.5 is concentrated about zero, instead of the tails of the distribution support, as was the case for fixed f and β. This behavior is exhibited over all f, an hence, assuming f to be a uniform prior, $f_{\tilde{\gamma}}$ will have the same general shape, as shown in Figure 4.8.

The maximum and RMS errors of $\tilde{\gamma}$ are summarized in Figure 4.6. Figure 4.6(a) displays the RMS error angle with $f \sim \mathcal{U}[0, f_{max}]$ for priors on β chosen to be uniform and truncated normal; Figure 4.6(b) compares the maximum error to the RMS error angle for uniform β and a given interfering scattering center relative magnitude, f. This figure demonstrates

107
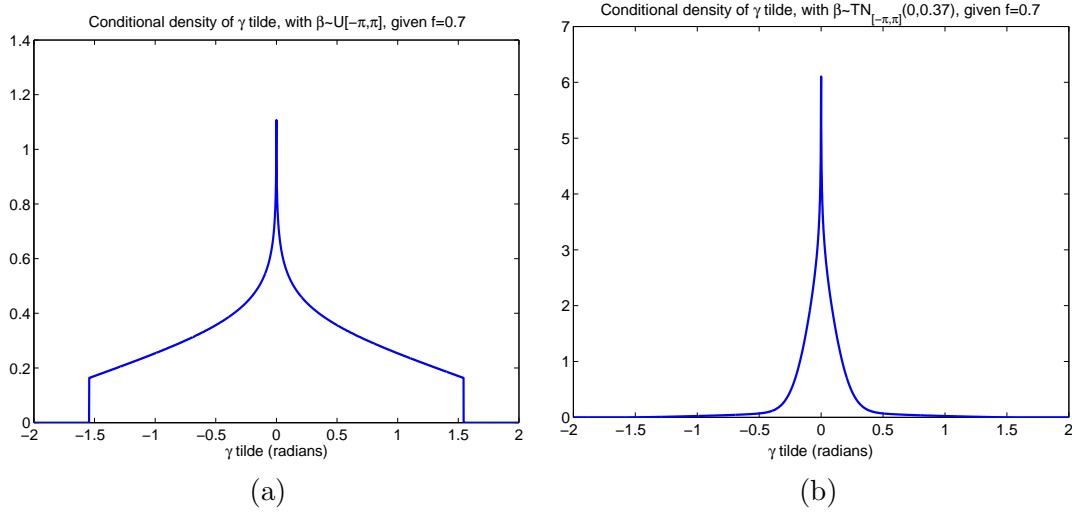
Figure 4.5: Conditional pdf of $\tilde{\gamma}$ for fixed $f = 0.7$ and two choices for the prior pdf of β. (a) $\beta \sim \mathcal{U}[-\pi, \pi]$. (b) $\beta \sim \mathcal{TN}_{[-\pi,\pi]}(0, 0.37)$.

how error angle is affected by the relative magnitude of the interfering scattering center. As might be expected, RMS error for the case when the interfering scattering height can be anywhere is larger than when the interfering scattering height is close to the dominant scattering center height with high probability, and RMS error is monotonic increasing as a function of the relative magnitude of the interfering scattering center.

Figure 4.6 provides a mechanism for analyzing IFSAR height error as a function of prior distributions on the parameters in (4.10). For example, we see from Figure 4.6(b) that, under these assumed prior probabilities on β and X-Band radar parameters, the RMS height estimation error, $\frac{1}{k_I}\sigma_{\tilde{\gamma}}$, is less than 1 meter if $f_{max} < 0.36$.

The preceding analysis complements a traditional noise error analysis for standard IFSAR. In particular, we can compare RMS height errors resulting from interference to those resulting from noise as given in equation (4.7).

4.3.2   Height Error Detection from Pixel Magnitudes

In this section we consider a method of detecting instances of large height error by using the pixel magnitudes corresponding to the two coherent SAR images. In particular, we analyze the efficacy of the $\tilde{m}$ feature in identifying pixels for which the height estimation error is high. Intuitively, the argument goes as follows. If $A_2 = 0$ (i.e., there is no interference scattering present), then $|s_i|$ are equal for $i = 1, \ldots, F$, and $\tilde{s}_i \equiv 1$. Thus, one might consider testing the (relative) magnitude difference between $\tilde{s}_1$ and $\tilde{s}_2$ as a way of detecting interference, and thus detecting height errors.
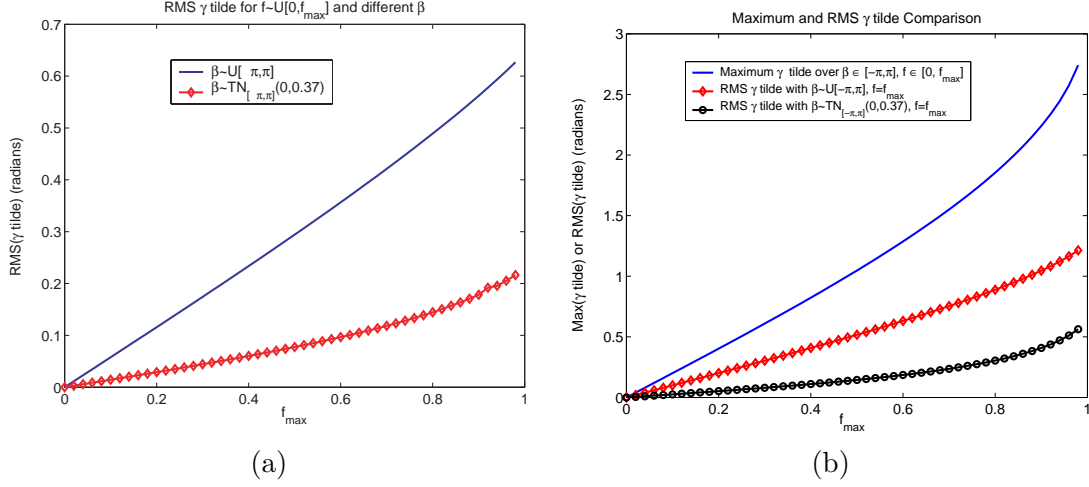
Figure 4.6: (a) RMS error angle for priors $f \in \mathcal{U}[0, f_{max}]$, $\beta \sim \mathcal{U}[-\pi, \pi]$, and $\beta \sim \mathcal{TN}_{[-\pi,\pi]}(0, 0.37)$, (b) Maximum error angle, RMS error angle for fixed $f = f_{max}$ and $\beta \sim \mathcal{U}[-\pi, \pi]$, and RMS error angle for fixed $f = f_{max}$ and $\beta \sim \mathcal{TN}_{[-\pi,\pi]}(0, 0.37)$.

A detection test using $\tilde{m}$ would keep height estimates if the relative pixel magnitudes are (nearly) equal, and reject height estimates otherwise; that is, the decision rule is

$$\begin{cases} \text{if } |\tilde{m}| \le \eta_m, & \text{keep height estimate} \\ \text{if } |\tilde{m}| > \eta_m, & \text{reject height estimate} \end{cases} \tag{4.14}$$

where η_m is some prescribed threshold. If the test is effective, height error will be small for accepted height estimates and large for the rejected estimates; that is, $\tilde{\gamma}$ is small when $\tilde{m}$ is small (recall that $\tilde{\gamma}$ is proportionally to the height estimation error).

We first consider this detection approach from a geometric perspective, using the vector signal diagram in Figure 4.1(b) or Figure 4.2. Consider fixed values of f and β. We see that the signal magnitudes $|\tilde{s}_1|$ and $|\tilde{s}_2|$ are nearly equal, $\tilde{m} \approx 0$, for values of α near 0 and π; that is, when the two points are near the leftmost or rightmost parts of the dotted circle. For these regions, however, $\tilde{\gamma}$ achieves its extremal values, so the height estimate error is maximum. Thus, for fixed f and β, the proposed detection procedure does the opposite of what we desire. However, our approach considers f and β over intervals of values; the performance of the test in this case is discussed next.

Observing how f and β vary in Figure 4.3 also provides geometric insight. The test $|\tilde{m}| \le \eta_m$ corresponds to accepting all points in a vertical "ribbon" centered at $\tilde{m} = 0$ in these figures. An ideal test would be to accept all points for which $|\tilde{\gamma}| < \eta_{\tilde{\gamma}}$, which is a horizontally-oriented "ribbon", but $\tilde{\gamma}$ cannot be measured; so, a test cannot be applied to it directly. For small values of f, when $|\tilde{m}| \le \eta_m$, $\tilde{\gamma}$ will also be small. However, for larger values of f, $\tilde{\gamma}$ may be very large even for small values of $\tilde{m}$. We investigate this observation and determine if η_m can be set so that the probability of large error angle pixels will decrease when the

threshold is applied.

The above insights can be made more quantitative by considering the joint pdf of $\tilde{m}$ and $\tilde{\gamma}$, $f_{\tilde{\gamma},\tilde{m}}$. Figure 4.7 shows two versions of $f_{\tilde{\gamma},\tilde{m}}$ calculated for two choices of prior distributions on f and β.
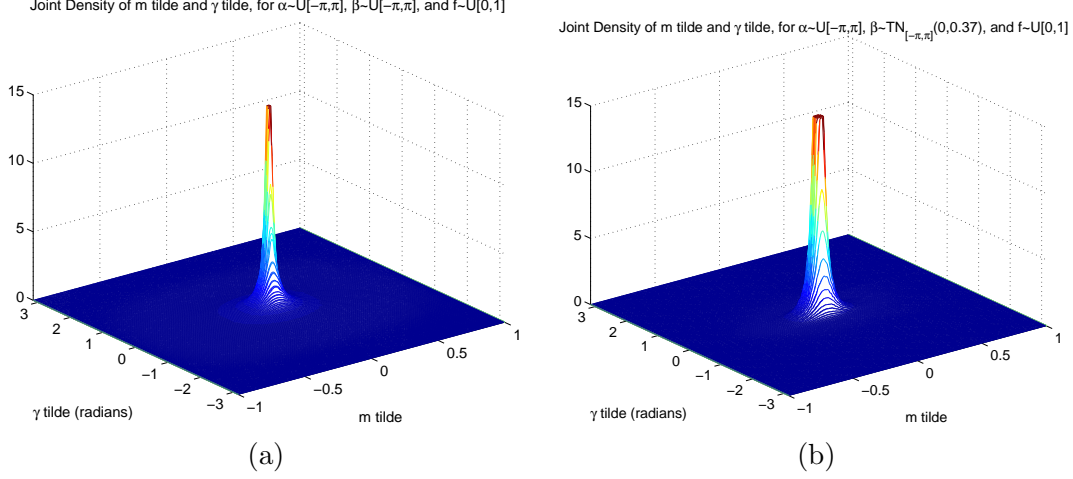
Figure 4.7: Joint pdf of $\tilde{\gamma}$, and $\tilde{m}$, $f_{\tilde{\gamma},\tilde{m}}$ when (a) $f \sim \mathcal{U}[0,1]$ and $\beta \sim \mathcal{U}[-\pi,\pi]$; (b) $f \sim \mathcal{U}[0,1]$ and $\beta \sim \mathcal{TN}_{[-\pi,\pi]}(0,0.37)$. Both pdfs peak at (0,0), but the figures are clipped near $\tilde{\gamma} = \tilde{m} = 0$ to more clearly illustrate the pdf shapes.

A noteworthy feature of these pdfs is that most of their density is concentrated about a region centered at $(\tilde{m}, \tilde{\gamma}) = (0,0)$. This suggests that the threshold filter introduced in (4.14) will not be able to reject all pixels with large error angle, but a majority of the accepted pixels will have error angles close to zero.

Figure 4.8 shows conditional pdfs of $\tilde{\gamma}$ overlaid on unconditional pdfs of $\tilde{\gamma}$. All are derived from the distributions in Figure 4.7 and the conditional pdfs in Figures 4.8(a) and (b) are conditioned on the events $\{\eta_m = 0.05\}$, and $\{\eta_m = 0.02\}$, respectively. In both cases, the conditional pdfs have more probability concentrated at low error angles than the unconditional pdfs do. So, the probability that error angle is below a certain level will be higher for the conditioned than for the unconditioned case. We note that approximately 70% of pixels are rejected using $\eta_m = 0.05$ in the $\beta \sim \mathcal{U}[-\pi,\pi]$ case, and about 53% are rejected in the $\eta_m = 0.02$ and $\beta \sim \mathcal{TN}_{[-\pi,\pi]}(0,0.37)$ case.

As suggested by Figure 4.8, threshold filtering does improve RMS error performance, as compared to the unfiltered case; furthermore, the value of a threshold and its effectiveness are a function of the distribution on β. These hypotheses are supported by the RMS plots shown in Figure 4.9 (a) and (b), which show the RMS error angle as a function of threshold values and the percentage of points rejected versus threshold for the two conditional pdfs in Figure 4.8. The RMS plots are monotonically increasing as a function of η_m, and $\eta_m = 1$ corresponds to having no threshold. Recall that for the X-band radar system considered,
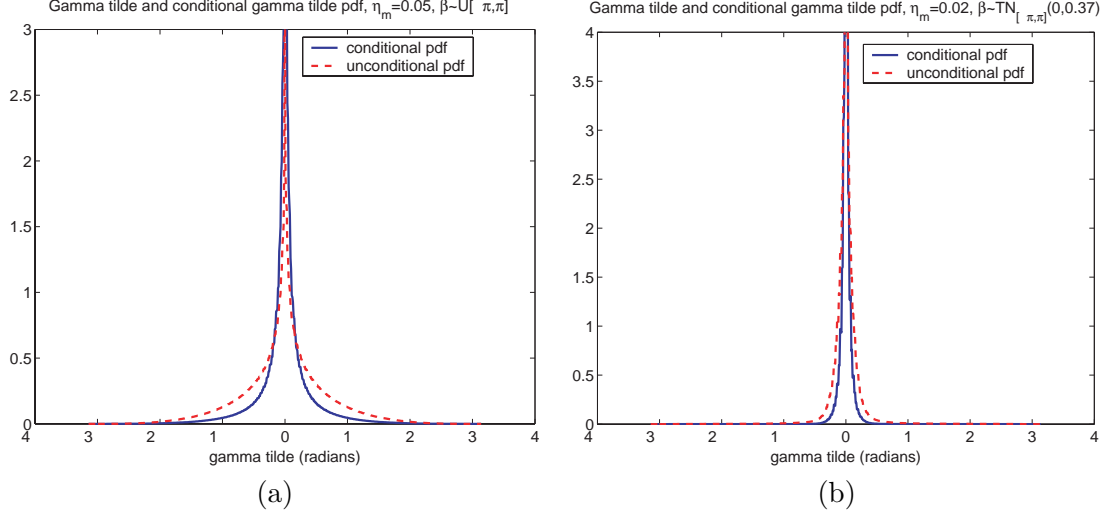
Figure 4.8: Comparison of $f_{\tilde{\gamma}}$ and $f_{\tilde{\gamma}|\eta_m}$ for $f \sim \mathcal{U}[0,1]$ and (a) $\beta \sim \mathcal{U}[-\pi, \pi]$ and $\eta_m = 0.05$, (b) $\beta \sim \mathcal{TN}_{[-\pi,\pi]}(0, 0.37)$ and $\eta_m = 0.02$

$k_I = 0.373$ rad/m, so RMS height errors with no thresholding are approximately 1.7 m for the distribution in Figure 4.8(a) and 0.64 m for the distribution in Figure 4.8(b). In both cases, a threshold of $\eta_m \approx 0.05$ results in decreasing the RMS height error by one-half, and eliminates around 25% and 75% of the pixel pairs, respectively.
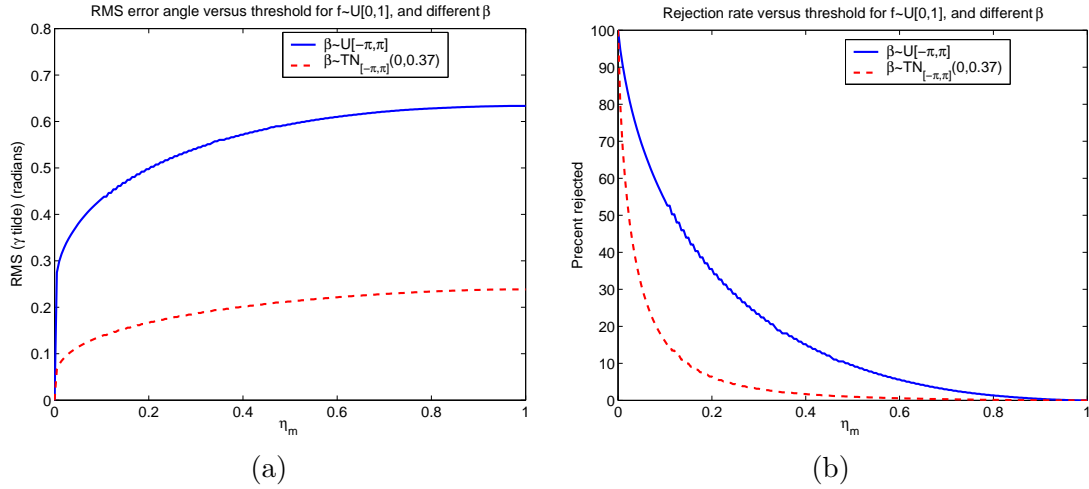
Figure 4.9: (a) Conditional RMS error of $f_{\tilde{\gamma}|\eta_m}$ as a function of η_m (b) Image pixel rejection percentage.

111

Figure 4.10 shows a ROC curve for a binary hypothesis testing problem, in which the hypotheses are:

$$H_0 : \quad \{|\tilde{\gamma}| \geq \eta_\gamma\}$$
$$H_1 : \quad \{|\tilde{\gamma}| < \eta_\gamma\}$$

(4.15)

and (4.14) is the decision rule. The pdf used, $f_{\tilde{\gamma},\tilde{m}}$, was derived from $\beta \sim \mathcal{TN}_{[-\pi,\pi]}(0, 0.37)$ and $f \sim \mathcal{U}[0, 1]$. For the X-band radar considered previously, $k_I = 0.373$ rad/m, so choosing $\eta_\gamma = 0.1119$ results in testing for height errors less than 0.3 m, and $\eta_\gamma = 0.1865$ tests for height errors less than 0.5 m.
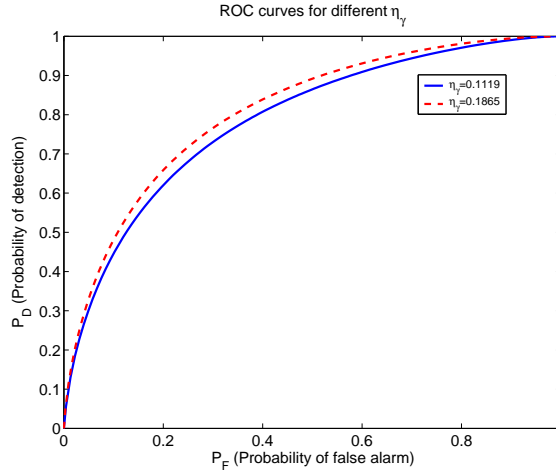
Figure 4.10: ROC curve showing probability of detection of the event $\{|\tilde{\gamma}| \leq \eta_\gamma\}$ versus its probability of false alarm, using $\tilde{m}$ as a test statistic for the pdf $f_{\tilde{\gamma},\tilde{m}}$ derived with $\beta \sim \mathcal{TN}_{[-\pi,\pi]}(0, 0.37)$ and $f \sim \mathcal{U}[0, 1]$.

This analysis shows that thresholding on $\tilde{m}$ does decrease the percentage of image pixels with large height error. The effectiveness of this threshold depends on the prior distribution of β, α and f. Given that 3D image quality is also a function of the number of pixels used in reconstruction, the rejection rate should also be considered when choosing a threshold.

4.4 Height Error Detection from Three or More Coherent Images

The previous analysis considered the case in which two coherent SAR images were used to estimate scattering height. In this section we consider the use of three or more SAR images.

One advantage of multiple images is that one can compute phase differences γ_i between two or more image pairs. For the case of no interference scattering ($A_2 = 0$), these phase differences are all equal. Thus, one might consider a test for detecting interference, and, hence, detecting cases in which height estimation error is large, by testing whether the phase differences are equal, or, equivalently by testing whether the phases are linear. Such a test

(a)Perfect linearity: $\tilde{\gamma}_1 = \tilde{\gamma}_2$ (b) Nonlinear phase difference: $\tilde{\gamma}_2 = -\tilde{\gamma}_1$
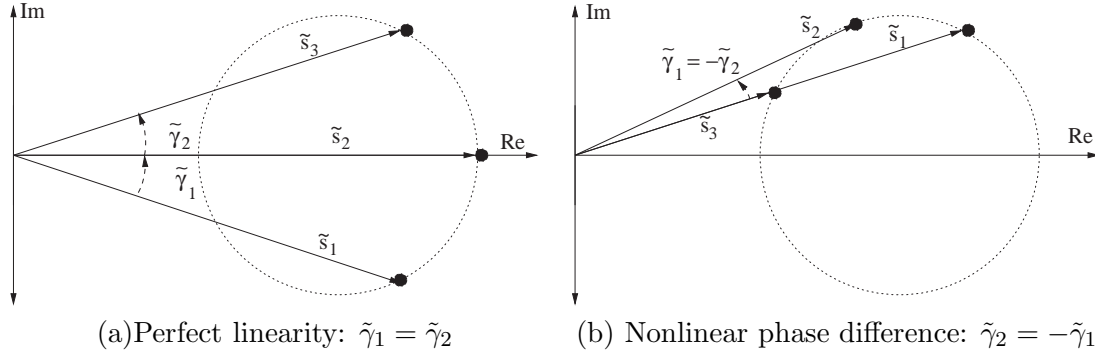
Figure 4.11: Vector diagram of resultant vectors at three elevation angles, (a) when the phases of $\tilde{s}_1$, $\tilde{s}_2$, and $\tilde{s}_3$ are perfectly linear; (b) when the phases are nonlinear.

would involve testing whether $|\gamma_2 - \gamma_1| = |\tilde{\gamma}_2 - \tilde{\gamma}_1| > \eta_\gamma$ for some prescribed threshold η_γ; if so, the phase linearity hypothesis is rejected. More sophisticated tests could use a more general combination of the phases and magnitudes from these F pixel values.

We submit that such tests have at best minor improvements over the detection test using two SAR images that is described in the previous section. We provide a geometric argument based on the vector diagram in Figure 4.11.

In this figure, we show the error vector diagram for $F = 3$, giving two image pairs (the figure and argument is similar for $F > 3$), and for two values of α. When $\alpha = -\beta$, then $\tilde{\gamma}_1 = \tilde{\gamma}_2$, and the phase linearity hypothesis is accepted for any threshold value. However, the resulting height estimate is in error by the amount $\frac{1}{k_I}\tilde{\gamma}_1$. In the second case, we have $\tilde{\gamma}_1 = -\tilde{\gamma}_2$, so the phase is maximally nonlinear over all values of α; on the other hand, the best linear phase fit effectively averages the phase errors $\tilde{\gamma}_1$ and $\tilde{\gamma}_2$, so the scattering height estimation error is zero in this case. Thus, phase linearity is complimentary to angle error $\tilde{\gamma}$ in the same manner as magnitude error $\tilde{m}$ is complimentary to angle error $\tilde{\gamma}$ for the two-image case discussed in the previous section. We thus see that the phase linearity detection test fails to detect large height errors for precisely those cases in which the $F = 2$ magnitude error test fails. As a result, the detection test using $F = 3$ is not expected to have significantly better performance than the $F = 2$ case. This reasoning applies also for $F > 3$. Given the additional (high) cost of collecting SAR data over several elevations, it does not appear that this cost is justified in terms of reducing scattering height errors caused by multiple scattering terms in a resolution cell.

The above arguments apply to interference scattering terms, and assume noiseless data. In practice, of course, the additional SAR images can be used to reduce the effects of height estimation error caused by noise. However, this reduction is modest; the height estimation standard deviation decreases at a rate of $\sqrt{F}$.

When $F \geq 4$, it is possible to simultaneously estimate the magnitudes and phases of both scattering terms in (4.8) using Prony's method.[53] There are some reasons to avoid a

113

Prony-based approach, however. First, Prony's method is very sensitive to noise, and the height estimation error due to noise could exceed the estimation error due to bias from interfering scatterers in standard IFSAR processing. Second, Prony's method is sensitive to modeling errors, and (highly) biased height estimates could result if the scattering response is composed of three or more scattering centers, a case that could well happen in practice. For these reasons, Prony's method is not expected to provide reduced height errors for this problem.

4.5   Example: Backhoe IFSAR Processing

In this section we present illustrative results of IFSAR processing to form a 3D reconstruction of a ground vehicle. Specifically, we consider a construction backhoe as shown in Figure 4.12(a). Using XpatchT scattering prediction software and a CAD model of the backhoe, high resolution, fully-polarimetric SAR images are generated across the entire "upper hemisphere" above the vehicle. Pairs of SAR images at the same azimuth and separated by 0.05° in elevation are used for coherent IFSAR processing, and are denoted as IFSAR image pairs.

Figure 4.12 shows results in which 3D scattering center locations are estimated from IFSAR image pairs, and then overlaid on a common coordinate system. The image pairs are centered every 5° in azimuth from 0° to 355°, and at elevations of $5n°$ and $(5n + 0.05)°$ for $n = 0, \ldots 17,$. Each SAR image has resolution of approximately 2in×2in, and each is processed to extract pixels whose RCS is within 40dB of the global RCS peak value; the height of each scattering center is estimated by applying equation (4.5) to each image pair. Finally, pixels are mapped to a common coordinate system and plotted. In Figure 4.12(b), all points are plotted, whereas in Figure 4.12(c), only points that pass a magnitude error threshold test in (4.14) are plotted. The threshold, η_m in this case is chosen to be 0.01. Points eliminated by the threshold test are shown in Figure 4.12(d).

These figures illustrate the effect that thresholding $\tilde{m}$ has on the 3D reconstruction of IFSAR data. In Figure 4.12 (b), the shape of the backhoe can seen from the IFSAR generated points, but the image is surrounded by many points that do not appear to correspond to a part of the backhoe. Figure 4.12 (c), showing the image after threshold filtering, is sharper than the image in (b), as many of the points not close to a backhoe surface are eliminated; these points are shown in Figure 4.12 (d). It should be noted that the threshold η_m was chosen qualitatively. If distributions on the priors f, β for the backhoe were known, a more suitable threshold may be found using the analysis in section 4.3. It should also be mentioned that Figures (b) and (d) are zoomed in and contain points outside the region of view, which were not present in (c).

(a)Backhoe facet model

(b)No threshold filtering

(c)Threshold filtering

(d)Rejected points from threshold filtering
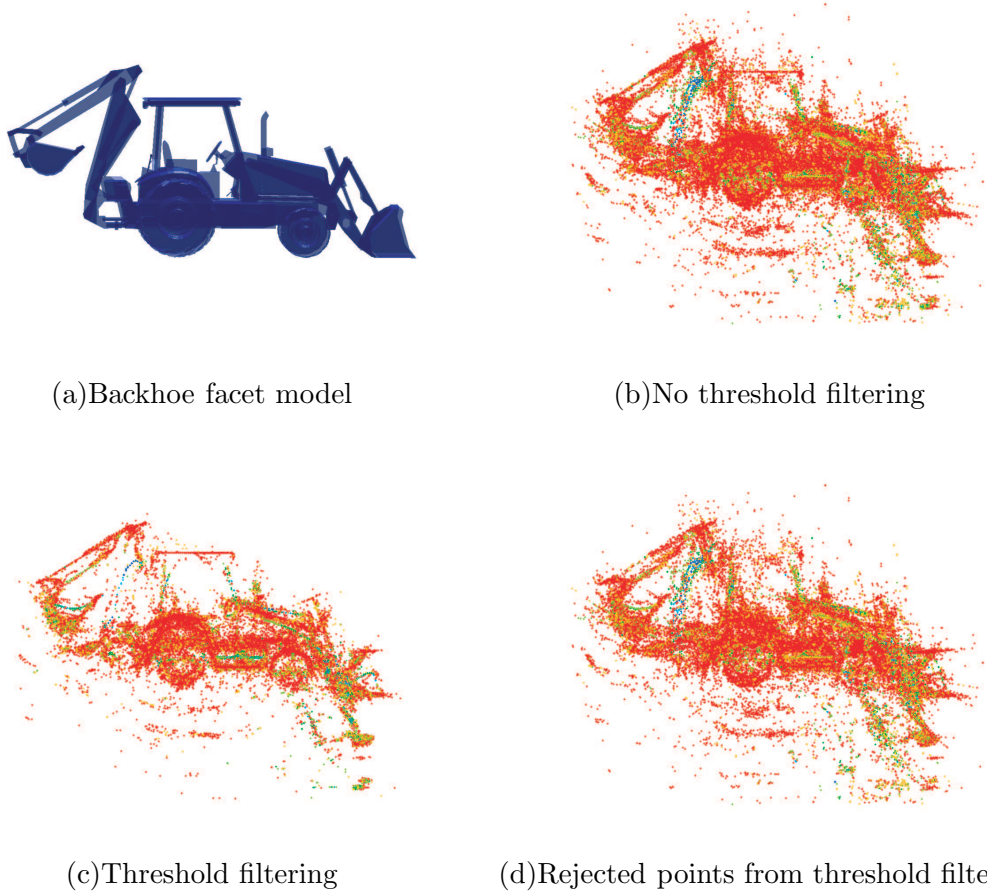
Figure 4.12: 3D IFSAR reconstruction of a backhoe from two IFSAR images, with and without threshold filtering. (a) Backhoe facet model (b) IFSAR image of all points 40 dB from the global RCS maximum (c) IFSAR image of all points 40 dB from the global RCS maximum and $\tilde{m} \leq \eta_m = 0.01$ (d) IFSAR image of all points 40 dB from the global RCS maximum and $\tilde{m} > \eta_m = 0.01$. In (b),(c),and (d), larger points correspond to scattering centers with larger RCS values.

4.6   Conclusion

In this chapter, we investigated IFSAR 3D image reconstruction when there is more than one scattering center per resolution cell. We developed a mathematical error model of two scattering centers per resolution cell. This model consists of three parameters, all with physical meaning with respect to the scattering centers in the resolution cell; furthermore, this model can be represented pictorially as a complex vector diagram. Using this model, a probabilistic description of height error (error angle $\tilde{\gamma}$) and normalized image magnitude difference ($\tilde{m}$) was presented. RMS height error was analyzed for different distributions on

model parameters. RMS analysis allows for comparison with IFSAR error introduced by noise. A threshold test on the $\tilde{m}$ statistic was introduced, and its effectiveness in reducing RMS height error was examined. This test did prove successful in reducing RMS height error, but its effectiveness depends on the distribution of the error model parameters. When setting a threshold, RMS height error and the percent of data rejected should be considered simultaneously because of the trade off in 3D image quality between the two. Testing for phase linearity using more than two elevation angles appears to offer little improvement in reducing error over the use of two elevation angles and a threshold on $\tilde{m}$, and for more than three elevation angles, Prony's method could be used to estimate the complex value of each scatter, but it is very sensitive to to deviations from an ideal noiseless mathematical model. To conclude, the $\tilde{m}$ threshold test was used to filter XpatchT backhoe data. The image with filtering appeared sharper than the one without filtering, showing that $\tilde{m}$ threshold filtering is capable of improve 3D IFSAR image quality.

5. LARGE BANDWIDTH SLOT ARRAY WITH WIDE SCAN ANGLE

5.1 Introduction

The uses of Unmanned Air Vehicles (UAV) are likely to increase in the future. These vehicles will be used for reconnaissance, surveillance as well as for mapping small areas. Because the platform size is relatively small and useable space for large antennas is at a premium, it is important to understand the relationship between viable antenna performance and radar system requirements. In particular for this study, a broad band wide scan angle Synthetic Aperture Radar (SAR) antenna array is of interest. The challenge is to design the array so that it can be placed on a relatively flat surface underneath the belly of the vehicle. Because of the directions that the SAR needs to operate relative to the array surface, wide scan angle ability is desirable. In addition, since future SAR systems' would benefit from the highest resolution possible, as large a bandwidth as possible is desired. All of these requirements present a difficult challenge for present day antenna manufacturing.

In this study, an antenna array design is determined that can provide the needed requirements for the desired radar system performance on such a UAV location. It can provide a thin conformal shape for the antenna elements and feed structure. Based on possible "behind the ground plane" components available in the next few years a one band design is achievable. It also easily provides for extension into a two band design when small enough components can be manufactured in the future.

In particular, the research efforts summarized here is to design an antenna array that will operate from 45 degrees to 70 degrees from the normal of the plane of the flat array and scan plus or minus 60 degrees in azimuth. Since it is intended to operate very close to grazing of a surface, vertical polarization is of primary importance. The long term goal is for it to operating over X and Ku bands simultaneously. The short term goal is to operate over X band. It has been shown that a very good design can be achieved at X band and still be able to accommodate the size of present day system components.

The following sections will briefly describe the approach and results for the antenna design. In addition, an oral paper on some general findings regarding wide scan angle slot array antennas were presented at the 2005 IEEE Antennas and Propagation Symposium and Radio Science Meeting in Washington D. C. July 5 - 8, 2005 [54].

5.2 Approach

Many phased array applications employ dipole antennas over a ground plane, yet at high elevation angles the dipole - ground plane element pattern is not omni directional in its

principal plane. This characteristic is undesirable for wide scan angles (approaching 70°). A successful design concept has been developed for wide band arrays based on closely spaced elements of dipoles [55]. So a simple approach would be to base the design on this type of configuration and try and push the limits on the scan angle. It was found however, that it is better to take advantage of the more desirable pattern of a slot element. Unfortunately, the interaction of the dipoles and ground plane are different than that of slots over a ground plane. The challenge for this design is then to use the same basic design philosophy to achieve bandwidth, while taking into account the underlying physics defining slots.

The basis for analyzing the array performance in both cases is the well validated Periodic Moment Method (PMM) code [56]. The scan impedance of the array is rigorously simulated in an infinite periodic array using Moment Methods on the elements with a spectral greens function of multilayered material slabs [57]. The design process entails studying the effect that various parameters have on the active antenna impedance. This is accomplished by determining the best combination of parameters by viewing the effect their size and material composition has on the behavior of the impedance on a Smith Chart.

The design process starts by looking at the behavior of the element, with respect to its size, in a thin dielectric "underwear" to isolate the elements from other layers. Inductance is added between elements to promote field continuity. Next the effect of the spacing between the ground plane and the element layer is determined. The dielectric constant is chosen for the thickness desired. A dielectric layer is added over the array to provide impedance stability over the desired range of scan angles. A permittivity value is chosen that causes the angle behavior of the transmission coefficient to compensate for the scan angle projection change. The goal is to position the impedance curve on the Smith Chart such a balun and matching line can be added that provides an acceptable VSWR which in this case is 2:1 in the central region and lower than 3:1 over the whole design range. Finally, a thin hard layer is added at the top for protection.

A thorough study of the parameters of interest was undertaken resulting in two prospective designs that meet the goals of the antenna performance. A detailed presentation of this study is under preparation [58]. The next section will briefly outline the final results for the two designs. It should be remembered that these results are for an infinite array. A finite array would need could have end effects that are usually minimized for a reasonable number of elements. In addition, load passive elements can be added at the ends to further reduce these effects.

5.3   Results

Figure 5.1 shows the top view and Figure 5.2 the side view for the so called large spacing configuration of the array. The spacing for this design focused on achieving good performance over one band of operation. At the center frequency, the slot elements have a length of $\lambda/3$, width of $\lambda/10$ and a spacing of $\lambda/3$. They are etched onto standard thickness di-

Top View
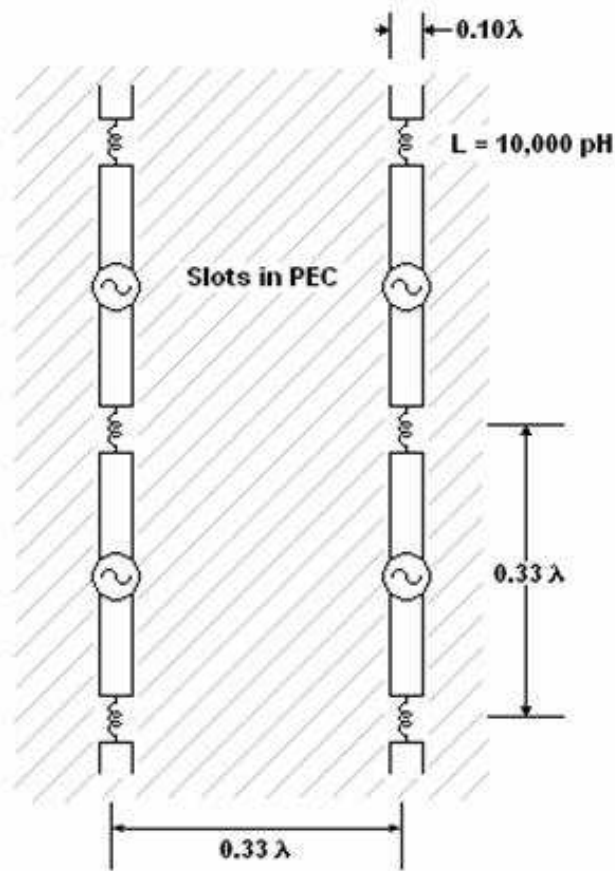
Figure 5.1: Top view of the one band design of the slot array

electric boards of relative permittivity 2.2 at 10 mils on both sides. Inductors are used to connect the ends of each element to help provide field continuity. In this case, 10,000 pH was found to be needed. The elements are spaced over the ground plane with a dielectric layer of relative permittivity of 1.7 and thickness of 0.137λ. To achieve large scan angles with stable impedance, a scan compensation dielectric layer is used with the dielectric constant of 1.3 and a thickness of 0.093λ. A standard thickness protective dielectric layer of 30 mils and relative dielectric constant of 3 is place on top. This results in a total thickness for the array above the ground plane to be less than $\lambda/4$. The advantage of this design is that at some frequencies of interest components will be available under the ground plane to feed the array.

These slots are presently fed by connecting a 100 ohm 0.067λ long matching section going

119
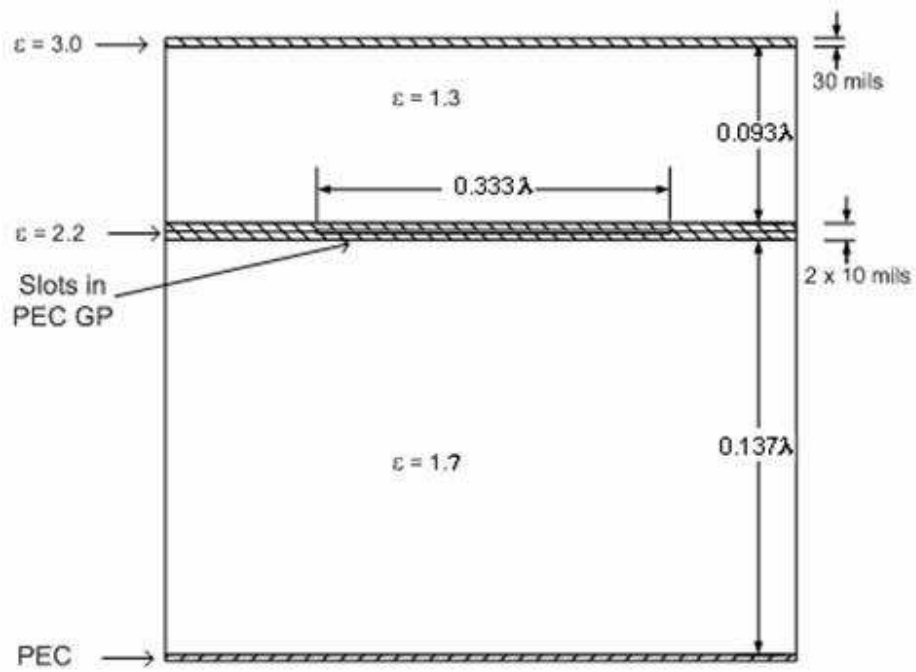
Side View

Figure 5.2: Side view of the one band design of the slot array

120

Figure 5.3: Impedance of one band slot array scanned to 45 degrees. Normalized to 350 ohms on Smith Chart.

Figure 5.4: Impedance of one band slot array scanned to 70 degrees. Normalized to 350 ohms on Smith Chart.
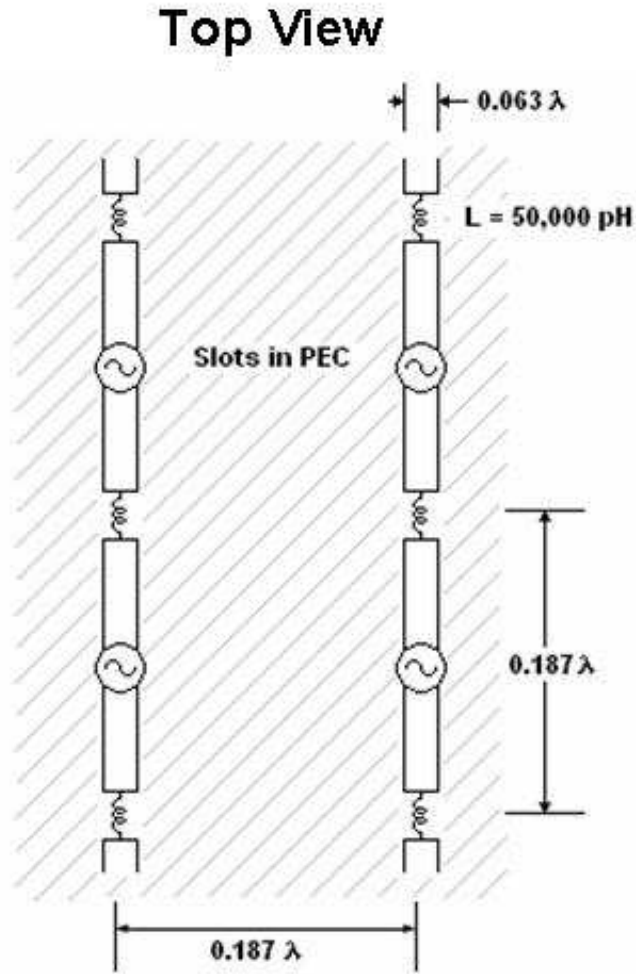
Top View

Figure 5.5: Top view of the two band design of the slot array

into a line representing a 350 ohm impedance. The best way to implement this balun transformer is under investigation.

Figure 5.3 and 5.4 shows the active scan impedance of the one band design at a scan angle of 45 degrees and 70 degrees, respectively on Smith Charts normalized to 350 ohms. For the 45 degree case, the resulting bandwidth is 2:1. For the 70 degree scan angle it is 1.5:1, which is sufficiently wide for X-band.

Figure 5.5 shows the top view and Figure 5.6 the side view for the so called small spacing configuration of the array. The spacing for this design focused on achieving good performance over two contiguous bands of operation. At the center frequency, the slot elements have a length of 0.187λ, width of 0.063λ and a spacing of 0.187λ. They are etched onto

123
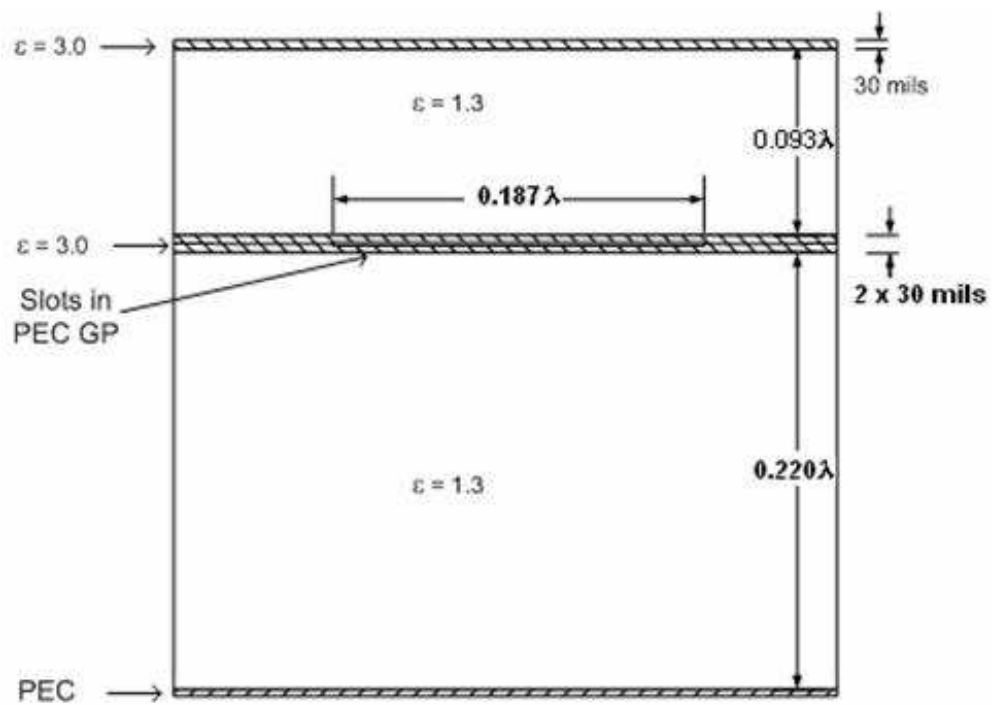
Figure 5.6: Side view of the two band design of the slot array

standard thickness dielectric boards of relative permittivity 3 at 30 mils on both sides. Inductors are used to connect the ends of each element to help provide field continuity. In this case, 50,000 pH was found to be needed. The elements are spaced over the ground plane with a dielectric layer of relative permittivity of 1.3 and thickness of 0.220λ. To achieve large scan angles with stable impedance, a scan compensation dielectric layer is used with the dielectric constant of 1.3 and a thickness of 0.093λ. A standard thickness protective dielectric layer of 30 mils and relative dielectric constant of 3 is place on top. This results in a total thickness for the array above the ground plane to be less than $\lambda/3$. The present disadvantage of this design is that at the components that will be needed under the ground plane to feed the array are still under development.

These slots are presently fed by connecting a 100 ohm 0.067λ long matching section going into a line representing a 200 ohm impedance. The best way to implement this balun transformer is under investigation.

Figure 5.7 and 5.8 shows the active scan impedance of the one band design at a scan angle of 45 degrees and 70 degrees, respectively on Smith Charts normalized to 200 ohms. For the 45 degree case, the resulting bandwidth is 2.4:1. For the 70 degree scan angle it is 1.9:1, which is sufficiently wide for X and Ku-bands.

5.4   Conclusion

A prospective design for a large bandwidth antenna array with a wide scan angle capability is discussed. The array is composed of closely spaced slot elements in several layers of dielectric material. The use of slot elements helps the array achieve a 70 degree scan angle and still maintain bandwidth stability. It is shown that by varying the size of the elements the bandwidth can be adjusted to meet requirements. In the larger spacing design, the band width is appropriate for one band use, with the advantage that soon to be available electronic components will be available. In the smaller spacing design, the bandwidth is appropriate for two band use, with the disadvantage that it the electronic components are still being developed. In both case, the above the ground plane antenna array uses commonly available materials and produces a low profile conformal configuration.
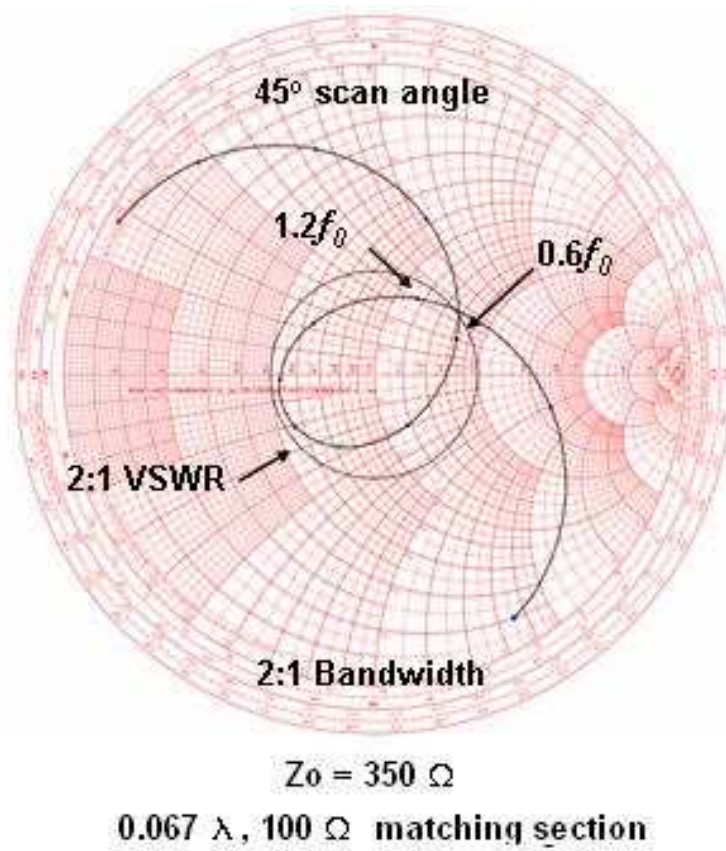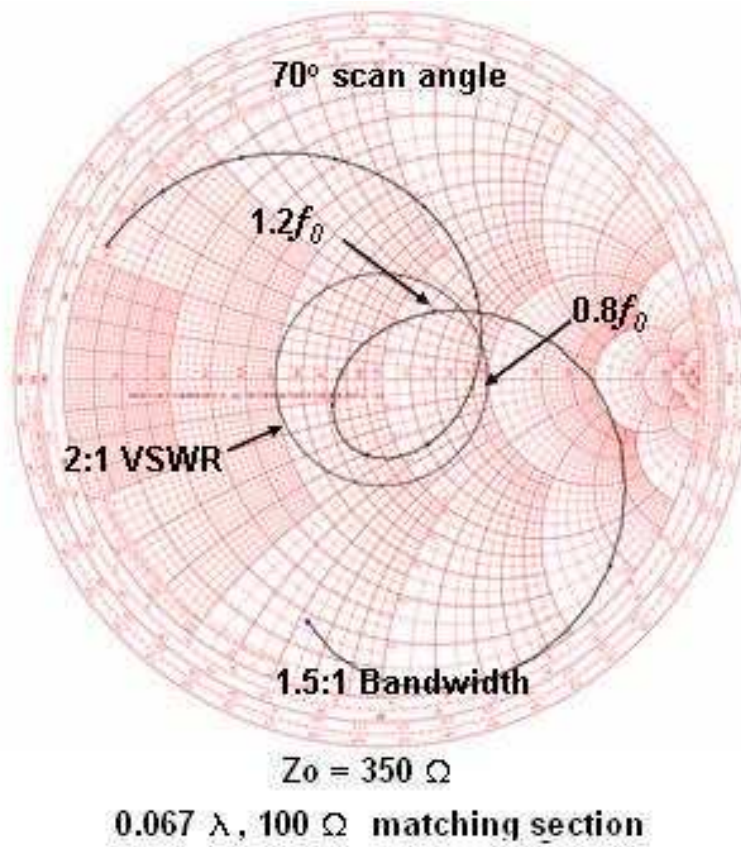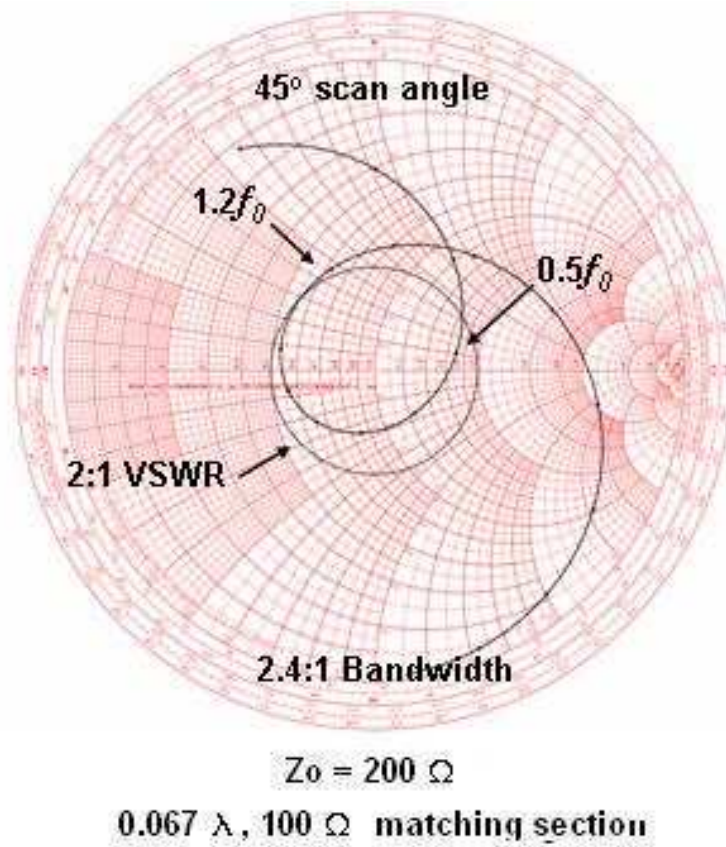
Figure 5.7: Impedance of two band slot array scanned to 45 degrees. Normalized to 200 ohms on Smith Chart.
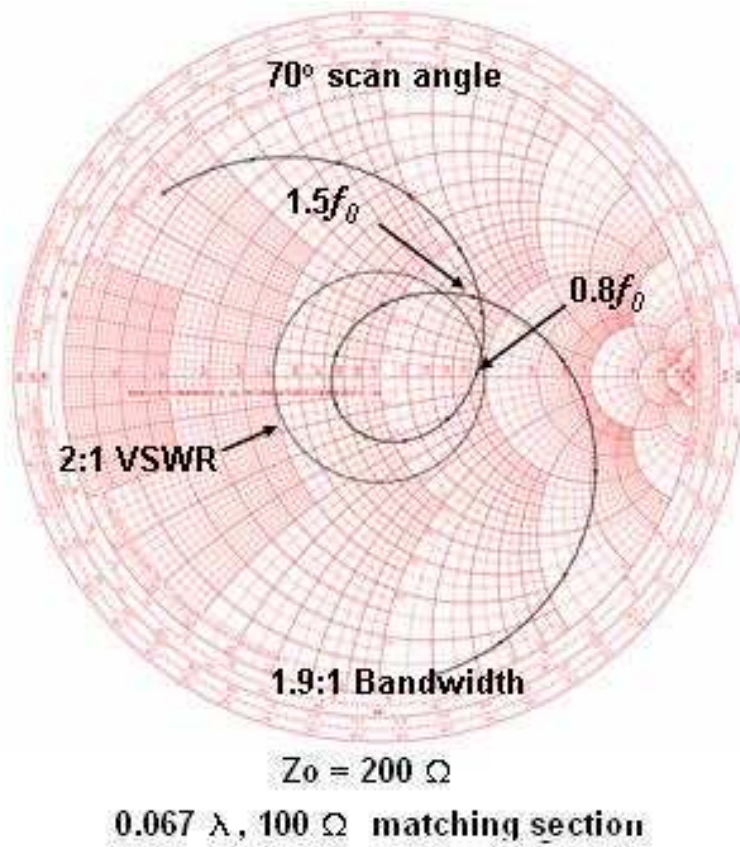
Figure 5.8: Impedance of two band slot array scanned to 70 degrees. Normalized to 200 ohms on Smith Chart.

6.   ROUGH SURFACE SCATTERING

6.1   Introduction

The performance of an ATR system can be strongly affected by the clutter environment in which the system is operating, particularly when used for stationary targets. For microwave sensors, understanding backscatter properties of the clutter environment is critical for designing ATR algorithms that remain robust in the presence of clutter. Physically-based models for clutter properties enable variations with a variety of sensor parameters to be investigated easily, if a reasonable model can be created. One such clutter geometry for which effective scattering models exist is that of a randomly rough surface; both terrain and sea environments can be approximately modeled by this geometry. Figure 6.1 illustrates an example ATR system, and demonstrates that clutter returns from the ground surface are ubiquitous in observations of ground-based targets. In addition, the possibility of interactions between target scattering and the ground (for example, in multi-path target returns) must be considered to produce accurate simulations of target signatures. Such interactions are not considered here, but have been explored in other work by the authors of this chapter [59]-[62].

Considering rough surface clutter alone, two classical models for scattering from rough surfaces are available in the high- and low-frequency limits [63]. More recently, a "small-slope" approximate (SSA) theory [64] has been proposed that bridges these two limits. Studies of clutter properties predicted from this theory are useful in testing and improving ATR systems for targets in the presence of clutter.

The lowest order SSA term can be regarded as second order in surface "quasi-slope" [65], and has a form similar to the PO approximation but multiplied by an alternate function of the
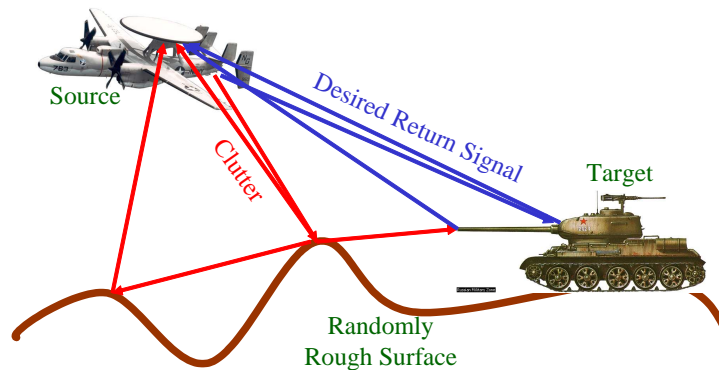
Figure 6.1: Example ATR observation including rough surface clutter
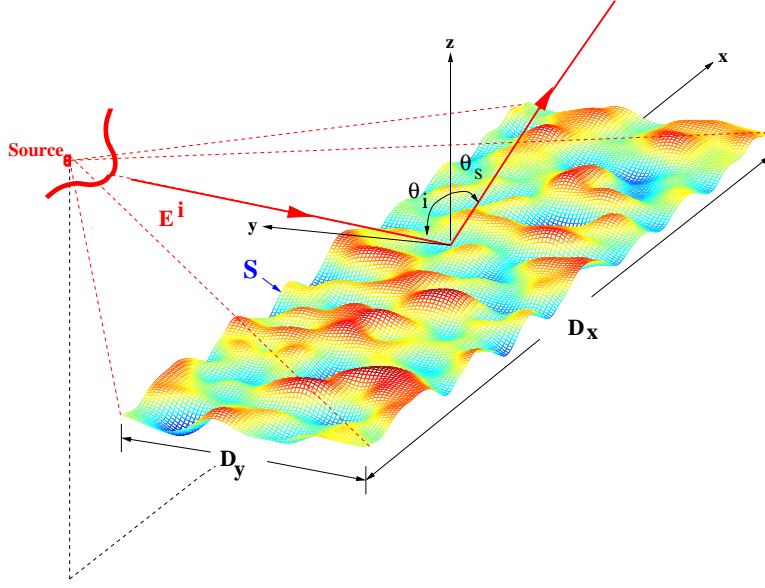
Figure 6.2: Geometry of problem considered

surface permittivity and of the incident and scattering angles. A recent paper [66] investigated the accuracy of the lowest order SSA through comparison with numerical simulations and found inaccuracies in the physical optics limit. However, reference [64] demonstrates that the SSA reproduces the PO theory when higher order SSA corrections (at third and partial fourth order) are included in the scalar, hard-boundary scattering problem. The first (third order) correction to the lowest-order SSA has a more complicated form involving a quadruple integral for computation of average cross sections. Averages of the first correction term can also be computed through a Monte Carlo simulation with a deterministic surface small slope approximation [67]-[68]. The complexity of both of these approaches, however, has limited the number of studies reported including higher-order SSA terms in the electromagnetic, penetrable surface problem.

Here a simplified form for the first SSA correction term is presented for penetrable surfaces under the assumption of a Gaussian random process surface with an isotropic Gaussian correlation function. While these surfaces are admittedly simple compared to many natural surface structures, the isotropic Gaussian correlation function surface remains a widely-used model in many applications. Surfaces in this case are described simply by the rms height h and correlation length l parameters.

6.2   Formulation

Figure 6.2 illustrates the scattering geometry considered. Define the z direction as normal to the mean surface plane, and pointing into free space. For a plane wave in free space
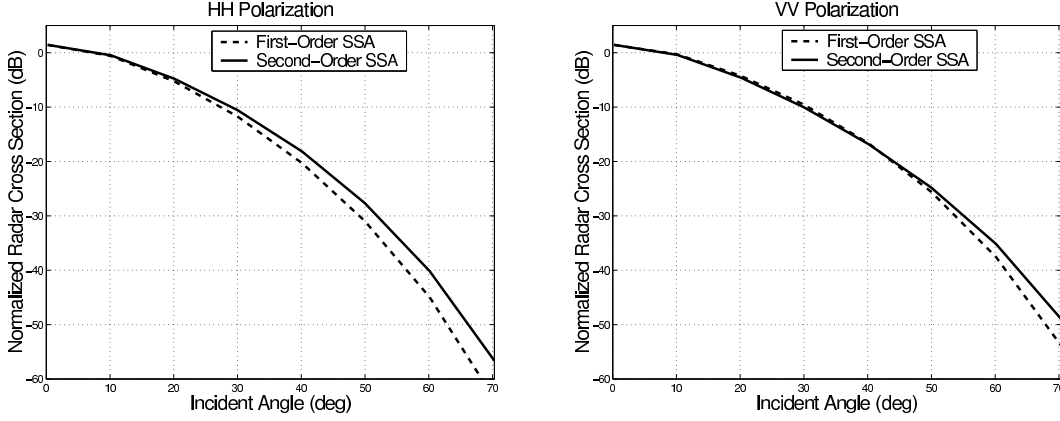
Figure 6.3: Backscattering Results for $kh = 1$, $kl = 6$

approaching from direction $\overline{k}_i = \hat{x}k_{ix} + \hat{y}k_{iy} + \hat{z}k_{iz}$, and for scattering measurements in direction $\overline{k}_s = \hat{x}k_{sx} + \hat{y}k_{sy} + \hat{z}k_{sz}$, the simplified expression for the first SSA correction term is:

$$\sigma_{SSA}^{(c)} = -\frac{k_{sz}^2}{\pi|k_{dz}|}\text{Re}\left\{i\left(g_{SPM}\right)\left[A_1 + A_2 - A_3\right]\right\} \tag{6.1}$$

where

$$A_1 = \sum_{n=1}^{\infty}\frac{\pi l^2(k_{dz}h)^{2n}e^{-k_{dz}^2h^2}}{n(n!)}\sum_{m=-\infty}^{\infty}(-1)^m e^{-im\phi}B_{n,m} \tag{6.2}$$

$$A_2 = (2\pi)^2 e^{-k_{dz}^2h^2}g_{SSA}^{(c)*}(-k_{dx}, -k_{dy})W(k_{d\rho}) \tag{6.3}$$

$$A_3 = (\pi D_I)\int_0^{\infty}dk_\rho\ k_\rho\ W(k_\rho)\ g_0^{(c)*}(k_\rho) \tag{6.4}$$

and $B_{n,m}$ above is defined as

$$\int_0^{\infty}dk_\rho k_\rho W(k_\rho)g_m^{(c)*}(k_\rho)I_m\left[\frac{l^2 k_{d\rho}k_\rho}{2n}\right]\exp\left[-\frac{l^2(k_{d\rho}^2 + k_\rho^2)}{4n}\right] \tag{6.5}$$

In these equations, $\sigma_{SSA}^{(c)}$ is the first correction to the lowest order SSA average normalized bistatic scattering coefficient, $\overline{k}_d = \overline{k}_i - \overline{k}_s = \hat{x}k_{dx} + \hat{y}k_{dy} + \hat{z}k_{dz}$, $k_{d\rho} = \sqrt{k_{dx}^2 + k_{dy}^2}$, I_m is the modified Bessel function of order m, and $W(k_\rho) = \frac{h^2 l^2}{4\pi}\exp\left(-k_\rho^2 l^2/4\right)$ refers to the power spectrum of the surface. The factors g_{SPM} and $g_{SSA}^{(c)*}$ are functions of the surface permittivity, radar frequency, polarization, and the incident and scattering angles, and are specified in [68]-[69], while the factor $g_m^{(c)*}$ is the m-th azimuthal Fourier series coefficient of $g_{SSA}^{(c)*}$. The factor D_I [63] arises in the PO theory with an isotropic Gaussian correlation

130
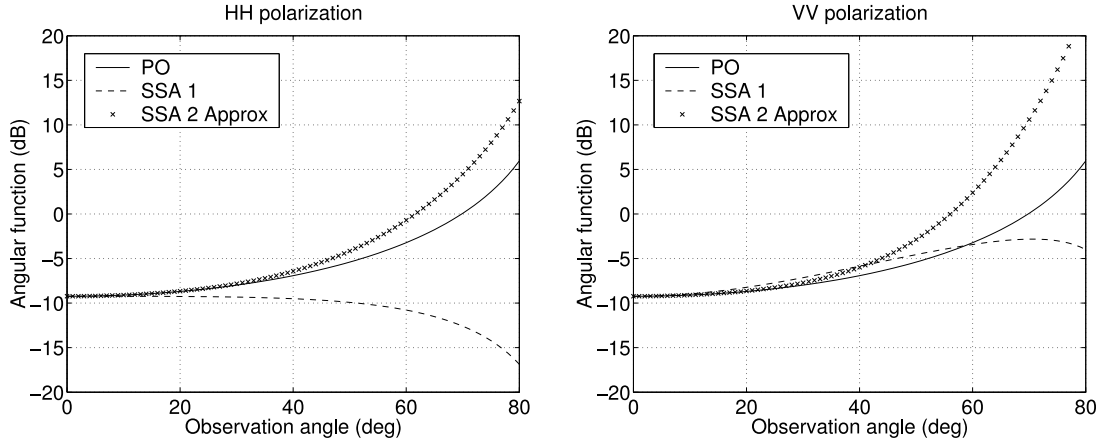
Figure 6.4: Backscattering angular functions for "long-wave" surfaces

function surface. Note the original quadruple integral is replaced by the double sum and single integration in the term A_1 for the isotropic Gaussian correlation function surface. The sum over m in the term A_1 is found to converge rapidly (typically needing no more than 32 terms) due to the limited harmonic structure of $g_m^{(c)}$, and the integrations $B_{n,m}$ also are well behaved due to the Gaussian functions involved.

A MATLAB-based code was developed to implement these equations, and results were found to match data from a previous Monte Carlo higher-order SSA simulation [67] well. The script is available upon request to the authors. As an example, Figure 6.3 illustrates HH and VV normalized backscattered cross sections versus observation angle for the case $kh = 1$, $kl = 6$, with $k = 2\pi/\lambda$ the electromagnetic wavenumber at wavelength λ. The surface relative permittivity was set to $4 + i$ in these computations. Results from the lowest order SSA (SSA1) and the lowest order plus the first correction (SSA2) are compared, and demonstrate that the correction is significant for this case, particularly in HH polarization at the larger observation angles. Results from repeated computations with the same surface permittivity and with varying kh and kl at observation angles of 10 and 70 degrees were obtained. Results showed that that the correction is significant when kl becomes larger independent of kh, or when kh approaches 30% of kl for smaller kl values. The correction term is generally larger in HH polarization.

6.3 Large scale approximation

To further investigate simplification of the SSA in the PO limit, an approximation to the original SSA2 expressions was developed. The complete SSA correction term was included in the analysis (i.e. including the third and partial fourth order terms [65]). Using a Taylor series about the origin $(g_{SSA}^{(c)}(k_x, k_y) \approx Ak_x + Bk_y)$, the resulting SSA expressions simplify

131

considerably. The final expression for the complete correction term has a form similar to the PO approximation, but again with a modified multiplying angular function. The entire higher-order SSA result then also is similar to the PO approximation, and comparison of the resulting total angular function to that from PO shows the relationship between the two methods. For perfectly conducting surfaces, tests showed the complete SSA angular function to be identical to the PO form within the numerical accuracy of the comparison, confirming that the SSA and PO are identical in this limit. For penetrable surfaces, the functions are identical near the specular region, but distinct in other angular regions. Figure 6.4 illustrates a comparison of the PO, SSA1, and approximated SSA2 "angular functions" versus observation angle for backscattering with surface relative permittivity $4 + i$. Note the approximated SSA2 brings SSA1 closer to PO results for the near-normal region, but differences remain at larger angles. These relationships are difficult to interpret given the uncertainty in forming the PO angular function for penetrable surfaces [63]. Due to these relationships, questions regarding the validity region of the PO approximation can potentially be rephrased as questions regarding the accuracy of a first order Taylor approximation to the function $g_{SSA}^{(c)}$.

6.4 Publications

Project results were published in two conference papers [70]-[71], an M. S. thesis [72], and a journal article [73]. After graduating in 2003, Michael Gilbert accepted a position with the Naval Surface Warfare Center in Dahlgren, VA.

6.5 Conclusions

This effort has developed a useful model for predicting the influence of terrain clutter on ATR systems. The model developed is applicable over a wide range of surface properties, and enables expected properties of terrain clutter to be investigated. Codes for implementing these models are available from the authors. Further information on the results achieved is available in [72]-[73].

7. STAP/SFAP BASED ADAPTIVE ANTENNAS

7.1 Space-Time Adaptive processing (STAP)

In STAP an N-length digital filter or tapped-delay line with adjustable weights is placed behind each antenna element. With L antenna elements and an N taps per element, the STAP-equipped array has $LN - 1$ degrees of freedom available. Theoretically, up to $LN - 1$ independent radio frequency interference (RFI) sources can be nulled providing a significant advantage over a conventional adaptive array which is limited to L-1 spatial degrees of freedom. However, this is only obtained for RFI with 0% bandwidth. Wideband interference is known to limit adaptive array performance and was the original motivation for introducing the weighted tapped delay lines . The effect of wideband RFI on conventional single-tap adaptive array performance has been studied in the past and it has been demonstrated that multiple spatial degrees of freedom (DOF) are consumed by wideband RFI where increasing the RFI power, bandwidth, or both will increase the DOF consumed. Lately, STAP performance in wideband multi-path environments is of high interest. Typically, wideband signals are attributed to the consumption of "N" degrees of freedom in STAP. Under this effort, it was demonstrated that a strong direct-path wideband RFI can consume more than "N" degrees of freedom in a multi-tap STAP wherein "wideband" is defined as a bandwidth equal to the sample rate or inverse tap delay of the STAP processor. Thus, the effect of a strong wideband RFI direct-path source on STAP performance can be similar to that of a dispersive multi-path environment.

A five-element linear array of ideal isotropic elements with constant half-wavelength spacing as shown in Figure 7.1 is used for the example results. The quiescent array pattern is also shown in Figure 1 for reference. The signals received by the array are processed in the time domain by a seven tap STAP with tap delays equal, T_0, to $1/32$ μs. A desired signal with a 20 MHz bandwidth flat power spectral density and input SNR of -20 dB centered at 2004 MHz is incident from broadside ($\theta = 0°$). A single direct-path RFI interference source is incident from $\theta = 30°$.

Consider RFI bandwidths of 0, 10 kHz, 8 MHz, and 32 MHz with fractional bandwidths of $\frac{\Delta f}{f_c}$ = 0%, $\sim$ 0%, 0.4%, and 1.6%. At input INR levels of 10 and 50 dB, the eigenvalue magnitudes (in decreasing order) for a 7 tap STAP are listed for the various bandwidths in Table 7.1. For a CW or 0% bandwidth, the signal is completely correlated between the various taps and elements and only one eigenvalue (first column) is greater than 0 dB. The remaining eigenvalues are due to thermal noise. The principal eigenvalue magnitude for the CW signal is equal to the signal power times the number of taps and elements, i.e.

$$|\lambda_{CW}| = P \times L \times N = 350 \rightarrow 25.44 \text{ dB}, \tag{7.1}$$

where P is the CW signal power. The next largest eigenvalue is over ten orders of magnitude

Antenna Geometry   Quiescent Array Pattern
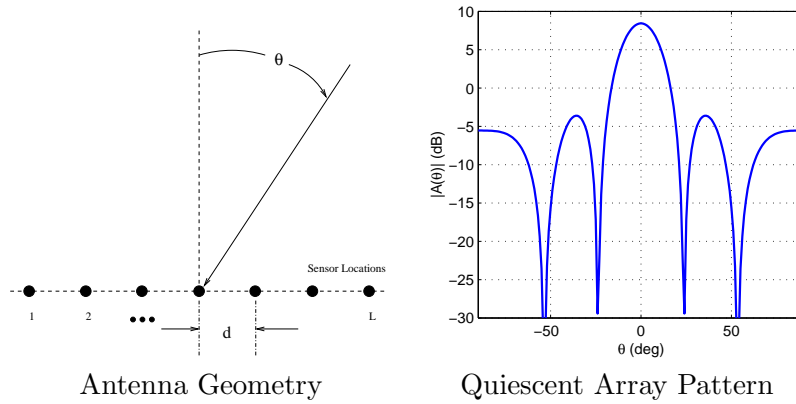
Figure 7.1: Antenna configuration and quiescent antenna pattern at 2004 MHz

Table 7.1: Eigenvalue Magnitudes (dB) for 7 Tap STAP

10 dB INR					50 dB INR			
CW	10k Hz	8 MHz	32MHz		CW	10k Hz	8 MHz	32MHz
25.4	25.4	22.9	17.0		65.4	65.4	62.9	57.0
-110.1	-33.5	21.0	17.0		-70.1	6.5	61.0	57.0
-110.1	-100.1	14.5	17.0		-70.1	-60.6	54.5	57.0
-110.9	-100.1	2.1	17.0		-71.0	-70.2	42.1	57.0
-111.0	-100.6	-14.4	17.0		-71.0	-70.2	25.6	57.0
-111.7	-111.2	-34.5	17.0		-71.7	-71.2	5.5	57.0
-111.7	-111.2	-58.8	17.0		-71.7	-71.2	-18.8	57.0
-112.6	-111.7	-97.5	-20.4		-72.6	-71.7	-57.5	19.6
-112.6	-111.7	-114.1	-27.2		-72.6	-71.7	-74.1	12.8
-113.2	-112.6	-116.5	-37.6		-73.2	-72.6	-76.5	2.4
-113.2	-112.6	-116.5	-50.6		-73.2	-72.6	-76.5	-10.6
-114.1	-113.5	-117.2	-65.8		-74.1	-73.5	-77.2	-25.8
-114.5	-113.5	-117.2	-83.6		-74.1	-73.5	-77.2	-43.5
-114.6	-114.2	-118.2	-104.6		-74.5	-74.2	-78.2	-64.6
⋮	⋮	⋮	⋮		⋮	⋮	⋮	⋮

less. If the input INR is increased to 50 dB, the eigenvalue also increases by 40 dB as shown in Table 7.1.

For the 10 kHz bandwidth, the second eigenvalue is still three orders of magnitude less than 0 dB (noise level eigenvalue) and about seven orders of magnitude larger than the third. A small fraction of the RFI energy is represented by the second eigenvalue-eigenvector pair. When the INR is increases to 50 dB, the second eigenvalue increases to 6.5 dB (right hand table). Once an eigenvalue exceeds the noise level, the adaptive weights react-suppressing the RFI energy of the eigenvalue-eigenvector pair. It is interesting that the small fractional bandwidth RFI can consume a second degree of freedom. Does this bandwidth exceed the

134

Table 7.2: Eigenvalue Magnitudes (dB) for Single Tap STAP

10 dB INR					50 dB INR			
CW	10k Hz	8 MHz	32MHz		CW	10k Hz	8 MHz	32MHz
17.0	17.0	17.0	17.0		57.0	57.0	57.0	57.0
-142.9	-93.0	-34.9	-22.8		-102.9	-53.0	5.1	17.2
-143.7	-142.2	-95.3	-71.2		-104.2	-104.7	-55.3	-31.2
-147.5	-144.9	-144.5	-124.6		-108.2	-106.7	-108.5	-84.6
-152.6	-148.1	-144.8	-144.2		-118.2	-118.3	-111.5	-108.0
⋮	⋮	⋮	⋮		⋮	⋮	⋮	⋮

narrow-band limit? Table 7.2 shows the eigenvalue magnitudes for the spatial covariance matrix (single-tap STAP) at 10 and 50 dB input INR. At the 10 kHz bandwidth, only a single eigenvalue exceeds the noise eigenvalues for both the 10 and 50 dB INR cases thus meeting the narrow-band definition. Multiple eigenvalues are excited in the STAP at 10 dB input INR for the 8 and 32 MHz bandwidths. In the single-tap STAP, multiple eigenvalues are present at the 50 dB INR level only.

We observe that a small finite bandwidth RFI excites multiple eigenvalues in the STAP space-time covariance matrix. In the example, the RFI fractional bandwidths are all less than 1.6%. However, the 1.6% bandwidth occupies 100% of the sampled spectrum. This "wideband" signal excites a full N eigenvalues at low INR levels consuming N degrees of freedom. In the conventional array, at low INR levels, the wideband signal still meets the narrow-band criteria. Increasing the INR to 50 dB consumes additional spatial degrees of freedom in the single tap STAP. Similarly, in the multi-tap STAP increasing the INR level of the "wideband" RFI excites more than "N" eigenvalues. At 50 dB INR, Table 7.1 illustrates that 10 eigenvalues are active for the 32 MHz bandwidth. Thus, a direct-path "wideband" RFI source can consume more than "N" degrees of freedom similar to the dispersive multi-path effects observed by in other studies.

Figure 7.2 shows the eigenvalue distribution and output INR for a CW RFI and RFI bandwidths of 8 MHz, 16 MHz, and 32 MHz for input INR levels between -20 and 80 dB. In Figure 7.2, the CW RFI excites only a single eigenvalue over the complete input INR range whereas the number of eigenvalues excited by the finite bandwidth sources are dependent on both interference bandwidth and power. Note that the wideband RFI excites "N" or 7 eigenvalues at low input INR levels. When the input INR exceeds 60 dB, the wideband source excites more than 10 eigenvalues. The output INR plot illustrates for low levels of input INR the output interference power increases linearly with the input INR. As the first interference eigenvalue magnitude approaches the noise eigenvalue, the adaptive weights react and start to suppress the interference. Increasing the input INR further drives the output INR lower. For the CW case, theoretically, the INR suppression continues indefinitely. In practice, numerical precision limits the suppression. Here, the precision limit for the CW bandwidth is reached when the input INR is 55 dB. This is due to the numerical
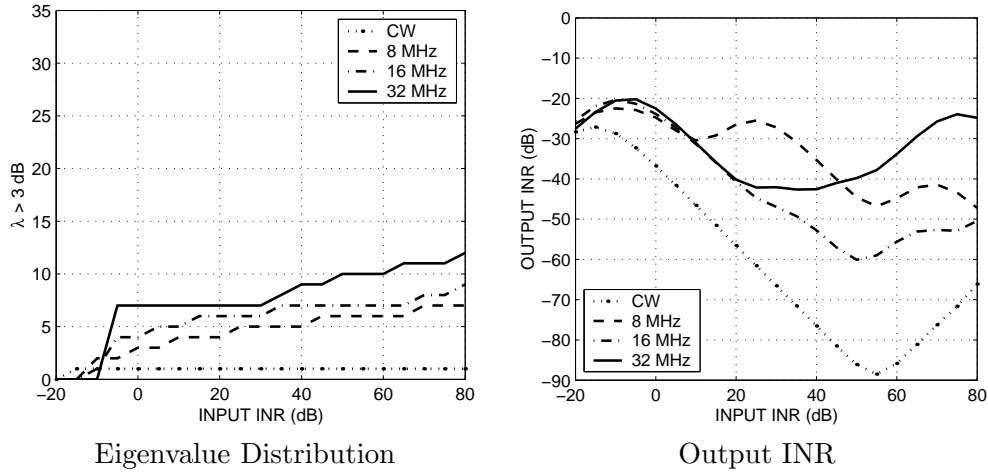
Figure 7.2: Results are shown for RFI bandwidths of CW, 8 MHz, 16 MHz, and 32 MHz

precision of MATLAB on the PC platform. For the finite bandwidth RFI cases, the precision limits of MATLAB are not reached. Additional eigenvalues become active before the principle or first eigenvalue magnitude hits the precision limit. As the additional eigenvalues become active, the STAP weights suppress the associated energy causing the observed oscillation in output INR. This behavior is similar to that observed in single-tap adaptive arrays.

The effects of reference tap selection on the performance of STAP was also studied. It was shown that though the output SINR if not affected the tap used as the reference tap, the center tap should be used as the reference tap for minimum distortion of the desired signal.

7.2 Space-Frequency Adaptive processing (SFAP)

Space-frequency adaptive processing (SFAP) is an alternate approach to STAP where the time domain signals received by various antenna elements are transformed to the frequency domain using the discrete Fourier transform. The constrained minimization is then carried out in the frequency domain to suppress interfering signals. Under ideal conditions the two approaches yield the same performance. In SFAP, however, one can process each frequency bin independently. This leads to sub-optimum performance but can decrease the computation cost significantly in that one has to manipulate only L x L matrices. Also, one can make up for the lost performance by increasing the number of frequency bins. Thus narrowband SFAP is a very attractive approach for interference suppression in digital receivers.

Under this research effort, the performance of a space-frequency adaptive processor receiving a spread spectrum like communications signal in strong RFI environment was studied.

The interfering scenario consisted of wideband as well as narrowband jammers. It was shown that for these type of interference scenarios, one can improve the performance of narrowband SFAP by windowing the time domain samples before transforming the samples to the frequency domain. The reason for the improved performance is that the windowing helps localize narrowband interferers to a few frequency bins, which in turn improves the performance of SFAP. Other researchers have reported the similar observation. However, the SFAP mathematical model used in their study is based on averaging the signal-to-interference-plus-noise ratio and interference-to-noise ratio at the output of various frequency bins. The average output ratios do not account for overlapping of samples in SFAP and do not provide true performance estimate of SFAP. The sample overlapping is very important in SFAP implementation and performance. We developed a better mathematical model for SFAP performance prediction. The mathematical model is based on the previous work of Godara in that the equivalent time domain weights are found. We have extended the model to include the window function. It was shown that the equivalent time domain weights depend on the output sample. The mathematical model was used to study the performance of SFAP. The study clearly indicated the need for sample overlapping in SFAP. It was shown that 20% to 25% sample overlapping is sufficient. This is a lot less than the present practice.

7.2.1 SFAP Mathematical Model

Let the antenna array consist of L elements. The signals received by these antenna elements are down converted to baseband and digitized. A block of N samples from each antenna element are multiplied by a window function, w_i, $i = 1, 2 \ldots N$ and are Fourier transformed to the frequency domain for space-frequency adaptive processing. The frequency domain samples for the mth block are then given by

$$\tilde{x}_l(k, m) = \sum_{n=1}^{N} w_n x_{ln}(m) e^{-j\frac{2\pi}{N}(n-1)(k-1)} , \qquad \begin{array}{l} l = 1, 2, \ldots, L \\ k = 1, 2, \ldots, N \end{array} \qquad (7.2)$$

where $x_{ln}(m)$ are the corresponding time domain samples for the lth antenna element. Note that index k in (7.2) denotes the frequency bin, and index m denotes the block number. Using vector notation, (7.2) can be rewritten as

$$\tilde{x}_l(k, m) = \mathbf{f}^T(k)\mathbf{x}_l(m) = \mathbf{x}_l^T(m)\mathbf{f}(k) \qquad (7.3)$$

where,

$$\mathbf{f}(k) = \begin{pmatrix} w_1 \\ w_2\, e^{-j\frac{2\pi}{N}(k-1)} \\ \vdots \\ w_N\, e^{-j\frac{2\pi}{N}(N-1)(k-1)} \end{pmatrix} \qquad (7.4)$$

and,

$$\mathbf{x}_l(m) = \begin{pmatrix} x_{l1}(m) \\ x_{l2}(m) \\ \vdots \\ x_{lN}(m) \end{pmatrix}.$$ (7.5)

In (7.3) superscript ^{T} denotes transpose. These frequency domain samples are used to estimate the spatial covariance matrix. Let M frequency domain samples be used to estimate the covariance matrix for the kth bin. Then the li^{th} element of the covariance matrix $\tilde{\mathbf{R}}(k)$ is given by

$$(\tilde{R}(k))_{li} = \frac{1}{M} \sum_{m=1}^{M} \tilde{x}_l^*(k,m)\tilde{x}_i(k,m) , \qquad l, i = 1, 2, \ldots, L$$ (7.6)

where superscript * denotes complex conjugate. Substituting (7.3) in (7.6), one obtains

$$\begin{aligned} (\tilde{R}(k))_{li} &= \mathbf{f}^H(k)[\frac{1}{M} \sum_{m=1}^{M} \mathbf{x}_l^*(m)\mathbf{x}_i^T(m)]\mathbf{f}(k) \\ &= \mathbf{f}^H(k)\mathbf{R}(l,i)\mathbf{f}(k) \end{aligned}$$ (7.7)

where $\mathbf{R}(l,i)$ is the N x N time domain covariance matrix between antenna elements l and i. Thus knowing the time domain covariance matrix, one can directly calculate the elements of the frequency domain covariance matrix for various frequency bins. Let the adaptive weights be selected to minimize the output power under a single constraint. Then the steady state weights for the kth frequency bin are then given by

$$\tilde{\mathbf{h}}(k) = \frac{\tilde{\mathbf{R}}^{-1}(k)\tilde{\mathbf{u}}_s(k)}{\tilde{\mathbf{u}}_s^H(k)\tilde{\mathbf{R}}^{-1}(k)\tilde{\mathbf{u}}_s(k)} , \qquad k = 1, 2, \ldots, N$$ (7.8)

where $\tilde{\mathbf{u}}_s(k)$ is the constraint vector for the kth bin and ^{H} is the Hermitian or conjugate transpose operator. In this study, $\tilde{\mathbf{u}}_s(k)$ is selected to be $[0, 0, 01000]^T$, i.e. the bin output is minimized subject to the constraint that the weight for one of the antenna elements is kept at unity. Note that with this choice of the constraint vector, one does not need to know the angle of arrival of the desired signal. However, it does not guarntee a fixed response in the desired signal direction. For strong desired signal (signal level is significantly higher than the thermal noise) the adaptive antenna weights may be selected to suppress the desired signal. In the case of weak desired signal, this constraint vector is a good choice since the presence of desired signal does not affect the adaptive antenna weights. Nevertheless, (7.8) can be used for any choice of the constraint vector.

138

Using (7.8), the output of the kth bin for the mth block is given by

$$\tilde{y}(k,m) = \sum_{l=1}^{L} \tilde{h}_l(k)\, \tilde{x}_l(k,m) \; , \qquad\qquad k = 1, 2,\, \ldots,\, N \; . \qquad (7.9)$$

The output of various bins are Fourier transformed to obtain the time domain output. The ith time domain output for the mth data block is then given by

$$y(i,m) = \frac{1}{w_i N} \sum_{k=1}^{N} \tilde{y}(k,m)\, e^{j\frac{2\pi}{N}(i-1)(k-1)} \; , \qquad\qquad i = 1, 2 \ldots N \; . \qquad (7.10)$$

Note that window compensation $(1/w_i)$ has been applied to the time domain output. This window compensation is required to maintain the desired signal level at the array output. Otherwise, the desired signal level can vary significantly from one sample to the next. Using (7.2) and (7.9) in (7.10), one obtains

$$y(i,m) = \frac{1}{w_i} \sum_{l=1}^{L} \sum_{n=1}^{N} w_n x_{ln}(m) \frac{1}{N} \sum_{k=1}^{N} \tilde{\tilde{h}}(i,k) e^{-j\frac{2\pi}{N}(n-1)(k-1)} \; , \qquad (7.11)$$

where,

$$\tilde{\tilde{h}}_l(i,k) = \tilde{h}_l(k) e^{j\frac{2\pi}{N}(i-1)(k-1)} \; . \qquad (7.12)$$

One can rewrite (7.11) as

$$y(i,m) = \sum_{l=1}^{L} \sum_{n=1}^{N} x_{ln}(m) h_{ln}(i) \qquad (7.13)$$

where,

$$h_{ln}(i) = \frac{w_n}{w_i N} \sum_{k=1}^{N} \tilde{\tilde{h}}_l(i,k) e^{-j\frac{2\pi}{N}(n-1)(k-1)} \; . \qquad (7.14)$$

Note that (7.13) also represents an equivalent time domain system where $h_{ln}(i)$ are the equivalent time domain weights and m is the output sample number such that $m \geq N$. The equivalent time domain system can be represented as

$$y(i,m) \;\; = \;\; \sum_{l=1}^{L} \sum_{n=1}^{N} x_l(m - (n-1)) h_{ln}(i) \; . \qquad (7.15)$$

One can use (7.15) to evaluate the SFAP performance. In theory, one should be able to use any time domain sample from a given block to study the SFAP performance. However,

139

since the equivalent time domain weights depend on the sample selected, the performance varies from one sample to the next. As will be shown later, the performance is the worst when the equivalent time domain weights are selected based on the first few or the last few time domain samples and then improves quickly as one moves away from the end samples. In practice, overlapping of the time domain samples is carried out to avoid the degradation in these end samples. As a rule of thumb 50% overlapping is carried out; i.e. out of N samples from a block, only N/2 samples are used and the rest are recovered by overlapping. This overlapping increases the SFAP implementation cost. We have shown that one does not need to carry out 50% overlapping. Instead 20-25% overlapping may be sufficient.

Next, assuming that the incident signals on the antenna array can be modeled as wide sense stationary processes, the mean power at the array output is given by

$$
\begin{aligned}
P_s(i) &= \frac{1}{2} E\{y^2(i,m)\} \\
&= \frac{1}{2} \mathbf{h}^H(i)\, \mathbf{R}\, \mathbf{h}(i) \; ,
\end{aligned} \tag{7.16}
$$

where $\mathbf{R}$ is LN x LN array covariance matrix in the time domain and $\mathbf{h}(i)$ is the equivalent time domain weight vector. Note that index i is used to indicate the sample dependency of the weight vector. Assuming that the various signals incident on the antenna array are uncorrelated with each other and with the thermal noise, (7.16) can be used to estimate the mean output power for individual signals. Next, one can calculate the expected signal-to-interference plus noise ratio (SINR) and interference-to-noise ratio (INR) at the array output. In the following result, these metrics along with the desired signal level are used to evaluate the performance of SFAP. Note that these metrics are directly related to the performance of a digital spread spectrum receiver.

7.2.2 Sample Results

A linear uniform antenna array consisting of seven elements is used in the study. All elements are assumed to be isotropic antennas with no coupling. One of the antenna elements (center element) is located at the coordinate origin. The interelement spacing is selected to be $\frac{\lambda}{2}$ (0.075 m). In this study, the constraint vector is selected to keep the center element weight fixed at unity. These antenna elements receive RF signals centered at 2.004 GHz. The signals are down-converted to baseband and sampled at a rate of 32×10^6 samples/second (complex sampling).

In a typical spread spectrum system, the desired signal angle of arrival can vary. In this study, the angle of arrival of the desired signal is varied between $-90°$ to $90°$. The desired signal has a spectrum similar to that of a rectangular pulse with a bandwidth of 20 MHz and pulse-width (chip width) of $\frac{1}{10}\mu s$. In the "spread" representation, the pulse represents

Table 7.3: The Interference scenario

Jammer #	Frequency (MHz)	Bandwidth (MHz)	θ (degrees)
1	2000.4	24	65
2	2000.4	24	-75
3	2000.4	24	80
4	2002.4	0.0	-45
5	1994.3	0.0	-25
6	1990.1	0.0	-15
7	2010.3	0.0	0
8	2004.3	0.0	10
9	1995.1	0.0	20
10	2007.3	0.0	30
11	1998.4	0.0	-40
12	2003.4	0.0	45
13	2008.4	0.0	50

a modulating chip sequence operating at a sub-carrier rate of 10 MHz. The desired signal is uncorrelated with the thermal noise in each channel. The thermal noise in various channels is also assumed to be uncorrelated with each other. The thermal noise is assumed to have flat power spectral density over the sampling bandwidth of 32 MHz. The signal to noise (SNR) of the desired signal at each antenna element is assumed to be -20 dB. Note that this SNR is before the correlator.

In addition to the desired signals, some interference is also incident on the antenna array. Three of the interfering signals are wideband signals (24 MHz bandwidth); whereas the other interfering signals are narrowband signals. The interference to noise ratio (INR) of each interfering signal at each antenna element is assumed to be 40 dB. Thus, each interfering signal is 60 dB above the desired signal level. Table 7.3 shows the angular locations, center frequency and bandwidth of various interfering signals. Note that the first three interfering signals are wideband signals. The wideband interfering signals also have flat power spectral density.

The signals received by the 7-element antenna array were processed in the frequency domain using a 128-bin SFAP. Three different window functions; namely, uniform (rectangular), Hamming and Blackman were used to weight the time domain samples before transforming them to the frequency domain.

Figure 7.3 shows the desired signal power level and SINR at the adaptive array output[1] when the interference scenario consists of three wideband RFI sources. The angle of arrival of the desired signal is 0° (broadside to the array). Performance for three window functions,

---

[1]For digital spread spectrum receivers, which are based on correlation, both quantities are important. One needs good SINR and the signal level should be maintained.
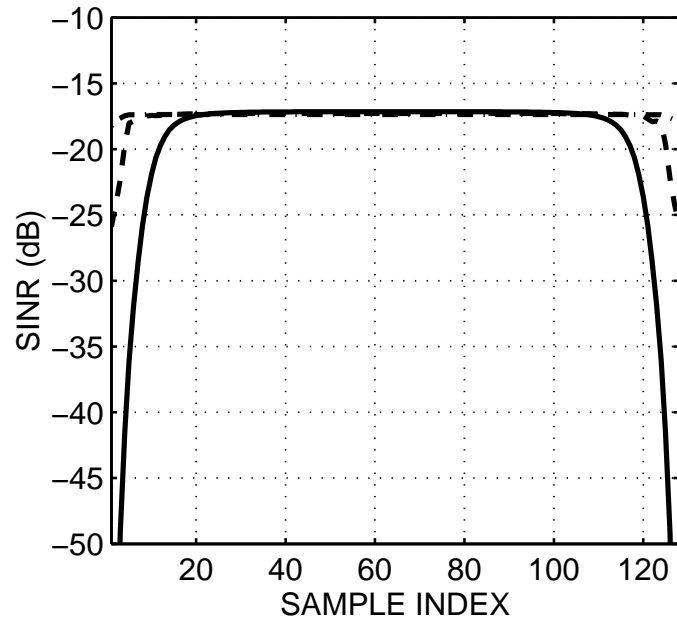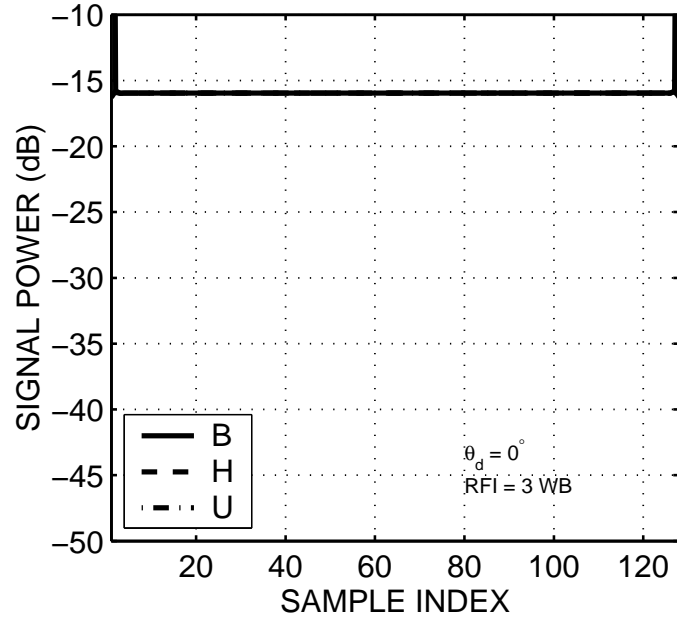
Figure 7.3: Output signal power and output SINR for 128 bin SFAP versus sample number (index) in the presence of three wideband interfering signals. The desired signal is incident from broadside direction.

namely uniform, Hamming and Blackman windows, is shown. The performance with respect to sample index is plotted. Remember that the equivalent time domain weights depend on the sample number of the 128-sample block. Ideally, the performance should be independent of the sample number. However, due to all the processing being performed on the data samples, one can see that the beginning and the end samples have lower SINR. For the uniform window function the degradation is minimal; whereas, for the Blackman window there is significant degradation. However, for 80% or more of the samples the performance is similar. Thus, one does not need 50% overlapping to obtain the optimum performance. Overlapping of 20% to 25% should be sufficient.

In the above example, the uniform window function performed better than the Hamming window as well as the Blackman window. This is because all the incident RFI sources were wideband in nature. Figure 7.4 shows the performance of the adaptive system when the interference scenario consists of the three wideband plus the first four CW RFI sources in Table 7.3. All other parameters are the same as before. Again, one can draw the same conclusions as before; i.e. the performance for the middle 80% of the samples is very similar. Thus, one does not need to carry out 50% overlapping. Instead 20 % to 25 % overlapping should be sufficient. Another observation to be made from these plots is that the Blackman window is performing (output signal and SINR level) much better than the other two window functions. Thus we observe that in the presence of wideband plus narrowband signals, the Blackman window function is a better choice. We will demonstrate this further under many interference scenarios. For Blackman window, the output signal power at the beginning and end of the block is very high; whereas the output SINR is quite low. As mentioned earlier, for good performance the output signal level should not change with sample index and the output SINR should be high. Thus, these samples should be recovered by sample overlapping. In the remaining examples, the performance is calculated using the equivalent time domain weights corresponding to the middle sample ($i = \frac{N}{2}$ in (7.16)). Remember, by using 20% to 25% overlapping of the samples, one can achieve the same performance for all samples.

Figure 7.5 shows the output INR of the adaptive array versus the number of CW interference sources. In addition to the CW sources, three wideband interference sources are also incident on the antenna array. The performance for the three window functions (uniform, Hamming and Blackman) is shown. Remember the input INR for each RFI source is 40 dB. Note that in the absence of CW interference (only wideband RFI is present), the output INR is very low. The output INR increases with the addition of CW interference. In the case of uniform window function the output INR increases very rapidly once the number of CW interference exceeds two. In the presence of six or more CW interfering signals, the output INR is 10 dB or higher, which may not be desirable. For Blackman window function, the output INR is less than -20 dB even in the presence of ten CW interfering signals. Thus, using the Blackman window function, one can achieve better interference suppression. For the Hamming window function, the interference suppression is somewhere in between the uniform window function and the Blackman window function.
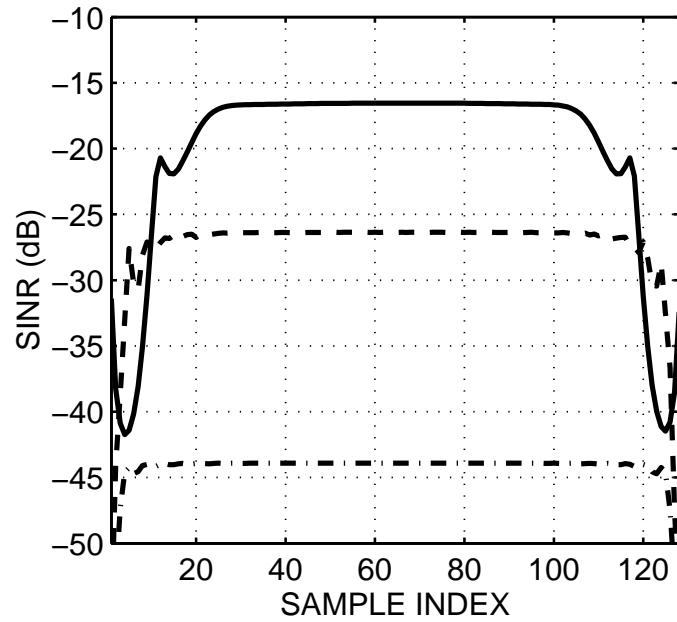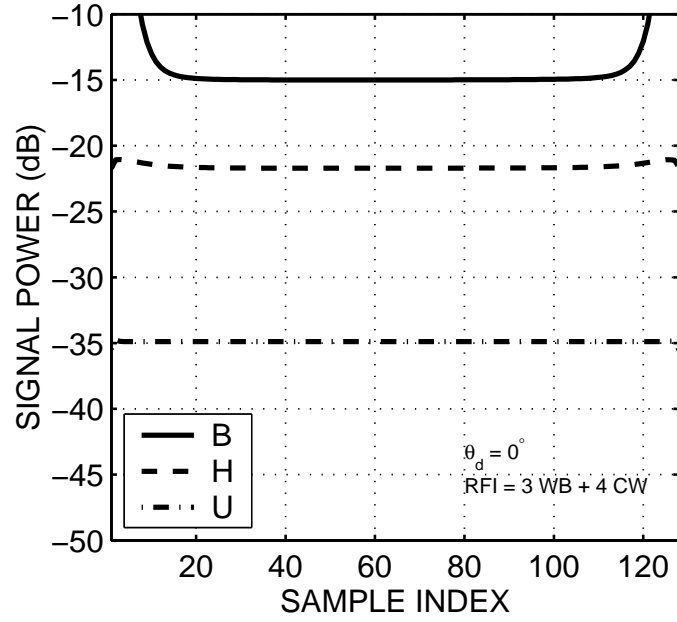
Figure 7.4: Output signal power and output SINR for 128 bin SFAP versus sample number (index) in the presence of three wideband plus four CW interfering signals. The desired signal is incident from broadside direction.

144
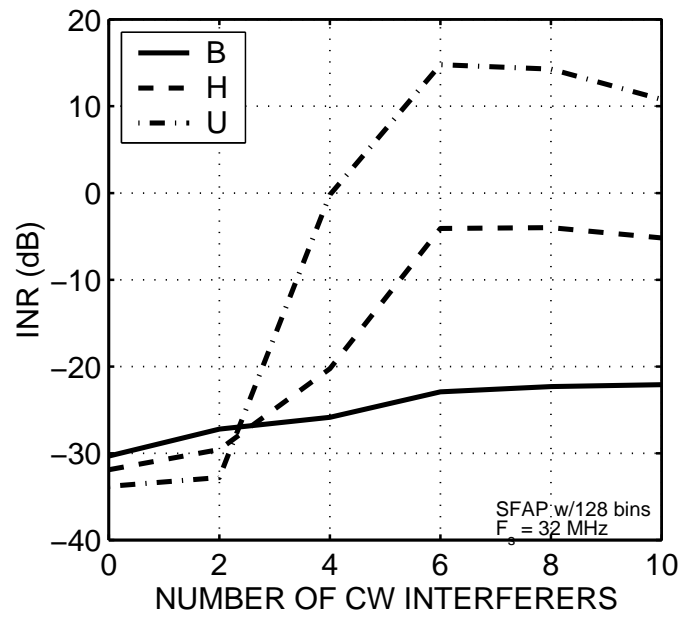
Figure 7.5: Output INR of 128-bin SFAP versus number of CW interfering signals. Three wideband interfering signals are also incident on the adaptive antenna.
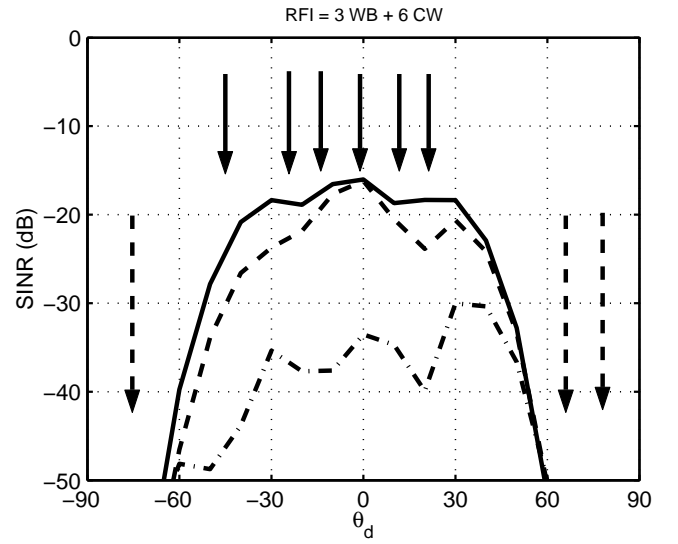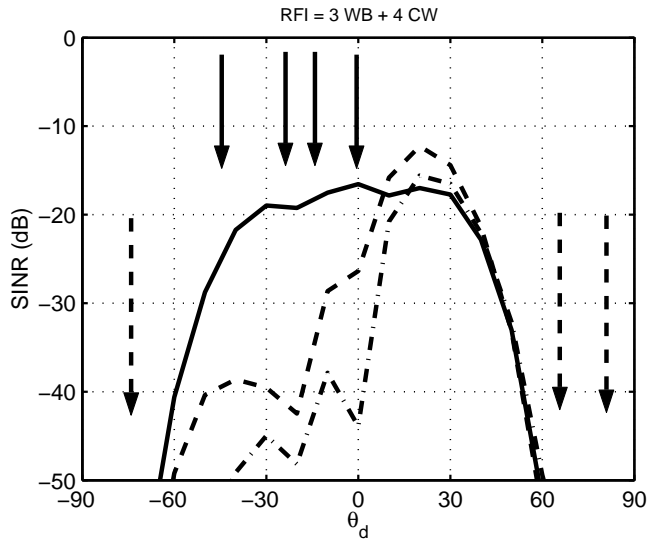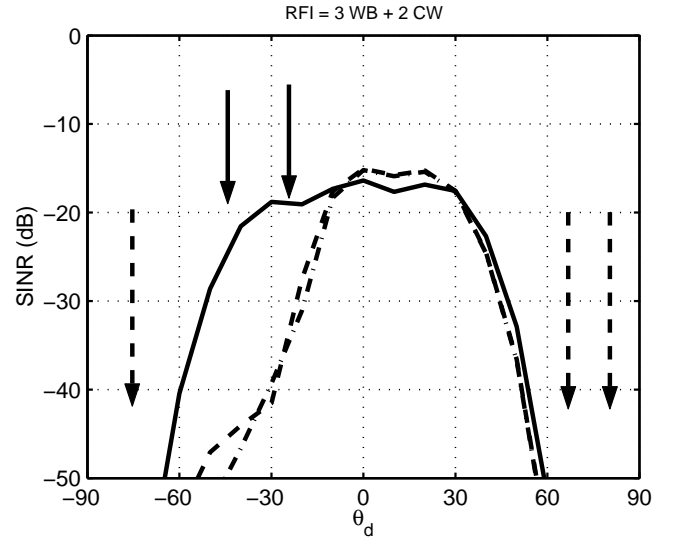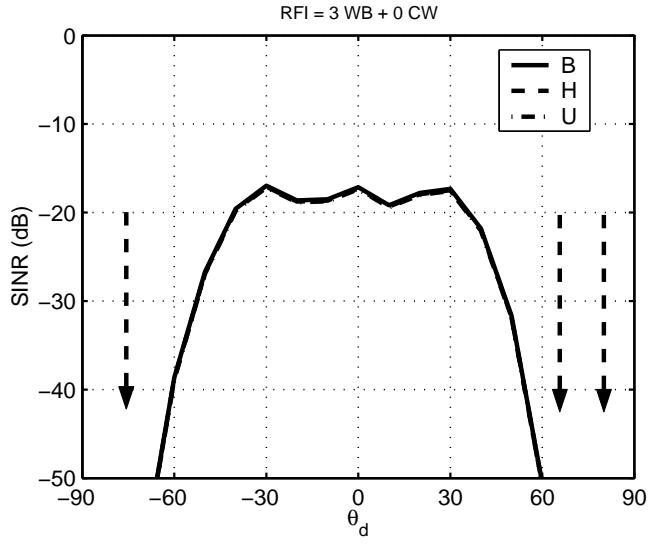
Figure 7.6: Output SINR of 128-bin SFAP versus the angle of arrival of the desired signal (θ_d). Wideband interfering signals (broken arrows), CW interfering signal (solid arrows).

146

For a communication system to operate properly, one needs to suppress the interfering signal while receiving the desired signal without significant degradation in the signal-to-noise ratio (SNR). To that end, Figure 7.6 shows the output SINR of the adapted antenna versus the angle of arrival of the desired signal. Again, the output SINR for the three window functions is shown when the interference scenario consists of three wideband sources only, three wideband plus two CW sources, three wideband plus four CW sources, and three wideband plus six CW sources, respectively. In this figure, the location of wideband sources are marked by broken arrows; whereas, the location of CW sources are marked by the solid arrows. Note that in the presence of wideband interfering signals only, the three window functions, as expected, have similar performance. In the case of uniform window function, the presence of CW interfering signals degrades the adaptive array performance. For the Blackman window function, the performance is almost unaffected by the presence of CW interfering signals. The Hamming window function performs better than the uniform window function, but not as well as the Blackman window function, and the reason for this is the sidelobe level associated with the two window functions. The sidelobe levels of a Hamming window function are not as low as those of the Blackman window function. Therefore, for narrowband jammers, a significant amount of energy leaks into the other frequency bins. Nevertheless, windowing (other than uniform) the time domain samples helps in improving the performance of SFAP in the interfering scenario consisting of wideband as well as narrowband jammers, and the Blackman window function seems to be a good choice.

7.3 Multipath Effects

The platform generated jammer multipath can limit the performance of adaptive antennas. We carried out a study to characterize the effects of jammer multipath on GPS AJ systems. Initially, we used an antenna array of seven half wavelength dipoles in our study. Six of the dipoles were uniformly distributed along a circle of 3.75 inch radius; whereas the seventh element was inside the circle. The middle element was displaced approximately an inch from the center of the circle. A moment method solution was used to calculate the in situ radiation patterns of individual elements in the presence as well as in the absence of a 20 inch square flat plate over 1555 MHz to 1595 MHz in 2 MHz steps. The flat plate was placed 40 inches away from the center of the array.

Two configurations with the flat plate were analyzed. In the first configuration, the antenna array faces an edge of the plate; whereas in the second configuration, the antenna array is in the boresight direction of the plate. Note that for the second configuration the flat plate will cause strong multipath. These calculated radiation patterns were Fourier transformed to obtain the in situ impulse response of various antenna elements along the incident signal directions. These antenna responses were next used to study the performance of a space-only and a 5-tap STAP based AJ system in the presence of a single strong (interference to noise ratio approximately 60 dB) wideband jammer of 22 MHz bandwidth, when the incident signals are sampled at the rate of 32 Mega samples per second. It was found that in the

absence of the flat plate, space-only as well as STAP steered a single deep null in the incident jammer direction. A certain number of degrees of freedom were consumed in nulling the jammer. In the presence of the flat plate, the adaptive antennas had a tendency of placing multiple nulls (one along the jammer direction and the other along the plate reflected signal direction). This was especially true for broadside plate. The number of degrees of freedom consumed in nulling the jammer increased. The presence of the jammer multipath affected space-only processing more than 5-tap STAP. These results areas expected, and helped us in verifying our computer simulations. Adaptive antennas mounted on more complex platforms (an aircraft) were considered next.

For complex platforms, we used an antenna array of seven circularly polarized patches in our study. The antenna array was mounted on an F-16 aircraft. A computer code named NEWAIR was used to calculate the volumetric patterns of various antenna elements in the L1 frequency band in 2 MHz step size. The computer code was developed at OSU-ESL in the early eighties and has been used extensively to analyze antennas mounted on various aircrafts. The computer code uses Uniform Theory of Diffraction (UTD) to calculate the radiation pattern of individual elements. In this computer code, mutual coupling between various elements is not included directly in the pattern calculation. Therefore, the mutual coupling between antenna elements was ignored. Each element of the antenna array was modeled by two pairs of magnetic dipoles. The two pairs are orthogonal to each other, and were fed with a 90 degree phase difference to generate circular polarization. The spacing between the elements of a pair was selected to be approximately half a wavelength at 1575 MHz.

We used these volumetric patterns of the 7 antenna elements to study the performance of a space-only, a 5-tap STAP and a 128-bin SFAP based adaptive antenna in the presence of multiple strong wide band jammers. Jamming scenarios consisting of up to five wide band jammers were considered. The elevation angle of the incident jammers was kept between $-30°$ to $+20°$ from the horizon. Each jammer had a bandwidth of 22 MHz. For each jamming scenarios, twenty five independent trials were performed. The finite impulse response of various antenna elements in the incident signal direction was convolved with the incident signals to simulate signals received by various antenna elements. It was found that the 5-tap STAP and the 128-bin SFAP performed better than space-only processing. 128-bin SFAP performed as well as or better than 5-tap STAP. The results of this study have been included in a technical report entitled, "Effects of platform generated multipath on GPS AJ systems." The report has limited distribution and can be obtained by contacting, Dr. Inder Gupta, who was PI for this effort. For reference it is Ohio State University ElectroScience Laboratory Technical Report 741718-2, June 2003.

7.4   Graduate Students

The research effort described above was carried out by two gradate students, Dr. Thomas D. Moore and Mr. Matthew L. Rankin who worked under the supervision of Dr. Inder

Gupta. Dr. Moore received his Ph.D. from the Ohio State University in December 2002, and Mr. Rankin received his M.Sc. in Electrical and Computer Engineering from the Ohio State university in June 2004.

8.   MINIATURE UWB ANTENNA

8.1   Introduction

Many target recognition applications require ultrawide bandwidth signals for extracting various target signatures associated with different geometry and material features of the target. In this study a small low profile and UWB antennas that operates from 50 MHz to 2000 MHz is investigated. Using conventional designs to cover such a vast frequency range with a single antenna would require an aperture size and profile which are too large for practical applications. Antenna miniaturization techniques such as dielectric [79, 80] or reactive loading [81, 82] are commonly used to increase the antenna's electrical size without increasing its physical size. However, each of these miniaturization techniques by itself faces important performance trade-offs for large miniaturization factors. In this chapter, a hybrid approach that involves both dielectric and reactive loading is used to maximize the miniaturization factor while minimizing any adverse effects. Our approach to miniaturizing an UWB antenna involves the use dielectric material on both sides of the antenna (substrate and superstrate) to maximize the miniaturization factor for a given dielectric constant [83]. In addition, the thickness of the dielectric material is tapered to suppress dielectric resonance oscillation (DRO) modes and surface waves as well as to maintain high-frequency performance [80, 83]. To maximize the miniaturization factor while minimizing the negative effects of dielectric loading, reactive loading or the artificial transmission line (ATL) concept [81] is also used. This allows us to minimize the dielectric constant which results in less impedance reduction, a minimal antenna weight and reduces possible surface wave effects. The following sections will discuss some of the issues associated with dielectric loading, the implementation of reactive loading for the spiral antenna and the miniaturization limit for the spiral antenna.

8.2   Spiral Antenna Miniaturization via Material

Dielectric material loading for the purpose of spiral miniaturization has its limits [83]. Specifically, while the low frequency gain is usually improved by dielectric material loading [80, 83], high frequency gain tends to decrease if high contrast material is used. To demonstrate this, we chose to simulate a four-arm spiral antenna that is 2" wide and 0.5" high above an infinite ground plane, with dielectric material the same size of the antenna sandwiched between. Specifically, we extract the broadside circular-polarized gain at two different frequencies and plot them as a function of dielectric constant (Figure 8.1). As can be seen, there exists an optimum value of dielectric constant of the loading material, above which high frequency gain starts to decrease.
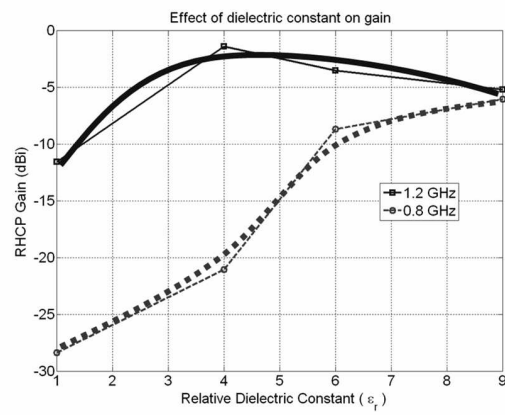
Figure 8.1: Effect of loading material's dielectric constant on spiral antenna gain.

Spiral Antenna Miniaturization Limit

The observation made above illustrates the difficulties associated with aggressive miniaturization. Besides the lowering of the high frequency gain, we also observe diminishing return in terms of increasing the low frequency gain as more aggressive miniaturization is applied. These difficulties can be explained by a model describing the spiral antenna operation. In terms of wave propagation, the spiral is modeled as a transmission line structure that is wrapped in a spiral shape. In terms of radiation, we chose to model the spiral antenna as a continuous set of concentric loops of different sizes. Each loop is associated with a radiation resistance that can be easily calculated from the geometry and is modeled as transmission line loss. This lossy-transmission line model for spiral antenna can accurately predict the antenna impedance over the entire frequency range [81]. Based on this model, we examine the effect of miniaturizing a spiral antenna by enforcing a slow-current condition on each loop separately and then re-calculate each loop's radiation resistance. The impact of miniaturization can be observed in both impedance and radiation pattern, as shown in Figure 8.2. It is observed while miniaturization can successfully shift the resonance toward lower frequency; the overall level of radiation resistance is lowered as well. It is further noticed that the slow-wave current rings have a lower directivity at resonance. Specifically, issues induced by aggressive miniaturization include impedance issue as well as pattern issue, and should be dealt with carefully. By applying Chu-Harrington's small antenna limit from a more global perspective, we also identify the limit of broadband spiral miniaturization to be approximately 65%, if no broadband complex matching is applied.

Embedded Inductive Loading

Based on the transmission line model for spiral antenna mentioned above, we proceed to miniaturize the spiral antenna by means of reactive loading as demonstrated in [81]. That is, we reduce the phase velocity of the guided wave by enhancing the inherent inductance and capacitance of the spiral antenna structure. This allows for additional wave slow down with negligible increase in the weight. In [81], this was accomplished by using lumped surface mount inductors placed in series with the spiral arm and lumped surface mount capacitors placed in parallel with the adjacent spiral arm (see Figure 8.3). This approach works well as long as the number of lumped elements remains small so that the losses associated with soldering and the elements inherent resistance is minimal. Since our miniature antenna uses dielectric loading in conjunction with reactive loading there is no need for any lumped capacitors which reduces the number of elements considerably. Nevertheless, it was found that for aggressive loading the use of lumped elements leads to an excessive amount of ohmic loss. Therefore, implementing reactive or inductive loading using lumped elements is not practical and alternative implementations must be used.

Another common way to achieve inductive loading is through meandering of the spiral arm [82]. However, the meandering approach does not result in a purely inductive loading.
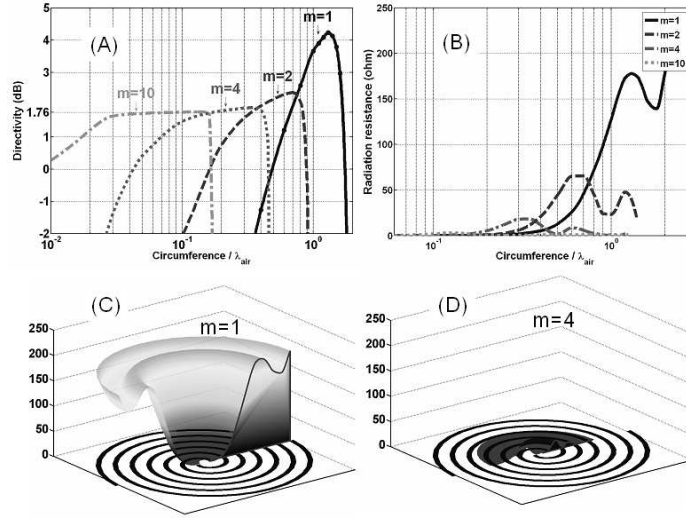
Figure 8.2: Effect of miniaturization on the spiral antenna. m is the miniaturization factor defined as $\lambda_{air}/\lambda_{current}$. (A) Broadside directivity of a current ring. (B) Radiation resistance of a current ring as a function of frequency and miniaturization. (C) Radiation resistance profile of a spiral when m=1 and circumference is 2 λ_{air}. (D) Radiation resistance profile of a spiral when m=4 and circumference is 2 λ_{air}. Although in this case resonance ring is formed closer to the spiral center, meaning resonance is easier to achieve, its radiation resistance level is low.
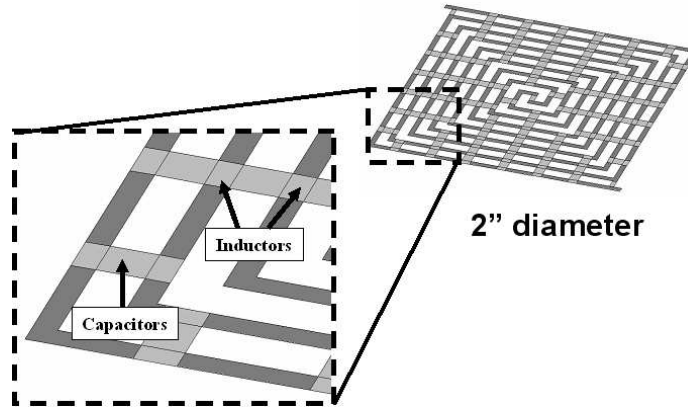

Figure 8.3: Illustration for a reactive loaded spiral using lumped L and C elements.

A better way to achieve inductive loading is by coiling the spiral arm such that the arm resembles a solenoid. This is accomplished by using standard PCB fabrication to create a coil by alternating a series of traces on the top and bottom layers of a board as illustrated in Figure 8.4. The traces are then connected using vias to form square loops. The amount of inductive loading is then primarily a function of the number of turns (pitch) and the loop area (arm width x board thickness) which can be varied to achieve the desired miniaturization. Figure 8.4 shows an example of this type of loading for a 6" diameter square spiral. For this design the pitch is 60 mil, the trace width is 30 mil and the via diameter is 20 mil. The board is FR4 with a measured $\epsilon_r = 4$, $tan\delta = 0.015$ and a thickness of 92 mil. This antenna also features multiple growth rates and a center section that does not have the inductive treatment. Both of these features help to provide a transition from the untreated section to the heavily inductive section. Figure 4 shows a comparison of the measured gain for the untreated and treated 6" spirals with the untreated spiral shown in the inset. The spiral with the inductive treatment was able to achieve a gain of -15 dBic at 146 MHz compared to only 266 MHz for the untreated spiral. This is a considerable improvement and was achieved with minimal increase in weight and profile. It is remarked that for future work the transition needs to be made more gradual to reduce reflections from the transition region. Doing so will improve the gain within 250MHz to 500MHz.
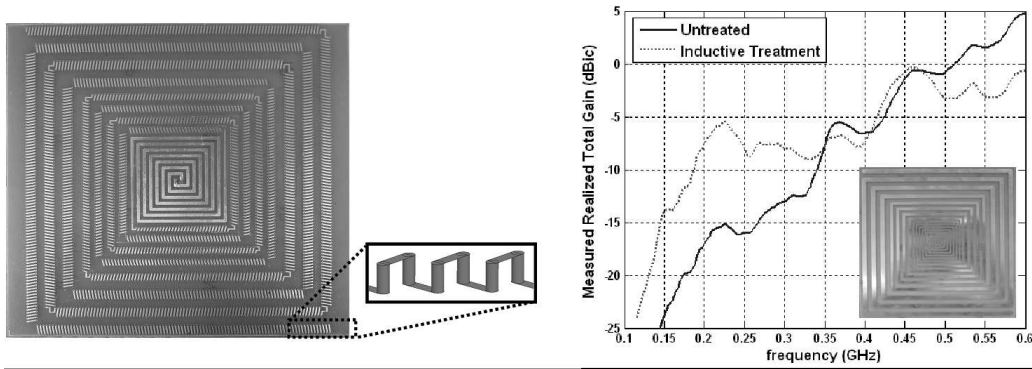

Figure 8.4: Left: Inductive treatment for a 6" square spiral (top layer of the board) with 3D illustration of a section of the coiled arm. Right: measured realized total gain for a square spiral in free space with inductive treatment.

Initial Results for the Integration of Dielectric and Inductive Loading

The real challenge in realizing a miniature antenna using both dielectric and reactive loading is the integration into a single antenna. The antenna in Figure 8.5 consists of a square spiral shown in Figure 4 sandwiched between two tapered dielectric pieces. Both the superstrate and substrate have $\epsilon_r = 9$ and are 0.625" and 0.75" thick respectively. The measured realized gain of the antenna is shown in Figure 8.5 and is -15 dBic at 142 MHz. This

means that the untreated cavity-backed spiral would need to be 2.35 times larger to achieve the same gain at this frequency. However, the dielectric is rather ineffective for further miniaturization. This is most likely a result of the coiled spiral arms not being embedded in the $\epsilon_r = 9$ dielectric material. Since the inductive treatment confines more of the field within the FR4 material, it is important to embed the spiral arms within the $\epsilon_r = 9$ dielectric material to maximize its affect. Improvements based on this embedding will be discussed at the conference. Additionally, we will address the possibility of overcoming the 65% or factor of 2.85 miniaturization limit.
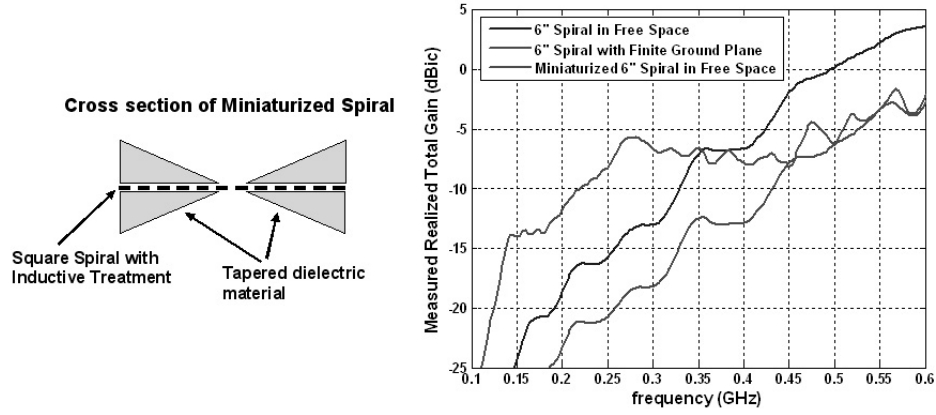

Figure 8.5: Initial results for the integrated 6-inch miniature spiral antenna.

9. REFERENCES

[1] E. K. P. Chong and S. H. Zak. *An Introduction to Optimization.* John Wiley and Sons, Inc., 1996.

[2] D. C. Munson, Jr., J. D. O'Brien and W. K. Jenkins. A Tomographic Formulation of Spotlight-Mode Synthetic Aperture Radar. *Proc. IEEE*, 71:917–925, August 1983.

[3] E. F. Knott, J. F. Shaeffer and M. T. Tuley. *Radar Cross Section.* Artech House, Boston, 1993.

[4] E. R. Keydel, S. W. Lee and J. T. Moore. MSTAR extended operating conditions: a tutorial. In *Algorithms for Synthetic Aperture Radar Imagery III*, pages 228–242. Proc. SPIE 2757, 1996.

[5] A. E. Fuhs. *Radar Cross Section Lectures.* American Institute of Aeronautics and Astronautics, New York, 1982.

[6] M. J. Gerry. *Two-Dimensional Inverse Scattering Based on the GTD Model.* PhD thesis, The Ohio State University, 1997.

[7] A. Grace. *Optimization Toolbox: For Use with Matlab.* The Mathworks, Inc, Natick, Mass., 1993.

[8] J. B. Keller. Geometrical theory of diffraction. *J. Opt. Soc. Am.*, 52(9):116–130, 1962.

[9] E. F. Knott. *Radar Cross Section Measurements.* Van Nostrand Reinhold, New York, 1993.

[10] M. A. Koets. Automated Algorithms for Extraction of Physically Relevant Features from Synthetic Aperture Radar Imagery. Master's thesis, The Ohio State University, 1998.

[11] D. L. Mensa. *High Resolution Radar Imaging.* Artech House, Inc., 1981.

[12] MSTAR (Public) Targets: T-72, BMP-2, BTR-70, SLICY. Available at http://www.mbvlab.wpafb.af.mil/public/MBVDATA.

[13] A. V. Oppenheim and R. W. Schafer. *Discrete-time Signal Processing.* Prentice Hall, Englewoods Cliffs, NJ, 1989.

[14] H. V. Poor. *An Introduction to Signal Detection and Estimation.* Springer-Velag, 2nd edition, 1994.

[15] B. Porat. *Digital Processing of Random Signals: Theory and Methods.* Prentice Hall, Englewood Cliffs, NJ, 1994.

[16] B. Rigling. Physics, Fisher, and Phase: Information Content in SAR Images. Master's thesis, The Ohio State University, 2000.

[17] M. I. Skolnik. *Radar Handbook*. McGraw-Hill, New York, 1990.

[18] J. Stach and E. LeBaron. Enhanced Image Editing by Peak Region Segmentation. In *Proceedings of 1996 AMTA Symposium*, October 1996.

[19] H. Stark and J. W. Woods. *Probability, Random Processes, and Estimation Theory for Engineers*. Prentice Hall, Englewoods Cliffs, NJ, 1994.

[20] P. Stoica and R. L. Moses. *Introduction to Spectral Analysis*. Prentice Hall, Upper Saddle River, NJ, 1997.

[21] G. Strang. *Linear Algebra and Its Applications*. Harcourt Brace Jovanovich, Inc., 3 edition, 1988.

[22] F. T. Ulaby. *Handbook of Radar Scattering Characteristics for Terrain*. Artech House, Norwood, MA, 1989.

[23] J. C. Curlander and R. N. McDonough, *Synthetic aperture radar: systems and signal processing*. New York: Wiley, 1991.

[24] E. R. Keydel, S. W. Lee, and J. T. Moore, "MSTAR extended operating conditions: a tutorial," in *Algorithms for Synthetic Aperture Radar Imagery III* (E. Zelnio and R. Douglass, ed.), pp. 228–242, Proc. SPIE 2757, 1996.

[25] T. W. Ryan and B. Egaas, "SAR target indexing with hierarchical distance transform," in *Algorithms for Synthetic Aperture Radar Imagery III* (E. Zelnio and R. Douglass, ed.), pp. 243–252, Proc. SPIE 2757, 1996.

[26] D. F. DeLong and G. R. Benitz, "Extensions of High Definition Imaging." in *Algorithms for Synthetic Aperture Radar Imagery II* (D. A. Giglio, ed.), pp. 165–180, Proc. SPIE 2487, 1995.

[27] J. Li and P. Stoica, "An adaptive filtering approach to spectral estimation and SAR imaging," *IEEE Trans. Signal Processing,* vol. 44, pp. 1469–1484, June 1996.

[28] J. Wissinger, R. Washburn, D. Morgan, C. Chong, N. Friedland, A. Nowicki, and R. Fung, "Search Algorithms For Model-Based SAR ATR," in *Algorithms for Synthetic Aperture Radar Imagery III* (E. Zelnio and R. Douglass, ed.), pp. 279–293, Proc. SPIE 2757, 1996.

[29] E. R. Keydel and S. W. Lee, "Signature Prediction For Model-Based Automatic Target Recognition," in *Algorithms for Synthetic Aperture Radar Imagery III* (E. Zelnio and R. Douglass, ed.), pp. 306–317, Proc. SPIE 2757, 1996.

[30] R. A. Fisher, "On the mathematical foundations of theoretical statistics," *Phil. Trans. Royal Soc. London*, vol. A222, pp. 309–368, 1922.

[31] M. J. Gerry, L. C. Potter, I. J. Gupta and A. van der Merwe. A parametric model for synthetic aperture radar measurements. *IEEE Transactions on Antennas and Propagation*, 47(7):1179–1188, July 1999.

[32] L. C. Potter, D.-M. Chiang, R. Carrière, and M. J. Gerry "A GTD-Based Parametric Model for Radar Scattering," *IEEE Trans. Antennas and Propagation*, vol. 43, pp. 1058–1067, October 1995.

[33] L. C. Potter and R. L. Moses, "Attributed scattering centers for SAR ATR," *IEEE Trans. Image Processing*, vol. 6, pp. 79–91, January 1997.

[34] J. B. Keller, "Geometrical theory of diffraction," *J. Opt. Soc. Am.*, vol. 52, pp. 116–130, 1962.

[35] R. G. Kouyoumjian and P. H. Pathak, "A uniform geometrical theory of diffraction for an edge in a perfectly conducting surface," *Proc. IEEE*, vol. 62, pp. 1448–1461, November 1974.

[36] M. Koets and R. Moses, "Image domain feature extraction from synthetic aperture imagery," in *Proc. ICASSP*, Phoenix, AZ, paper no. 2438, March 1999.

[37] H. White, "Maximum likelihood estimation of misspecified models," *Econometrica*, vol. 50, pp. 1–25, 1982.

[38] H. L. Van Trees, *Detection, estimation, and modulation theory part I.* New York, NY: Wiley, 1968.

[39] J. A. O'Sullivan, R. E. Blahut, and D. L. Snyder, "Information-theoretic image formation," *IEEE Trans. Information Theory*, vol. 44, pp. 2094–2123, October 1998.

[40] M. P. Clark, "On the resolvability of normally distributed vector parameter estimates," *IEEE Trans. Signal Processing*, vol. 43, pp. 2975–2981, December 1995.

[41] S. P. Bruzzone and M. Kaveh, "A criterion for selecting information-preserving data reductions for use in the design of multiple parameter estimators," *IEEE Trans. Information Theory*, vol. 29, pp. 466–470, May 1983.

[42] G. Ettinger, G. A. Klanderman, W. M. Wells, and W. Grimson, "A probabilistic optimization approach to SAR feature matching," in *Algorithms for Synthetic Aperture Radar Imagery III* (E. Zelnio and R. Douglass, ed.), pp. 318–329, Proc. SPIE 2757, April 1996.

[43] H.-C. Chiang, *Feature-based classification with application to synthetic aperture radar*, Ph.D. Thesis, The Ohio State University, Columbus, OH, 1999.

[44] C. H. Papadimitriou and K. Steiglitz. *Combinatorial optimization algorithms and complexity.* Prentice-Hall, Englewood Cliffs, New Jersey, 1982.

[45] M. L. Miller, H. S. Stone, and I. J. Cox, "Optimizing Murty's ranked assignment method," *IEEE Trans. on Aerospace and Electronic Systems*, vol. 33, no. 3, pp. 851–861, July 1997.

[46] Y. Lamdan, J. T. Schwartz, and H. Wolfson, "Affine invariant model-based object recognition," *IEEE Trans. on Robotics and Automation*, vol. 6, no. 5, pp. 578–589, October 1990.

[47] I. Rigoutsos and R. Hummel, "A Bayesian approach to model matching with geometric hashing," *Computer Vision and Image Understanding*, vol. 62, pp. 11–26, July 1995.

[48] *MSTAR (public) targets: T-72, BMP-2, BTR-70, SLICY.* Available at http://www.mbvlab.wpafb.af.mil/public/MBVDATA.

[49] C. V. Jakowatz Jr., D. E. Wahl, P. H. Eichel, D. C. Ghiglia, and P. A. Thompson, *Spotlight-Mode Synthetic Aperature Radar: A Signal Processing Approach*, Kluwer Academic Publishers, Boston, 1996.

[50] S. M. Sherman, *Monopulse Principles and Techniques*, Artech House, Dedham, MA, 1984.

[51] W. Blair and M. Brandt-Pearce, "Monopulse doa estimation of two unresolved rayleigh targets," *IEEE Transactions on Aerospace and Electronic Systems* **37**, pp. 452–469, April 2001.

[52] W. Zhen, A. Sinha, P. Willett, and Y. Bar-Shalom, "Angle estimation for two unresolved targets with monopulse radar," *IEEE Transactions on Aerospace and Electronic Systems* **40**, pp. 998–1019, July 2004.

[53] S. M. Kay, *Modern Spectral Estimation, Theory and Application*, Prentice Hall, Englewood Cliffs, NJ, 1988.

[54] J. F. McCann, R. J. Marhefka and B. A. Munk, "Design of a Large Bandwidth Array of Slot Elements with Wide Scan Angle," 2005 IEEE Antennas and Propagation Symposium and Radio Science Meeting in Washington D. C. July 5 - 8, 2005.

[55] B. A. Munk, Finite Antenna Arrays and FSS, Wiley, 2003, pp. 181 - 213.

[56] L. W. Henderson, "Introduction to PMM, Version 4.0," Technical Report 725347-1, The Ohio State University, ElectroScience Laboratory, July 1993.

[57] B. A. Munk, Frequency Selective Surfaces, Theory and Design, Wiley, 2000.

[58] J. F. McCann, thesis under preparation, The Ohio State University, Dept. of Electrical & Computer Engineering.

[59] J. T. Johnson and R. J. Burkholder, "Coupled canonical grid/discrete dipole approach for computing scattering from objects above or below a rough interface," *IEEE Trans. Geosc. Rem. Sens.*, vol. 39, pp. 1214-1220, 2001.

[60] J. T. Johnson, "A study of the four-path model for scattering from an object above a halfspace," *Microwave Opt. Tech. Letters,* vol. 30, pp. 130–134, 2001.

[61] J. T. Johnson, "A numerical study of scattering from an object above a rough surface," *IEEE Trans. Ant. Prop.,* vol. 40, pp. 1361–1367, 2002.

[62] J. T. Johnson, and R. J. Burkholder, "A study of scattering from an object below a rough interface," *IEEE Trans. Geosc. Rem. Sens.,* vol. 42, pp. 59–66, 2004.

[63] L. Tsang, J. A. Kong, and R. T. Shin, *Theory of Microwave Remote Sensing,* New York: Wiley, 1985

[64] A. Voronovich, *Wave Scattering from Rough Surfaces,* Heidelberg: Springer, 1994.

[65] S. L. Broschat and E. I Thorsos, "An investigation of the small slope approximation for scattering from a rough surface: part II- numerical studies," *J. Acoust. Soc. Am.,* vol. 101, pp. 2615–2625, 1997.

[66] G. Soriano, C. Guerin, and M. Saillard, "Scattering by two-dimensional rough surfaces: comparison between the method of moments, Kirchhoff, and small-slope approximations," *Waves in Random Media,* vol. 12, pp. 63–83, 2002.

[67] H. T. Ewe, J. T. Johnson, and K. S. Chen, "A comparison study of surface scattering models", *IGARSS'01,* conference proceedings, 2001.

[68] S. McDaniel, "Acoustic and radar scattering from directional seas," *Waves in Random Media,* vol. 9, no. 4, pp. 537–549, 1999.

[69] J. T. Johnson, "Third order SPM for scattering from dielectric rough surfaces," *J. Opt. Soc. Am. A,* vol. 16, pp. 2720–2736, 1999.

[70] M. S. Gilbert and J. T. Johnson, "Implementation of the higher order small slope approximation for scattering from a Gaussian rough surface," *IEEE Geoscience and Remote Sensing Symposium,* conference proceedings, 2002.

[71] M. S. Gilbert and J. T. Johnson, "A study of rough surface scattering effects using the higher-order small slope approximation," *IEEE Antennas and Propagation/URSI Symposium,* conference proceedings, 2003.

[72] M. S. Gilbert, "A study of the higher-order small slope approximation for scattering from rough surfaces," *M. S. Thesis,* Department of Electrical and Computer Engineering, The Ohio State University, 2003.

[73] M. S. Gilbert and J. T. Johnson, "A study of the higher-order small slope approximation for 3-D scattering from a dielectric Gaussian rough surface," *Waves Random Media,* vol. 13, pp. 137–149, 2003.

[74] T.D. Moore, "Analytical study of space-time and space-frequency adaptive processing for radio frequency adaptive processing," *Ph.D. Dissertation,* The ohio State University, 2002.

[75] I.J. Gupta and T.D. Moore, "Space-frequency adaptive processing (SFAP) for radi frequency interference mitigation in spread-spectrum receivers," *IEEE Trans. Antennas Prop.*, Vol.52, pp. 1611-1616,June 2004.

[76] T.D. Moore and I.J. Gupta, "The effect of interference power and bandwidth on space-time adaptive processing," *IEEE AP Society's International Symposium*, Columbus, OH, Vol. 4, pp. 599-593, June 2003.

[77] T.D. Moore and I.J. Gupta, "Comparision of SFAP and STAP for interference suppression in GPS receivers," *Proc. Of ION's 57th Annual Meeting*, Albuquerque, NM, classified session, June 2001.

[78] I.J. Gupta and M.L. Rankin, "Effects of platform generated jammer multipath on GPS AJ systems, *Technical Report 741718-2*, the Ohio State university ElectroScience Laboratory, June 2003.

[79] Y. P. Zhang, T. K. Lo, Y. Hwang, "A dielectric-loaded miniature antenna for micro-cellular and personal communications," *Proc. IEEE APS-Symposium*, Newport Beach, CA, pp. 1152-1155, June 1995.

[80] B. A. Kramer, M. Lee, C.-C. Chen, J. L. Volakis, "Design and Performance of an Ultra Wideband Ceramic-Loaded Slot Spiral," *IEEE Transactions on Antennas and Propagation*, Vol. 53, No. 7, pp. 2193- 2199, July 2005.

[81] M. Lee, C.-C. Chen, J. L. Volakis, "Ultra-Wideband Antenna Miniaturization Using Distributed Lumped Element Loading," *IEEE AP-S International Symposium and URSI National Radio Science Meeting*, 2005.

[82] D.S. Filipovic, J.L. Volakis, "Broadband meanderline slot spiral antenna," *IEE Proc. Microwaves, Antennas and Propagation*, Vol. 149, Issue 2, pp. 98-105, April, 2002.

[83] B. A. Kramer, C.-C. Chen, J. L. Volakis, "The Development of a Mini-UWB Antenna," *26th Annual AMTA Meeting and Symposium*, Oct. 2004.